Trinity College Dublin
Coláiste na Tríonóide, Baile Átha Cliath
The University of Dublin

School of Physics

Modelling, development and characterisation of Microwave Kinetic Inductance Detectors for optical astronomy

Mario De Lucia

October 10, 2022

A Thesis submitted in partial fulfilment
of the requirements for the degree of
Doctor of Philosophy

Guagliù stateme a senti': questo è il bene [?] e questo è il male [!]. Il bene è il dubbio, quando voi incontrate una persona che ha dei dubbi state tranquilli, vuol dire che è una brava persona, vuol dire che è democratico, che è tollerante, quando invece incontrate questi qui [!], quelli che hanno le certezze, la fede incrollabile, e allora *stateve accorte*, vi dovete mettere paura, perché ricordatevi quello che vi dico: la fede è violenza, la fede in qualsiasi cosa è sempre violenza.

Gli uomini, invece, gli uomini si dividono in uomini d'amore e uomini di libertà, a seconda se preferiscono vivere abbracciati l'uno con l'altro oppure preferiscono vivere da soli per non essere scocciati.
Come esistono uomini d'amore e uomini di libertà, ci sono poi i popoli d'amore e i popoli di libertà. Io su questa cartina dell'Europa ho dipinto in nero i popoli d'amore e in bianco quelli di libertà. L'Italia, la Spagna, l'Irlanda, la Polonia, la Grecia appartengono al mondo dell'amore; l'Inghilterra, la Scandinavia, la Germania, invece, appartengono al mondo della libertà. Poi ci sono i grigi che sono quelli che hanno un po' d'amore e un po' di libertà. Gli inglesi, popolo di libertà, hanno il culto della privacy. In Italia, gli inglesi sono i milanesi.
Gli uomini d'amore non hanno bisogno di spazio, fosse per loro vivrebbero abbracciati l'uno con l'altro.

Luciano De Crescenzo, Così parlò Bellavista, 1984

Agli uomini d'amore.

Declaration

I hereby declare that this project is entirely my own work and that it has not been submitted as an exercise for a degree at this or any other university.

I have read and I understand the plagiarism provisions in the General Regulations of the University Calendar for the current year, found at `http://www.tcd.ie/calendar`.

I have also completed the Online Tutorial on avoiding plagiarism 'Ready Steady Write', located at `http://tcd-ie.libguides.com/plagiarism/ready-steady-write`.

Signed: ____________________ Date: ____________________

Acknowledgements

First and foremost I want to thank my supervisor Prof. Tom Ray for giving me the opportunity to pursue a PhD and for the guidance he's given me and the whole MKIDs group in DIAS over the last four years. I also would like to thank the post-docs that made this work possible: Ivan, Colm, Jack, Oisín and in particular Gerhard whom I'd like to thank for all he has taught me. I would also like to thank Eoin whose scientific contribution to the project was invaluable and whose human contribution was even more so. I would also like to thank my supervisor in TCD, Plamen Stamenov, and his group including Simon Lenne and Gweneal Atcheson who facilitated this work along with Neal O'Hara, Mike Finneran and Riley Gatensby. This material is based upon works supported by the Science Foundation Ireland under Grant No. grant 15/IA/2880. The imaging/analysis for this project was partly carried out at the Advanced Microscopy Laboratory (AML), Trinity College Dublin, Ireland. The AML (www.tcd.ie/crann/aml) is an SFI supported imaging and analysis centre, part of the CRANN Institute and affiliated to the AMBER centre. Some of the fabrication has been carried out at the Tyndall National Institute and I would like to acknowledge their crucial contribution to the results presented in this work.

I want to thank my family: mom, dad, Nonna and Stefania for the support I was given while carrying out this work away from home and through difficult times.
I want to thank my friends. We're scattered all over the globe but I never felt I was too far from you. Vincenzo and Marica, thanks for your priceless friendship. Now, these words are the hardest for me to write as I don't believe I can do justice to your importance, and perhaps I won't try to do it right as I wouldn't be able to regardless. Ada, Antonella, Cacca, Carlo, Davide, Ele, Giovanni, Guido, Nicola, Parillo, Silvia, Stefania. Smè, Tì. Dana, Ale, Misa; Rento, Rob, Silvio, Andrea. You are home.

I want to thank the people who've been around me for the duration of this project: Eileen for taking care of us, none of this would have been possible without your support. Rubén and Maria K., the senior PhDs, thank you for the welcoming environment you created for us when we started. Everyone in the office: Eoin, Anton, Maria M., Camille, Aoife and Ciara, Pearse, Johnny, Shilpi, Dev and Pauline, Antonella.
Lastly, but only to remark your importance, I want to thank Kiara and Gianluca who have been my family in Dublin for three years and Janneke whose impact on my life was beyond equals.

In mezzo a tanti uomini di libertà, siete tutti uomini d'amore.
Mario

Abstract

In this thesis I report on the research I carried out on the topic of Microwave Kinetic Inductance Detectors (MKIDs) over the last four years.

After an introduction chapter and a literature review on MKIDs, Chapter 3 describes the work carried out during the commissioning of a cryogenic laboratory in DIAS. Here, I introduce the primary equipment that was used, including the cryostat and it's electronics, alongside some custom-made parts which I designed, such as the sample boxes for the MKIDs. The fourth chapter includes a description of the two pieces of LabVIEW software that I have developed. The first enables the interfacing of a computer with a resistance bridge in order to perform critical temperature measurements. The second is used to control a monochromator that, along with other sources, was used to illuminate the detectors and to perform optical characterisation of ARIEL dichroics. The two subsequent chapters describe the full development process of an MKIDs array, from the design and simulation of an array (Chapter 5) to the cleanroom fabrication process that I developed (Chapter 6). In Chapter 7, I discuss the importance of understanding and simulating the behaviour and performance of MKIDs in terms of fabrication yield and energy resolution. Chapter 8 addresses the issue of improving the fabrication yield; I propose the DC-bias of selected resonators to re-tune their resonant frequency and achieve an overall 12.5% improvement in fabrication yield. I present a feasibility study, published an SPIE proceedings, and suggest a possible design to reach an 87.5% yield. Chapter 9 details the characterisation process and results of two developed MKID arrays. I also describe the first detector which was capable of producing a detectable pulse when illuminated. It was used as a proof of concept and it exhibits moderate resolving power in the order $R \sim 2 - 3$ in the optical and near-infrared. I Chapter 10 summarises the main results of the experimental research that I have carried out during this PhD. Chapter 11 presents a literature review on the application of MKIDs outside visible and near-infrared astronomy and discusses where else the work presented in this thesis could be applicable; this study forms the basis of a review paper published by the DIAS MKIDs group. Finally, Chapter 12 presents further work that will be conducted at the Dublin Institute for Advanced Studies alongside possible technological improvements on Microwave Kinetic Inductance

Detectors.

In the appendices, the reader can find further details on the experimental setup, the derivation of some equations used in the body of the text and some further discussion on the noise performance of the MKIDs. In Appendix A1, the reader can also find a side project I undertook, which is the optical characterisation of the D-3 dichroic for the Ariel telescope.

List Of Publications

- **M. De Lucia**, E. Baldwin, G. Ulbricht, C. Bracken, P. Stamenov, and T. P. Ray "Multiplexable frequency retuning of MKID arrays using their non-linear kinetic inductance", Proc. SPIE 11454, X-Ray, Optical, and Infrared Detectors for Astronomy IX, 114542Z (13 December 2020); https://doi.org/10.1117/12.2560384
- **M. De Lucia**, E. Baldwin, G. Ulbricht, and T. P. Ray "Modelling the figures of merit of an MKIDs array: understanding fabrication yield and energy resolution", (*in prep.*)
- **M. De Lucia**, E. Baldwin, G. Ulbricht, J.D. Piercy, O. Creaner, C. Bracken and T. P. Ray " Characterisation of a Microwave Kinetic Inductance Detector produced from an annealed TiN/Ti/TiN mulitlayer film", (*in prep.*)
- Ulbricht, G.; **De Lucia, M.**; Baldwin, E. Applications for Microwave Kinetic Induction Detectors in Advanced Instrumentation. Appl. Sci. 2021, 11, 2671. https://doi.org/10.3390/app11062671
- E. Baldwin, **M. De Lucia**, C. Bracken, G. Ulbricht, O. Creaner, J. Piercy, and T. Ray "Frequency Domain Multiplexing for MKIDs: Comparing the Xilinx ZCU111 RFSoC with their new 2x2 RFSoC board", (*under review*)
- C. Bracken, E. Baldwin, G. Ulbricht, **M. De Lucia**, T. Ray "Modeling Results and Baseline Design for an RF-SoC-Based Readout System for Microwave Kinetic Inductance Detectors" (*under review*)
- **M. De Lucia**, E. Baldwin, G. Ulbricht, J. Piercy, D. Coffey and T.Ray, "Low temperature characterisation of the D3 dichroic prototype for ARIEL" (*internal report to the ARIEL collaboration*)
- Thurareithinam V., Baldwin E., Coffey D., **De Lucia M.**, Hawkins G., Piercy J. D., Ray T. P., Savini G., Ulbricht G. "Monte Carlo transmission line modelling of multilayer optical coatings for performance sensitivity of a dichroic filter for the ARIEL space telescope" (*in prep.*)

Contents

List of Figures

List of Tables

List of abbreviations

ADC	Analogue to Digital Converter
au	Astronomical Unit
ARIEL	Atmospheric Remote-sensing Infrared Exoplanet Large-survey
CCD	Charge Coupled Device
CRANN	Centre for Research on Adaptive Nanostructures and Nanodevices
DAC	Digital to Analogue Converter
DIAS	Dublin Institute for Advanced Studies
ELT	Extremely Large Telescope
ESA	European Space Agency
ESO	European Southern Observatory
FPGA	Field Programmable Gate Array
HST	Hubble Space Telescope
HZ	Habitable Zone
IF	Intermediate Frequencies
MKID	Microwave Kinetic Inductance Detector
MSPS	Mega Samples Per Second
NASA	National Aeronautics and Space Administration
PMT	Photomultiplier Tube
VNA	Vector Network Analyser
SCCM	Standard Cubic Centimetre per Minute
S.D.	Standard deviation
T_c	Critical temperature
TES	Transition Edge Sensor
TLS	Two Level Systems
UCSB	University of California Santa Barbara

List of constants

All constant are in standard units as defined by the International System unless stated otherwise:

1 au	1.496×10^{11} m
$\hbar$	$1.0545718 \times 10^{-34}$ m^2 kg/s
K_B	1.380649×10^{-23} J/K
K_B	$8.617333262145 \times 10^{-5}$ eV /K (non S.I.)

1 Introduction

1.1 Photon Detectors

Light detection is crucial for many applications, ranging from astronomical detectors in highly technological telescopes, to commercial cameras intended for the general public. From sophisticated body scanners in airport security and health sciences, to specialised machinery in factories. Even though there is a wide variety of photon detectors, which can be more or less suitable to each different application, there are only a few detection mechanisms. Most of them are based on the idea that the detection and processing of variations in an electrical signal is easy, at least in theory. Among these, the most commonly used detection mechanisms involve:

- The photoelectric effect
- Thermal excitation
- Pair breaking

While any further details on the first mechanism is redundant, the basic details can be found in Einstein's 1905 paper that resulted in him being awarded a Nobel Prize (21) in 1921, thermal excitation describes the phenomenon whereby photons heat up a detector changing its temperature which in turn induces a change in the electrical properties of the readout circuit. Pair breaking refers to exciting a superconductive Cooper Pair out of its superconducting state, thus generating brand new type of particles which are often referred to as quasi-particles.

The first category features the two most widespread types of photodetectors, Photomultiplier Tubes (PMTs) and Photodiodes (which exploit the internal photoelectric effect) (22). PMTs were originally developed in the 1930s and used extensively until, and even beyond, the year 2000; mostly for scientific applications such as Super-Kamiokande (23) and the most recent update of the Pierre Auger Observatory (24). Their basic operating principle is the deployment of a standard vacuum tube with multiple secondary-emission electron amplification stages. The first electron is created when a photon strikes the photo-cathode made from material favouring the photoelectric effect in the wavelength range of interest. A series of electrodes in the vacuum tube produce further electrons through secondary-emission, effectively amplifying the signal. The electrons are collected at the anode, which produces an electrical signal, after a time Δt from the extraction of the first electron, as a response to the photon hit. Semiconductor-based detectors are currently the most commonly used photodetectors in almost every field of application due to their small size and their great integrability. Photodiodes exploit a p-n junction as the light-sensitive element. A photon penetrating a photodiode produces an electron-hole pair in the bulk material. When an electric field is applied across the junction, the charges thus generated can be collected at either electrodes of the diode, hence producing an electrical signal. Depending on technological needs, semiconductor-based photodetectors may or may not not exhibit amplification and energy resolution, and may have significantly different detection efficiencies at different wavelengths. Most astronomical instruments deploy semiconductor-based detectors, such as the Wide Field Camera 3 on the Hubble Space Telescope (25), and the forthcoming Cherenkov Telescope Array (26).

Thermal detectors, or bolometers, are mainly used for very niche applications, mostly in astronomy and particle physics. Instruments such as Herschel (27), Scuba-2 (28), and LNGS's experiment CUORE (29) deploy bolometric detectors. Bolometers rely on the change of a physical quantity, such as the conductivity of a material with varying temperature. An example is the so-called Transition Edge Sensor (30)(31), a particular subclass of cryogenic superconducting detectors which are operated at temperatures very close to their critical temperature. When a photon strikes, the detector heats up and might experience a transition to its normal state. The transition generates a change in conductivity, which is then read out.

Finally, pair breaking detectors rely on photons exciting, directly or indirectly, superconducting Cooper Pairs into their normal state, thus changing the superconducting current density. This has different effects for Superconducting-Nanowire Single Photon Detectors, SNSPDs, (32) or Microwave Kinetic Inductance Detectors, MKIDs,(33). MKIDs, in comparison with semiconductor-based detectors, are sensitive to light in a wide range of wavelengths: from the millimeter to X-Ray bands. Furthermore, MKIDs exhibit inherent energy resolution shortward of the infrared band, are single photon sensitive, and being operated at cryogenic temperatures, can count photons with no thermal noise. MKIDs are the main topic of this thesis and the coming pages will describe the applications of this technology in the field of astronomy.

1.2 Astronomical applications

One of the big challenges in astronomy for the next few decades is the study of extra-solar (exo) planets and *here MKIDs may play an important role in the future.* For example, ESA and NASA funding for Ariel (34), LUVOIR (35) and HABEx (36) missions underscores the importance of this topic in modern astronomy. The study of exoplanets is starting to answer one of the "big questions" of mankind. In 400 B.C., Aristotle started debating whether the world we live in is the only one possible and we are alone in the universe or if there is a "plurality of worlds", which he could not imagine. Currently, the scientific community does not have an answer to this question, yet humanity is now at a stage where it is deploying space missions and ground-based facilities to try and at least examine the possibility of life outside the Solar System. Furthermore, planet-forming systems are still a hot topic of interest, thus further, high quality, observations will be of great interest for the scientific community.

The habitable zone (HZ) was firstly introduced in 1959 by Su-Shu Huang (37) and describes the orbital area surrounding a star, within which, life as we know it is possible. Practical considerations on a star's stability, over long time scales, provide an initial guess on which stars could possibly host inhabited or habitable exoplanets. Huang suggests that the most reliable candidates would be lying on the main sequence and would be class F (late), G or K (early) stars.

The size of the habitable zone, arguably, depends on the luminosity of the star; brighter stars have a larger HZ and *viceversa*. Nonetheless, the inner and outer limits of the HZ are well defined and reflect the temperature of the planet. The inner limit is given by the distance at which the greenhouse effect in the planet's atmosphere is blocking thermal radiation from the planet's surface, resulting in the evaporation of liquid water on its surface. The outer limit is given by the distance where the greenhouse effect fails to keep the surface of the planet warm, and any water, if present, would only be found in the form of ice.

There are multiple indirect ways to detect exoplanets, such as radial velocity and transit spectroscopy. However, a direct detection is desirable as, with the right detectors, this would allow for broad spectroscopic measurements of their atmosphere in order to understand their composition. There are a number of challenges when it comes to observations of exoplanets. The habitable zone of most stars only extend to a few astronomical units (au) which, given the distance of even the nearest exoplanets, means they are very close to their parent star in angular terms (typically a fraction of an arcsecond). This makes the observation of such planets extremely difficult due to (a) the enormous contrast in brightness between the star and its planets (a factor of 10^{10} in some cases) and (b) the angular resolution needed being less than the typical seeing for ground-based telescopes. The answer to (a) is to equip the telescope with a coronagraph thereby considerably reducing the light from the central star. The response to (b) is to use Adaptive Optics (AO) to reduce the effects of atmospheric turbulence, i.e. to improve the Point Spread Function (PSF). AO involves challenging technology employing rapidly deformable mirrors in the optic train. The combination of AO and chronograph will, for example, be fundamental to

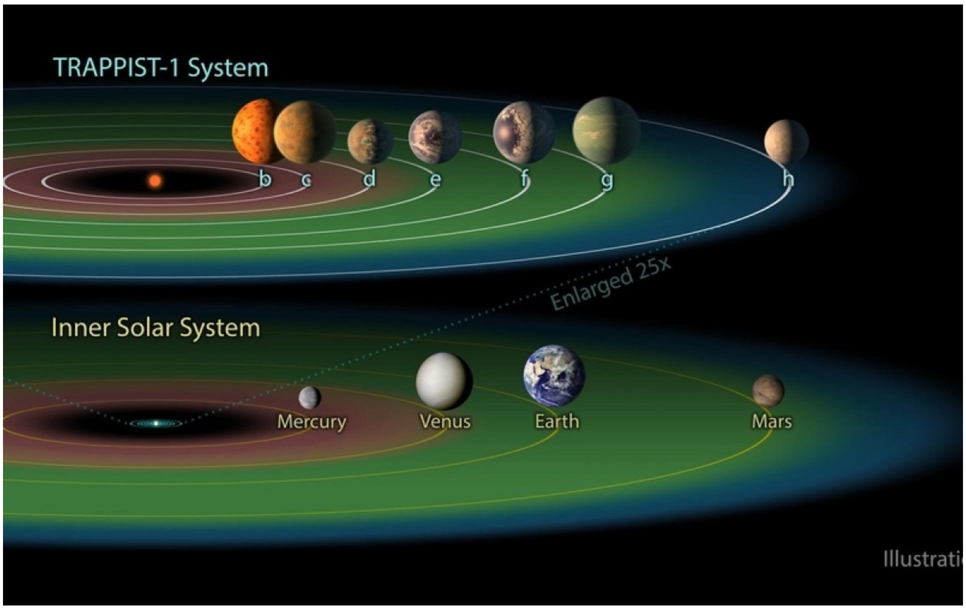

Figure 1.1: Diagram of the habitable zone of the TRAPPIST-1 system compared with the habitable zone of the Solar System. The area shaded in red is too warm for liquid water to exist and the area shaded in blue is too cold. The habitable zones are shaded in green. credit: NASA/JPL-Caltech

the instrumentation of ESO's Extremely Large Telescope (ELT) if it is to reach its goal of imaging earth-like planets (38).

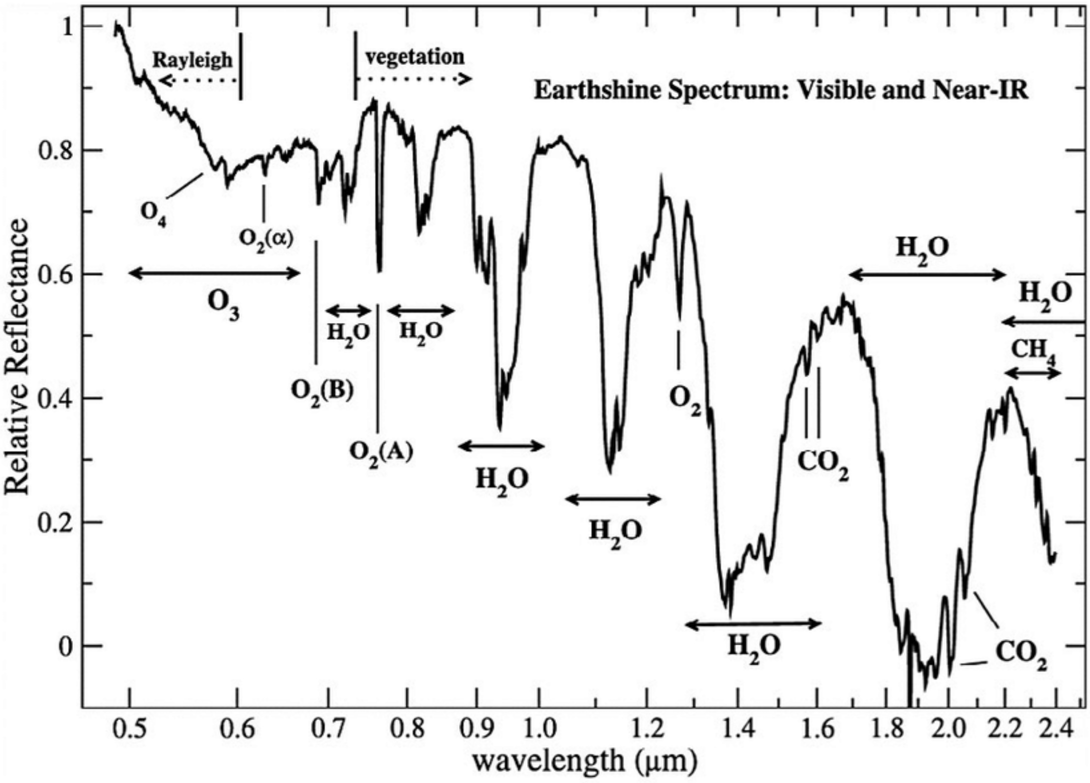

Figure 1.2: Earthshine spectrum in the visible and near infra-red. Republished after (1)

Figure 1.2 shows the spectrum of the light reflected from Earth (1). The top left

section of the spectrum uniquely depicts our planet, it accounts for the Rayleigh scattering which makes the planet the *pale blue dot* it is known to be. With increasing wavelengths, Oxygen compound peaks start to show: molecular Oxygen, O_2, Ozone, O_3, and gaseous water, H_2O. In the infrared, Carbon peaks start appearing; CO_2 appears in the H-band and again in the K-band, along with CH_4. It is important to re-state that the exoplanets are extremely faint objects and a telescope would only receive a few tens of photons per second per square meter. It is therefore necessary that the least amount of photons are "wasted". In other words, single-photon sensitive detectors are essential for any instrument that aims to perform direct observations of exoplanets. Here, Microwave Kinetic Inductance Detectors can play a role of great relevance, as they are naturally sensitive to single photon events in a very broad range of wavelengths, including the near-infrared where common Si CCDs begin to fail. When compared to CCDs, the readout time of MKIDs is about three orders of magnitude faster (39, 40). Their μs readout time can be extensively used with Adaptive Optics systems in order to maximise the speckle reduction capability of the instrument. Furthermore, MKIDs have a moderate energy resolution that combined with the fast readout can make MKIDs perfect as wavefront sensors at telescope sites where Adaptive Optics is deployed.
To date, the direct observation of habitable exoplanets has not been attempted; both ARCONS and DARKNESS, two MKIDs instruments developed at UCSB, were deployed at Palomar Observatory, where observations were carried out. ARCONS (Array Camera for Optical to Near-IR Spectrometry) observed the interacting galaxies Arp 147 as a proof of concept. Figure 1.3 shows the image captured with the MKIDs based instrument compared to a HST picture of the same system.

It is important to explain the origin of the differences between the quality of the ARCONS image compared to its HST counterpart. Two factors come into play to justify the visual differences: ARCONS is a 2000 pixels instrument while Hubble has several million pixels. More importantly, HST is a 2.5 m space telescope and atmospheric turbulence and speckles do not affect the sharpness of its picture, whereas ARCONS was deployed in Palomar Observatory on the Hale Telescope.

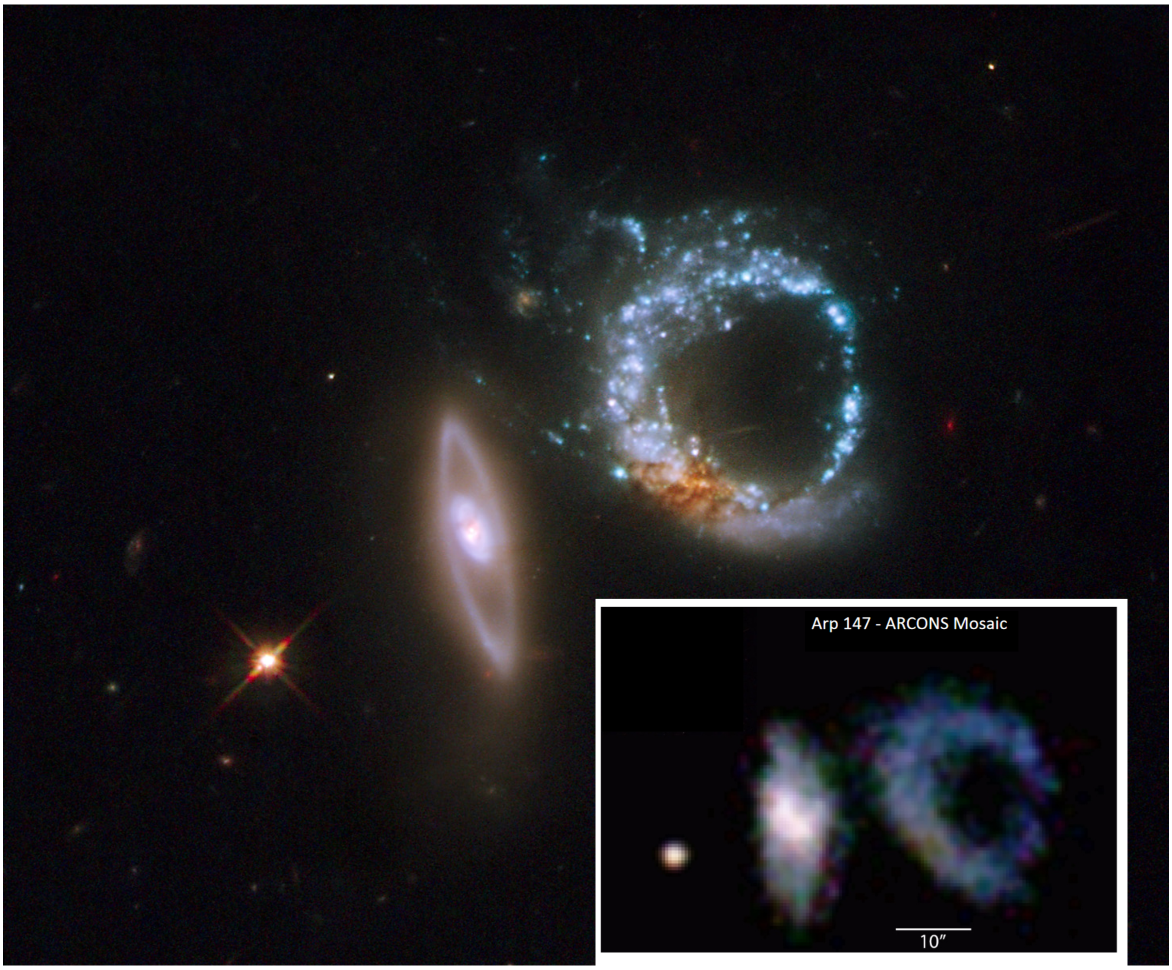

Figure 1.3: Arp 147 as observed by the Hubble Space Telescope. Credit: NASA, ESA, and M. Livio . Inset: Arp 147 as observed by ARCONS (2)
.

The latter is a 5 m ground-based telescope, and its pictures are strongly affected by the Earth's atmosphere. DARKNESS observed the multiple star system 10 Uma (3), a binary system where the stellar companion is separated by $0.4''$. The picture obtained by this observation is shown in Figure 1.4. DARKNESS resulted in an effective proof of concept where MKIDs have been successfully used to improve the contrast ratio at the telescope and to shadow the host star and reduce the speckles produced by the atmospheric turbulence.

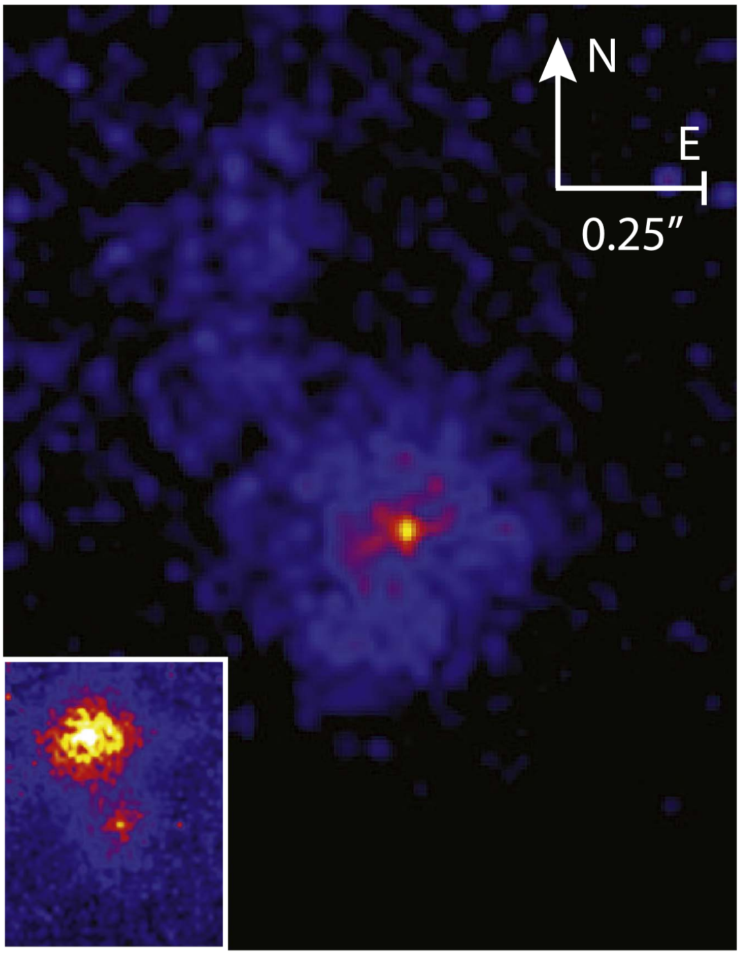

Figure 1.4: 32 Pegasi Ab as observed by DARKNESS. Most of the light from the main star was blocked by a coronagraph. The inset shows the binary system where the light from the main star is not stopped (3).

2 Scientific background

The first chapter of this thesis is intended as a literature review that provides the reader with an overview of the state of the art and enough background information to make the rest of this work intelligible. Firstly, a phenomenological introduction to superconductivity and a brief discussion of what kinetic inductance is. An in-depth introduction to Microwave Kinetic Inductance Detectors is presented before presenting the readout technique and a brief discussion on the materials that can be used for the fabrication of such devices.

2.1 Solid State Physics: Theory

The first section of this chapter includes a phenomenological discussion of superconductivity. Here the most important effects are described including the loss-less transport of a current of charged carriers (Cooper pairs), the shielding of magnetic fields (Meissner effect), and the opening of a superconducting bandgap. This section also describes Drude's model for a metal which describes the phenomenon of kinetic inductance and why it is only relevant in superconductors when high frequency AC current is flowed through them.

2.1.1 Phenomenology of superconductivity

The Dutch Physicist Kamerlingh Onnes started experimenting with metals at sub-liquid helium temperature in 1911. It was well known that resistance decreased as the temperature of the metal decreased (Figure 2.1), but, to everyone's surprise, while experimenting with mercury he noticed that, at temperatures close to that of liquid helium, its resistance would vanish completely. The mercury had transitioned into a new state which he named "superconductive". Further studies have been carried out on metals to properly understand the phenomenon of superconductivity. The phenomenology of these metals is briefly described in this paragraph.
Superconductivity arises when an attractive interaction between outer shell electrons occurs. The mechanism is well described by the Bardeen-Cooper-Schreiffer (BCS) theory (41).
For temperatures below the critical temperature, defined as the temperature at which

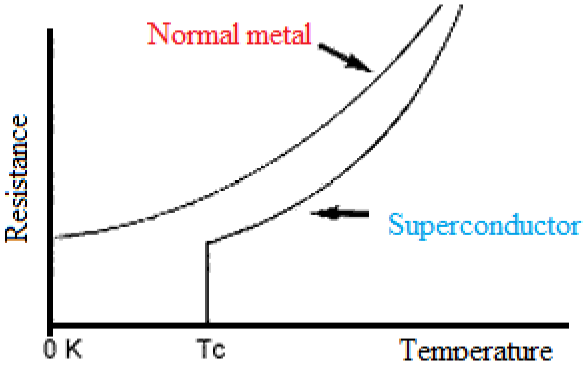

Figure 2.1: Resistance versus Temperature for both a normal metal and a superconductor.

the resistance of the metal drops to zero, the attractive interaction leads to the formation of a bosonic state in which electrons are highly-correlated (Cooper pairs). The main properties evident from this state-transition are not only perfect conductance, but also perfect diamagnetism, an anomalous specific heat and the creation of an energy gap, $2\Delta_{qp}$, in the quasi-particle spectrum. (4)

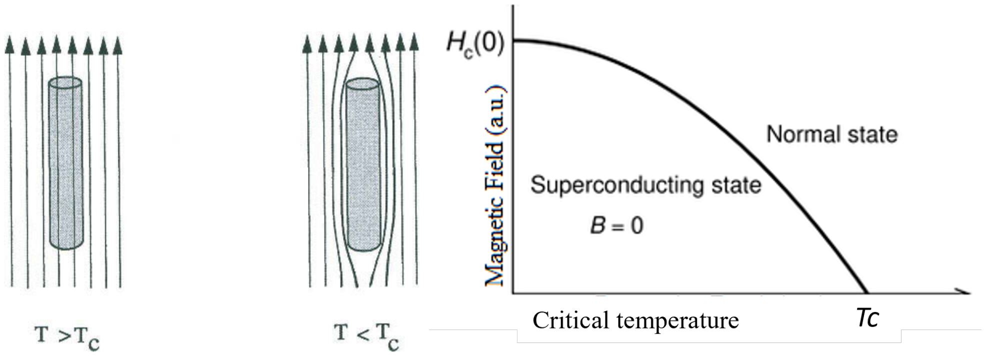

Figure 2.2: (left) Exclusion of a weak external magnetic field from the interior of a superconductor, from (4). (right). A schematic phase diagram of a Type-I superconductor in a magnetic field, after (5)

If a not-too-strong external magnetic field is applied to a superconductor which is in thermal equilibrium at a temperature below its critical temperature, superconductive currents are generated on the surface of the metal. These currents are so that the magnetic field they generate cancels out completely the magnetic field inside the superconductor. This is known as the Meissner Effect (42). As the external magnetic fields increase, two phenomena can occur, either the superconducting state is fully suppressed (Type-I) or, above a lower threshold H_{c1} and below H_{c2}, the magnetic field partially penetrates the surface creating so-called *vortices*. Past the second threshold, H_{c2}, the superconducting state is fully disrupted. The super currents are distributed in a small volume around the surface, the distance which is penetrated by a magnetic field before it is suppressed by a factor e, is commonly known as the London penetration depth λ_L.

When a metal transitions to the superconducting state, an energy gap of $\Delta_{qp}$is created as shown in Figure 2.3. Here, and in an analogous way to the operation of a semiconductor, the bond between paired electrons (Cooper Pairs), can be broken only if the energy delivered to them is greater than $2\Delta_{qp}$. The value of which increases with the decrease of the temperature. In the limit of $T \to 0$, $\Delta_{qp} \to \Delta_s$. The analytical form of which, according to Mattis-Bardeen's theory (4), is

$$\Delta_s = 1.764 k_B T_C \tag{1}$$

The occurrence of an energy gap, defined with respect to the so-called Fermi level, in

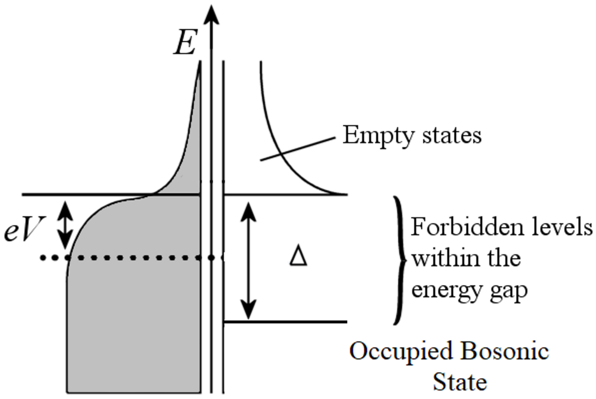

Figure 2.3: Diagram of a normal metal (left) and a superconductor (right). A normal metal has no gap in its single particle spectrum, while it is clear that about the Fermi Energy there is a gap of Δ that divides the occupied and unoccupied states.

the excitation spectrum of a superconductor gives rise to serious property changes, that are sensitive to modifications at and near the Fermi level. For the sake of clarity, the Fermi level is defined as halfway between the superconducting bandgap. Among these, and of relevance to practical uses, are perfect conductance, magnetic shielding, and photon absorption.

2.1.2 Kinetic Inductance

Kinetic inductance is a reactive phenomenon that arises in superconductors when immersed in an AC electromagnetic field and is physically related to the inherent inertia of an electron in an oscillating field. Drude's model, despite it being fully-classical, shows the arising of an inductive component in loss-less metals. For the computation of the Drude model for metals, electrons are assumed as gas-like particles free to move within the volume of the metal and ions are considered to be immobile in their atomic sites (42). The classical equation of motion for each electron of this system, when immersed in an external electric field $\mathbf{E}(\mathbf{r},t) = \mathbf{E_0} e^{i(q\cdot r-\omega t)}$ is the following (4):

$$m\,\ddot{r} = \frac{-m}{\tau}\dot{r} + (-e)\mathbf{E_0} e^{i(q\cdot r-\omega t)} \tag{2}$$

where $\mathbf{r}$(t) is the coordinate of each particle, (q) is the wave vector, ω is the frequency of the external electric field and τ is a phenomenological relaxation time. The dissipative term (first term on the right-hand side of the equation) refers to a mechanism in which random collisions occur between electrons and whatever kind of impurities. The solution of this equation is beyond the this work and can be found in (4). The electrical conductivity then becomes

$$\sigma(\omega) = \frac{ne^2\tau}{m}\frac{1}{1-i\omega\tau} = \frac{ne^2\tau}{m}\frac{1}{1+\omega^2\tau^2} - i\frac{ne^2\omega\tau^2}{m}\frac{1}{1+\omega^2\tau^2} \tag{3}$$

For a standard metal in a non-superconducting state, the relaxation time τ is normally of the order of 10^{-14} s and, for frequencies lower than 100 GHz,the imaginary component of the conductance can be neglected with respect to the real one. In fact it is only significant in superconductors where the relaxation time $\tau \rightarrow \infty$. Under these conditions, the second term of Equation 3 becomes

$$-i\frac{ne^2}{m\omega} = -i\frac{1}{\omega l_k} \tag{4}$$

where $l_k = \frac{m}{ne^2}$ is a reactive component,equivalent to an inductance, arising from the finite mass of the electrons. For a wire of length l and cross section A, the inductive component of the conductance is

$$L_k = l_k\frac{l}{A} = \frac{m^*}{ne^{*2}}\frac{l}{A} \tag{5}$$

Where m^* and e^* take into account the mass and the charge of the carriers for either normal or superconducting metals. The kinetic inductance increases as the carrier density goes down. The physical reason behind this is that a smaller number of carriers needs to have a greater velocity to sustain the same current.

Having described here a classical model it does not hold under all circumstances. For instance, if the thickness of the superconductor is comparable to the London

penetration depth of the superconductor. For the sake of this thesis, understanding the classical argument for the origin of the kinetic inductance is sufficient. Further details on the kinetic inductance of superconductors can be found here
(4, 43, 44)

2.1.3 Kinetic inductance non linearity

The electrodynamics of superconductors has been studied intensively and it has long been known that the kinetic inductance of a superconductor, when a current flows through it, has a non-linear dependence on the amplitude of such a current (45), (46). In the limit $T \ll T_c$, the kinetic inductance of a superconducting strip can be expanded as:

$$L_k = L_0 \left(1 + \frac{I^2}{I_0^2} + ...\right) \tag{6}$$

It is clear that any odd term in the expansion has to be zero, due to symmetry reasons, and an expansion to its second, non zero term, is accurate enough to model the phenomenon. Here, L_0 is the kinetic inductance as defined in the previous section, I is the current flowing through the superconductor and I_0 is a scaling factor and, according to literature, it is known to be of the same order of the critical current, (39),(47)

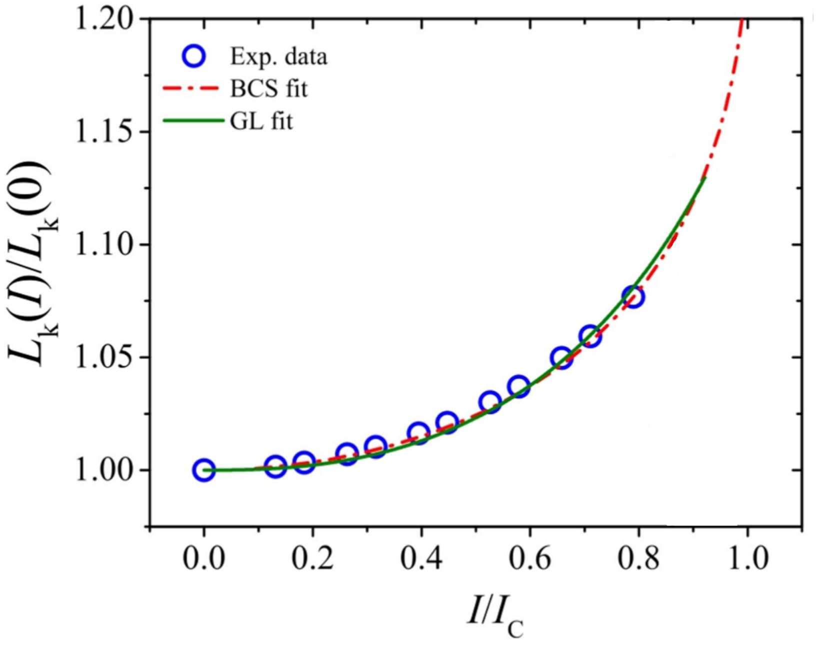

Figure 2.4: Measured current dependence of the relative kinetic inductance fitted with BCS and Ginzburg-Landau theory. Adapted from Doerner S. et al., (6)

2.2 Microwave Kinetic Inductance Detectors

This section will describe in detail what Microwave Kinetic Inductance Detectors are, their working principles and the parameters that determine the quality of their performances. Figure 2.5 (left) shows the components that make up an MKID, and a schematic of its design. Figure 2.5 (right) shows a 10 kilo pixel MKIDs array produced in UCSB for their DARKNESS instrument (7).

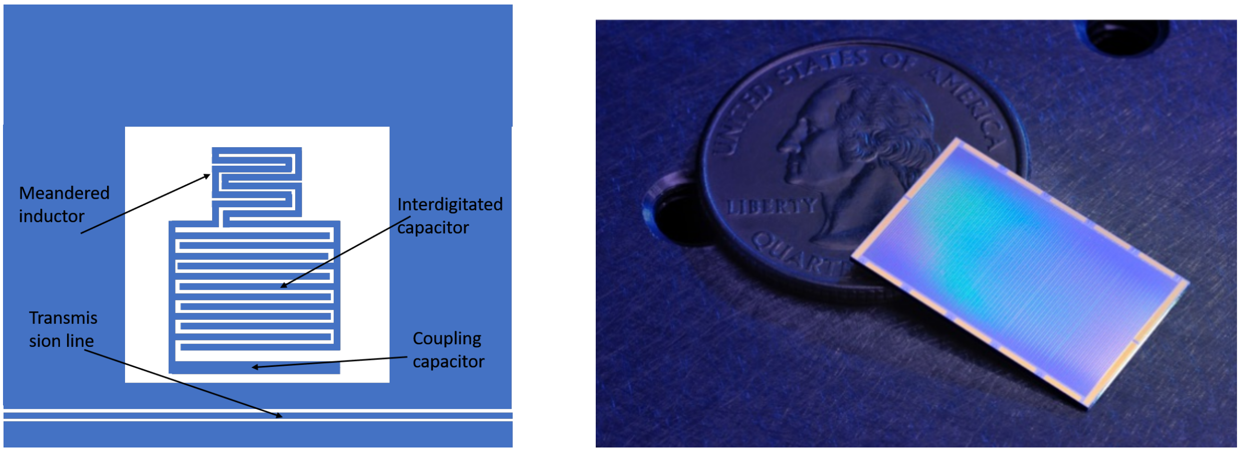

Figure 2.5: Left: Heads-on view of a Microwave Kinetic Inductance Detector, all its elements are highlighted. The meandered inductor, on the top part of the figure, is the light sensitive element. The silicon substrate is shown in white. Right: A 10 kilo-pixel MKIDs array produced by Ben Mazin's group at UCSB. (7)

2.2.1 Superconducting micro-resonators

Microwave Kinetic Inductance Detectors, MKIDs, are $L - C$ superconducting resonators, coupled to a transmission line through a coupling capacitor, and originally proposed by Peter Day et al. in 2004 (33). A schematic representation of an MKID is shown in Figure 2.6. In Figure 2.6(b) the resonator is a $LC - parallel$ circuit coupled via a capacitor to the transmission line. Here the inductance is shown as a variable inductor that is struck by a photon of energy $h\nu$. Thus the inductor is envisaged as the photosensitive element and that, a photon absorbed by the resonator temporarily changes the kinetic inductance of the superconductor, and hence the resonant frequency of the MKID. Figure 2.6(a), instead, shows the mechanism by which a photon excites a Cooper Pair out of its superconducting state creating quasi-particles, effectively unpaired electrons, before condensating again in the superconducting ground state. Figure 2.6 (c) and (d) describe the shift in resonance frequency and phase. The resonant frequency of an $L - C$ circuit is known to be $f_0 = 1/\sqrt{LC}$. An increase in kinetic inductance, due to an impinging photon, produces a shift, towards lower values. This effect can either be seen as a shift, and an attenuation of the resonator's dip (c), or by monitoring the dephasing between the input and the output signal. In the latter framework, it is the zero-dephasing frequency that shifts to the left, producing a non-zero dephasing at $f = f_0$, as shown in (d). After (33)

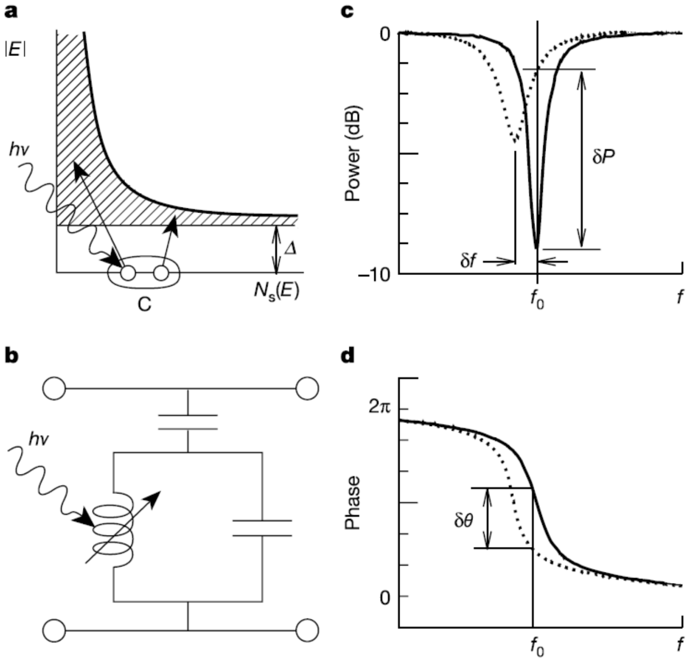

Figure 2.6: a: the pair-breaking process by which a photon with energy greater than 2Δ creates quasi-particles and increases the kinetic inductance of the superconductor. b: schematic of a Microwave Kinetic Inductance Detector, described as a variable inductor in parallel with a capacitor, the LC circuit is then coupled via a capacitor to a transmission line. c: frequency shift and dampening as produced by a photon impinging on the MKID. d: The shift in resonant frequency produces a measurable dephasing $\delta\theta$ at $f_0 = 1/\sqrt{LC}$

It is important to note that the number of quasi-particles created, N_{qp}, strongly depends on the energy of the photon $h\nu$, and the superconducting energy gap Δ_s: $N_{qp} = \frac{\eta h\nu}{\Delta_s}$. Where η is the energy conversion efficiency (48). The remaining energy is dissipated through phonons and other processes. From Mattis-Bardeen (49) considerations, it is possible to evaluate the fractional impedance $\frac{\delta Z_s}{Z_s}$ change due to the photon hit (49),(7).

$$\frac{\delta Z_s}{Z_s} \approx \frac{n_{qp}}{2N_0\Delta_s} \tag{1}$$

In this picture, n_{qp} is the quasi-particle density, N_0 is the density of states at the Fermi energy and Δ_s is the superconducting energy gap. It is meaningful to stress that this change in impedance depends linearly on n_{qp}, therefore on the energy on the striking photon and inversely on the superconducting gap energy.

The excited quasi-particles tend to recombine into their ground-state of bosonic Cooper pairs with a time constant that is usually referred to as quasi-particle lifetime τ_{qp} which ranges widely from a tens of μs up to a few seconds (7, 39, 50, 51). MKIDs respond to a photon event with fast change in their resonance frequency and a slow exponential relaxation back into their "resting" position. Thus a photon-induced pulse can be as long as five to ten τ_{qo}.

An easy visualisation of an MKID, described in full details in (12) begins with a simple model of an $LC - parallel$ circuit coupled to two transmission lines of impedance $Z0$ as shown in Figure 2.7. As described in (52), the circuit can be further simplified to an element of admittance Y, which describes the MKID and two transmission lines of admittance Y_1 and Y_2.

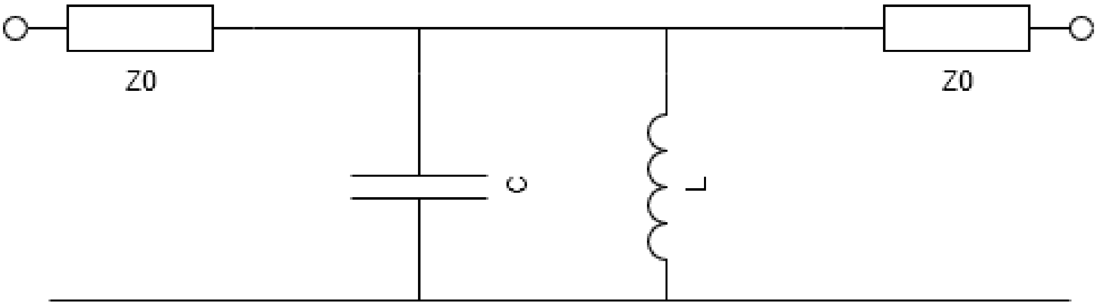

Figure 2.7: A network schematic of an LC-resonator connected to a transmission line with impedance Z_0. After (8)

$$\begin{pmatrix} S_{11} & S_{12} \\ S_{21} & S_{22} \end{pmatrix} = \frac{1}{Y_1 + Y_2 + Y} \begin{pmatrix} Y_1 - Y_2 - Y & 2\sqrt{Y_1 Y_2} \\ 2\sqrt{Y_1 Y_2} & Y_1 - Y_2 - Y \end{pmatrix} \tag{2}$$

where $Y_1 = Y_2 = \frac{1}{Z0}$ and $Y = \frac{1}{i\omega L} + i\omega C$. It can be shown (8, 12) that the forward transmission element from the transfer matrix S_{21} can be evaluated as:

$$S_{21}(\omega) = \frac{1}{1 + Q_{tot}\left(\frac{\omega - \omega_0}{\omega_0}\right)^2} \tag{3}$$

Where $\omega_0 = \frac{1}{\sqrt{LC}}$ is the resonant frequency f_0, and $Q_{tot} = \frac{\omega_0 Z_0 C}{2}$ is a parameter referred to as the total quality factor. Its importance will be discussed in the next pages. Once the complex trans-characteristics (Y) are known, the real and imaginary parts can be plotted to describe the resonance loop in a complex I-Q plane. A far more accurate model is described in Jiansong Gao's PhD thesis (53). He provided the following equation for the transmission of an MKID:

$$S_{21}(\omega) = ae^{-2\pi i\omega\tau_{cable}}\left[1 - \frac{Q_{tot}/Q_c e^{i\Phi_0}}{1 + 2iQ_{tot}\left(\frac{\omega - \omega_0}{\omega_0}\right)}\right] \tag{4}$$

Where a is a complex constant that depends on gain and phase shifts on the transmission line (7), τ_{cable} is the cable delay. The first block, $ae^{-2\pi i\omega\tau}$, describes the properties of the transmission line, it basically creates an attenuation and a global phase shift depending on the length of the cabling and the probe frequency ω. Φ_0 is related to the phase angle, which describes the position of the resonant loop in the I-Q plane. The phase angle is of crucial importance when it comes to fitting algorithms. and Q_C is a quality factor that represents the coupling of the resonator to the transmission line through the amount of power lost in the coupling. A high value of Q_C indicates weak coupling, and *vice-versa.* Typical values are in the order of $Q_C = 15000 - 50000$. Q_i,the internal quality factor, describes the power lost inside the superconductor itself and it strongly depends on the material, its deposition process and the fabrication of the resonator. Again, a high value of Q_i indicates low losses, and can be used as a figure of merit to indicate the *quality* of the superconducting film. Ideally, the higher the internal quality factor, the least impact it has on the total quality factor Q which, for an ideal superconductor is equal to the designed coupling quality factor Q_C. Unfortunately, it is not possible to readily tune the internal quality factor to a desired value, but rather, the whole fabrication process has to be optimised in order to yield the best resonators possible. Typical values of Q_i are $\approx 10^5$, but for TiN on Si and $PtSi$ on sapphire, values of 10^6 have been demonstrated (7). Fitting the resonator loop in the I-Q plane to S_{21}, the best estimate for the values of Q_C and Q are determined. Knowing the quality factor sum rule:

$$\frac{1}{Q_{tot}} = \frac{1}{Q_C} + \frac{1}{Q_i} \tag{5}$$

the best estimate for Q_i can therefore be evaluated. Figure 2.8 shows a fitted I-Q loop with best estimates for the quality factors, as well as the fitted amplitude and phase components of the I-Q loops.

2.2.2 Multiplexing

One of the great advantages of MKIDs over other competing cryogenic detectors, is their inherent multiplexing. Multiple MKIDs can be read out at once with the same transmission line provided that each single resonator has its unique resonant frequency. High quality resonators can be close packed on one single transmission line: for example if the total quality factor $Q_{tot} = 30000$, reflecting a line width of 200 kHz, it is, in principle, possible to have resonators with resonant frequencies that are only 2 MHz apart. This limitation is only inferred by the Fast Fourier Transform (FFT) and its speed. The longer is the signal fed into the FFT, the narrower is the FFT bin thus produced. A state of the art optimum is given by a 1 readout time, which results in 1 MHz wide FFT bins. The 2MHz limitation is for extra safety. Further details on the readout and the frequency constraints can be found in Eoin Baldwin's PhD thesis (8). Since the widest octave low-noise High Electron Mobility Transistors (HEMTs) (54) exhibit a band pass 4 GHz wide, and given the finite width of each individual resonator, it is possible to lay up to 2000 pixels on a single transmission line. This property is of crucial importance when it comes to the readout electronics: first of all, in order to read out a 10K pixel array, it is only necessary to avail of 10 coaxial cables, and 5 HEMTs. Furthermore, since each single feed-line has to be read out through its unique readout electronics board, again, only

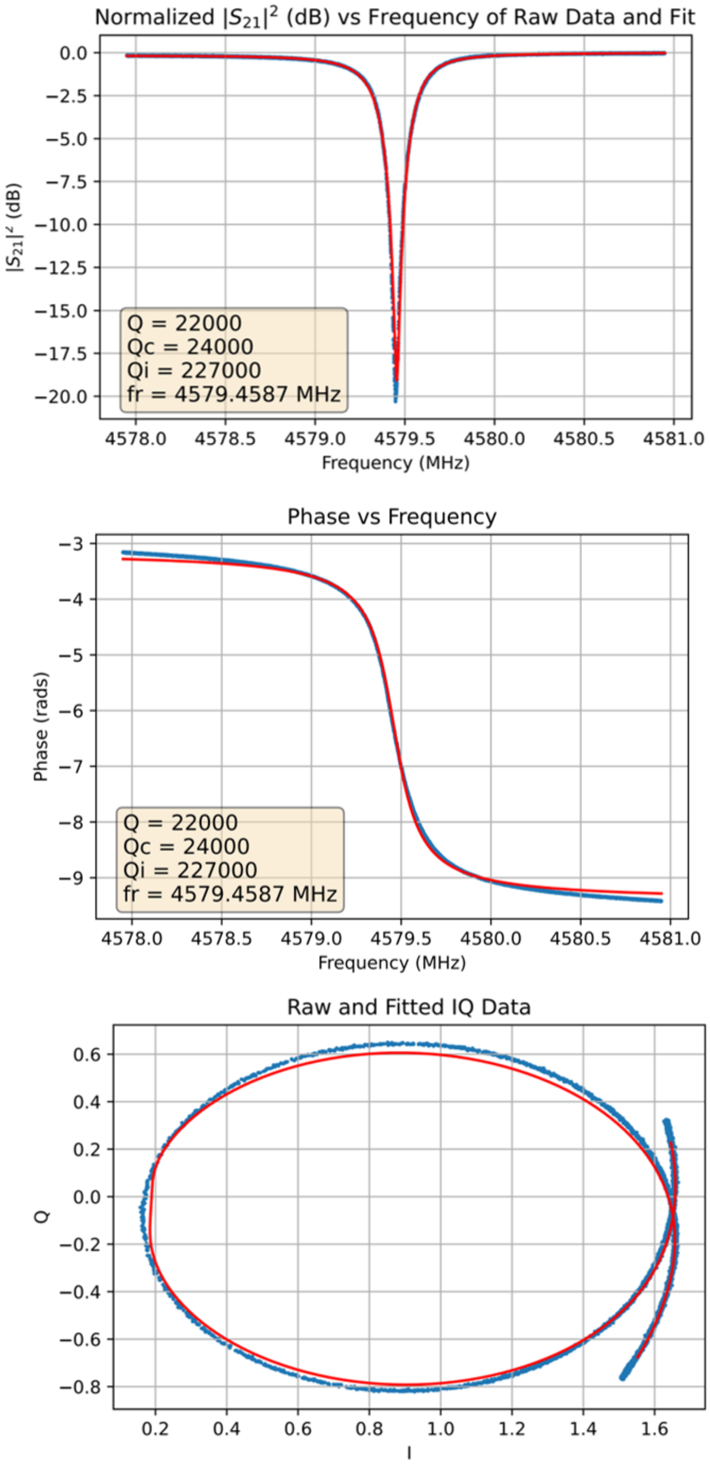

Figure 2.8: Top: S_{21} as a function of frequency, fitted curve in red. Centre: Phase as a function of frequency, fitted curve in red. Bottom: Resonant loop in the IQ plane, fitted curve in red. Data from Chapter9

5 boards are necessary. This is a great advantage over competing technologies when it comes to cost, power consumption and the footprint of the readout electronics itself. Figure 2.9 shows a scan in frequency of the real part of S_{21}. Multiple resonance dips are seen in the figure, each single one of them represents an MKID with its unique resonance frequency.

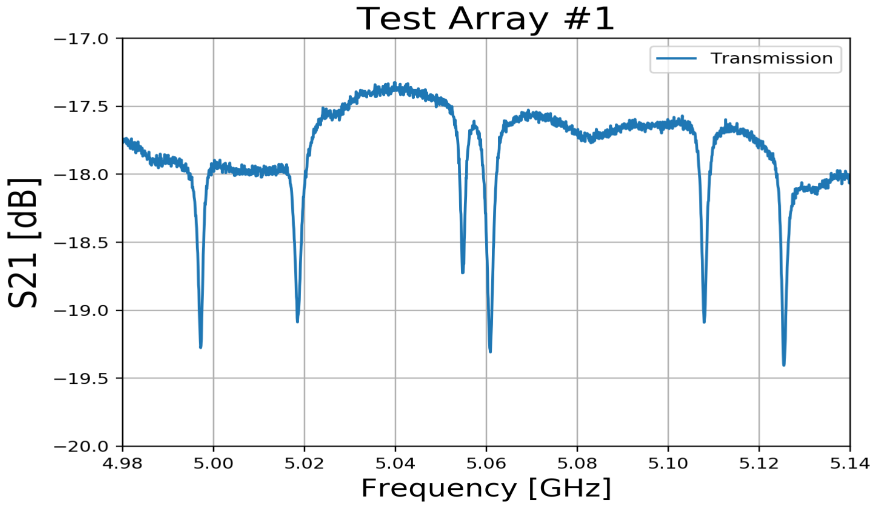

Figure 2.9: Multiple resonators can be placed on the same feedline provided that they have unique resonance frequencies. Each peak represents one individual MKID. Acknowledgement: Pieter deVisser for the fabrication of this test array that was lent to DIAS for initial development of the readout electronics.

2.3 Figures of merit / Performances

It is important to understand what makes an MKIDs array a good array, therefore it is necessary to determine what figures of merit are to be considered when talking about MKIDs. Establishing what properties determine the performance of an MKIDs array is essential in order to optimise the detector to its current technological limits and to evaluate what needs to be done to go beyond the state-of-the-art. A brief discussion on these quantities can be found in the next pages.

2.3.1 Yield

Pixel yield, or total fabrication yield, is, probably, the most important parameter when it comes to MKIDs for astronomical applications. The yield of an array defines the quality of the array in its deepest sense. Imperfections in all the stages of the fabrication process can drastically reduce the yield. A precise definition of pixel yield can be given as the ratio between the number of distinguishable pixels with a well defined and unique resonant frequency, $N_{visible}$ and the total number of pixels that were designed to be on the array N_{tot}.

$$YIELD = \frac{N_{visible}}{N_{tot}} \tag{1}$$

Current MKIDs instruments, such as MEC (55) and DARKNESS (7) are optimised so to embed up to 2000 resonators, with unique resonance frequencies, on a single co-planar wave-guide transmission line.

This yield is known, and understood to depend, on both the design of the array and its fabrication process. In particular, it is understood that increasing the spacing, in frequency, between two adjacent resonators provides great results in maximising the yield, but, given the one-octave constraint, doing so would drastically reduce the total amount of pixels that can be coupled to a single transmission line, which, in turn, also means that more sophisticated, and expensive, electronics is necessary to read out the same number of pixels. Also, increasing the spacing between adjacent pixels, implies the use of an excessive number of coaxial lines at the cold stage of the cryostat, the scarcity of which is one of the main strength of MKIDs when compared to competing technologies. Two resonators are said to *clash*, or *collide*, when they resonate at the same resonant frequency. The main cause of clashes is known to be non uniformity in critical temperature across the array. A large shift in frequency arises from a variation of less than 100 mK. Micro-regions where the critical temperature differs from the designed value, produce significant shifts in resonant frequency for many resonators at once. The effect of this phenomenon is described and modelled in detail in Chapter 7. The reader is invited to go back to Section 2.5 after the discussion in Chapter 7 to look back on the material choice in light of a deeper understanding of the phenomenon.

2.3.2 Quantum efficiency

Quantum efficiency (QE) is defined as the ratio between the number of photons detected by the array divided by the total number of photons illuminating its surface. The reflective nature of the metals used to construct MKIDs can be the reason for an inherently low QE.

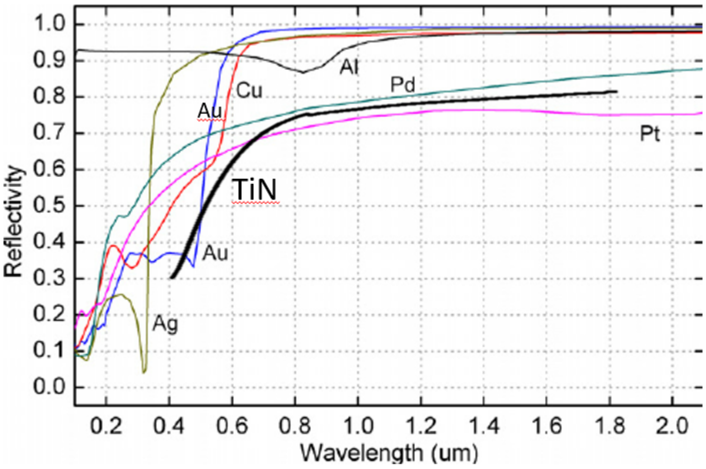

Figure 2.10: Reflectivity of common metals, as if they were infinitely thick. Adapted from (9) and (10). The transmission spectra of the optical elements of the cryostat can be found in Chapter 3 and Appendix A4

In particular, a very versatile material like aluminium (Al), which is easy to deposit with high uniformity and etch away in a lithographic process, has a reflectivity greater than 90% over the optical/IR band (Fig. 2.10). In turn this leads to too many impinging photons being reflected and a resultant low QE. On the other hand, metals like gold (Au) and platinum (Pt) which have a significantly lower reflectivity, do not transition to a superconducting state. Of course it is important to focus the light, using for example, micro-lens arrays so as to ensure a minimal number of photons are lost to the silicon substrate, i.e. increasing the so-called fill factor (7). Nevertheless, a wise choice of metals is extremely important as it is a critical limiting factor.

2.3.3 Energy resolution

Arguably, the most interesting characteristic of MKIDs is their inherent energy resolution. Unlike CCD-based instruments, where energy resolution is achieved through multichroic beam splitting and wavelength-filtering, it is possible, from the phase signal produced by an MKID when struck by a photon, to reconstruct its wavelength. When a photon is absorbed, the phase signal ramps up, with a rise time of $\approx 1\,\mu$s, to its maximum value. When the resonator is illuminated with monochromatic light, it responds with a phase shift, and the resultant maxima vary in a finite range of values. The histogram of the signal's maxima produced as a response to monochromatic light is not an infinitely sharp peak, instead it has a finite width (as shown in Figure 2.11). The sharper the peak, the higher the energy resolution of the resonator; which, can be defined by the ratio

$$R = \frac{E}{\Delta E} \tag{2}$$

Modern MKIDs instruments such as DARKNESS (7) exhibit an energy resolution $R = 8$ for $\lambda = 1\mu$m, therefore it is extremely important to understand what factors are limiting the energy resolution the most. Among the candidates, HEMT noise and Two-Level Systems (TLS) noise are top of the list (as further discussed in Chapter 7, but it is also important to remember that sampling frequency of the readout electronics also plays a fundamental role. The readout electronics is limited to a 1 MHz sampling rate by the Fast-Fourier Transform algorithm and the Shannon-Nyquist sampling theorem (56, 57). The time interval between two different data points, 1μs is comparable to the rise time of the phase signal. This might lead to random inaccuracies in the determination of the real peak height, which is then reflected in a broadening of the histogram. Further details can be found in Chapter 7 where a study is carried out in order to understand, model, and determine the entity of the role of the main sources of phase noise.

2.3.4 Responsivity

The responsivity represents the variation in intensity of the output signal as a response to a variation of the optical/NIR input. In short, it describes how apt the

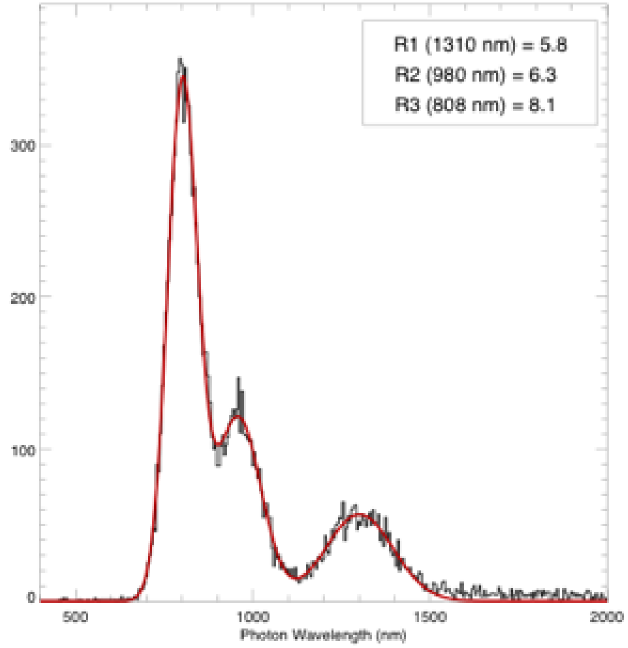

Figure 2.11: From Szypryt et al. (11). Energy resolution measurement of a MKID. The three peaks are characteristic of three different wavelengths the MKID was illuminated with. The widths of each curve are representative of the energy resolution of the specific MKID.

detector is for a specific application. A resonator that is meant to produce a high phase signal for an NIR photon hit, will probably produce a saturated 180° phase shift when a *blue* photon strikes it. The opposite, if an MKID is optimised so to have a moderately high, such as a 30° phase shift in the blue end of the spectrum, it will probably not produce a detectable signal when a $1.5\,\mu$m photon strikes it. Here the intention is to state that by slightly adjusting the design of the resonator, it can be tweaked so to have the responsivity properties required. In particular, it is the current density figure that is central for such optimisation as the change in impedance is proportional to the carrier current density,as described by Equation 1. Further details can be found in (12) where a formula for the responsivity $\frac{d\theta}{dN_{qp}}$ is calculated by applying a Mattis-Bardeen theory:

$$\frac{d\theta}{dN_{qp}} \propto \frac{\alpha Q}{V} \tag{3}$$

where α is the fraction of the total inductance strictly due to the kinetic inductance effect, Q is the total quality factor and V is the volume of the superconductor. This proportionality shows that in order to get high responsivity, it is necessary to aim for the highest possible total quality factor Q and the smallest volume of the resonator. Reducing the thickness of the film not only increases the responsivity by lowering the volume V, but it also contributes by increasing the kinetic inductance fraction α.

2.4 MKIDs readout technique

MKIDs can be read out through some complex electronics. The setup revolves around a configurable board equipped with a Field Programmable Gate Array (FPGA) capable of performing fast real-time operations on multiple channels. The board is also supplied with a number of Analogue to Digital Converters, (ADC), and Digital to Analogue Converters (DAC) which are an interface to the MKIDs array. A second board, called an Intermediate Frequencies board (IF), has the purpose of interfacing the frequencies in the $4-8$ GHz bandwidth, down mixing them to much lower frequencies, $[-2GHz; +2GHz]$ GHz, which are processed by the FPGA.
The read out technique is quite easy in principle, the array is fed with a comb of specific frequencies to drive all the resonators with their own resonant frequency. This signal is considered to carry "null" information. The signal coming out of the MKID array is then read out through the setup just described and carries any potential information. The two combs are then compared and their difference is evaluated to decode the phase shifts of each single pixel which is only due to the impinging photons. This process, called homodyne detection, is common when phase information of a signal is to be carried out. Figure 2.12 shows a broad schematic of the detection technique.

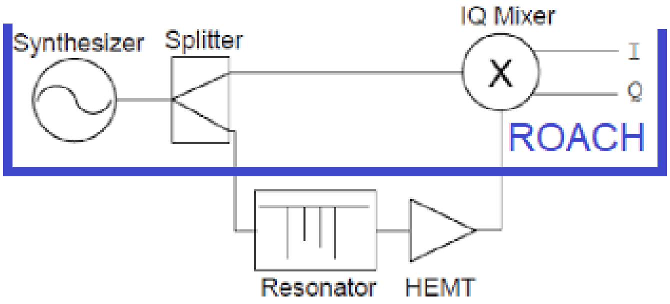

Figure 2.12: Scheme depicting a homodyne detection: the signal produced by the ROACH board is split and sent both to the resonators and to the IQ Mixer. By comparing the signal produced by the board and the one coming out of the array, the I and Q components are obtained. Adapted from (12)

In reality, the whole process is more complex and relies on heterodyne detection, but the difference lies mainly in technicalities. The signal coming out of the array is amplified with the use of a High Electron Mobility Transistor (HEMT) before being wired to the high-frequency port of an IQ mixer. The other port of the IQ mixer is fed with a local oscillator (LO) at 6 GHz. This way an in-phase (I) and quadrature (Q) signals are produced. Each of the signal is then down-mixed to a suitable range with the IF board and digitised with an ADC. The digitised signal is then transferred to an FPGA where it is analysed in real time. The FPGA will deconstruct the frequency comb (generated by the FPGA to probe the MKIDs array and then fed through it) into an amount of sampling bins centred around each single resonant frequency. This process is called channelisation (58). The main element of this process is the Polyphase Filter Bank that ensures a flat response across every single sampling bin, therefore making sure that the read out electronics produces a signal that only depends on the dephasing of the signal and not on the transfer function of the electronics. Further details of the signal processing are beyond the scope of this work and will not be discussed, but can be found in (59) and (60).

The data represented in the complex I-Q plane is described by a large loop, that is typical of the complex impedance of the cables, and a smaller loop that represents the phase shift across the resonator. In order to maximise the phase signal a further step is necessary. An arbitrary phase is added in order to rotate the loops and make the amplitude component of the resonant loop lie parallel to the I axis. Details of the rotation process can be found in (8). Figure 2.13 shows the loops before (blue curve) and after (red curve) the rotation process.

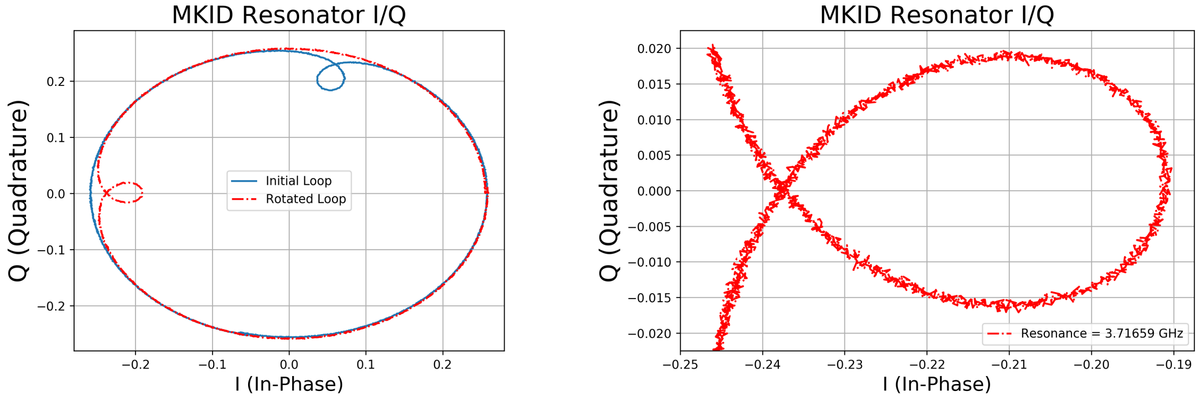

Figure 2.13: Left: The resonant loop just before the rotation (in blue) and the rotated loop (in red). Right: Close up on the resonant loop after the rotation.

After the loop has been rotated, the origin of the IQ plane is translated in order to match with the centre of the resonator loop. This allows enlarging the range of the phase signal from a few degrees into a whole 180° increasing dramatically the resolution of the instrument and its dynamic range. Figure 2.14 shows a phase signal produced by an MKID when struck by a cosmic ray.

2.5 Material science

The physical properties of the superconductor of choice are of critical relevance when it comes to the development of MKIDs. In Section 2.3 the main figures of merit were discussed. It is now clear how the Q.E. is strongly affected by the reflectivity of the adsorbing material. Another crucial parameter is the superconducting gap Δ_s, which is reflected in the critical temperature T$_C$. A T$_C$ fluctuation in the superconductor localised at the n-th resonator is reflected in a variation in both quality factor Q and resonant frequency f_0 of the resonator (see Chapter 7 for further details). The responsivity of a single resonator also depends on the superconducting gap and the

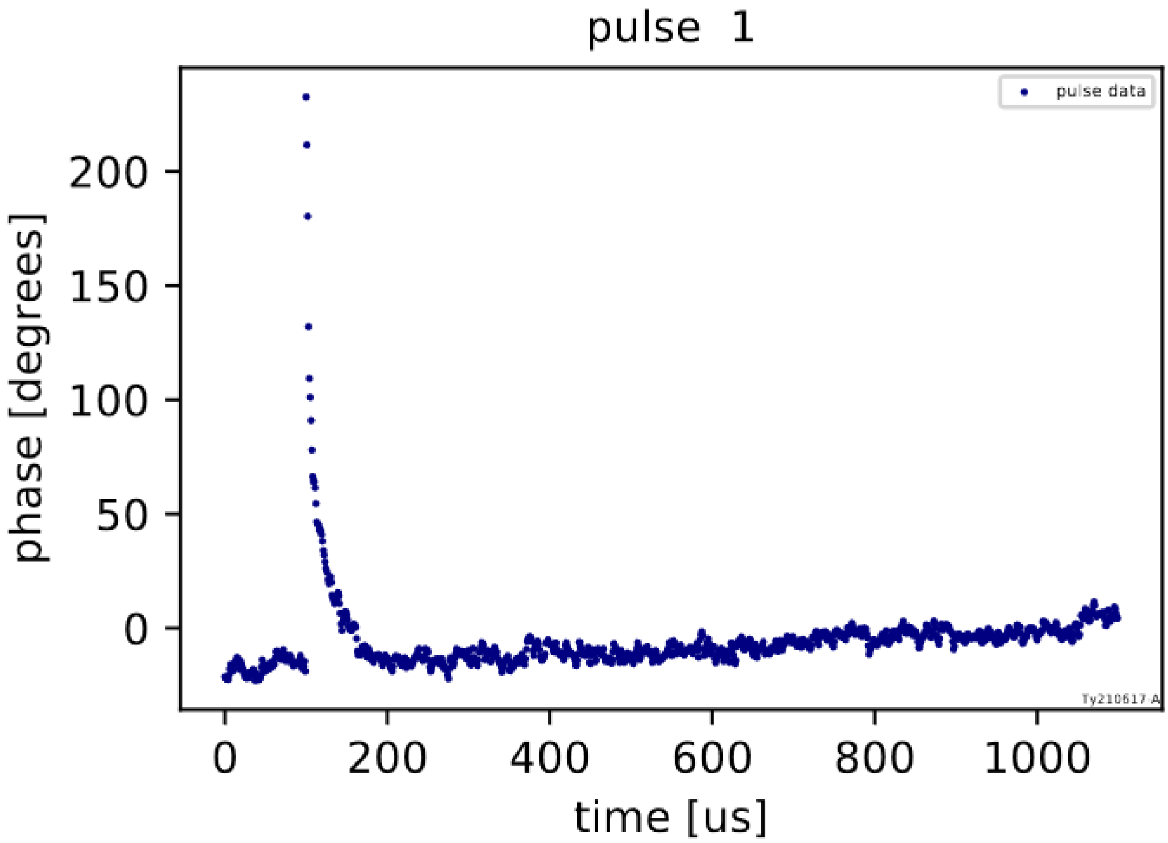

Figure 2.14: Cosmic ray event as detected by a resonator in DIAS. The resonator was fabricated on a TiN/Ti/TiN stack with respective thickness of 4nm, 10nm and 4nm. The critical temperature was $1.5\,K$ and the sheet inductance is $\approx 4.5\,pH/square$

thickness of the adsorbing layer. Moreover, the energy resolution depends on the gap Δ_s, the thickness of the layer and the quasi-particle lifetime, which is inherently dependent on the superconductor of choice. As a general rule, the lower is the critical temperature, and therefore the smaller the bandgap, the higher is the responsivity and energy resolution of the detector. As a final remark, in order to fully deplete the superconductor from unpaired electrons, the detector has to be operated at a temperature that is $1/8 - 1/10$ the critical temperature of the film. A good operating temperature is usually 100 mK which constrains the critical temperature to be between $800 - 1000\,mK$.
Here follows a list of the desired properties of the ideal superconductor:

1. Thickness uniformity
2. T$_c$ uniformity ≈ 800 mK
3. Easy to deposit
4. Low reflectivity (VIS and NIR)
5. High internal quality factors Q$_i$
6. High Kinetic Inductance

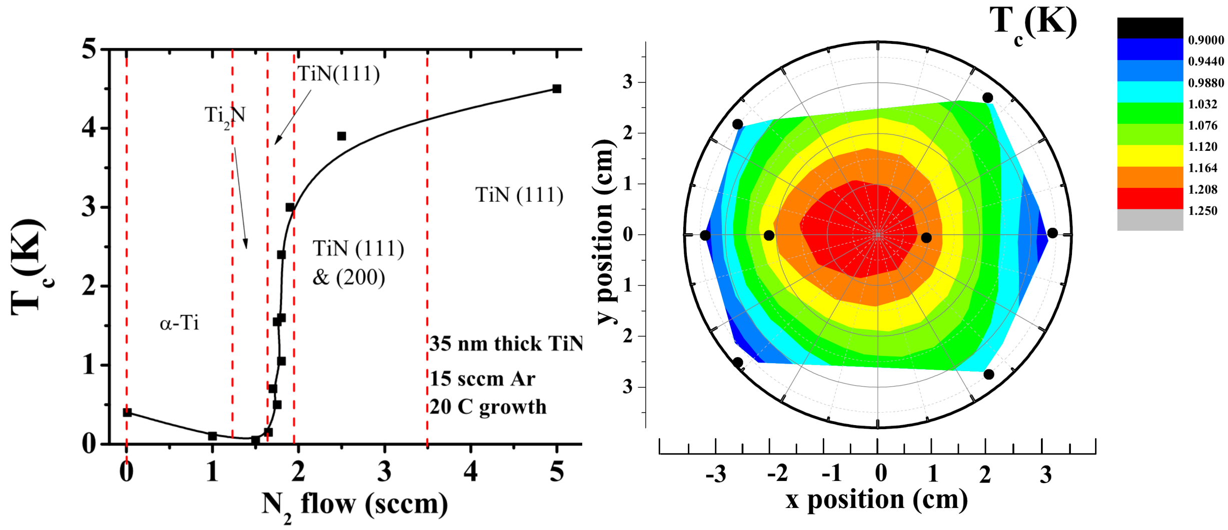

Figure 2.15: (Left):Critical temperature of TiN_x as a function of the $Ar-to-N_2$ ratio. The Ar flow-rate was kept at 15sccm, whereas the N_2 flow rate was varied between 0 and 5 sccm. (Right): Critical temperature across a 3 Inch wafer. The contour plot is an interpolation of 17 measured locations. Adapted from (13)

Among the many possibilities, three options have been identified as interesting for this work: Substoiochiometric Titanium Nitritde, TiN_x, a multi-layered stack of Titanium *Ti*, and Titanium Nitride *TiN*, and granular aluminium *grAl*.

2.5.1 Substoichiometric Titanium Nitride

Multiple studies have been carried out on the possibility of using Titanium (Ti) compounds as prime superconductors for MKIDs (61),(15),(7) . Ti, in its atomic form, has a critical temperature of 400 mK (62); which varies with thickness. The superconducting transition occurs at a temperature which would make operation at $T \approx T_C/10$ extremely challenging, moreover, Ti tends to quickly react with Oxygen (O_2) resulting in uncontrolled Titanium Oxides with properties that are dramatically different than those of atomic Ti. Titanium Nitride (TiN), is known to have a much higher critical temperature 5.6 K (63), but this value is known to be dependent on stoichiometry and thickness (63) , Nitrogen (N_2) to Ti ratio (64). Common deposition technique is magnetron sputtering from a Ti target (99.999% purity) in an Argon (Ar) atmosphere with a controlled flow of N_2. M. Vissers et al show (13), as in Figure 2.15 (Left), how the argon-to-nitrogen ratio affects the critical temperature of the superconductor. For the sake of this experiment, the Ar flow-rate was fixed at 15 sccm (standard cubic centimetres per minute) , and the total pressure in the chamber was kept constant at 2 mTorr and the N_2 flow-rate ranges from 0 to 5 sccm (65).

Based on this mechanism, small fluctuations in the $Ar-to-N_2$ ratio, are known to cause the stoichiometry of the TiN_x to vary across the wafer. Since the target critical temperature ≈ 800 mK, lies in the region where T_c changes dramatically with flow rates, it has been observed that a deviation as little as 0.5% can yield a variation in

T_c as big as 1 K (13). Figure 2.15 (Right) shows that T_c values can vary by more than 25% from the centre to the edge of the wafer. The paper by M. Vissers et al. (13), from which this information is reported, documents that across the same substrate, the thickness only varies by less than 1% (13). Although the typical value of the internal quality factor in TiN_x resonators is about 10^5, values as high as $Q_i > 10^6$ have been demonstrated in substoichiometric TiN_x (65).

2.5.2 Multilayer stacking

One possibility to improve the T_c uniformity is to move away from non stoichiometric compounds of Ti and N_2 and exploit proximity effect to tune the superconductor to the target temperature. The proximity effect arises from the non locality of electrons, and cooper pairs, in metals; at the interface between two superconductors, the Cooper pairs produced in the first superconductor S' can be carried over to the other superconductor S" and *vice-versa* affecting the superconducting gap at the interface. If the two superconductors S' and S" are very thin, the extent to which the paired states are carried over is larger than the total thickness and the two superconductors blend into one material with, effectively, only one superconducting gap given by the contribution of S' an S". Obviously, there is no principle which limits the number of layers to be 2. Multiple layers of different superconductors can be stacked and produce the desired effect as long as the total thickness of the stack is consistent with the coherence length of the cooper pairs. Stacks of atomic Titanium and stoichiometric Titanium Nitride are currently under investigation in the scientific community as optimal superconductors for optical MKIDs. The growth of thin layers of both Ti and TiN has already been optimised in order to be reliable and uniform at the sub-nm level. Previous studies (15) demonstrated that the superconducting transition for a $TiN/Ti/.../TiN$ multilayer can be controlled with acceptable accuracy by changing the relative thickness of the layers (14). Moreover, a 2013 paper by M. Vissers et al., (15), proved high uniformity in critical temperature across the wafer, measuring variations in the order of 1.5%. The same work demonstrated the feasibility of resonators the internal quality factor of which is as high as $Q_i = 2.5 \times 10^5$. Figure 2.16 shows the two results just elaborated, (Left) is explanatory of how the the critical temperature can be tuned by varying the relative thicknesses of the different materials, whereas (Right) shows the T_c uniformity of a multilayer stack of Ti and TiN .

2.5.3 Granular Aluminium

Granular Aluminium (grAl) is a long known superconductor, but in the last few years it became a hot topic thanks to its outstanding sheet inductance; typical values of kinetic inductance have been measured to be ranging in between 0.1 and 1.3 nH/square (50) (66). Granular Aluminium, as the name might suggest, is made up of

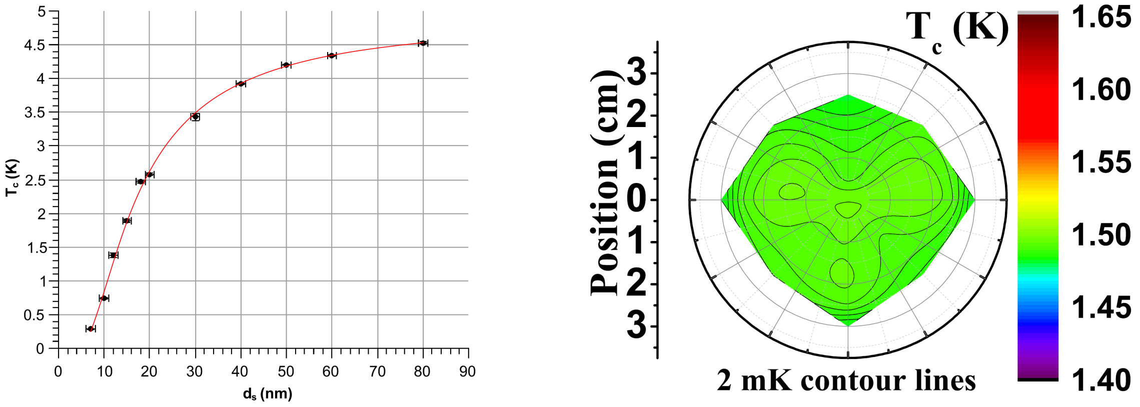

Figure 2.16: (Left): T_c dependency of a 5 layer stack as a function of the thickness of the TiN layer. The Ti layers are 10 nm thick. After (14). (Right) T_c uniformity for a 5 layer stack over a 3 inch wafer. Adapted from (15)

nanometer-size grains of superconducting aluminium (Al) coupled to each other through Josephson junctions where the insulating layer is made of Aluminium Oxide. Changing the grain size, and the size of the aluminium oxide insulating barriers, the properties of the superconductor can be adjusted to match the desired specifications. This process that regulates this phenomenon, and the superconductor to insulator transition, of course depends on the coherence length of the cooper pairs and is somewhat akin to the proximity effect previously discussed. Further details would be redundant for the scope of this work, but can be found in the following paper by Bertrand et al. (51). Recent studies (50, 67), showed the feasibility of using grAl to produce superconducting resonators with relatively high internal quality factors $Q_i \approx 10^5$, but light detection performances of grAl based detectors are still to be investigated. As a final remark, it is worth mentioning that the quasi-particle recombination time for grAl substrates is in excess of 1s and that it depends on the drive power of the resonator (51). For the sake of clarity, it is important to openly address the issue of quasi-particle bursts, the unexpected creation of quasi-particles in the superconductor, which appear to occur randomly in grAl in intervals of ≈ 20 s (67), (50). The origin of this peculiar effect is still unclear and the detrimental effects of such on a MKIDs array are still to be investigated, although it is thought that quasi-particle traps might be beneficial in reducing the burst rate (68).

2.5.4 Comparison

Table 2.1 shows a comparison between the three materials just discussed. For the sake of clarity, for each material, only the features that are strictly necessary for MKIDs applications are discussed. Further details can be found in the referenced literature.

	TiN_x	$TiN/Ti/.../TiN$	$grAl$
Critical temperature (T_c)	$0.05 - 5.6$ K	$0.05 - 5.6$ K	$1.2 - 3.15\,K$
Internal quality factor (Q_i)	$> 10^6$	$> 10^6$	$> 10^5$
Kinetic Inductance (50 nm)	$5 - 40pH/square$	$20 - 40pH/square$	$0.1 - 1.3nH/square$
Quasi − particle lifetime (τ_{qp})	$100\,\mu s$	$50\,\mu s$	$> 1s$
Deposition	1 step	multiple steps	1 step
T_c excursion(centre − edge)	25%	1.5%	N/A
Vis − NIR reflectivity	Moderate	Moderate	N/A

Table 2.1: Comparison between TiN_x, $TiN/Ti/.../TiN$ and $grAl$.

2.6 Improving upon the current generation of MKIDs

To summarise what was discussed through this chapter, I want to discuss what are the current limitations of Microwave Kinetic Inductance Detectors and what needs to be further improved on. In principle, improving on all figures of merit would be nice. For a number of reasons, including the issues that come with the funding of RD projects, improving on some characteristics is more important than improving on others.

- **Energy resolution** the ultimate goal is to build an imaging camera with the highest energy resolution possible. Fano statistics will put a hard constraint to a resolving power of about 100 for visible and near-IR photons. One of the main selling arguments for MKIDs is their inherent energy resolution, coupled to the single photon detection capability. Viable options to improve the energy resolution of MKIDs are discussed further into this thesis and include the reduction of electronic noise and new possible geometries.

- **Readout optimisation** Compared to other technologies, the electronics required to read out an array of MKIDs is quite expensive, currently sitting at about 10$ per pixel. The cost just for the readout electronics of a 50 kilo-pixel camera is in the order of half a million dollars. It appears obvious that such figure has to be reduced dramatically in order to be competitive with CCDs. Xilinx is developing more powerful boards that can reduce the readout cost to about 1$ per pixel. This comes along with a reduced power consumption and reduced mass, all of which, in turn might result in the possibility of deploying MKIDs also in space-born missions.

- **Fabrication yield** Increasing the fabrication yield is of crucial importance. While the full imaging is still achievable by tiling, i.e. the overlap of images captured in sequence and so that the the position of the elements in the sky is slightly different in each of the multiple exposures. This requires extra observation time at the telescope and, partially, defeats the purpose of deploying single-photon sensitive detectors. The most promising options in this direction include using high uniformity TiN/Ti/TiN multilayers as superconducting thin films, post-fabrication trimming and DC-current biasing of selected resonators. This thesis discusses in full detail the DC-bias approach and provides preliminary results on the uniformity of TiN/Ti/TiN multilayers.

3 Experimental setup

3.1 Adiabatic Demagnetisation Refrigerator

As previously discussed, MKIDs have to be operated at milli-Kelvin temperatures, in order to comply with the critical temperature of the superconductor and to insure the full depletion of the thin film of all possible normal-state electrons. To cool down the samples to such low temperatures, a cryostat is needed. For the sake of these experiments, an Adiabatic Demagnetisation Refrigerator (ADR) manufactured from *Entropy GmbH* is being used. The next pages will discuss very briefly the working principle of the DIAS ADR. In order to use MKIDs as a photon detector, it is necessary that an optical signal can be fed into the cryostat for the MKIDs to detect. To do so, it is necessary to equip the cryostat with a viewport and a stack of optical filters. The filtering stages are also discussed in this Section.

3.1.1 Adiabatic Demagnetisation Refrigeration

Helium liquefies at a temperature of 4.2 K at atmospheric pressure, by the means of a Pulse Tube Refrigerator (PTR) the lowest temperature obtained is 1.2 K. (69). To reach milli-Kelvin temperatures, one approach is be the adiabatic demagnetisation refrigeration. This technique takes advantage of the property of paramagnetic materials, salt pills, that their entropy while immersed in a magnetic field is lower than when no field is applied.

When a magnetic field is switched on the magnetic moments of the atoms making up the paramagnetic align to the field. The first part of the cool down cycle consists of an adiabatically insulated salt pill which is immersed in an external magnetic field that aligns the magnetic moments and heats up the paramagnetic. The second part of the cycle consists of ensuring thermal contact to cool down the salt pill while the magnetic field is kept at a constant value. The thermal contact is finally removed and the magnetic field ramped down, hence the name: adiabatic demagnetisation. As the magnetic field is reduced the entropy of the paramagnet creeps up and the temperature drops resulting in a cooling of the paramagnetic object itself.

For typical refrigeration cycles, the heat sink is a bath of liquid helium and, to reach milli-Kelvin temperatures, more ADR stages that work in "tandem" are required.

The hold time of such refrigerators can be as long as a couple of days. The ADR used for the sake of this work is a two stages ADR cryostat working with a Gadolinium-Gallium Garnet (GGG) stage that goes as low as 650 mK and a Ferric Ammonium Alum (FAA) stage that reaches the base temperature of 30 mK.

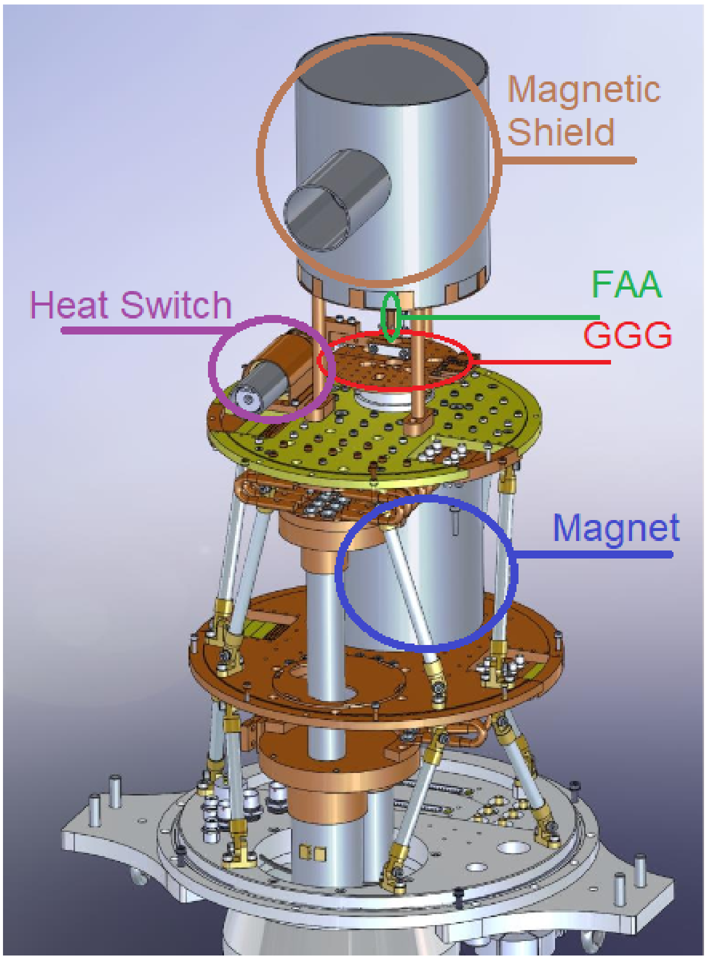

Figure 3.1: CAD drawing of the inside of the Adiabatic Demagnetisation Refrigerator from Entropy GmbH. The red and green circles highlight, respectively, the GGG and FAA stages. Adapted from Entropy's proprietary drawings.

The plate shown at the bottom of Figure 3.1 is vacuum tight and is in thermal contact with the outside world. It is connected through ceramic rods to the 70 K plate and further up to the 4 K stage. On this plate is anchored the super-magnet (in blue), the heat switch (in purple) to which both the FAA (green) and GGG (red) stages are attached. A magnetic shield, with an opening to allow light in is placed around the FAA stage defining the sample space and reducing for as much as possible the effects of the super-magnet inside the sample space.

3.1.2 Optical Filters

The optical signal is fed to the detector through a viewport in the cryostat. It is basically a vacuum-tight window made of borosilicate glass, which exhibits a transmission greater than 90% over a wide band of wavelengths: from 350 nm up to

$3\,\mu$m. The bandwidth of the optical window then allows the detection of visible and NIR photons. Of course, in order to illuminate the detector, it is necessary that the two internal thermal shields also present optically transparent windows on the same axis as the viewport and the detector.The thermal shields emit thermal radiation of which the spectral density $B_\lambda(T)$ is described by Planck's law. A high influx of thermal photons, in the best case scenario only reduces the hold time of the cryostat, and in the worst case scenario heats up the substrate to a temperature higher than the superconductor's critical temperature T$_c$. Both effects are to be reduced as much as possible, one optimal solution to this problem is mounting a stack of optical filters on the 70 K and 4 K stages. The filtering occurs through two stages, at 70 K and 4K, of Asahi YSC1100 Supercold Filter (19), of which the transmission is $T_{Asahi,\lambda}$ and BK7 glass (20), the transmission of which is $T_{BK7,\lambda}$. The notation becomes a little more convoluted as the thickness of the two BK7 glasses are different at the two stages: 5 mm at 70 K and 25 mm at 4K. The overall spectral density e_λ can be calculated as in Equation 1 once the geometrical contributions are taken into account. Figure 3.2 (top) illustrates the configuration and the geometric contributions.

$$
\begin{aligned}
e_\lambda = \frac{\pi}{2}B_\lambda(4K) \; + \; tan(\alpha)^2 B_\lambda(70K)\, T_{BK7,25mm,\lambda}\, T_{Asahi,\lambda} + \\
+ \, tan(\alpha)^2 B_\lambda(300K)\, T_{BK7,25mm,\lambda}\, T_{BK7,5mm,\lambda}\, T^2_{Asahi,\lambda}
\end{aligned}
\tag{1}
$$

It is possible to bin the impinging thermal load in 2 nm bins, and knowing the fill factor of the MKIDs, their dimensions and the size of the chip, to evaluate the number of photons, which strike on each pixel per second per wavelength bin. Such plot is shown in Figure 3.2 (bottom).

The transmission curves for the Asahi YSC1100 and BK7, as well as the transmission of the borosilicate glass that constitutes the optical window of the cryostat can be found in Appendix A4

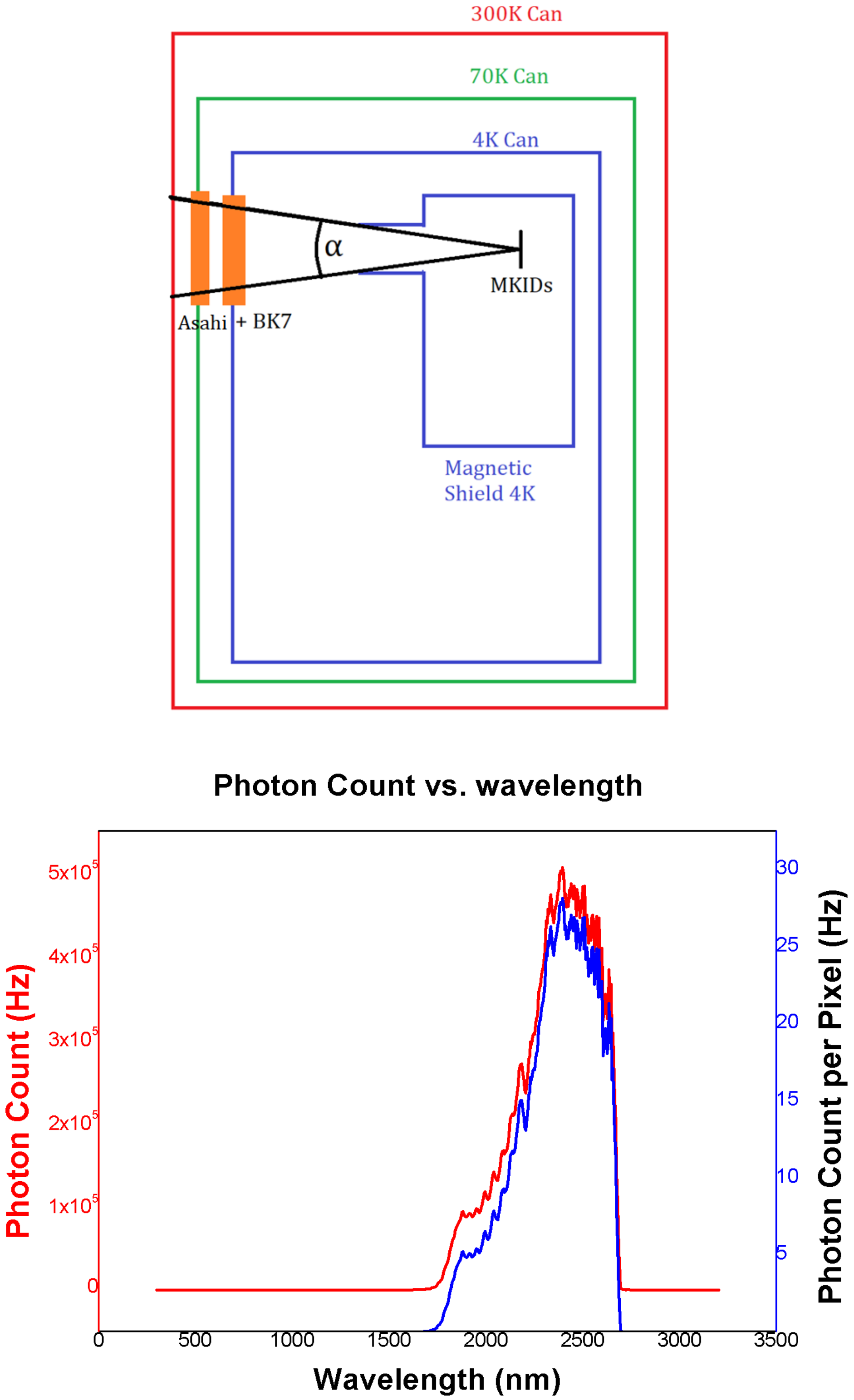

Figure 3.2: Top: Schematic of the cryostat, The two orange blocks represent each one Asahi Supercold filter and a BK7 glass. The angle α is the aperture of the cone from the centre of the array and is defined by the nozzle of the magnetic shield. Bottom: Number of photons and number of photons per pixel hitting the detector as a function of the wavelength of the thermal photons. Parameters used: 95% fill factor, $18 \times 18\,mm^2$ chip size, $50\,cm$ distance between window and chip, resonator size of $200 \times 200\,\mu m^2$ and spectral bin of $5\,nm$.

3.2 Critical Temperature Setup

In order to fully characterise the materials used for the fabrication of MKIDs it is critical to measure the critical temperature of the thin films. This is performed by acquiring four-point resistance measurements while controlling and measuring the temperature of the cold stage of the cryostat. Plotting resistance against temperature it is possible to obtain the typical figure that shows a superconductive transition. The main piece of equipment used to perform critical temperature measurements is an AC resistance bridge (Stanford Research Systems SIM921) mounted in the SRS mainframe (SIM 900) from the same manufacturer. Small pieces of the silicon wafers with the superconductors deposited on top are glued to a chip carrier (Global Chip Materials - SB20172602 KD-82447) which is installed on the FAA stage of the ADR, mounted on a custom made copper rod. The electrical connection to the Resistance Bridge is ensured through custom designed Printed Circuit Boards (PCBs) which are then soldered to a room temperature 37-pin D-Sub connector through a Manganin loom cable that is thermally anchored on each plate of the cryostat. In order to fully automate the measurement process, a LabVIEW VI (Virtual Instrument, a programme) has been developed to continually read out the resistance value of each individual sample and cross-reference it with the temperature of the FAA stage of the cryostat. Further details on the LabVIEW VI are discussed in Section 4.1

3.3 Cryogenic Amplifiers

The signal coming out of an MKIDs array has to be amplified in order to be read out. This process usually happens through two amplification stages. One which exploits a low-noise cryogenic amplifier to increase the signal to noise ratio and the second stage with a room temperature amplifier to further boost the signal and to compensate for the losses due to the coaxial cables inside and outside of the cryostat. As per every multi-stage amplifier chain, the first amplifier has the biggest contribution to the total signal to noise, so it is required that the amplifier on the $4\,K$ plate of the cryostat is as noiseless as possible. While two possibilities exist, kinetic inductance based travelling-wave amplifiers (70) are not widely available as commercial products. The best off-the-shelf option is utilising a low-noise High Electron Mobility Transistor to amplify the signal produced by the MKIDs array.

3.3.1 HEMT Amplifier

A HEMT is an amplifier based off a hetero-junction, typically between GaAS and AlGaAs. The different band structure of the two semiconductors produces a hetero-junction with a conduction channel in the high purity undoped GaAs that allows for high electron mobility, low losses and high switching frequencies. Our experimental setup incorporates HEMTs (LNF-LNC48C) from the Low Noise Factory, and while the details of the hetero-junction are not disclosed, the specifications of the amplifiers are reported in Table 3.1 and more information can be found on the manufacturer's website (lownoisefactory.com) .

Parameter	Test Conditions	Value	Unit
Gain	$4-8\,GHz$	42	dB
Noise	$4-8\,GHz$	1.5	K
Input Return Loss	$4-8\,GHz$	13	dB
Output Return Loss	$4-8\,GHz$	20	dB
P_{1dB}	$5\,GHz$	-12	dB
OIP3	$5\,GHz$	-2	dB

Table 3.1: High frequency characteristics of the HEMT

3.4 Sample box and cryogenic cabling

The array is inside the magnetic shield, mounted on the FAA plate, on axis with, and perpendicular to, the optical window of the cryostat so that it can be illuminated with monochromatic light the chosen wavelength. In order to ensure good thermal conductivity and good electrical conductivity to the electronics, the samples are mounted inside a tailored gold-plated sample box machined for us from a block of Oxygen Free High Conductivity Copper (OFHC Cu). The sample lodgement space is $20mm \times 20mm$ and is $1mm$ deep. The box is equipped with six cryogenic SMA connectors that allow for the readout of up to three feedlines simultaneously.

The electrical connection to the feed-line and the grounding of the chip is ensured with two custom made transition boards to which the sample is bonded with the help of a wedge-bonder. The thermal contact between sample and box is ensured through back-gluing of the substrate and four teflon springs that press onto the film without scratching it.

Six coaxial cables connect the SMAs on the room temperature plate of the cryostat to the sample. The first two stages, from $300\,K$ to $70\,K$ and from $70\,K$ to $4\,K$, are equipped with stainless steel coaxial cables. The last two stages, from $4\,K$ to the GGG plate first, and then from the GGG plate to the sample, mounted on the FAA plate, are equipped with Nb-Ti coax cables. Nb-Ti is superconductive for temperatures lower than $10\,K$ and therefore has a minimal contribution to the heat-load of the cryogenic stages and has a negligible contribution to the signal power loss, helping to maintain a high signal-to-noise ratio.

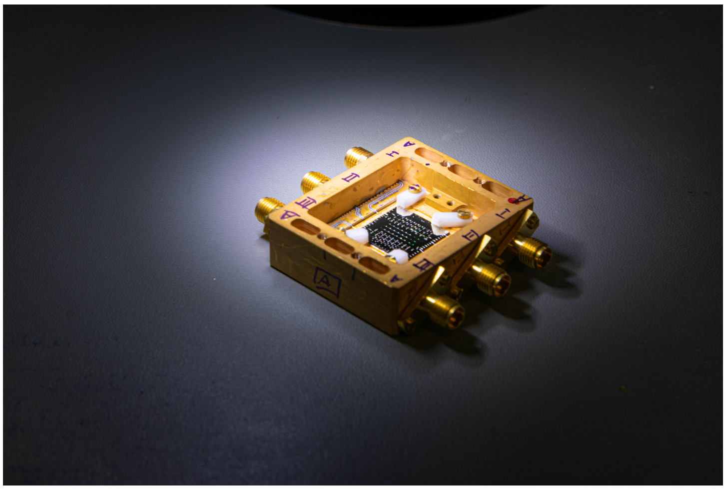

Figure 3.3: A sample box with an MKIDs array mounted on.

3.5 Laser box and monochromator

In order to illuminate the resonator array with monochromatic light, so that the resolving power of each individual MKID can be measured with the smallest uncertainty possible, an optical enclosure which couples four lasers into an optical fibre was built. The four lasers are off the shelf products from Thorlabs and they radiate at the following wavelengths: $450\,nm$, $635\,nm$, $808\,nm$ and $980\,nm$. Each laser has its individual switch so that it can be turned and off at will. The coupling is achieved by pointing the lasers at the optical aperture of the laser box while introducing a diffusing layer, bubble wrap works great for this purpose, in the optical path. Such a low coupling is ideal for our applications as it is producing an output of a few photons per second which makes the laser box an inherently safe (class 1) piece of equipment.

The lab is equipped with a monochromator that was used for the characterisation of some optical filters at cryogenic temperature as described in Appendix A1.

3.6 Readout electronics

In order to read-out the detectors array a number of electronic instruments are necessary. This section will contain a brief description of the front end electronics required in order to document what is being used in the lab and to present the general readout principle. A more detailed description of the equipment and the signal-processing can be found in (8).

The signal coming out of the cryostat is further amplified with a room temperature amplifier in order to boost its amplitude. The amplified signal is fed into an Intermediate Frequency (IF) Board which is meant to "down-mix" the signal (from the $4-8$ GHz octave) down to the range $[-2;+2]$ GHz, which meets the constraints of the Analogue-to-Digital Converter (ADC) which digitises the signal for further processing as described in Section 2.4. The digitised data stream is then further analysed on a Field Programmable Gate Array (FPGA) chip that was purposefully programmed. The FPGA chip performs channelisation through a Fast Fourier Transform (FFT) which allows the code to gather data from each individual resonator, finally the data from each resonator is fed into an I/Q mixer to get in phase (I) and quadrature (Q) values that were previously described in Section 2.4.

3.6.1 FPGA board

The prototype readout was developed on the Reconfigurable Open Architecture Computing Hardware (ROACH) board developed from the CASPER collaboration. The board incorporates a Virtex-5 FPGA and is equipped with two 16-bit Digital-to-Analogue converters with a sampling speed of 1000 Mega Samples Per Second (MSPS), and two 14-bit Analogue-to-Digital converters with a sampling speed of 400 MSPS that were developed for MKIDs readout. The transition board (MUSIC IF) is also developed by Techne Instruments for the CASPER collaboration for MKIDs readout.

The ROACH board is a legacy piece of equipment and its performance is limited. A ROACH board has the capability of reading up to 256 pixels simultaneously. This is sufficient for a prototype array, but it starts to be a limiting factor when it comes to kilo-pixel arrays. The state of the art allows for up to 2000 pixels per feedline and a more powerful readout board is necessary. Currently, the Xilinx RFSoC (**?**) seems to be the most promising board to maximise the pixel per feedline readout and in order to reduce the cost-per-pixel down to a couple of euros per pixel. In addition, Xilinx has recently released an evaluation board (RFSoC 2x2) which at a fraction of the price of the RFSoC results in the possibility of developing a readout system for about one euro per pixel. Further improvements are possible on the IF board side, and currently a group at the University of Durham is developing custom made IF boards for MKIDs readout systems. Further details can be found in (8)

3.7 ROACH board readout

Discussing at a very high level the flowchart of the readout electronics will help create an organic understanding of the experimental setup and the results drawn from it. Further details can be found in Eoin Baldwin's PhD thesis (8) and other sources such as (71, 72, 73).

The first and most important thing is that the ROACH board has to produce a comb of frequencies in order to drive the resonator(s) with the desired power. All of this is done digitally in the building block called " Frequency generator". The Digital to Analogue Converter (DAC) converts the information thus coded into an analogue signal (two actually, one for the I and one for the Q component) which is then fed into an IQ-mixer that produces the signal that is fed into the MKIDs array.

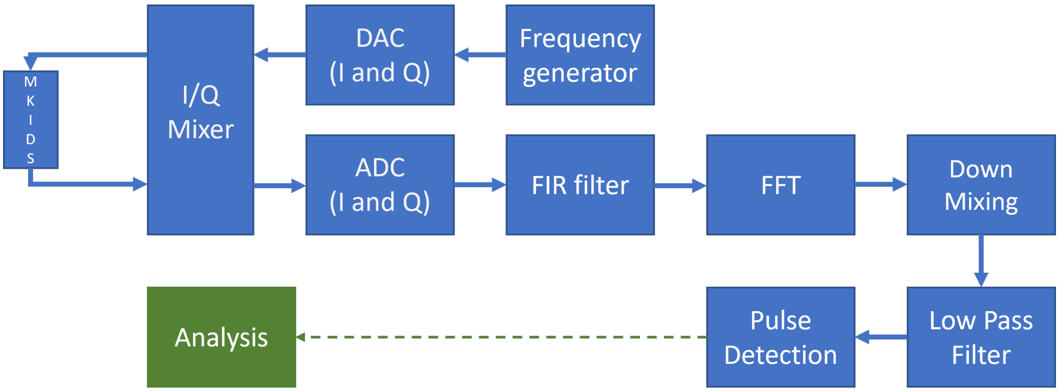

Figure 3.4: Simplified flowchart of the readout electronics where each element represent a macroscopic building block. The readout encompasses all the resources and codes that are required to monitor an MKID and the pulse detection mechanism is responsible for identifying the response of the MKID to the interaction with an energetic particle. The analysis of said data is carried out separately through a series of Python codes.

The signal fed through the MKIDs is then re-fed into an IQ-mixer to separate it into its two main components which are then re-digitised with the help of an Analogue-to-Digital converter.
The digitised data is then further processed by the FPGA, the next two blocks represent the stage called channelisation and, as the name might suggest, breaks down the full bandwidth into a number of channels. This is achieved through a Finite-Impulse-Response filter and a Fast Fourier Transform. The signal in each channel is then down-mixed and a Low Pass Filter is applied to each channel to get rid of spurious signals produced in the process. The data acquired is then fed to the Pulse detection mechanism that constantly monitors the data stream and acquires 1200 μs of data when the baseline of the signal exceeds a certain threshold set by the user. The data is stored on a computer and need to be further analysed with the help of a Python code that then plots each pulse and produces a histogram of plot heights which will be helpful in the determination of the energy resolution of the resonator(s) under examination.

3.8 Vector Network Analyser (VNA)

One instrument of critical importance in the testing of our setup is the Vector Network Analyser, which allows the accurate identification of the resonators on the feed-line. A VNA is a very powerful tool. It consists of two terminals: an output port, typically a signal generator (or source), and an input port, typically a receiver. The VNA is normally used to source a signal through a device and perform comparisons between the sourced signal and the signal processed by the device and returned to the VNA. While sourcing a known signal, the VNA measures both the signal it outputs, and the signal reflected at the device's input port. The measured signals are processed in an internal computer and are displayed on the screen. Our VNA's bandwidth ranges from 9 kHz to 9 GHz and the VNA can sweep any frequency interval that is bigger than 9 kHz in this interval. The most common type of measurements performed by the VNA are transmission and reflection measurements (S-parameters). While the identification of resonators is most trivial by observing dips in transmission (S_{21}), in order to gather the most information about the resonators, including the coupling quality factor Q_c and internal quality factor Q_i; I-Q data from a polar diagram is preferred. A VB-script code was developed to save to file I-Q data from the VNA once some parameters are specified: resonance frequency, frequency span and output power.

4 LabVIEW codes

In order to control scientific equipment, it is often necessary to produce a code that communicates with the instruments and controls the status of the tools and deals with data transfer from and to a computer. In particular, for the sake of the measurements that will be presented in this work, I had to work on the software that controls an AC resistance bridge which has been used for critical temperature measurements and a monochromator, which through diffraction grating produces monochromatic visible and near infrared light with spectral widths in the order of a few nm. This has been used to measure the transmission of the optical filters (reported in Appendix A1) and to illuminate the DIAS MKIDs array.

4.1 Resistance Bridge

The Stanford Research Systems SIM900 mainframe module equipped with the SIM921 AC Resistance Bridge module is the instrument that we avail of to perform critical temperature measurements. The tool's main purpose is to allow four-point resistance measurements, therefore obtaining accurate resistance values bypassing the resisting components of the leads between the instrument and the sample. The way the SIM921 achieves such precise measurements, while minimising the power applied to the sample, is by applying a sinusoidal excitation to a reference resistor which is connected in series to the unknown resistor. By reading out the voltages across both resistors, it is possible to compute the vector quantities $\mathbf{I}$ and $\mathbf{V}$ and from them the value of the unknown resistance. In order to obtain the best measurements, the user is required to control a series of parameters including: the excitation power, the resistance range, and the stabilisation time.

Range

The Range control selects the reference resistor in steps between $20\,\mu\Omega$ and $20\,\mathrm{M}\Omega$. An appropriate reference resistor is necessary in order for the reading to be accurate, if the voltage drop is mostly occurring across one of the two resistors, the signal to noise ratio would be significantly worse than when the two resistors are of comparable resistance.

Excitation

This control selects the excitation amplitude for the measurement in steps between $3\,\mu V$ and $30\,mV$. The amplitude together with the excitation mode determine the conditions for the measurements. While the code allows for a different set of excitation modes, "Constant Current" is the default one and further information on the excitation can be found in the SIM921 user manual. In this configuration, the SIM921 will flow a current through the resistance bridge with rms amplitude of the excitation voltage divided by the reference resistance.

Stabilisation time

Higher time constants will reduce measurement noise at the cost of a slower settling time. The time constant can be controlled in steps between $0.3\,s$ and $30\,s$.

4.1.1 Graphical User Interface

The Graphical User Interface (GUI) presents itself as a simple panel where each individual channel of the resistance bridge can be programmed in terms of the three aforementioned parameters, a series of toggle switches to select the channels through which one wants to scan and an initialisation controller where the parameters for the communication between the computer and the resistance bridge are input as well as the path to the log file. The measured data can be visualised in terms of graphs (both resistance vs. time and resistance vs. temperature) and as numerical digits. It is important to notice that the log file path has to be input before running the code or issues with data logging could arise.

Ch #	Parameters	Resistance	Units	Description	Temperature	Units
1	20 mOhm 3 uV 0.3 s	0.0000	Ohms		0.0000	K
2	20 mOhm 3 uV 0.3 s	0.0000	Ohms		0.0000	K
3	20 mOhm 3 uV 0.3 s	0.0000	Ohms		0.0000	K
4	20 mOhm 3 uV 0.3 s	0.0000	Ohms		0.0000	K
5	20 mOhm 3 uV 0.3 s	0.0000	Ohms		0.0000	K
6	20 mOhm 3 uV 0.3 s	0.0000	Ohms		0.0000	K
7	20 mOhm 3 uV 0.3 s	0.0000	Ohms		0.0000	K
8	20 mOhm 3 uV 0.3 s	0.0000	Ohms		0.0000	K

Select Channels: Ch 1 Off Ch 2 Off Ch 3 Off Ch 4 Off Ch 5 Off Ch 6 Off Ch 7 Off Ch 8 Off

RS-232 COM port: ASRL3:

GPIB Address: 19

Log file path: C:\Users\MKIDs\Desktop\test.txt

Figure 4.1: Graphical User Interface of the LabVIEW code for the Resistance Bridge

4.1.2 LabVIEW code walk through

It is not sensible to go in full details of every section of the code as this would be extremely lengthy and would not be profitable for the purpose of this thesis; nevertheless a brief description of the code is beneficial to clarify how critical temperature measurements are performed.

Upon starting the program, a .txt file at the log file path destination is created with its header that describes the layout of the file.

Depending on the parameters input in the Initialisation Controls panel, a connection with the instrument is established through a GPIB or RS232 interface; in both cases the remainder of the program is identical.

A state machine reads which channels are flagged "to be read out" (ON) and switches between the channels as their response has been produced by the instrument and then correctly read out and displayed by the software. As per the manufacturer's explicit recommendation, the code in between switching through different channels goes into a grounded state `"--"` so to reset its input and output ports and produce a correct reading. Upon switching to a new channel, the desired values of Range, Excitation and Stabilisation time are read out and, if the user has changed from the previous reading, the new values are passed to the resistance bridge and set.

The resistance bridge now performs the measurement as per the way it is been instructed to. In parallel to the resistance measurement, a TCP/IP bridge to the computer that controls the cryostat is established and is used to read out the temperature sensor at the cold stage of the cryostat. The resistance and temperature values thus obtained are added to the resistance vs time and resistance vs temperature plots in the GUI for quick data visualisation and stored in a temporary buffer.

Once all the channels selected are read out through the same process described here, a finite state machine writes to file a full line with resistance and temperature data from each channel. In order to avoid unnecessary confusion, if a channel was not read out during the last cycle, the finite state machine prints "Inf" to file. The choice of "Inf" over "0" can be motivated by our interest in producing critical temperature measurements, therefore measuring very small values of resistance, of the order of milli Ohms or smaller, and a value of "0" would fall too close to some real values measured by the resistance bridge; "Inf" on the other hand, is a digital value the resistance bridge would not be able to output as the reading of any resistance greater than $10\,\mathrm{M\Omega}$ would produce a value of $10\,\mathrm{M\Omega}$. Once the data has been written to file, the buffer is emptied and the code starts again from the state machine that reads out which channel will be read out during the next cycle.

4.2 Monochromator

The purpose of this code is to connect two standalone pieces software drivers: one from Quantum Design, the manufactures of the monochromator, and the other from Thorlabs that supplied us with the room temperature photodetectors. As stated, the main purpose of the monochromator software was to help with the characterisation of the filters for the Ariel Exoplanet Mission (34, 74, 75) (Appendix A1).
What is required of this code is to allow a scan of the transmission spectrum of the filters, in order to do so the monochromator is asked to produce monochromatic light between 400 nm and 2500 nm. Quantum Design provided us with a LabVIEW drivers necessary to configure the monochromator to filter out all the wavelengths except the desired one. A Finite State Machine was developed to feed the pre-existing code from Quantum Design with the value of the next wavelength and an integration time, which will be discussed.
The second section of the code is meant to interface the photodiodes, get a voltage reading and consult the calibration curve and further to calculate the number of impinging photons on the detector. The detector produces 3000 readings per second, therefore when analysing the data produced by the code, it is of great importance to remember to average these values and compute the error on each measurement point by fitting to a gaussian distribution.
The code that was developed is rather simple, per se, it is noteworthy that getting the timing right is not trivial. The aforementioned integration time, which is the length of the time interval (in seconds) for which the detector is read-out is then translated in a bigger time window for the monochromator in order to allow the movement of the diffraction grating in its desired position, it then allows some time for the light output produced by the monochromator to stabilise, the integration time and some extra time at the end of the measurement in dark conditions for the detector to be re-set before being illuminated again.

4.2.1 Graphical User Interface of the monochromator's VI

The GUI appears a lot more minimalist than that of the Resistance Bridge code. It has string controls to input the date in which the data has been measured, it also asks for the user to indicate where they want the file to be saved. Rather obviously, the three commands start, stop and increment indicate the range that the user wants to scan and the scanning pitch. Integration time is as per just described and then average count, set to 1 by default can be used to slow down the readout speed of 3000 Hz, but it is not advisable to change it unless necessary. It is also necessary a calibration file (called configuration file from the manufacturer)for the monochromator to produce the desired wavelengths, whereas the detectors' calibration file is stored inside the detectors themselves. Lastly, the toggle switch

"Run Dark Calibration?" allows the user to decide whether they want the code to run a dark calibration of the sensor.

The code was also developed to allow the illumination of the DIAS MKIDs array with monochromatic light. If the code is written in a way that if it receives as an input value for the "Start" wavelength and "Stop" wavelength the same number, regardless of the "Increment", it will produce monochromatic light at the specific wavelength selected by the user for an extended period of time which is controlled through the "Integration Time" panel. This feature was used to illuminate the DIAS MKIDs array with monochromatic light to produce the results described in Chapter 9.

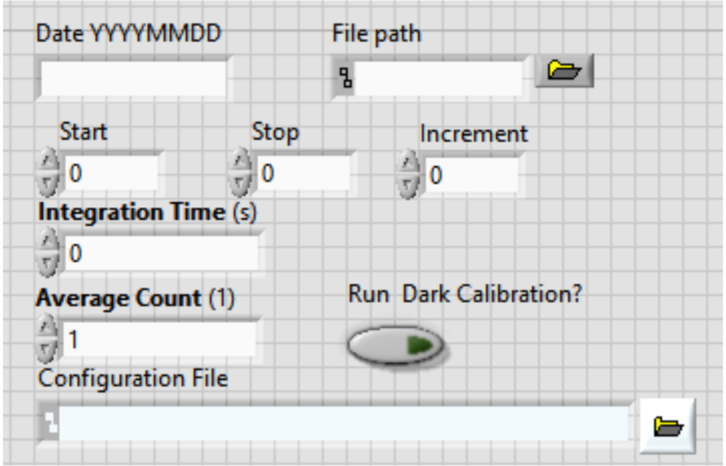

Date YYYYMMDD

File path

Start 0

Stop 0

Increment 0

Integration Time (s) 0

Average Count (1) 1

Run Dark Calibration?

Configuration File

Figure 4.2: Graphic User Interface of the software that controls the monochromator and the photodetectors.

5 Design and simulation

Before fabricating any resonator, it is necessary to put some time into designing their geometry and simulating it so to make sure that the fabricated MKID's behaviour is somewhat predictable. Of course it would be impossible to recreate a resonator of identical behaviour to that of the simulated one, and it would be impossible to simulate all the complex mechanisms that occur in reality when reading out a resonator, so all can be done is a rough estimate of the real characteristics of the simulated resonator.

5.1 Design requirements

As also discussed in Chapter 7, based on the desired properties of the resonator array the coupling quality factor and the resonance frequencies need to be designed with some degree of precision. It is not easily possible to account for the losses inside the superconductor and therefore the Q_i value. When simulating a resonator, the Q-value of the dip, only represents the coupling quality factor Q_c as the superconductor is modelled as a lossless material with infinite Q_i.

While in Chapter 7 the link between Q_{tot} and the fabrication yield is explicit, the main purpose of this chapter is to simulate the value of Q_c and basing our simulations on the assumption that $Q_i \gg Q_c$, it is possible to reflect Q_c in Q_{tot} with an acceptable degree of accuracy.

For the sake of this thesis, the MKIDs are designed to resonate in the bandwidth of operation of the HEMT, between $3\,GHz$ and $8\,GHz$. Although for any real applications it is only possible to place the resonators within one octave, either between $3\,GHz$ and $6\,GHz$ or between $4\,GHz$ and $8\,GHz$ to avoid undesired collisions between resonators; the development of a test array, when the characteristics of the thin superconducting film are unknown, is one of the few cases where not only this is acceptable, it is also beneficial.

Along with a few geometry changes, which include difference in length and width of the interdigitated capacitor, resonators with different Q_c values between 2×10^4 and 4×10^4 were simulated. In order to easily distinguish the resonators when reading out the feedline, they were displaced in small groups of close packed resonators with

similar characteristics which are separated by large intervals of frequencies with no resonators.
Multiple feedlines have been designed to accommodate for different possible surface inductance values of the superconducting thin films, but they all exhibit the same features. The sheet inductance values designed for the sake of this work are 0.3, 5, 10, 20 and 40 $pH/square$.

5.2 Electromagnetic Simulations

The design and simulation is carried out through an EM simulation software and CAD called SONNET (76). SONNET Suites models planar circuits and antennas at RF resulting in accurate simulations of S-parameters. The software requires a physical description of the circuit to simulate both in terms of geometry and physical properties for metal and dielectrics, and employs a rigorous Method-of-Moments EM analysis based on Maxwell's equations that includes all parasitic, cross-coupling, enclosure and package resonance effects. The desired information is provided to the software through the so called Sonnet Design Suite. In the Sonnet Design Suite the user can draw polygons to describe the geometry of the circuit to be analysed, and specify the size and pitch of the grid which will be used for the analysis and, on top of that, the Sonnet Design Suite allows the user to insert the physical properties of the metallic layer and the insulating substrate. Finally, the user can insert a number of electrical constraints (such as grounding the ground plane of a circuit) and "ports" as if it was connected to a Vector Network Analyser. The user can eventually set up the em software in order for it to perform the simulation as desired by the user and, after running it, data such as the circuit's response, a dynamic current density and the far-field emission can be visualised through its own data-viewer.

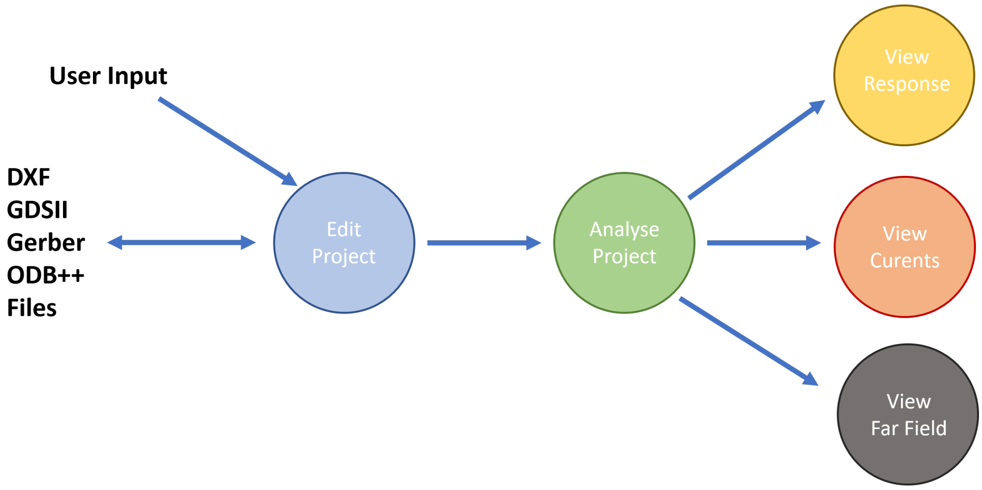

Figure 5.1: Process flow of SONNET's interface and em software

5.2.1 em analysis

The em software uses Fast Fourier Transform analysis to efficiently calculate the electromagnetic coupling on and between each surface. The analysis is complete as it can include phenomena such as dispersion, loss and stray coupling. There are only two limitations to the analysis which are due to, in the first place, the finite numerical precision of any digital calculator and, secondly, the subdivision of the circuit into cells (also referred to as subsection) the dimensions of which can be defined by the user.

Each subsection generates an electric field everywhere on the surface of the substrate, but the total tangential electric field must be zero on the surface of any lossless conductor. The boundary conditions for the simulation of a superconductor and in order to put together the data coming from every subsection is given by the definition of a superconductor which is defined by a zero voltage on the border of the metalisation. In case the metalisation loss has to be taken into account, the tangential electric field has to be proportional to the current in the subsection. Following Ohm's law the resistivity defined by the user gives the proportionality coefficient.

5.2.2 Analysis Sweep

The Adaptive Band Synthesis is a technique that provides a fine resolution response. The em software performs a full analysis at the beginning and end of the frequency span, then does the same for discrete points, between one hundred and two thousand, across the span. The result is then a combination of data points and synthesised data, commonly called adaptive data.

5.2.3 Parametric Sweep

One of the most interesting features of the em server is the parametric sweep. It is possible to define a number of variables (for example the dimensions of a certain polygon) and, given a certain range for the parameters to vary in, the em software will compute all the different possibilities. The user then can decide, after having seen the S-parameters of the different designs, which one is best. As a final remark, it is worth mentioning that SONNET has of late the capability of being interfaced with Python and it is now possible to run Monte Carlo optimisation with a set of desired requirements that have to be met and based off the change of multiple variables. On this basis, it is then easily possible to optimise a general MKID for a selected resonance frequency and a chosen value of Q_c.

5.3 Lithographic Mask

Once all the resonators have been designed and simulated, the lithographic mask is drawn with the help of L-EDIT, a hierarchical physical layout editor (77). L-EDIT is a powerful tool that allows the creation of GDSII files on a $1\,nm$ scale grid and supports the designer with simple graphic tools. This way it was possible to design each chiplet so to have three feedlines with resonators optimised for different values of sheet inductance. The feedlines are placed on the chiplet so that their bond-pads match with the position of the transmission lines on the transmission board that eventually connect the chips with the SMA on the sample box. The chiplets also feature ten cross-hairs to allow the alignment of a microlens array on top of the box to further improve the light collection. The resonators are well distributed along each feedline to minimise cross-talk between resonators that are adjacent in frequency space. Four copies of three different chiplets are placed on the lithographic mask. Each one has three feedlines one per each designed value of sheet inductance.

6 MKIDs Fabrication

Before progressing further in the discussion of MKIDs it is appropriate to describe in some detail the general process of MKIDs fabrication and it is also worth discussing the specific fabrication process developed in CRANN and the Tyndall National Institute. Regardless of where the fabrication is carried out, the general process is the same and can be summarised in the following six steps:

- Silicon Oxide removal - HF etch
- Metal deposition
- Photolithography
- ICP Etch
- Dicing
- Bonding

The different sections in this chapter will describe briefly the process and the challenges that needed to be overcome to develop the optimal process recipe. While reading the individual sections will not be exhaustive, a detailed process sheet is available at the end of this chapter.

6.1 HF etch

While some MKIDs are fabricated on sapphire wafers, the standard substrate material for MKIDs is high resistivity un-doped (1,0,0) silicon. One of the benefits of a sapphire substrate is immediate when it comes to an optical photodetector: the absence of photon absorption that produces highly energetic phonons. Phonons can break-up superconducting cooper pairs allows for a better performing detector. Unfortunately the uniform deposition of materials such as Titanium and Titanium Nitride is very challenging.

When purchased, silicon wafers come with a coating of approximately $100\,nm$ of silicon dioxide SiO_2.

Silicon oxide can be highly detrimental when it comes to fabricating resonators with low losses, and therefore a high internal quality factor. The amorphous nature of the

silica can result in high frequency losses through Two-Level System (TLS) effects. This eventually results in lossy and broad resonators that can also exhibit a poor noise performance.
In order to get rid of the natural silicon dioxide an etch step in hydrofluoric acid (HF) is necessary, the chemical reaction is as follows (78):

$$SiO_2 + 6HF \longrightarrow 2H^+ + SiF_6^{2-} + H_20$$

In order to slow down the reaction to get a more uniform etch rate through the whole process, the HF solution in water is buffered with ammonium fluoride (NH_4F) 7:1.The buffering contributes to controlling the kinetics of the reaction producing a more uniform and controllable process. The etching recipe developed in CRANN calls for a $120\,s$ long etch to get rid of the silica. The timely constraints on this process are not extremely strict as the buffered HF will not react with the silicon wafer once the silicon dioxide layer has been etched away. The wafer is then cleaned of any acid remains in de-ionised water and is loaded inside the cassette module of the Trifolium Dubium, CRANN's Ultra High Vacuum (UHV) sputter system for the baking process within 30 minutes of the etching.
An important remark has to be made on the hazardous nature of acids. HF, even when buffered, is a harmful solution even at very low concentrations. HF is not only corrosive, but it is also very poisonous when a human is exposed to it either through contact or inhaling the fumes. Hydrofluoric acid can cause severe burns that could be lethal if untreated rapidly. Only trained users should use the HF wet-bench, and must make sure the correct PPE is worn. Cleanroom managers can train users and show the existent health and safety procedures for the correct use of the acid wet-bench.

6.2 Metal Deposition

The second step of the fabrication process is the deposition of the superconducting thin film on the freshly etched silicon surface. In order to have good control over the deposition rate, the thickness of the layers and the stoichiometry of each of them, we use of the Trifolium Dubium, a Ultra High Vacuum Sputter System available in CRANN's Clean Room.
Sputter deposition uses a gaseous plasma generated in an area that contains the "target", which is a bulk of the material to be deposited. The target's surface is eroded by the high energy ions of the plasma and the atoms produced are accelerated towards the substrate to form a thin film. In order to get rid of contaminants, and to increase the mean free path of the atoms and ions, the chamber is usually evacuated to pressures below $10^{-9}\,mbar$ then the high purity sputtering gas, usually Argon (Ar), is flowed into the chamber to reach the ideal process pressure, which is usually in the

mbar range. The plasma is ignited by applying an electric voltage between the target and the chamber wall. A high enough voltage removes some electrons from the gas atoms, and the ions are then accelerated towards the cathode creating an avalanche-like process that produces even more ions this eventually results in high energy collisions with the surface atoms of the target. Each of these collisions can accelerate the atoms enough that they can fly through the plasma and re-deposit on the substrate's surface giving rise to the deposition of a thin film.

In order to produce a higher density plasma and higher deposition rates, a magnetic field is exploited to confine the plasma. This deposition technique is called Magnetron Sputtering.

Often it is desirable to flow, alongside the sputtering gas, reactive gas (usually Oxygen or Nitrogen) in the chamber. Increasing the partial pressure of the reactive gas, produces the "poisoning" of the surface of the target i.e.the transition from a purely metallic state to an oxide or nitride state. Changing the partial pressure of the reactive gas then results in a change in the stoichiometry of the deposited thin film.

6.2.1 Trifolium Dubium

The UHV sputter system available in CRANN, named the Trifolium Dubium, is a 5-chamber assembly from DCA Instruments. It incorporates two sputter chambers, S1 and S2, a Pulsed Laser Deposition chamber, an Molecular-Beam Epitaxy chamber and an X-ray Photo-electron Spectroscopy chamber. Upon loading the substrates in the cassette module, an automatic bake out occurs. The chamber is heated up to $200°C$ for two hours. This is necessary to ensure that most of the water on the surface of the wafer is evaporated and to allow transfer to a UHV chamber, such as in any of the process chambers. Sputter 2 (S2) is the chamber where reactive sputtering is allowed and therefore it holds our titanium (Ti) target. The chamber is equipped with a throttle valve to control the total pressure inside the chamber when the gaseous mixture is flowed into it. The gas flows are controlled by two mass flow controllers (between 2 and 139 sccm). The gases can be pre-mixed and injected in the chamber in proximity of the substrate's surface or ejected by two different nozzles on the side wall of the chamber. For all of our applications we are only using the pre-mixed gas mixture as we expect a better gas homogeneity in proximity of the surface as this might lead to a higher layer homogeneity and therefore a higher homogeneity in critical temperature.

As we can see in Figure 6.1, the critical temperature of the TiN_x films depends strongly on the Nitrogen to Argon ratio in the atmosphere of the sputter chamber. Figure 6.1 shows that if there is "enough" Nitrogen in the atmosphere, the critical temperature of the films reaches a plateau around $3\,K$, while by reducing the relative amount of nitrogen the critical temperature of the film reduces as well. The lowest

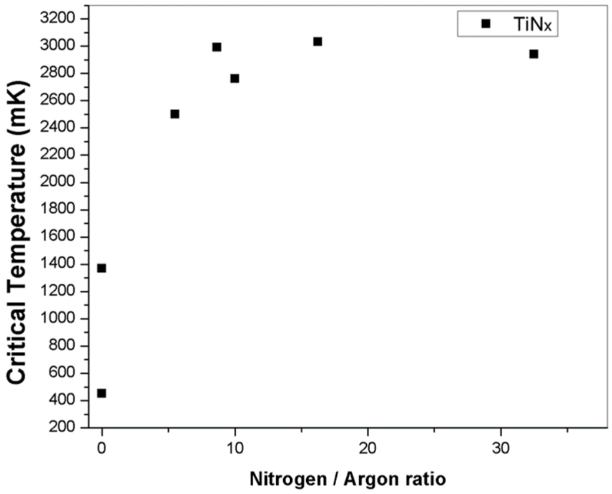

Figure 6.1: Critical temperature of the thin films of substoichiometric TiN_x plotted against the Nitrogen/Argon gas ratio flowed into the sputtering chamber. Measurement errors smaller than the size of the points.

value of critical temperature achieved in the Trifolium Dubium is $1.4\,K$ at the very edge of the capability of the instrument with 2 sccm of Nitrogen and 139 sccm of Argon. Unfortunately, the mass flow controller is not reliably stable below 2 sscm and when it is fully open it flows 139 sccm.
The Ti target is a 2-inch target and the best homogeneity is achieved by angling the sputter gun at a $26°$ angle from the vertical (As optimised by Atcheson G. and Lee H., personal communication).
While films with an ideal critical temperature of $0.8 - 1.0$ K cannot be deposited in the Trifolium as it currently is set up, nevertheless a new possibility opens up: given that the Tc reaches the plateau at around $3\,K$ as opposed to the usual $4,5\,K$ as per often reported in literature, it is possible to produce TiNx/Ti/TiNx multilayers which would exploit high uniformity layers of Ti and a high-Tc TiN_x to produce a stack. This multilayer stack can be thinner than corresponding TiN/Ti/TiN stacks, therefore allowing for more responsive MKIDs with relatively high sheet inductance. This might be an interesting way of mitigating the well known inhomogeneity of TiN_x films which have a Tc in the $0.4 - 1.4\,K$ range and to produce resonators with high internal quality factors on films in the same range of temperatures. Unpublished research from other groups (private communications) seems to indicate that that low-Tc multilayer stacks also exhibit a reduced internal quality factor. This phenomenon could perhaps be explained by a non fully-proximised stack. To the best of my knowledge, the cause for such low internal quality factors has not been investigated yet by the authors.

6.3 Photo-lithography

The third stage of the fabrication process is the photo-lithography which consists in covering the film with a thin layer of photoresist, photosensitive polymers in solution. Much like silver halide based photography, when the photosensitive polymer is illuminated, it hardens (or softens) so that through a masking, illumination and development process, a pattern can be impressed on the photoresist.

According to whether the photoresist hardens or softens when illuminated, it is classified in "Negative" or "Positive" photoresist respectively. Our process was optimised for a positive photoresist, $SPR\,220 - 3.0$ which is ideal for photolithographic processes where the critical dimension is as small as $1\,\mu m$.

The coating occurs with the help of a spinner, here a turntable, rotating at 2000 rpm, ensuring a $3.0 \pm 0.1 \mu m$ uniform coating of the metalised substrate.

Changing the Argon to Nitrogen ratio it is possible to tweak the critical temperature of the thin films. The data sheet suggests a $90\,s$ pre-exposure bake at $115^\circ\,C$ to have most of the solvent to evaporate and harden the photosensitive layer. In reality, given the non-uniformity of surface of the hot plate where the baking occurs, it was experimentally observed that a $180\,s$ pre-exposure bake produced a more vertical side profile of the unexposed photoresist, which eventually results in a better overall lithography.

The exposure occurs through an AOI 800 Mask Aligner. For the illumination, the data sheet suggest a dose of $210\,mJ/cm^2$ which is equivalent to $20\,s$ of exposure time in the instrument.

In order to complete the chemical reaction started during the exposure, a post-exposure bake (PEB) is common practice in photo-lithography. Once again the data sheet suggests a PEB at $115^\circ C$ for $90''$. For the same reasons just discussed, the PEB time is extended to $180''$ too.

In order to remove the now softened photoresist a development process is necessary. The developer we use for this process is the Microposit $MF - 319$ which is a solution of tethramethylammonium hydroxide (2.2%) and a non-disclosed surfactant in water (95%). The immersion of the processed wafer in the developer starts a reaction by which the softened polymers of the exposed photoresist start dissolving in the water-tethramethylammonium hydroxide solution and the surfactant helps lifting them from the surface of the metal-film. The development process involves $43\,s$ of immersion in the solution, with constant agitation and a $160''$ rinse in a DI water tank to stop the developing reaction and to ensure the dilution of the developer.

At this stage the wafer should be as described in Figure 6.2 (3), with a thin metal film deposited on a bulk silicon wafer and some free-standing hardened photoresist features on part of the wafer. If using a positive photoresist and a correctly designed mask, the photoresist should be gone from most of the wafer except from the areas

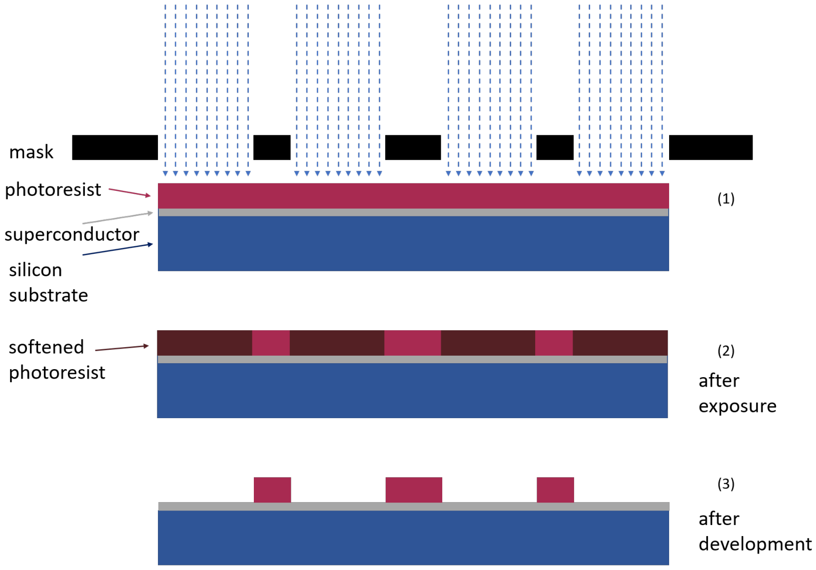

Figure 6.2: The photo-lithographic process in three stages: (1) exposure in the mask aligner with the mask blocking off the light from reaching the photoresist. (2) the exposed photoresist softens and (3) after development only the unexposed photoresist remains.

that we want to keep metalised in the designed circuit.

6.4 ICP Etch

The fourth process stage is the removal of the excess metal from the film and this is achieved with an Inductively Coupled Plasma etcher. This process, in a way the opposite of sputtering, removes the metal atoms from the surface of the sample. One main difference with the sputtering process is that the plasma is not inert, rather it uses a reactive plasma to etch away the elements on the surface of the sample. The photoresist previously patterned covers the areas of the surface where we want to keep the metal and protects it from etching away. Of course the ICP process will start attacking the photoresist as well, but it is approximately 3μm thick while the thickness of the metallic layer is in the order of a few tens of nm.

In an ICP etcher the plasma is ignited through a high-power RF coil in a low-pressure chamber which is filled with the chemically reactive gases. The radicals in the plasma are then accelerated towards the sample space with an electric field. Upon striking the exposed metallic atoms, the ionised atoms in the plasma they react with the different elements at play producing volatile etch products that are eventually pumped out of the chamber.

The etching recipe developed for the MKIDs fabrication process in CRANN is centred around fluorine-based chemistry as this is the only subclass of reactive gases available in CRANN. In order to keep the process stable Ar and O_2 gases are also introduced into the process chamber.

After the etch, the excess metal is no longer present on the exposed surface of the

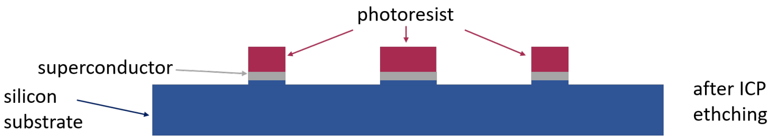

Figure 6.3: Schematic of the process after the ICP etch. Here the unexposed photoresist is still present on the surface of the wafer, the unprotected metalisation has been removed and an amount of under-etch in the silicon is visible. The under-etch is necessary to ensure that the etch of the metal layer is complete.

sample, while the photoresist exposed to the chemical reactive plasma, will have hardened and has to be stripped off. This process occurs in a two-baths process which involve 1165 photoresist remover heated at $80°C$. The sample is first ultrasonicated while standing vertical in a bath of 1165 for $60\,min$ and then in a second bath of fresh 1165 heated at the same temperature for additional $15\,min$. Finally the sample is cleaned in a five stage process in baths of DI water ($5\,min$), Acetone ($5\,min$), IPA ($5\,min$) and DI water (twice for $5\,min$).

6.5 Dicing and Bonding

By this stage the process is complete. The wafer has to be diced into individual chiplets according to the pattern designed on the photo-lithographic mask. This is done with a disco dicer which is equipped with a special blade to dice through silicon wafers and that can be programmed to perform extremely accurate sequential cuts. During the process, silicon dust is produced and it could be left as debris on the surface of the wafer. In order to prevent this, the wafer has to be spin coated with protective photoresist before undergoing dicing. Once the wafer is diced, individual chiplets will have to be cleaned from the photoresist in a process identical to the one described in the previous section.

The diced chiplet now has to be glued into a sample box, subsequently electric connections have to be established between the pads on the chiplet and the centre strip of the feedline on the transition boards that lead to the SMA connectors on the sample box. To do this, the sample is connected through $50\mu m$ aluminium wires. A wire bonder is used for this purpose. As with a sawing machine, a thin aluminium wire is fed through the tip of a wedge to which, upon reaching the surface of the chiplet, ultrasonic power is applied this welds the aluminium to the surface and ensures electrical conductivity.

Three types of connections are necessary:

- pad to feedline
- ground plane to ground plane
- air-bridges

The first kind ensured a connection between the SMAs on the side of the sample box to the feedline on the chiplet. The second kind is necessary to connect the ground plane on the chiplet to the common ground on the sample box. The third kind connects the ground plane on both sides of the feedline on the chiplet. This is to keep the ground plane at zero potential when a radio frequency signal is fed into the feedline.

6.6 CRANN Process sheet

Here we present a mock-up of the process sheet for a generic wafer produced in CRANN.

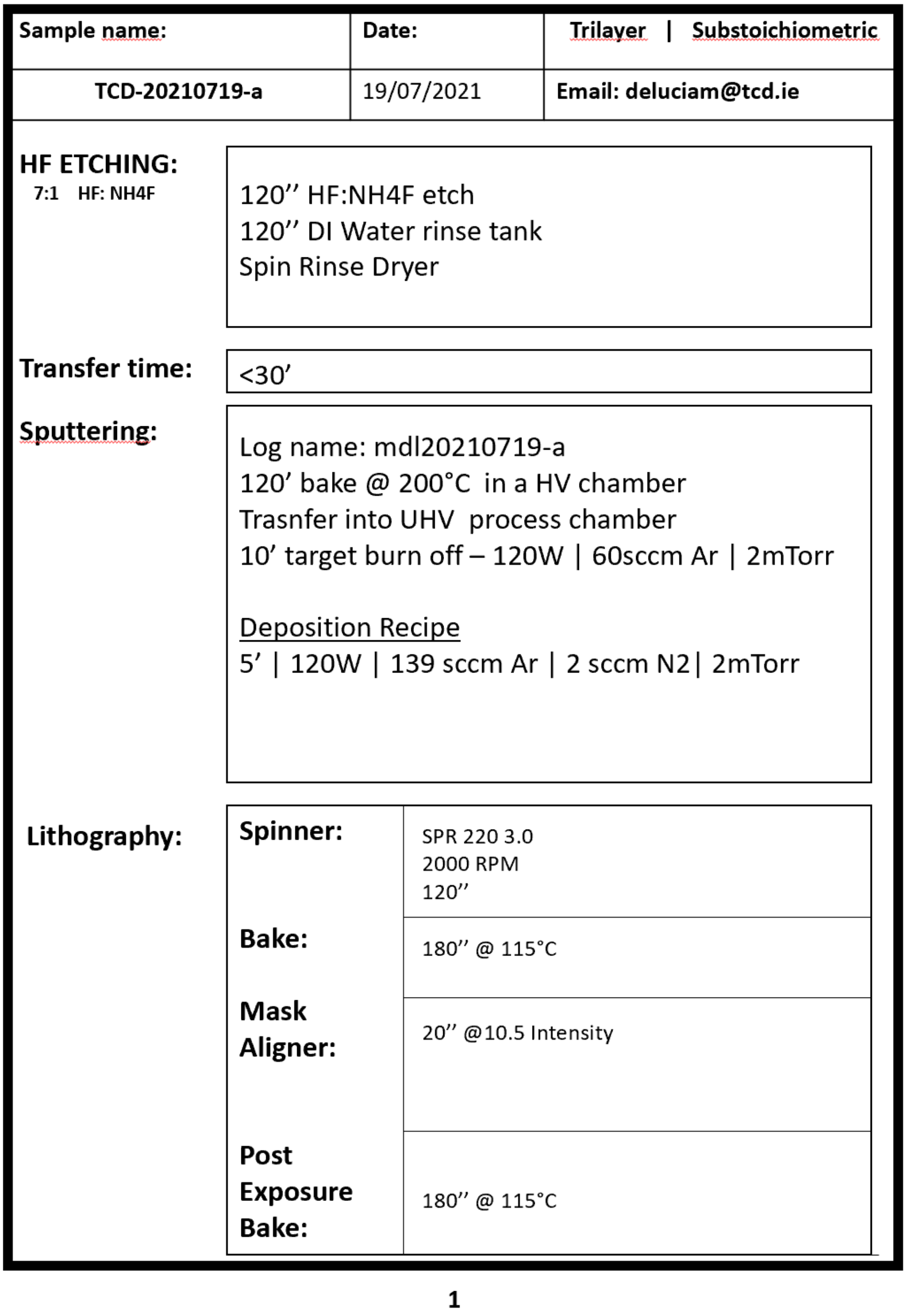

Sample name:	**Date:**	**Trilayer | Substoichiometric**
TCD-20210719-a	19/07/2021	**Email: deluciam@tcd.ie**

HF ETCHING:
7:1 HF: NH4F

120’’ HF:NH4F etch
120’’ DI Water rinse tank
Spin Rinse Dryer

Transfer time: <30’

Sputtering:

Log name: mdl20210719-a
120’ bake @ 200°C in a HV chamber
Trasnfer into UHV process chamber
10’ target burn off – 120W | 60sccm Ar | 2mTorr

Deposition Recipe
5’ | 120W | 139 sccm Ar | 2 sccm N2| 2mTorr

Lithography:

Spinner:	SPR 220 3.0 2000 RPM 120’’
Bake:	180’’ @ 115°C
Mask Aligner:	20’’ @10.5 Intensity
Post Exposure Bake:	180’’ @ 115°C

1

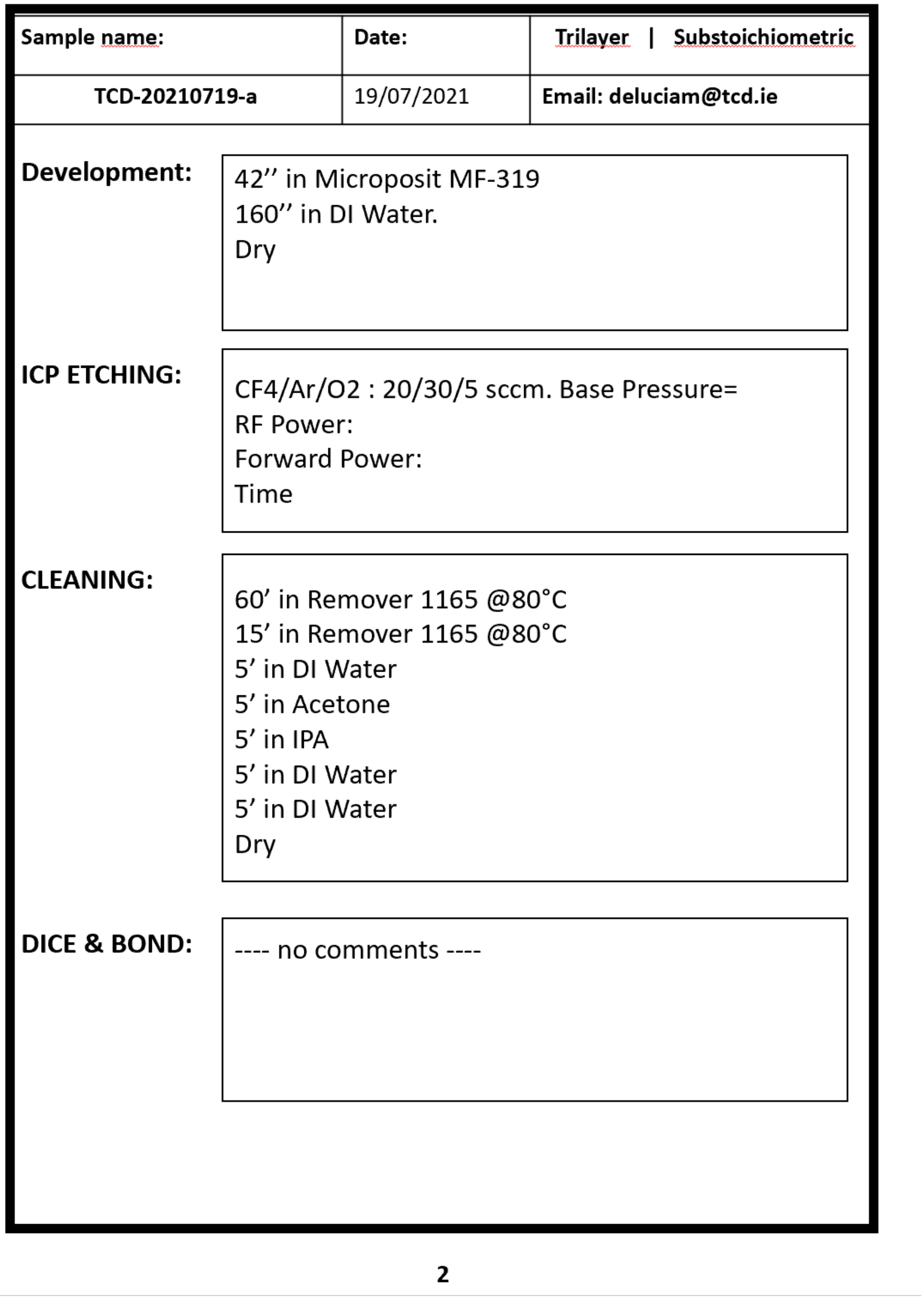

Sample name:	**Date:**	**Trilayer | Substoichiometric**
TCD-20210719-a	19/07/2021	**Email: deluciam@tcd.ie**

Development:

42’’ in Microposit MF-319
160’’ in DI Water.
Dry

ICP ETCHING:

CF4/Ar/O2 : 20/30/5 sccm. Base Pressure=
RF Power:
Forward Power:
Time

CLEANING:

60’ in Remover 1165 @80°C
15’ in Remover 1165 @80°C
5’ in DI Water
5’ in Acetone
5’ in IPA
5’ in DI Water
5’ in DI Water
Dry

DICE & BOND:

---- no comments ----

2

6.7 Tyndall fabrication

With the Cleanroom in CRANN being non fully operational for several months due to the COVID pandemic, we contracted the Tyndall Institute in Cork to deposit and fabricate for us a number of wafers. In order to differentiate the work carried out in CRANN from that in Tyndall, and since I was mostly focused on the deposition of sub-stoichiometric TiN_x in CRANN, Tyndall was asked to deposit TiN/Ti/TiN trilayers for us and pattern them.

As previously discussed, it is possible to control the critical temperature of the stack exploiting proximity effect. Changing the thickness of the three layers, and accordingly the overall composition of the stack, results in a change in critical temperature.

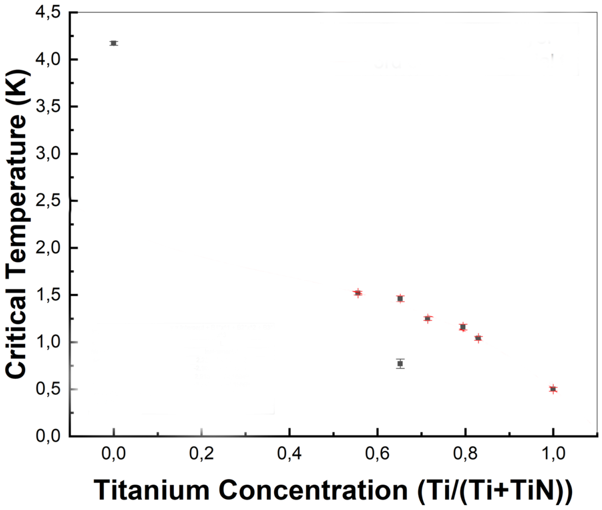

Figure 6.4: Critical temperature dependence of TiN/Ti/TiN multilayers as a function of the Ti to TiN ratio. The TiN film was discarded in order to get better fitting to the region of interest and the point at 0.65 because EDX analysis on the film showed a high concentration of Tin (Sn). The thickness of the two TiN layers is kept constant (4nm) and the the thickness of the sandwiched Ti layer is varied.

Preliminary critical temperature measurements were performed on Pure Ti layers, stoichiometric TiN layers and multilayer stacks. The purpose of these measurements was to measure the critical temperature of both Ti and TiN and have a reference point in order to tweak the thickness of each layer of the stack to obtain the desired critical temperature of the film. Figure 6.4 shows the data points on a Cartesian graph. While the physics that governs the process might not be described by a third level polynomial, an easy fitting function has been used to obtain a first order approximation of where the critical temperature of a specific multilayer shall sit. It was proven that critical temperatures between 0.8K and 1.5K can be achieved through this stacking process.

It is important to state that the deposition occurs in a High-Vacuum chamber (HV) in Tyndall instead of a Ultra-HV chamber like the one available in CRANN and that the metalisation is etched away with a Chlorine-based (Cl) process, rather than a Fluorine-based (F) one as in CRANN.

6.8 SEM Pictures

For the sake of the documentation, it is interesting to include a few SEM pictures captured while inspecting the quality of the fabrication. The pictures captured with the Scanning Electron Microscope show the different designs that are engraved on the lithographic mask and are used to produce the resonator array. A Scanning Electron Microscope uses an an electron beam, focused and accelerated to the user's needs, to probe the surface of a specimen. The imaging is achieved through the analysis of back-scattered electrons and secondary emission electrons. The secondary electrons play the primary role of detecting the morphology and topography of the specimen while back-scattered electrons are used to analyse the composition of the elements of the specimen. Contrast in the back scattering image is induced by electron counts and is and the back-scattered cross section is a good identification of the material. Further details on Scanning Electron Microscopy are beyond the scope of this thesis and can be found in standard textbooks (79, 80, 81).

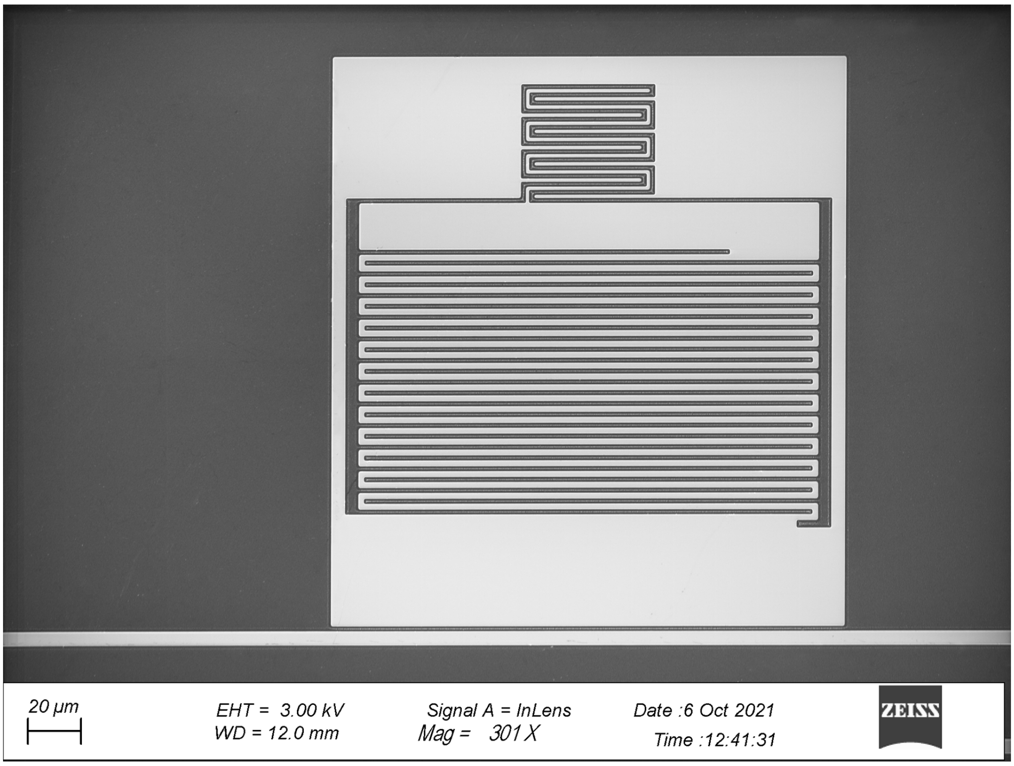

Figure 6.5: Design #1: SEM picture of an MKID fabricated in CRANN where the meandered inductor and the interdigitated capacitor are clearly visible.

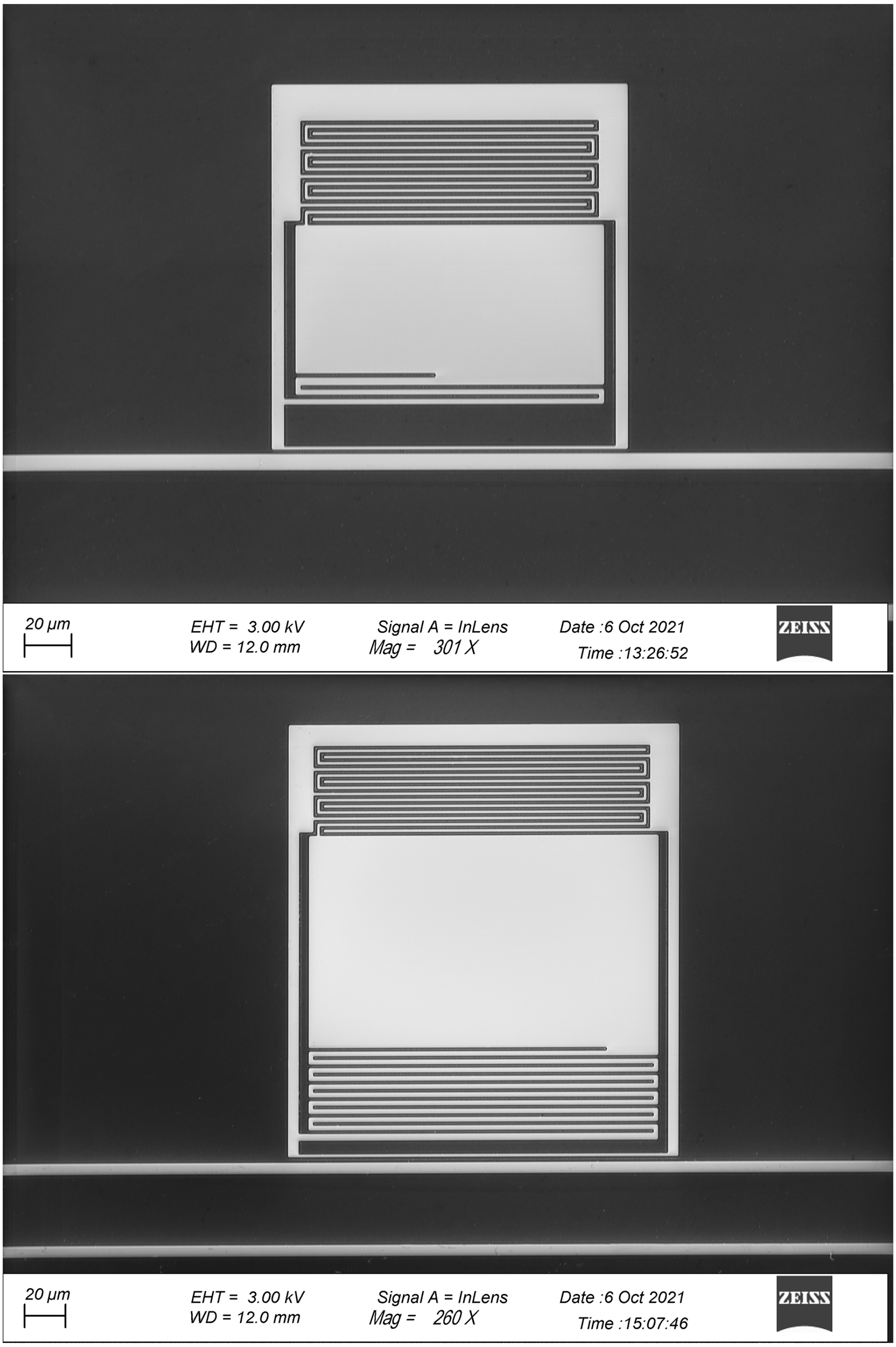

Figure 6.6: Top: Design #2: SEM picture of an MKID fabricated in Tyndall where the meandered inductor and the interdigitated capacitor are clearly visible. This design also involves a larger inductor, and a large coupling bar. Bottom: Design #3: SEM picture of an MKID fabricated in Tyndall where the meandered inductor and the interdigitated capacitor are clearly visible. This design also involves a larger inductor, but a moderately sized coupling bar

6.8.1 Profile Etch

One further thing that has to be verified, aside from the quality of the lithography, is the quality and reliability of the etching process. In order to do so, a cross-section scan can be of great help. Figure 6.7 shows the side profile of a leg of an MKID. The cursors show that the designed critical dimension of $1\,\mu m$ is met and that the metalisation is completely etched away and that the side profile of the etch is nice and vertical. The bright thin line represents the metalisation (TiN/Ti/TiN in this case) and is $40\,nm$ thick. The cross-section scan shows a clear vertical etch of the profile. In addition to this, the etch has been run long enough to not only etch away the metallic layer, but also to etch partially into the silicon so to make sure the etch is complete and also to hopefully reduce the noise levels due to Two Level Systems.

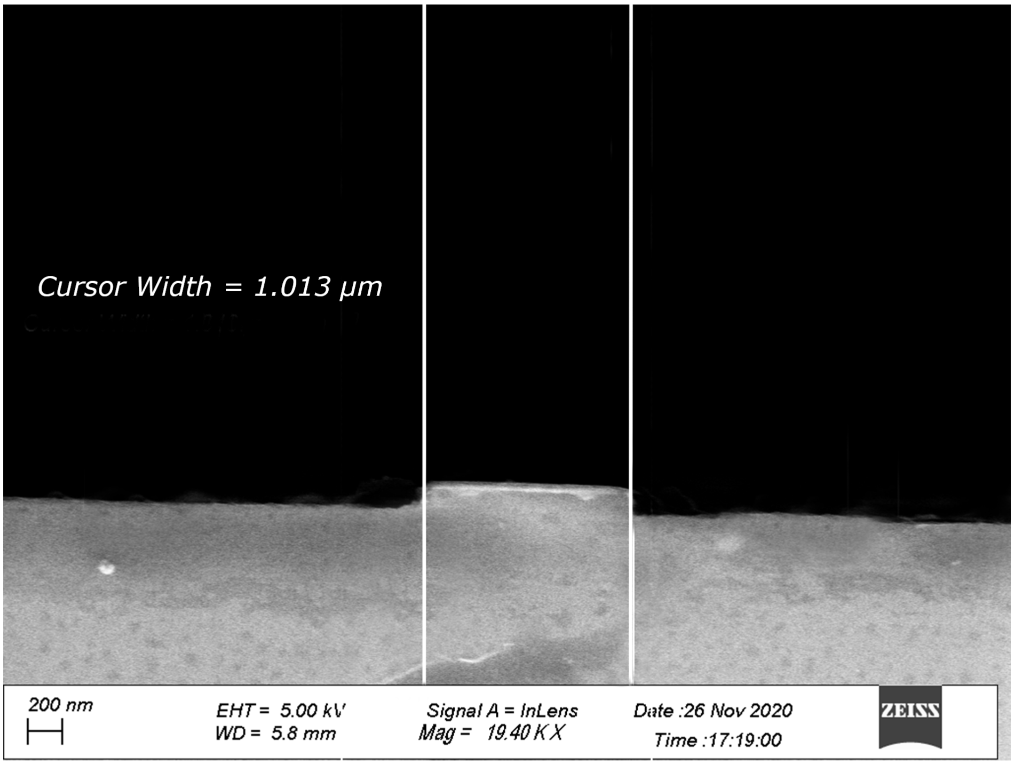

Figure 6.7: Side profile of a leg of an MKID fabricated in Tyndall. The bright line represents the metalisation and the edge profile is vertical.

6.8.2 Microscope Pictures

For the sake of comparison, this section shows pictures of an MKID as acquired through an optical microscope. In picture 6.8(Top), all the distinctive elements of a resonator are visible: the meandered inductor, the interdigitated capacitor and the coupling bar. The feedline to which it is coupled is also clearly distinguishable and the number 5460 engraved in the ground plane is meant to indicate the resonance frequency, in MHz, of that individual resonator for a sheet inductance value as per the simulated model.

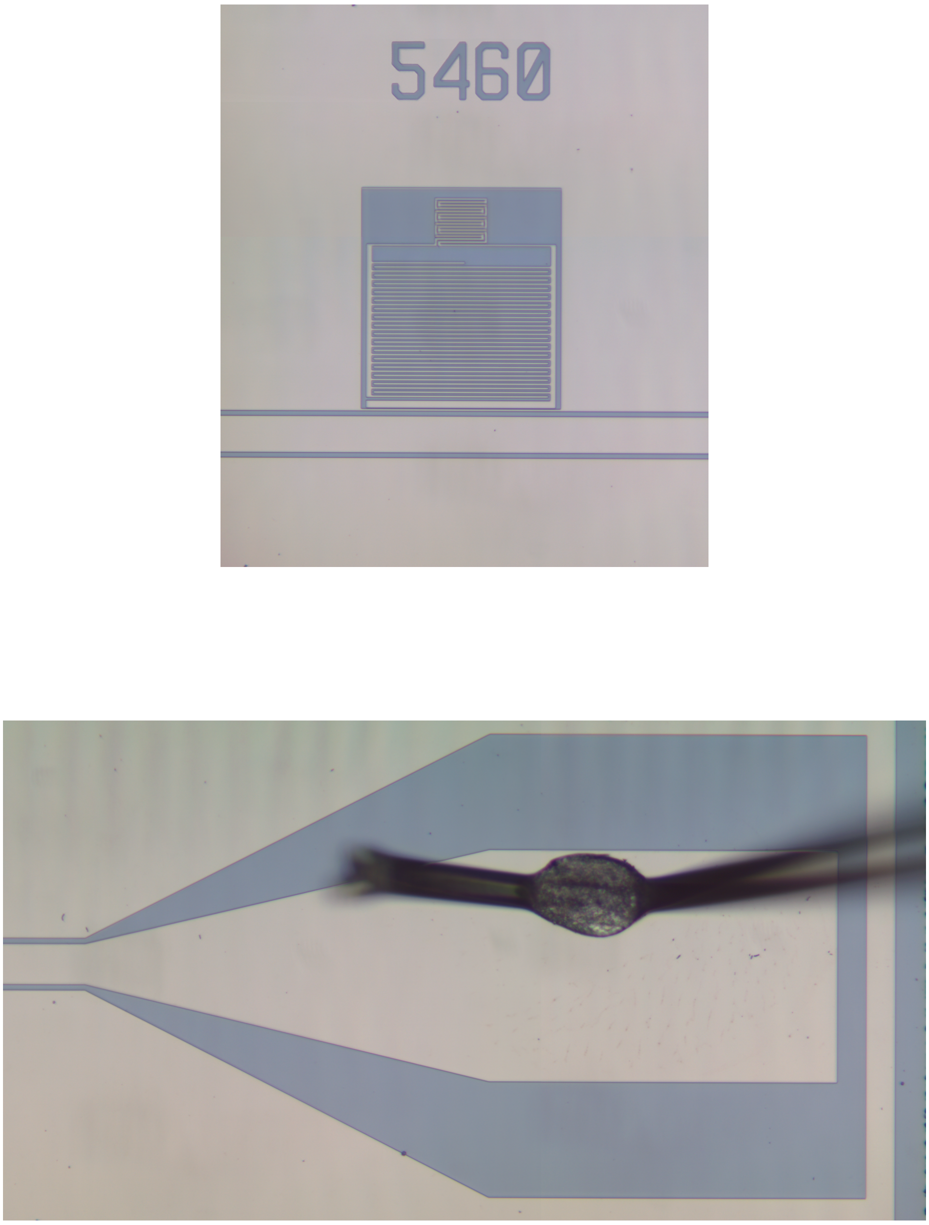

Figure 6.8: (Top) Optical microscope picture of a Microwave Kinetic Inductance detector fabricated in Tyndall and simulated to resonate at 5460 MHz if the sheet inductance of the film is 5 pH per square. All the typical elements of an MKID are clearly visible: the interdigitated capacitor, the meandered inductor and the coupling bar. (Bottom) Bond pad to ensure electrical connection to the transmission line on the transition board. The bond wire is also visible on the surface of the bond pad.

Picture 6.8 (Bottom) shows the bond-pad to which a bond-wire is attached and how it connects to the transmission line of the transition board embedded in the sample box. The 50Ω pad, which is also large enough to accommodate one or more bond wires ensures electrical connectivity.

7 Model and numerical simulation of MKIDs

This chapter describes a study to model two main figures of merit that can describe the performances of an array. The fabrication yield is defined as the number of resonators, expressed as a percentage of the total, with individually-distinguishable resonance frequencies. This represents the amount of pixels that can be used to reconstruct an image. Two resonators with the same resonance frequency, or with frequencies that are too close to each other, are inherently indistinguishable, therefore it is impossible to trace back which MKID generated the signal.
The second parameter of great interest is the energy resolution of each single resonator. The energy resolution describes the smallest possible difference in energy of the impinging photons, ΔE, the detector can identify.
A more in-depth description of these figures of merit is given in the next sections along with the description of a model that simulates the behaviour of MKIDs in order to predict, optimise and design the best array possible.

7.1 Fabrication Yield

The fabrication of the detectors for such instruments is performed in research-grade clean rooms, through processes which are almost completely human-controlled and not automated. These processes have plenty of room for optimisation, although the fraction of non-responding pixels is less than $1\,\%$. Two or more resonators that resonate at the same frequency while they were not designed for this purpose, are said to be *clashing* or *colliding*. Currently, it is thought that most of the clashes are due to random variations of the critical temperature of the superconductor. Although a systematic radial distribution, over a large area , of critical temperature is known to arise during $\mathrm{TiN_x}$ sputtering deposition (13), it only plays a negligible role for detectors of chip size is ≈ 4 cm^2 as its effect can be dramatically mitigated with an accurate placement of the resonators on the test mask that aims to even out possible drifts in critical temperature and film inhomogeneity . The current state of the art is that most arrays exhibit a fabrication yield of $75\,\%$ and only for the best ones it goes

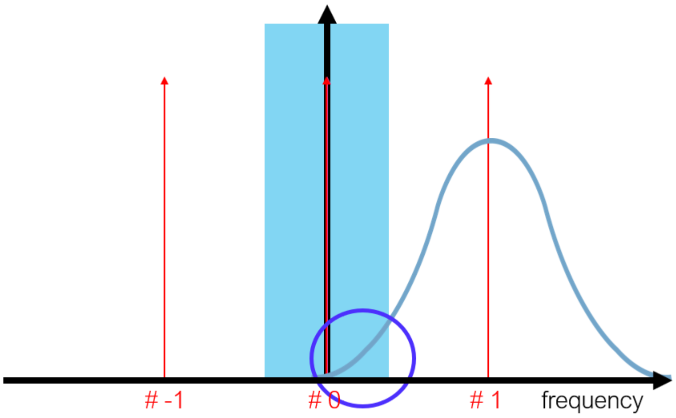

Figure 7.1: Representation of the simple model of the MKIDs array. Resonances #0 and #±1 are shown as well as the collision window. The probability of two resonators colliding is given by the area underneath the bell curve within the limits of the collision window.

as high as 80 % (17).

The model here discussed is based off the approach described by X. Liu et al in (82). This simple model relies on a few basic assumptions:

1. the array of resonators is infinite on both sides of resonator #0
2. the distance, in frequency space, between two adjacent resonators is designed to be: $f_{n+1} - f_n = \Delta = 2$ MHz
3. the n-th MKID's resonance frequency is randomly distributed about Δn according to a gaussian distribution $G(f_n, \sigma) = \frac{1}{\sqrt{2\pi\sigma}} e^{-\frac{1}{2}\left(\frac{(f_n - n\Delta)}{\sigma}\right)^2}$
4. given a defined window, a resonator that falls within said window is defined to be clashing.

The probability that the 0th resonator does not clash with the nth resonator, P$_{n0}$, can be evaluated, according to (82), as one minus the overlapping area defined by the gaussian distribution and the collision window as described in Figure 7.1. Furthermore, due to the translation symmetry of the model, it is only necessary to evaluate P$_{n0}$ for all values of $\pm n$. The benefit of an infinite array is that allows the following identification:

$$P_{n0} = 1 - \frac{Erf\left(\frac{n\Delta + \chi w}{\sqrt{2}\sigma}\right) - Erf\left(\frac{n\Delta - \chi w}{\sqrt{2}\sigma}\right)}{2} \tag{1}$$

Where the integral of a gaussian is evaluated through the error function Erf(x) defined as in Equation 2

$$Erf(x) = \frac{1}{\sqrt{\pi}} \int_{-x}^{+\text{inf}} e^{-t^2} dt \tag{2}$$

Here, Δ is the nominal spacing between the resonators, and χw identifies the collision window through two parameters: w represents the resonator's line-width and a $\chi = 5$ is assumed under the hypothesis that the resonators are well distinguishable when separated by 5 line-widths. This is to say that the profile of the 0-th resonator is well contained in a window five times larges than its typical line-width. Assuming all the resonators to be independent, the total yield is derived as:

$$Yield = \prod_{n=-n_{max}}^{n_{max}} P_{n0} \tag{3}$$

For the sake of a model, it was assumed that the MKID $\#0$ resonates at the central frequency of the working bandwidth, 6 GHz. And only the first 1000 resonators left and right have been taken into consideration. The identification 3 is only valid in the case of an infinite array of evenly spaced resonators. The analysis of this model will be carried out in the next few pages and the dependencies of the yield from physical parameters such as the quality factor of the resonators and the critical temperature of the superconductor will be investigated. It is possible to observe that while increasing the spacing Δ between two consecutive elements of the array, the yield increases accordingly.

A question left unanswered, this far, is how the frequency of an ideal resonator changes when the desired T$_c$ is not met. A simple approach follows the discussion described in (83) and (43); the dependence of the kinetic inductance as a function of the temperature can be evaluated as:

$$L_k = \frac{l}{w}\frac{R_s h}{2\pi^2 1.76 T_{c_0}} \tanh\left(\frac{1.76 T_{c_0}}{K_B T}\right) \tag{4}$$

Where R_s is the resistivity of the film in its normal state, l and w are the physical length and width of the film, h is its thickness, T_{c0} is the critical temperature of the film and k_B is Boltzmann's constant.
Given the change in kinetic inductance, and knowing that the resonance frequency of an LC circuit $f_r = \frac{1}{\sqrt{LC}}$ the fractional frequency shift in resonance frequency induced by a change in critical temperature, therefore a local change in kinetic inductance, is easily obtained provided three assumptions are met :

1. The capacitance of the resonator is only due to its geometry

2. The inductance is only due to the kinetic inductance. The kinetic inductance fraction $\alpha = 1$

3. Any change in sheet resistivity R$_s$ with T$_c$ is negligible.

Under these circumstances, the fractional frequency shift is given by Equation 5

$$\frac{\Delta f}{f_r}(Tc) = \frac{\frac{1}{\sqrt{L(T_c)C}} - \frac{1}{\sqrt{L(T_{c_0})C}}}{\frac{1}{\sqrt{L(T_{c_0})C}}} \tag{5}$$

Here the previous assumptions take a critical part, as $L(T_c) = L_K(Tc) + L_g$ where the latter term represents the geometric inductance.The hypothesis that $\alpha \approx 1$ allows to neglect L_g with respect to L_K and the assumption that R_s does not change with stoichiometry allows to simplify Equation 5 as:

$$\frac{\Delta f}{f_r}(Tc) = \frac{\sqrt{\frac{1}{T_c}\frac{1}{\tanh\left(\frac{1.76T_{c0}}{2k_BT}\right)}}^{-1} - \sqrt{\frac{1}{T_{c0}}\frac{1}{\tanh\left(\frac{1.76T_{c_0}}{2k_BT}\right)}}^{-1}}{\sqrt{\frac{1}{T_{c0}}\frac{1}{\tanh\left(\frac{1.76T_{c0}}{2k_BT}\right)}}^{-1}} \tag{6}$$

Where $\Delta f = f_r(Tc) - f_r(T_{c0})$, T$_c$0is the desired critical temperature, 800 mK for the sake of this discussion; T is the equilibrium temperature at which the MKIDs array is operated, 100 mK. Figure 7.2 shows the absolute value of Equation 6 as a function of the temperature difference $T_c - T_{c0}$.

The main purpose of this calculation is to try and estimate reasonable boundaries for the width σ of the distribution of the frequencies about their mean value f_n. Although, Equation 5 is asymmetrical around T$_{c0}$, for small T_c variations, the two branches can be considered symmetrical as a fist order approximation. It is assumed that only 0.1% of the resonators have a critical temperature that differs by more than 200 mK, thus a shift in resonance frequency that is greater than 1.2 GHz. This justifies the assumption of an upper limit for $\sigma = 0.300$ GHz. Such a broad distribution would be catastrophic for any real array and is certainly overestimate of any realistic value of σ in any well-behaved array .

A first evaluation of the fabrication yield is carried out to understand how well this simple model describes the collective behaviour of an array of MKIDs. A particular choice of the free-parameters is made; it is worthwhile describing the fabrication yield as a function of a varying σ in order to justify how big an effect our previous assumptions have, and instead of evaluating the line-width of the resonators, the current working assumption is that the total width of the collision window is 0.5 MHz.

Figure 7.2 (Right) shows the yield starting to roll off as soon as the standard deviation of the distribution of the resonance frequency around its centre value is comparable to the spacing between two adjacent resonators Δ_r. The yield eventually flattens for values of $\sigma \geq 0.2$ GHz at about 75%. Unfortunately, due to its inherent limitations, it is quite difficult to compare the results produced by the model with experimental results. Nonetheless, it is important to also include in the dissertation how the total quality factor Q_{tot} of the resonators comes into play in this model. By definition, the higher the quality factor Q, the sharper is the resonator's dips Q is

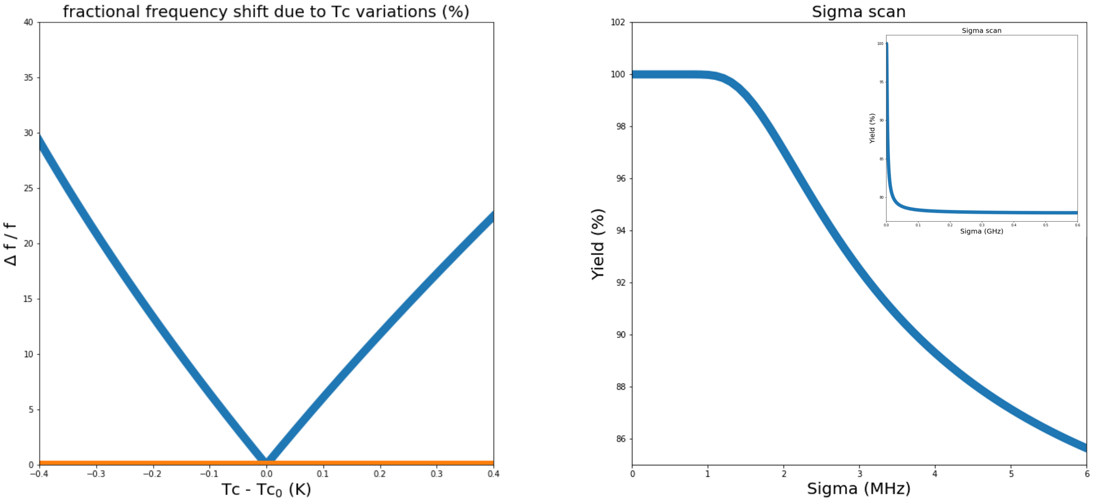

Figure 7.2: Left: fractional frequency shift as a function of critical temperature fluctuations. Right: yield as a function of σ, evaluated for a collision window of 0.5 MHz. The inset shows a wider span of values of σ, up to 0.6 GHz.

inversely proportional to the line-width $w = \frac{f_0}{Q}$ where f_0 is the characteristic resonant frequency. Assuming a $\Delta_r = 2$ MHz, and based on formula 3, Figure 7.3 shows a 2D plot of the fabrication yield as a function of both σ and Q. Two trends are visible in the plot. The yield increases with increasing quality; this says that the sharper the resonator, hence the smaller their line-width and the clashing window, the higher the fabrication yield is. Also, as expected, the smaller the width of the frequency scatter distribution, the higher the yield per fixed values of Q.

Very strongly coupled resonators with low quality factors, such as $Q_{tot} < 15000$, represent the case where the resonator's rejection window is intrinsically larger than the spacing Δ_r reducing dramatically the yield to a mathematical zero based on previous assumptions. For very high values of σ, the model is, in fact, describing an almost random distribution of resonant frequencies. It therefore makes sense that the yield becomes proportional to the rejection window size, thus to the total quality factor Q_{tot}.

It is crucial to state the flaws and the limits of this model and discuss the possible improvements of said picture. There are two main issues to discuss: first of all, a gargantuan value of σ would produce a 100% yield as it would scatter most of the resonators outside the working-bandwidth,$4 - 8$ GHz. It was observed that the yield starts increasing from $\sigma = 1$ GHz onward. Another limit of the model is that, when evaluating the probability of a collision, only one of the two resonator's dips is broadened, while the other is still regarded as if it was infinitely sharp. This effect is only relevant for very strongly coupled resonators, $Q_{tot} > \frac{1}{\sigma}$, therefore it is not significant for the plot in Figure 7.3. Further improvement, which is a higher-order approximation to what has been discussed so far resides in the evaluation of the

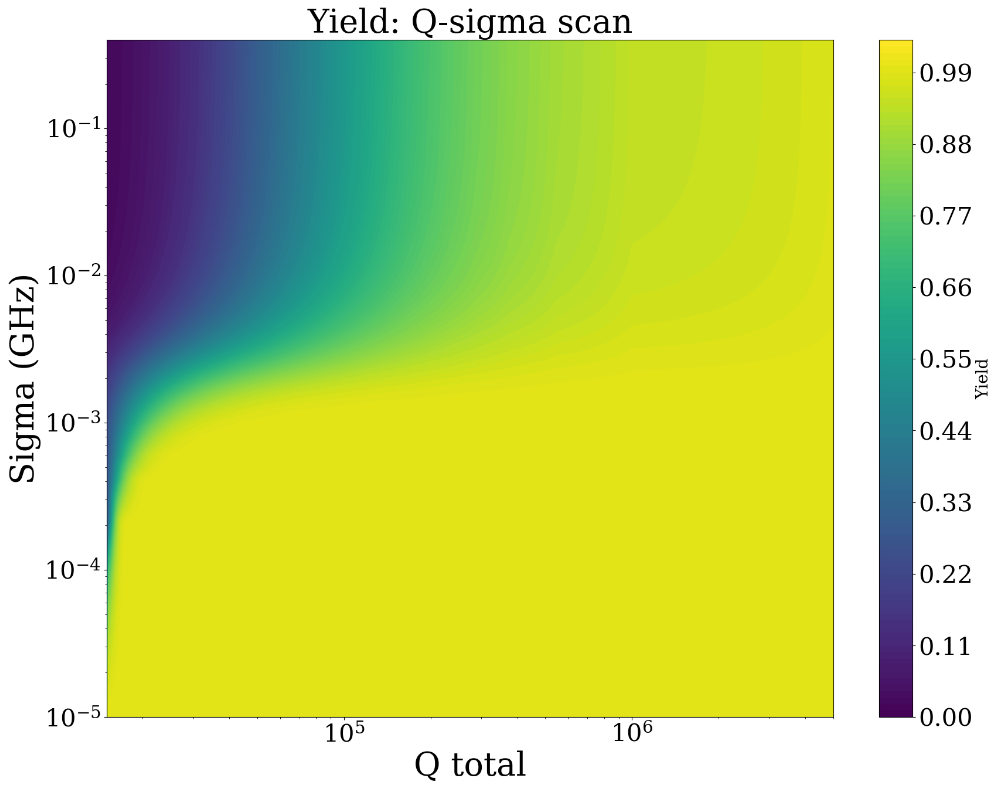

Figure 7.3: Fabrication yield as a function of the overall quality factor Q and the width of the frequency scatter distribution, σ.

line-width as a function of the specific resonator's resonance frequency. In order to summarise the results described in the previous pages, Table 7.1 represents some numerical results for interesting parameters.

$\sigma\,(MHz)$	Q_{tot}	Yield (%)
0.8	20000	79.8
0.6	20000	89.9
1.8	30000	73.8
1.4	30000	85.5
1.0	30000	95.7
2.4	50000	75.8
1.8	50000	87.8
1.4	50000	95.3
4.2	100000	74.4
2.8	100000	84.0
1.8	100000	94.8

Table 7.1: Table representing the yield of a 2000 pixel array as a function of σ and the total quality factor Q_{tot}

7.2 Resolving Power

For detectors, such as MKIDs, that can measure the energy of the incident radiation, energy resolution is a critical figure of merit. The best way to describe it is, borrowing Dr. W. R. Leo's words, " [...] the extent to which a detector can distinguish two close lying energies" (84). An ideal detector, when illuminated by monochromatic light would produce a spectrum that is also monochromatic, and hence described by a Dirac's δ function. In reality, the width of the spectral lines is finite, broadened by several factors which lead to what is experimentally observed. For the sake of clarity, the energy resolution of a detector is intended as $\frac{\Delta E}{E}$, The quantity that will be evaluated most of the time is its inverse $\frac{E}{\Delta E}$ is referred to as the Resolving Power. At present, deVisser et al. (85) claim that the best resolving power achieved corresponds to $\frac{E}{\Delta E} \sim 55$ for wavelengths between $402 - 1545$ nm. The next few page will describe how the following effects come into play in broadening the spectral peak:

1. Statistical processes in the MKID
2. Amplifier noise - High Electron Mobility Transistor
3. Current density inhomogeneity
4. Readout frequency
5. Two-level systems

7.2.1 Energetic processes in the MKID

Detectors that rely on statistical processes for the generation of a detectable signal, such as MKIDs which rely on pair-breaking, suffer from inherent limitations that are due to the statistical processes that occur inside the detector. For example, during the cascade, a number of phonons are excited, and if their energy is not sufficient to further break cooper pairs, that energy is "wasted". The statistical process that is the cascade eventually results in a broadening of the response of the detector. Naturally the nature of the broadening can be addressed to a fluctuation in the number of cooper pairs that are broken down by a single photon of given energy . As stated in (16), the best energy resolution an MKID can achieve as a pair-breaking detector is given by $R = \frac{\Delta E}{E} = 2.355\sqrt{\frac{F\Delta_s}{\eta h\nu}}$, where $\eta \approx 0.57$ is the pair-breaking efficiency (48), $h\nu$ is the energy of the impinging photon, $\Delta_s = 1.72 k_B T_c$ is the superconducting gap energy of the adsorbing material. F is the Fano factor, the effect of which encompasses all the statistical processes that do not lead to pair-breaking. A typical value of the Fano factor for superconductors is $F = 0.2$. These parameters yield a maximum energy resolution of 0.011 for $\lambda_0 = 650$ nm. Unfortunately, there is little room for improvement. For other kind of energy resolving detectors, such as gas and silicon based ionisation detectors, the Fano factor seems to vary, quite significantly, with the material (86, 87). The Fano factor is an inherent property of the material and can be changed by changing the superconducting material of which MKIDs are made. The pair-breaking efficiency, which compares the average number of quasiparticles produced per photon with the maximum number of quasiparticles that can be produced, can be marginally improved by changing the design of the resonator (88). Studies carried out in SRON by deVisser et al. (85) suggest that hot-phonon loss accounts for some of the losses. In particular, hot-phonon loss contributes to increasing the Fano factor by a factor J.

$$R = \frac{\Delta E}{E} = 2.355\sqrt{\frac{(F+J)\Delta_s}{\eta h\nu}} \tag{1}$$

An analytical model and experimental measurements demonstrated that for both Si and SiN substrates, $J \approx 3$, whereas it is higher for Sapphire substrates. The same paper (85) proposed the implementation of MKIDs where the inductors are fabricated on a membrane so to reduce phonon losses. This should reduce the energy loss through phonon mediated processes to the silicon substrate, effectively eliminating phonon loss and thus maximising the pair breaking efficiency. Unfortunately, a value of $\eta = 1$ cannot be achieved since any photon of energy greater than 2Δ but smaller than 4Δ will only create 2 quasi particles and phonon excitations that can not break up any further amount of Cooper Pairs. For higher energies, the efficiency depends on phonon trapping factor (88)where improvement is possible.

7.2.2 High Electron Mobility Transistor noise

High Electron Mobility Transistors are likely one of the main limiting factors when it comes to Energy Resolution. The HEMT discussed here is the Low Noise Factory LNF-LNC4_8C which is a ultra-low noise cryogenic amplifier operating in the 4-8 GHz bandwidth. Its nominal noise temperature, as stated by the manufacturer, is 2.1 K.

The HEMT random noise affects the phase signal. In particular, when a photon strikes the MKID, the phase signal generated is added to this noise and, of course, the height of the phase-jump has an uncertainty given by the noise contribution of the HEMT itself. Referencing Figure 7.4, the quantity that has to be evaluated is $\mathcal{R} = \frac{\Delta\alpha}{\alpha}$. Assuming that the MKID taken into consideration is optimised to respond with an $\alpha = \pi$ phase shift when struck by a photon of wavelength $\lambda_0 = 650$ nm. Figure 7.4 shows the angles just discussed and is of critical importance for the understanding of the model.

HEMT noise induces random fluctuations in both I and Q. Therefore, a non illuminated MKID produces a signal in the I-Q plane that is represented as a scattered cloud. When a photon is detected, the cloud is added to the photon induced phase signal generating inaccuracy regarding the photon's phase signal $\Delta\alpha$.

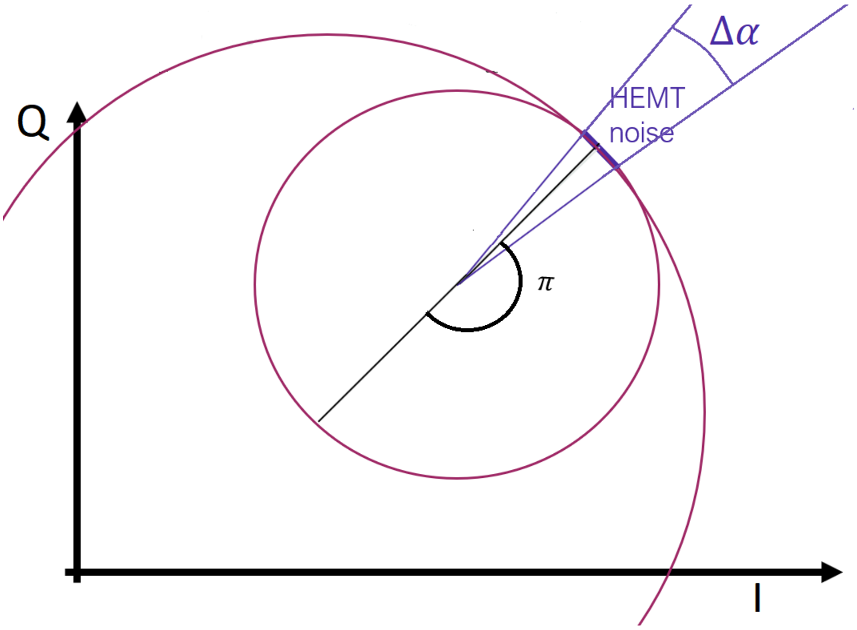

Figure 7.4: Schematic of a resonance loop. The large circle describes the cable delay, the smaller circle is that characteristic of a resonator. Two angles are highlighted: π and $\Delta\alpha$. The latter describes random phase fluctuations due to the HEMT noise. For the sake of clarity, the centre of the IQ plane was shifted away from the centre of the loop.

To clarify, the quantity to evaluate is $\Delta\alpha$, the angle defined by the radius of the resonant loop and the amplitude of the phase noise. In particular, it is not trivial to understand how the noise temperature of the amplifier is then translated into phase noise.

Jonas Zmuidzinas' 2012 review (39) helps; assuming that the amplifier noise is equally distributed between the I and the Q component the noise component can be described by the following equation:

$$HEMT\_noise = \sqrt{\frac{k_B T_A G}{2P_{MKID}} BW} \tag{2}$$

A thorough derivation of the equation is given in the Appendix A2 where k_B is Boltzmann's constant, T_A is the noise temperature of the amplifier, G is the gain of the amplifier, P_{MKID} is the power at the HEMT and BW is the bandwidth given by the Fast Fourier Transform sampling rate, 1 MHz. Equation 2 describes both the I and Q components of the HEMT noise in I and Q units. Now, geometrical considerations, based on maximum and minimum transmission (S_{21}), lead to a simple formula for $\Delta\alpha$

$$\Delta\alpha = \frac{HEMT\_noise}{radius} \tag{3}$$

Where $HEMT_{noise}$ is the length of the arc described by the cloud, and *radius* is the radius of the resonant loop. Assuming perfect transmission in the cable delay loop, which is described by a circle of unit radius. Knowing the distance from the origin of the resonance frequency of a non illuminated MKID is $min|S_{21}|$, and by definition of Q_c (39), $Q_C = \frac{Q}{1-min|S_{21}|}$, it is possible to obtain

$$\Delta\alpha = 6\frac{HEMT\_noise\ Q_c}{Q} \tag{4}$$

Where Q_c is the coupling quality factor, Q is the total quality factor of the MKID. The value of $\Delta\alpha$ would only describe the rms of said quantity. There is an additional factor of 3 to account for the conversion from a rms quantity to a peak-to-peak quantity.

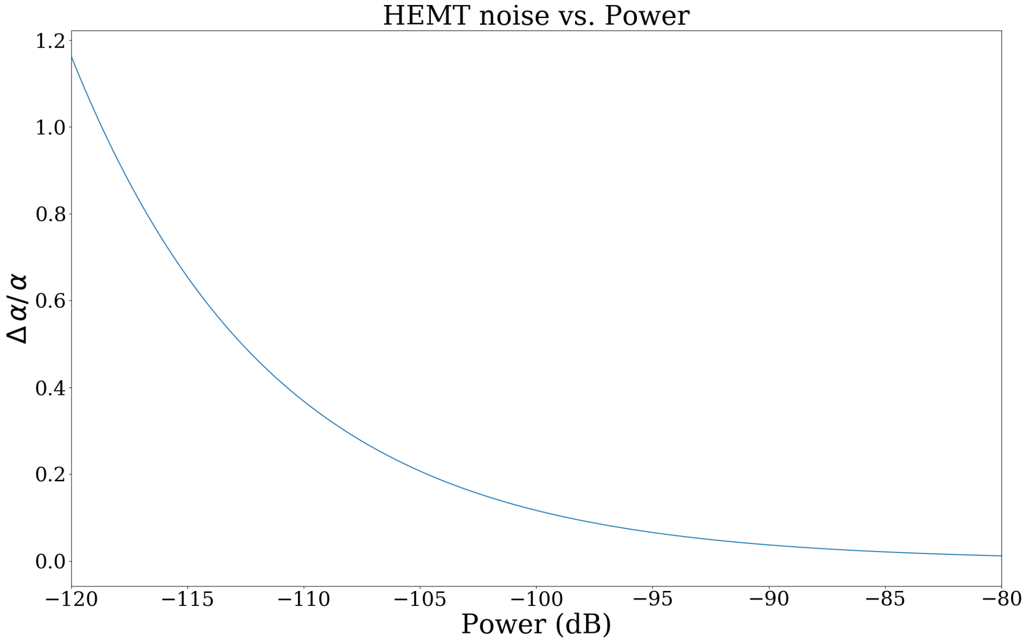

Figure 7.5: HEMT noise, $\frac{\Delta\alpha}{\alpha}$ as a function of the power at the resonator. Standard operating powers are in the -100dB range.

While it may seem that the noise component is very low, it is important to observe that usual readout power, before entering the cryostat, would be ≈ -50 dBm, in addition to that, two 20 dB attenuators have to be taken into account as well as the attenuation of the coaxial cables going into the cryostat. Assuming a total power at the HEMT of about -90dBm, $Q_i = 100000$ and $Q_c = 45000$, $\frac{\Delta\alpha}{\alpha} \approx 0.037$. It corresponds to a noise fluctuation of $\pm 3.3°$ in good agreement with common measurements of $\pm 5°$ white noise in baseline. As a final remark, figure 7.6 shows a 2D plot which clarifies the dependence of $\Delta\alpha/\alpha$ on both the internal quality factor Q_i and the coupling quality factor Q_c. The plot here shown refers to a power value $P_g = -90$ dBm. The area shaded in yellow depicts a portion of the parameter space where $\Delta\alpha/\alpha \geq 0.2$, or $\pm 36°$.

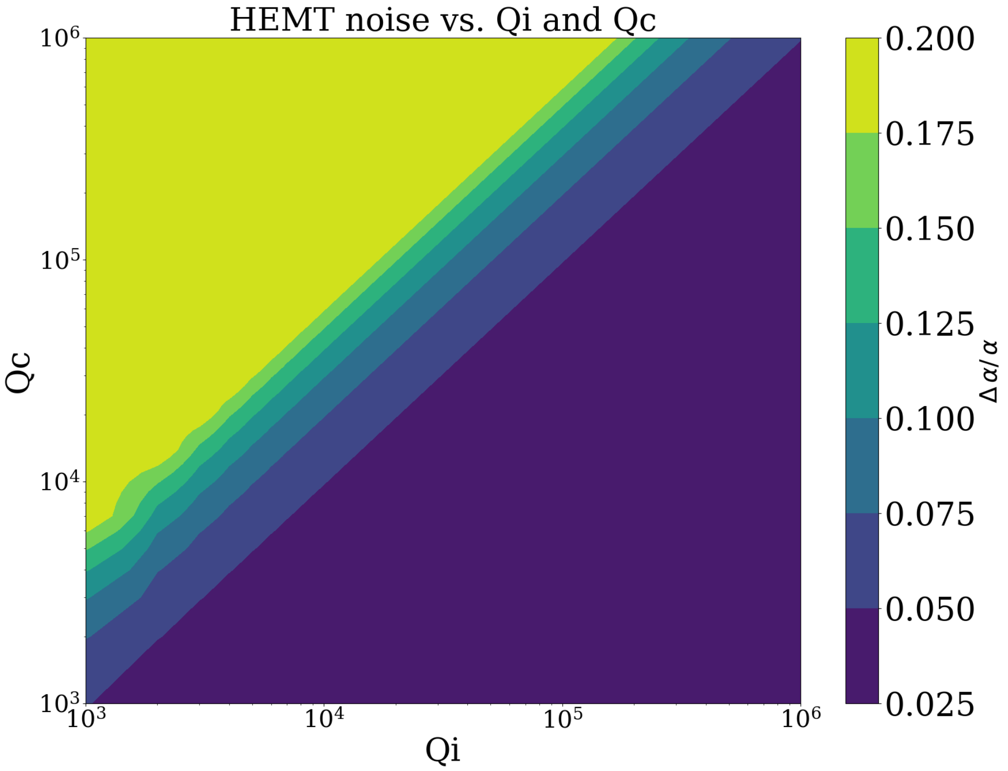

Figure 7.6: 2D graph showing the dependency of the HEMT noise in degrees, at a fixed power and assuming that a photon produces a 180° signal, as a function of the coupling quality factor Q_c and the internal quality factor Q_i. It is important to observe that the area shaded in yellow,represents the parameter space where the HEMT noise is equal o greater than 36°.

7.2.3 Current density inhomogeneity

Another source of uncertainty in the response of an MKID is inhomogeneity of the current density across the inductor. If the current density varies spatially across the inductor, the resulting signal from an absorbed photon will depend on absorption location as variations in current density lead to changes in responsivity $d\theta/dN_{qp}$; where θ is the phase angle, the measured response of the MKID to a photon strike, and N_{qp} is the number of quasi-particles produced by the photon. Current density uniformity strongly depends on the resonator's geometry. Current crowding at right angles is a well known effect for both normal metals and superconductors (89). The current density is affected by the capacitance of the interdigitated capacitor. The charge carriers tend to slow down and create high electric field as they drift towards the two plates of the capacitor resulting in a small, but non negligible gradient in current. The current density is highest at the top of the inductor (far from the capacitor) and sees a typical 5% reduction in proximity of the capacitor. This is because the change in density of the super current induced by a photon depends non-linearly on the intensity of the current. This reflects its effect on both the shift in resonance frequency and the total quality factor Q_{tot}. The change in Q_{tot} accounts for an internal change in Q_c which depends on the resonant frequency of the resonator, while a more significant change in Q_i can be attributed to losses through normal-state electrons produced by pair breaking. In order to evaluate the effects of current density inhomogeneities, the current density data, simulated with SONNET with a grid size in both x and y direction of $0.125\,\mu$m is imported to a Python script I developed.The data is read in by the programme and it is then normalised to the average value over the whole inductor. This creates a current density map which is, for the most part, in the range [0,1] with values greater than 1 only in the inner part of right-corners, where there is a significant current crowding. The working assumption for the next steps is that each single element of the inductor, as defined by the simulation through the grid size, contributes to the total kinetic inductance of the resonator with its elemental contribution and the total kinetic inductance is given by the the sum of the contributions of all the single elements. The resonator is designed in such a way that its resonant frequency is $f_0 = 6$ GHz and $Q_c = 30000$.

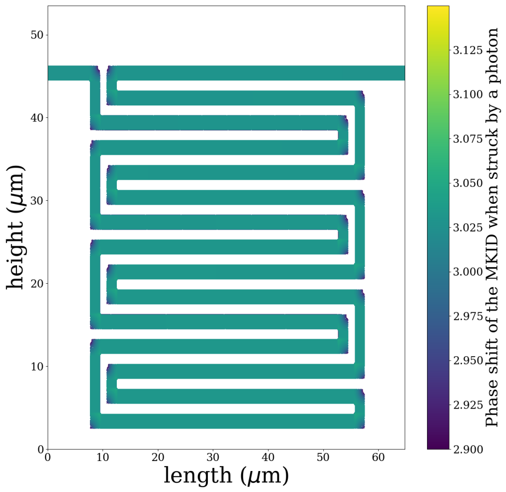

Figure 7.7: Phase shift when struck by a photon as a function of the (x,y) position.

The Python programme, was fed the current density data produced by SONNET, translates the current density 2D-map first into a Kinetic Inductance 2D-map, by knowing the inductance depends on the current density at the location of each of the cells. Once the kinetic inductance of the whole circuit is known, its resonant frequency is immediately given by $\frac{1}{\sqrt{L_K C}}$. When a photon strikes on a specific point of the inductor, it depletes the region around it of charge carrying Cooper Pairs increasing the kinetic inductance of the resonator. As a consequence of this increase of kinetic inductance, the aforementioned shift in resonance frequency, and phase, occurs. Figure 7.7 (Left) shows the expected resonance frequency shift according to where the photon strikes on the inductor. Here, for the sake of simplicity the diffusion of the quasi-particles in the superconductor was not taken into account.

It is possible to evaluate the phase shift registered at the readout frequency, 6 GHz for the sake of this simulation, and it can be iterated for all the possible grid elements produced by SONNET. Manipulating equation 3 to obtain the phase component, it is possible to produce the 2D map shown in Figure 7.7 (Right). Here the phase shift is shown, measured at $f_0 = 6$ GHz, due to an impinging photon as a function of where the photon hits the inductor. In order to simulate an optimised resonator at the impinging wavelength, the depletion considered was that which produces a $\geq 0.95\,\pi$ phase shift.

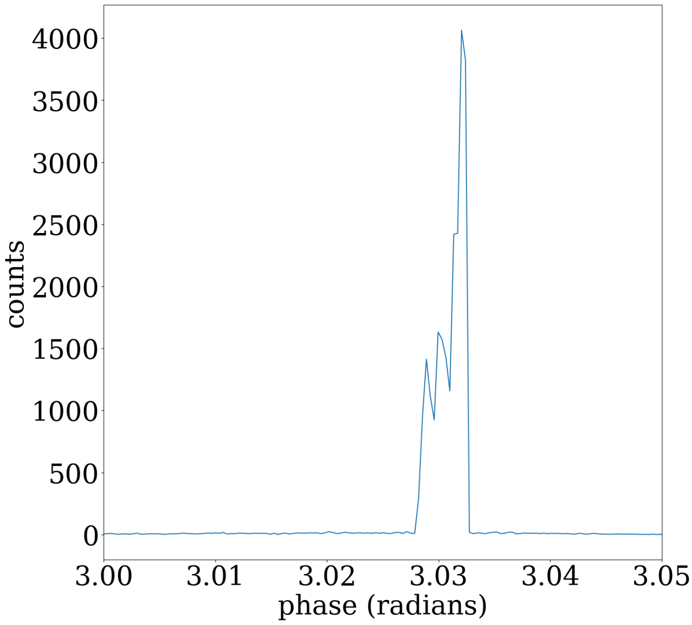

Figure 7.8: Histogram of Figure 7.7. Where α is $\approx 0.965\,\pi$ radians. The designed resonant frequency, in dark, is 6 GHz and the total quality factor is $Q_{tot} = 30000$.

As discussed previously in Section 7.2.2, the Energy Resolution $R = \frac{\Delta E}{E}$, can be described in terms of $\frac{\Delta\alpha}{\alpha}$. Figure 7.8 represents the frequency histogram of the phase values in Figure 7.7 (Right). The full width of the profile represents $\Delta\alpha$, whereas the peak value is representative of α. Under these circumstances and, based on these assumptions, for $f_0 = 6$ GHz and $Q_{tot} = 30000$, $\frac{\Delta\alpha}{\alpha} = 0.004$.

As a final remark, it is interesting to evaluate if and how $\frac{\Delta\alpha}{\alpha}$ depends on the total quality factor Q_{tot}. A plot of such dependence is shown in Figure 7.9. This model hints that a small improvement can be obtained by increasing the resonator's total quality factor.

In reality, the model does not include the effects of dissipative effects induced by the excited quasi-particles, which behave like normal-state electrons. These losses account for a reduction in the internal quality factor Q_i and have not been included in the discussion.

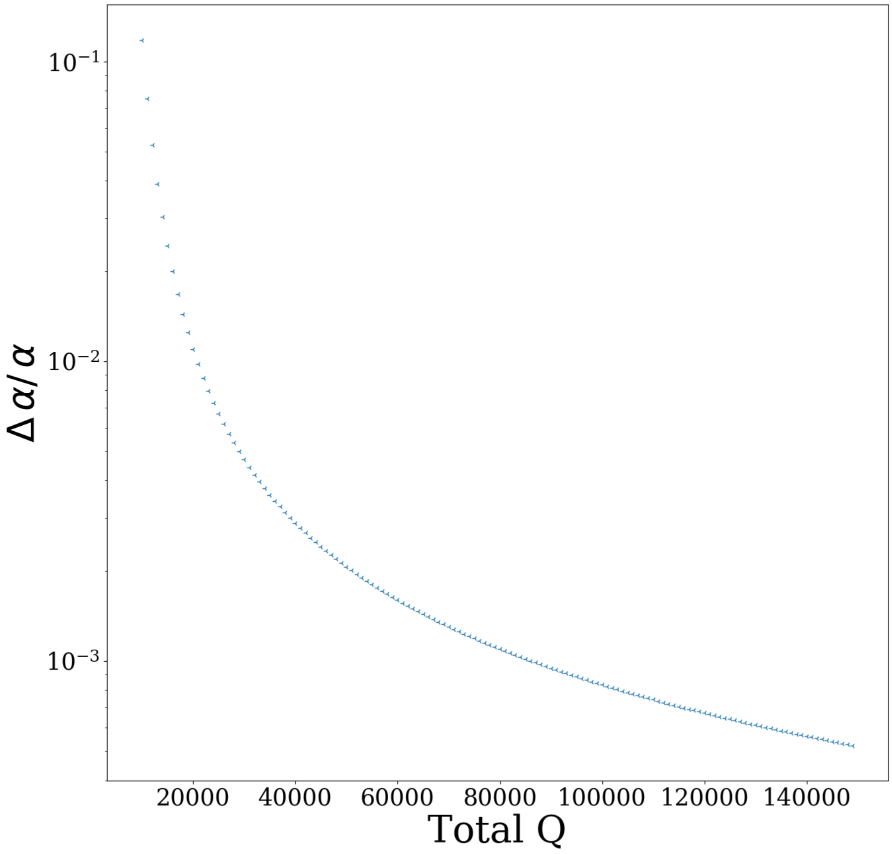

Figure 7.9: Dependence of $\frac{\Delta\alpha}{\alpha}$ as a function of Q

7.2.4 Sampling frequency

The last effect that is taken into consideration is the interplay between the sampling rate of the ADCs, that also affects the amplification noise, see Section 7.2.2 in the readout electronics, and the quasi-particle lifetime. The *cardinal theorem of interpolation*, as formulated by Nyquist (57) and Shannon (56), describes a classical problem in sampling. When the ADC digitises the analogue signal at its input, it creates a form of uncertainty in the maximum of the phase signal. According to the aforementioned theorem, during sampling, the frequencies higher than half of the sampling frequency, cannot be properly sampled and reconstructed, therefore both the rising and the trailing edge of the phase signal are subject to uncertainties. It is impossible to identify with absolute certainty where the peak lays and what its real value is. The ADC used on ROACH boards is commonly operated with a 1 MHz sampling rate, therefore, it is possible to constrain the location of the maximum within a $1\,\mu$s time frame. In particular, $1\,\mu$s is enough time to take account of the ring-down time of the resonator. Given this uncertainty, and knowing the quasi-particle recombination time, it is easy to evaluate how a $1\,\mu$s interval is reflected into an error on the phase value. A schematic picture is shown in Figure 7.10. The recombination time for this model is $100\,\mu$s; which is a typical value for TiN$_x$ resonators.

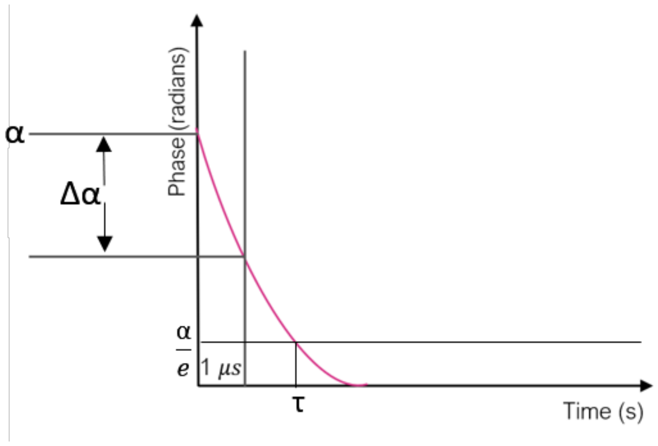

Figure 7.10: The uncertainty on phase angle depends on the sampling rate and the quasi-particle recombination time.

$$\frac{\Delta\alpha}{\alpha} = 1 - e^{-\frac{\Delta t}{\tau_{qp}}} \tag{5}$$

Where Δt is the time interval between two points being sampled and τ_{qp} is the quasi-particle recombination time. For a sampling rate of 1 MHz and a recombination time of $100\,\mu$s,

$$\frac{\Delta\alpha}{\alpha} = 0.00995 \tag{6}$$

Obviously, a faster sampling rate coupled to a faster FFT would help, as one order of magnitude alone would result in an improvement in $\frac{\Delta\alpha}{\alpha}$ from ~ 0.01 to ~ 0.001. The other option, would require the use of a superconducting layer with an intrinsic recombination time that is longer than $100\,\mu$s. Although this is possible in theory, depending on the application, it may not be possible for practical reasons as a longer recombination time would imply a longer *dead time* of the detector.

7.2.5 Other noise sources

MKIDs exhibit an "excess" phase noise that is not fully described by the components previously discussed which is commonly referred as two-level systems (TLS) noise. The internal quality factor Q_i of a resonator is often limited not by the losses internal to the superconductor, rather by dissipation through TLS. TLS noise is primarily due to the coupling of the electric dipole moment of two-level systems with the electric field of the resonator. In particular, since the interdigitated capacitors tend, by their own nature, to sustain high electric fields the capacitors are considered the TLS-noise producing element of an MKID. Even though a semi-empirical model for TLS noise has been developed (90), I will not delve into it. Furthermore,

Generation-Recombination (GR) noise should be discussed. GR noise is produced by the dynamic nature of cooper pairs. As the name suggests, their number in a superconductor is a time-average, therefore extra coooper pairs can form and break down spontaneously. GR noise is material dependent. In order to keep this model as simple as possible I'm only discussing the critical temperature of the film. I decided to include TLS and GR noise in one term. The baseline fluctuations due to TLS and GR noise is responsible for reducing further the resolution of the detector.
When probing MKIDs arrays with tones at -90 dBm, a typical phase noise of $\pm 5°$ has been observed. According to the calculations carried out in the previous section, one might assume the HEMT phase noise of $\pm 3.3°$; with the remainder, $\pm 1.7°$ can be addressed as TLS+GR noise. Table 7.2, shows the value of $\frac{\Delta\alpha}{\alpha}$ for different values of the noise component due to TLS and GR.

Extra noise	$\pm 0.5°$	$\pm 0.7°$	$\pm 2.5°$	$\pm 10°$
$\frac{\Delta\alpha}{\alpha}$	0.0056	0.0189	0.0278	0.111

Table 7.2: Contributions to $\frac{\Delta\alpha}{\alpha}$ for different values of TLS+GR phase noise, in degrees.

7.2.6 Energy resolution

The connection between the energy resolution $R = \frac{\Delta E}{E}$ and the parameter here discussed $\frac{\Delta\alpha}{\alpha}$ still has to be established. First of all, a cumulative value for $\frac{\Delta\alpha}{\alpha}$ can be obtained on the hypothesis that the four contributions are independent and their quadratures can be added up to an overall distribution width.

$$\frac{\Delta\alpha}{\alpha} = \sqrt{\left(\frac{\Delta\alpha}{\alpha}\right)^2_{HEMT} + \left(\frac{\Delta\alpha}{\alpha}\right)^2_{Currents} + \left(\frac{\Delta\alpha}{\alpha}\right)^2_{Readout} + \left(\frac{\Delta\alpha}{\alpha}\right)^2_{extra}} = 0.0429 \quad (7)$$

Where the HEMT noise accounts for the most part, and the contribution due to the current inhomogeneity is about an order of magnitude smaller than that of the HEMT. The three quantities are represented in Table 7.3.

$\left(\frac{\Delta\alpha}{\alpha}\right)_{HEMT}$	$\left(\frac{\Delta\alpha}{\alpha}\right)_{Currents}$	$\left(\frac{\Delta\alpha}{\alpha}\right)_{Readout}$	$\left(\frac{\Delta\alpha}{\alpha}\right)_{extra}$
0.037	0.004	0.0095	0.0189

Table 7.3: Typical contributions to $\frac{\Delta\alpha}{\alpha}$ from the main sources of noise: HEMT, Current inhomogeneity, Readout frequency and TLS.

Even though it is intuitive that $\frac{\Delta\alpha}{\alpha}$ and $R = \frac{\Delta E}{E}$ are related, it is not straightforward to compare $R_{Fano} = 0.01116$ and $\frac{\Delta\alpha}{\alpha} = 0.0385$. While deriving an analytic function that describes the angular displacement in the IQ plane as a function of the photon energy is possible, and an attempt is described in Appendix A2, it is perhaps not the optimal choice for the sake of this work. A more practical approach when working with detectors is to use a number of calibration wavelengths. By illuminating the detector with monochromatic light of selected wavelengths ($\lambda_i ... \lambda_n$) and based on the response of the detector at each wavelength, it is possible to trace a calibration curve. Often times, this curve is simply given by a linear interpolation between every two adjacent calibration points. In each segment of the calibration curve the identification described by Equation 8 is correct:

$$\frac{\Delta E}{E} = \frac{\Delta\alpha}{\alpha} \tag{8}$$

The only assumption that is necessary to explicit is that at every wavelength the width of the angular distribution $\Delta\alpha$ caused by a a photon of wavelength λ is either confined within the individual $<$ segment defined by $\lambda_j < \lambda\lambda_{j+1}$ or on its extrapolation. Based on these assumptions, the energy resolution is $\frac{\Delta\alpha}{\alpha} = 0.0429$. The two contributions to the energy resolution can now be added in quadrature:

$$R = \sqrt{R_{Fano}^2 + R_{\alpha}^2} = 0.0612 \tag{9}$$

This means that when illuminated by a red photon, $\lambda = 650$ nm, the wavelength used as an example for the entire length of this chapter, the MKID taken into consideration will detect its energy to be 1.91 ± 0.06 eV corresponding to a resolving power, $P = \frac{E}{\Delta E} = 16.31$.

It is worth taking a moment to break down the different contributions that limit the detector's performance. In order to do so, it is possible to individually neglect the elements in Equations 7 and 9 and then list them from the most to the least detrimental: The noise component that limits the performance of the detector the most is that induced by the HEMT. If one could, ideally, reduce it to zero, the resolving power would increase to $P = 20.47$. The second element that contributes is given by hot-phonon losses. If one could reduce phonon losses to a negligible amount, the resolving power would increase to 41.83. Then comes two level systems and generation recombination (TLS+GR) noise, neglecting which, would bring the resolving power up to $P = 85.45$. The readout electronics reduces the resolving power from $P = 90.92$ and finally the contributions given by the Fano noise and current inhomogeneities, which, when the contribution due to all the other noise sources have been neglected, alone limit the resolving power to $P = 142.50$. One final comment is on the wavelength dependencies of some the main contributors that limit the energy resolution. In particular, it is clear that the readout sampling frequency has no dependence on the wavelength at which the resonator is being illuminated. It is intuitive that the current inhomogeneity is independent of the impinging photon wavelength. Obviously, a resonator optimised to produce a $180°$ phase shift for 650 nm will produce a smaller signal when detecting less energetic photons, and the ratio $\frac{\Delta\alpha}{\alpha}$ due to it is dependent on the wavelength.

The situation get more complicated when considering the effects of the HEMT, and

its noise temperature, on the signal. In this case, $\Delta\alpha$ can be assumed to remain constant independently on the wavelength on the impinging photon, whereas the absolute value of α changes with wavelength, effectively decreasing the signal to noise ratio, hence reducing the energy resolution of the detector.
Finally, the Fano contribution R_{Fano} of course is wavelength dependent, and ranges from ≈ 0.075 for highly energetic blue photons (300 nm) to ≈ 0.017 for infrared photons (1500 nm).

7.2.7 Energy dependence

Following the previous section, it is interesting to evaluate the Energy Resolution as a function of λ. Investigating in detail the effect requires great effort, moreover, interlinking the different processes that contribute is not easy. An easier approach is to imagine a resonator of which the response is above the noise level over the whole range of wavelengths of interest: from 650 to 1650 nm. Ideally, the resonator would be optimised to produce a 180° phase signal when struck by a 650 nm photon and would produce a signal which is still discernible from the noise at 1650 nm, let us assume one order of magnitude above the noise threshold, e.g. a 50° phase shift. Ideally, one could imagine the phase shift produced by the resonator to be directly dependent on the wavelength of the impinging photon. Under these assumptions, the height of the phase pulse would be described by Equation 10

$$\alpha = 180 - 0.13(\lambda - 650) \tag{10}$$

The different components that make up $\frac{\Delta\alpha}{\alpha}$ might or might not be dependent on α: the contributions due to current crowding and inhomogeneity, TLS+GR noise, and the HEMT noise depend on the pulse height. The same amount of noise produced by the resonator or the HEMT will have a different impact on the detector's performance depending on the height of the phase pulse. On the contrary, given the self-similarity of the exponential decay, the contribution due to the readout electronics and its sampling frequency does not depend on the height of the signal. Under these assumptions, Equation 7 becomes:

$$\frac{\Delta\alpha}{\alpha}(\lambda) = \sqrt{\left(\frac{\Delta\alpha}{\alpha}(\lambda)\right)^2_{HEMT} + \left(\frac{\Delta\alpha}{\alpha}(\lambda)\right)^2_{Currents} + \left(\frac{\Delta\alpha}{\alpha}(\lambda)\right)^2_{extra} + \left(\frac{\Delta\alpha}{\alpha}\right)^2_{Readout}} \tag{11}$$

where the λ dependency of the parameter α is described by Equation 10. The curve described by Equation 11 is shown in Figure 7.11. The equation that links $\frac{\Delta\alpha}{\alpha}$ to the energy resolution $\frac{\Delta E}{E}$ is only accurate when the resonators are optimised for the specific wavelength, which means, when the phase pulse it produces is $\approx 180°$. Keeping in mind that this identification is only exact for wavelengths close to 650 nm, it is possible to extend it over the whole wavelength range of interest in order to gather qualitative information about the trending of the curve, which is shown in Figure 7.11. The scatter plot shows resolving power values measured by different groups for MKIDs made of different materials: Guo et al., (16), (Green) for their TiN/Ti/TiN MKIDs measured a value of $P = 3.7$ at 1550 nm, in agreement with what predicted by the model $P = 3.77$, Szypryt et al., (11), (Red) obtained a resolving power in the wavelength range $808 - 1310$ nm between $8.1 - 5.8$; and Mazin, (17), (Cyan) reports a resolving power of 10 at 808 nm for hafnium (Hf) MKIDs. The experiments seem to be in good agreement with the trending of the modelled curve.

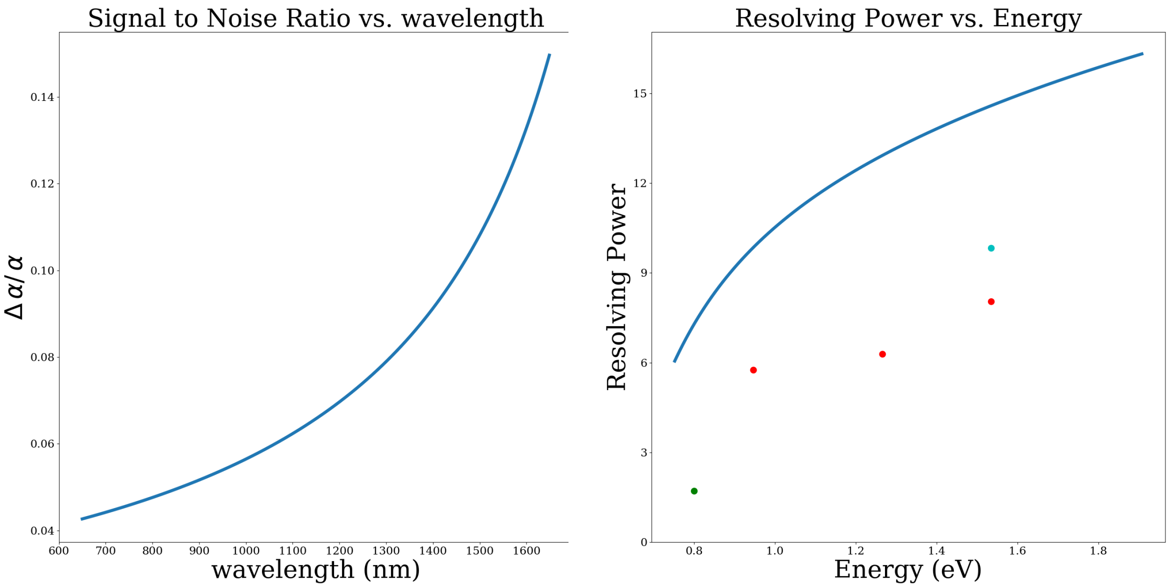

Figure 7.11: Left: Signal to noise ratio $\frac{\Delta\alpha}{\alpha}$ as a function of the wavelength of the impinging photon. Right: Resolving power $\frac{E}{\Delta E}$ as a function of the energy of the photons that illuminate the resonator. The scatter plot represents experimentally measured points as collected from: Green - (16), Cyan - (17), Red - (11). The same plot with the addition of data from prototype DIAS MKIDs is shown in Fig 9.15.

7.3 Possible improvements

A final section is necessary to point out the results described in the previous pages and what technological improvements might be relevant to future work. When it comes to the yield of an array, there is very little improvement that can be foreseen for superconductors such as TiN_x for which it is known that T_c homogeneity is very difficult. Other superconductors can exhibit a better uniformity, $TiN - Ti - TiN$ multilayers have not been tested thoroughly yet. The deposition of uniform and high quality thin films is well optimised for both Ti and TiN. From a more technological standpoint, an enhancement in the maximum frequency at which a low noise-temperature HEMT can operate, might allow the choice of not increasing the

number of resonators per feed-line in order to increase their frequency spacing which, in turn, provides an improved the pixel yield. A further approach to maximise the yield would be the retuning of the colliding resonators through post-production processes such as trimming and DC-bias retuning (91) (See chapter 8).
As previously discussed, the importance of the energy resolution of the detector is central and it is crucial for most application that it is as optimised as possible. The last few pages describe a model created *ad hoc* to investigate the effects of several parameters on the energy resolution of an MKID: the noise temperature of the HEMT, which appeared to be the most significant contribution, the inhomogeneity in current density in the inductor of the resonator, the sampling frequency of the readout electronics and the Fano noise that dominates the pair breaking process. The dominant contribution is provided by the HEMT, and very little can be done to minimise it. Of course a better HEMT has been in the community's wish list for several years now, and hopefully the parametric amplifiers currently under development (70) might play a significant role. That said, Figure 7.6 shows that a higher internal quality factor Q_i can help improve the signal to noise ratio. Further improvement, of non dominant factors, is possible. New geometries can be investigated in order to maximise the current homogeneity, among these, a design with a large inductor could be interesting in order to minimise the effects of the current crowding at the right turns, whereas a tapered inductor could reduce the current density gradient. An in-depth study of the physical properties of new materials, such as the multilayers and Granular Aluminium, might produce interesting results in terms of quasi-particle life time, which would impact the contribution to the energy resolution given by the readout electronics. The Fano component issue is currently being addressed by the SRON group in the Netherlands, by maximising the pair breaking efficiency η. In the case of semiconductors (86) and gases (87), the Fano factor has been observed to be material dependent. It might be worth investigating if there is a significant change in Fano noise across a broad variety of superconductors.

8 Retuning an array exploiting the non-linearity in kinetic inductance

The collective behaviour of an array of Microwave Kinetic Inductance Detectors is understood and has been modelled with sufficient accuracy. Standard TiN_x is known to be quite non-uniform when it comes to its T_c. As previously discussed, in Chapter 7, even the smallest variations in T_c can lead to a drastic decrease in the total number of resonators with a unique resonant frequency. The ratio between this number and the total number of resonators is commonly defined as fabrication yield.

Fabrication yield highly depends on the design parameters, as it is known that MKIDs optimised for sub-millimetre applications have higher yield than those optimised for visible and near infra-red purposes; for the latter case, most arrays exhibit a yield of $\approx 75\%$ and only the best ones go as high as 80%.

Over the last decade, multiple approaches have been attempted in order to increase the yield. Among these, the *a posteriori* trimming of the interdigitated fingers of the inductors so that the frequencies can be re distributed uniformly over the whole bandwidth showed great results (92). Another very interesting approach, pioneered in 2015 by M.R. Vissers et al., exploits the non linear dependence of kinetic inductance to induce a controlled shift in resonant frequency, and therefore increasing the number of distinguishable resonators on the feed-line. The first approach, can, in principle, decouple all the resonators, providing a 100% yield, but requires a very difficult post-production process involving a secondary lithographic process or a Focused Ion Beam milling of the excess metal. The second approach, instead, can only produce a limited increment in yield, and makes the multiplexing of several pixels quite complex.

Over the next pages, I will discuss a possible way to implement and improve the latter approach.

8.1 Kinetic Inductance non-linearity

The electrodynamics of superconductors has been studied intensively and it has long been known that the kinetic inductance of a superconductor, when a current is flowed through it, has a non-linear dependence on the amplitude of such current (45), (46). In the limit $T \ll T_c$, the kinetic inductance of a superconducting strip can be expanded as:

$$L_k = L_0 \left(1 + \frac{I^2}{I_0^2} + ...\right) \tag{1}$$

It is clear that any odd term in the expansion has to be zero, due to symmetry reasons, and an expansion to its second, non zero term, is accurate enough to model the phenomenon. Here I_0 is a scaling factor and, according to the literature, it is known to be of the same order of the critical current, (39),(47)

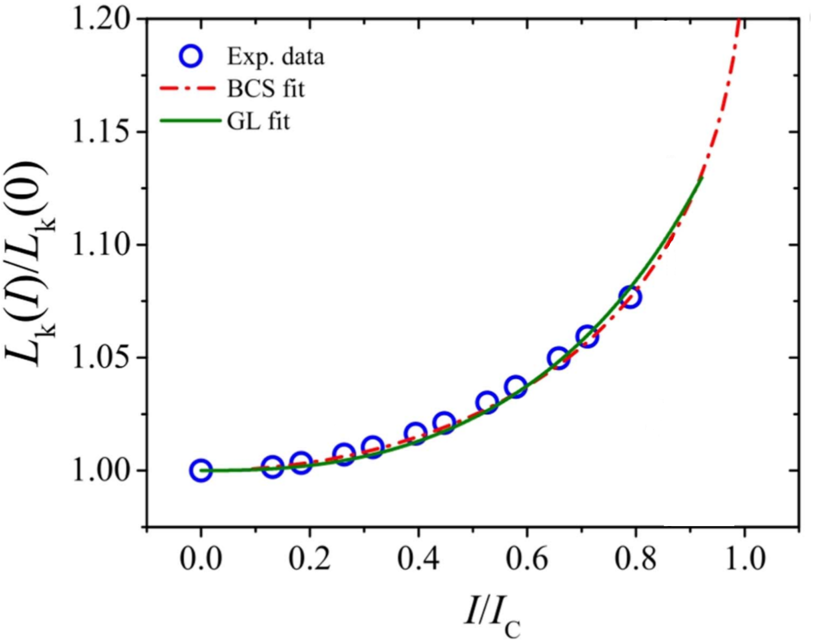

Figure 8.1: Measured current dependence of the relative kinetic inductance fitted with BCS and Ginzburg-Landau theory. Adapted from Doerner S. et al., (6)

In the limit that the film thickness is small compared to the London penetration depth of the superconductor, the surface inductance L_s is given by:

$$L_s = \frac{\hbar R_s}{\pi \Delta_0} = \frac{\hbar \rho_n}{\pi \Delta_0 t} \tag{2}$$

Where R_s is the sheet resistance of the film, ρ_n is the normal state resistivity of the metal and t is its thickness. A strip of length l and width w has a kinetic inductance of $L_k = L_s(l/w)$. The expected fractional change in kinetic inductance, according to Kher (18), is given by

$$\frac{\delta L_k}{L_k} = \frac{I^2}{I_0^2} = \kappa_* \frac{J^2}{J_0^2} \tag{3}$$

where κ_* is a parameter of the order of unity, J is the current density and J_0

$$J_0 = \sqrt{\frac{\pi N_0 \Delta_0^3}{\hbar \rho_n}} \tag{4}$$

Here N_0 is the single-spin density of states per unit energy and unit volume (18). ρ_n is the normal state resistivity and Δ_0 is the superconducting bandgap at 0K. The resonance frequency ω_r of an LC resonator is $1/\sqrt{LC}$, therefore a change in its nominal inductance due to a current bias, leads to a change in its resonance frequency $\delta\omega$. Its fractional shift, due to this current bias is (47).

$$\frac{\delta\omega_r}{\omega_r} = -\frac{\delta L}{2L} = -\frac{I^2}{2I_0} \tag{5}$$

Previous papers, (47) and (18) showed interesting results in this direction. In both cases, a frequency shift up to 4% of the designed resonance frequency was achieved, with little (47) to no (18) degradation in quality factor and some of these results are shown in Figure 8.2

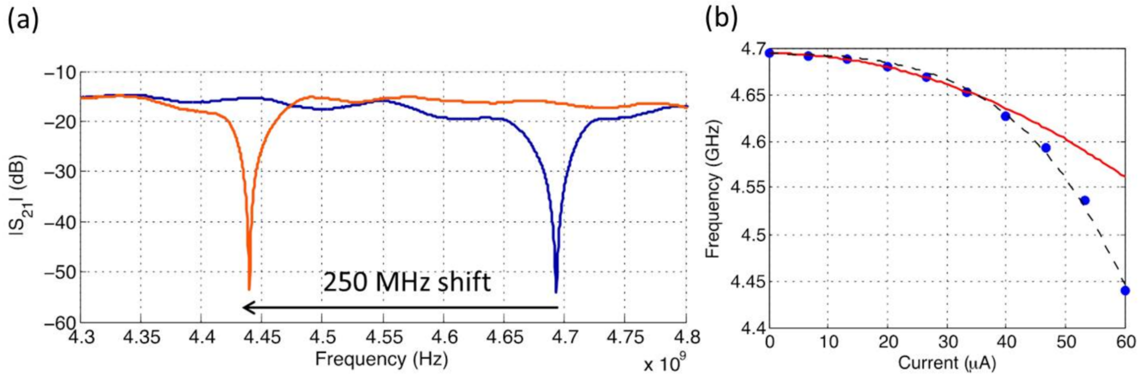

Figure 8.2: (a): Amplitude of transmission through the chip. The blue curve shows the transmission without any current bias, the red curve shows the transmission with current bias of $60\,\mu A$. The total frequency shift is about $250\,MHz$, about 5% of the resonance frequency. (b) Full current response data for the resonator. Above $60\,\mu A$, critical current of the superconductor, the resonance disappears. The red curve is a quadratic fit to the data, whereas the dashed curve is a quartic fit to them. Reprinted from (18)

8.2 Retuning multiple pixels

The two approaches described in the previous section only focus on the retuning of a single resonator, but it is interesting to evaluate what improvement can be obtained when selectively biasing some of the resonators of the array. It is unimaginable that each pixel of the array, several thousand resonators per chip, is individually contacted and biased. There are two main reasons for this: The amount of cables required at the milli-kelvin stage of the cryostat would be comparable to the amount of cables needed to read out an array of Transition-Edge Sensors, therefore losing one of the main strengths of MKIDs. The second reason is that, in order to do so, the fabrication of an MKIDs array with that many biasing lines would become more and more complicated, and another strength of MKIDs would be lost. One acceptable compromise is to use one biasing current that is then equally redistributed between all the biased resonators. This section inquires how big an improvement this would be and the feasibility of this approach when moving from a single pixel approach to a whole array.

8.2.1 Numerical model

The first evaluation of the benefits of the selective retuning of individual resonators was done through a Python code. The code is divided in two main parts: the first one is mainly meant to verify the feasibility of the retuning by blindly biasing one of two clashing resonators, for every clash that occurs on the feed-line. The second part deals with the possible benefits of a smart choice of the pixels to bias. The first part is intended to be a simple toy model in order to compare it with the second part, therefore, it only takes into account an array with 1000 pixels per feed-line where the resonance frequencies are evenly distributed across a 4 GHz bandwidth and 125 randomly-chosen resonators with the same exact resonance frequency as 125 other pixels. The programme scans through one thousand evenly spaced values of current from 10 μA to 10 mA and keeps track of the best case scenario, i.e. the current value by which there are the least amount of pairs of resonators within 0.5 MHz of each other. This scan was run one thousand times with a randomised set of colliding resonators times to gather data with statistical significance and then a histogram was produced as shown in Figure 8.3 The second stage of the process goes further to simulate a realistic MKIDs array. The number of resonators laid on each single feed-line is now increased to current standards, 2000, therefore reducing by a factor 2 the average spacing between two adjacent resonators. Furthermore, a random shift around the designed resonant frequency in the range of ±5 MHz is taken into account. Only after this randomisation, any 250 resonators are indiscriminately chosen and assigned to have the same resonant frequency of 250 other ones, only then the frequencies are rearranged in increasing order. This way a 75 % yield is induced in the array. The optimisation of the retuning process is described in the block diagram in Figure 8.4 and goes as follows:
Starting from the colliding MKID with the highest resonant frequency, and given a value for the current bias in the range (10 nA to 10 μA) five checks are performed:

1. is it closer than 0.5 MHz away from another resonator?
2. given the bias current, what would its new target frequency be?

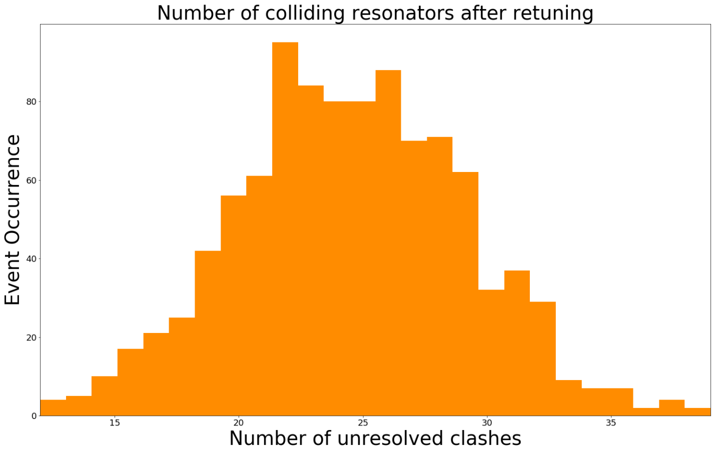

Figure 8.3: Number of paired resonators after having blindly biased one of the resonators of each pair. Starting parameters are 1000 resonators evenly distributed over 4 GHz of bandwidth. Of the 1000 resonators, 125 have the same resonance frequency as 125 others. A gaussian fit of the peak points towards a mean value of 30 couples left to decouple and a S.D. $\sigma = 5$

3. is the collision removed?

4. does the newly biased resonator collide with another one?

5. is the target frequency in the bandwidth of our interest (4-8 GHz)?

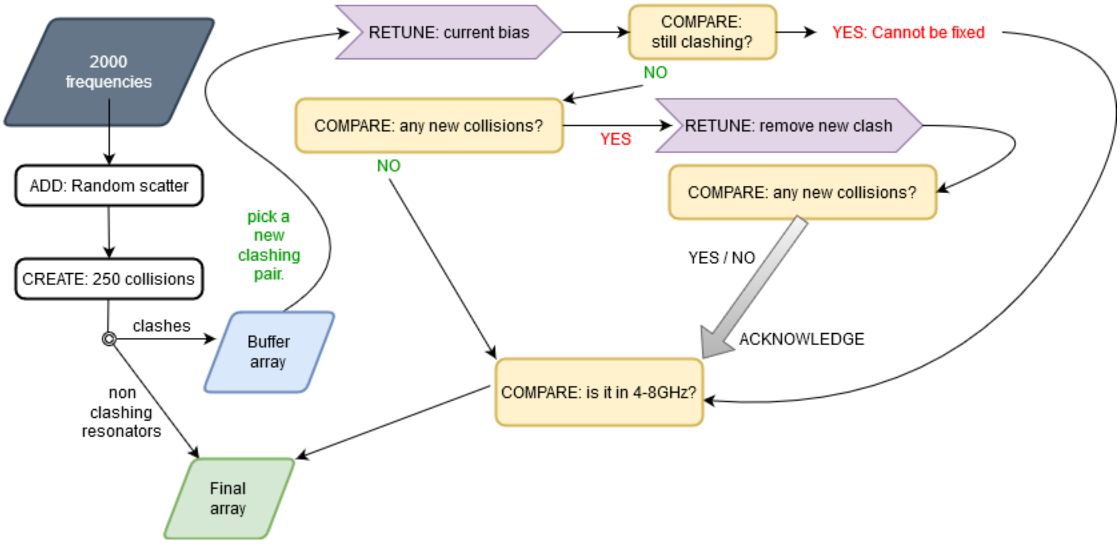

Figure 8.4: Flowchart of the algorithm for the identification of the resonators that need to be re-tuned.

The programme is meant to check the resonators in descending order, and as soon as it detects two clashing resonators, it tries to remove the degeneracy by applying a current bias. Two further checks are necessary at this stage: are the two MKIDs still colliding? i.e. are the two resonators of the pair further than 0.5 MHz away? and, *in secundis*, is a new collision created with this shift? If so, the clashing resonator also has to be immediately re-tuned. Unfortunately, at this stage, independently whether a new collision is created, the programme will not try to remove it. Now, the final check that has to be performed is making sure that all the pixels resonate within our bandwidth of interest. The upper end is of little to no interest as the process of retuning a resonator can only decrease its resonant frequency. The resonators with the lower characteristic frequencies, on the other hand, could be shifted to a different octave, which could lead to a clash between pixels when considering that resonators can be driven with their second harmonic frequency.

These steps are re-iterated over different values of bias current, in order to find the current value that yields the best array possible. The whole process is re-iterated eight-hundred times with randomised starting conditions in order to gather data with statistical significance. The results of this process are shown in Figure 8.5. The left plot shows the full data set. Two peaks are clearly visible; the small peak on the left represents the events of multiple non-resolvable collisions. What is interesting to us, though, is the main peak on the right which as expected contains more events than the other. The plot on the right, shows a close up of said peak along with a gaussian fit of the data. Neglecting the smaller peak on the right, a gaussian fit of the data, yields a mean value of 125 ± 7 pairs of resonators with degeneracies that could not be removed. This values, corresponds to a total yield of $85.3 \pm 0.7\,\%$ which results in a $10\,\%$ overall improvement in fabrication yield. A better algorithm to determine which resonators to bias and which ones to keep unbiased might further improve the overall yield by a few percent as well as a higher number of data points, possibly obtained with a current scan that is finer than $10\,n$A. Unfortunately, asking for a finer scan and more data points means cluttering a machine for longer time. Only an optimisation of the algorithm might allow for that, as its scaling order is O^3.

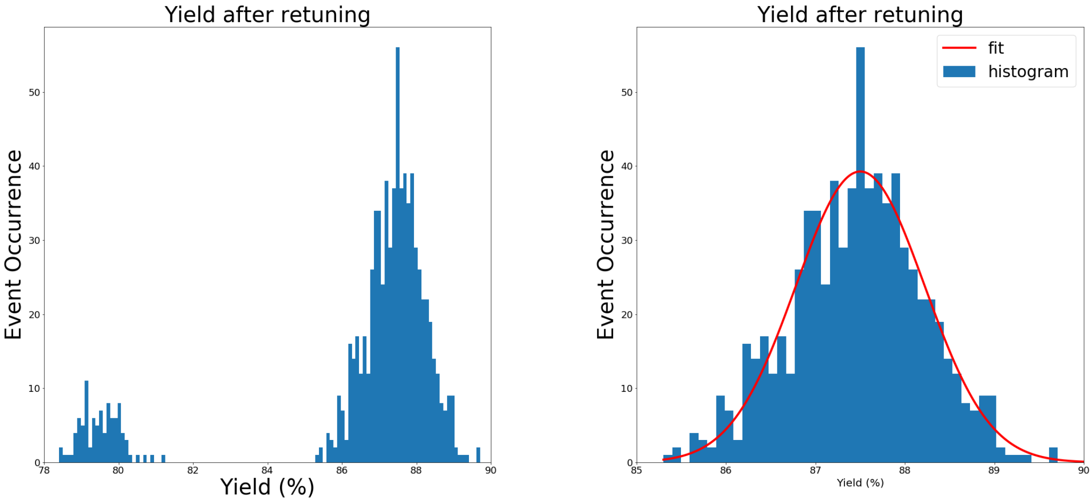

Figure 8.5: Left: Yield after the retuning process. A total of 800 events have been taken into account for this plot. Right: close up of the main peak from the left plot and the gaussian fit of the data.

8.3 Mask design and electromagnetic simulations

This section covers the electromagnetic simulations of a novel MKIDs design that should allow for DC biasing of multiple pixels without giving up on the multiplexibility of a array on a single feed-line. Just before diving into the description and analysis of our newly designed resonators and their DC-biasing line, it is important to note that a thorough description of SONNET, the electromagnetic simulations software used for the design of all the circuital elements can be found in Chapter 8.3.1.

8.3.1 Resonator design

Although different MKID designs can be adapted to accept a DC current bias, our main interest is not to give up on the *Lumped Element* geometry, therefore keeping the structure of an interdigitated capacitor and a meandered inductor. In order to bias the resonator, one can no longer rely on a floating ground at the middle point of the inductor, but a physical ground is now necessary. Furthermore, a superconducting supply line is required to connect, at will, the resonator with the line distributing the current in parallel to as many resonators as it is required. A diagram of this geometry, drawn and analysed with the EM simulation programme SONNET(76) is shown in Figure 8.6. The elements previously discussed are still featured in this design, and in addition it is easy to identify the hard-wiring to the ground plane and the supply line that connects to the current distribution line. The details of this connection are intentionally not shown in this graph as further discussion is necessary.
Figure 8.6 shows the two usual elements of the resonator: an interdigitated capacitor and a meandered inductor as well as the feed-line to which the MKID is coupled. In particular, it is interesting to notice that the feed-line, and the rest of the geometry, are not made of the same materials. The feed-line (in blue) is made of a material with a sheet inductance value of $\approx 20\,pH/sq$ while the ground plane, the current distribution line and the resonator (in red), are designed to be made of a high kinetic inductance material, such as granular aluminium (grAl) which can have sheet inductance values as high as $500\,pH/sq$ (50).

8.3.2 Material Choice

Of fundamental importance is the choice of superconducting materials chosen for different elements of this project. The most important parameter is the critical temperature of the film. Materials such as Hf, PtSi, TiN_x have been proven to be suitable for MKIDs. Moreover, since a significant current might have to flow through the superconductor, it could be beneficial to use a material with a T_C higher than $1\,K$ in order to allow a higher critical current. Besides the critical temperature, a high

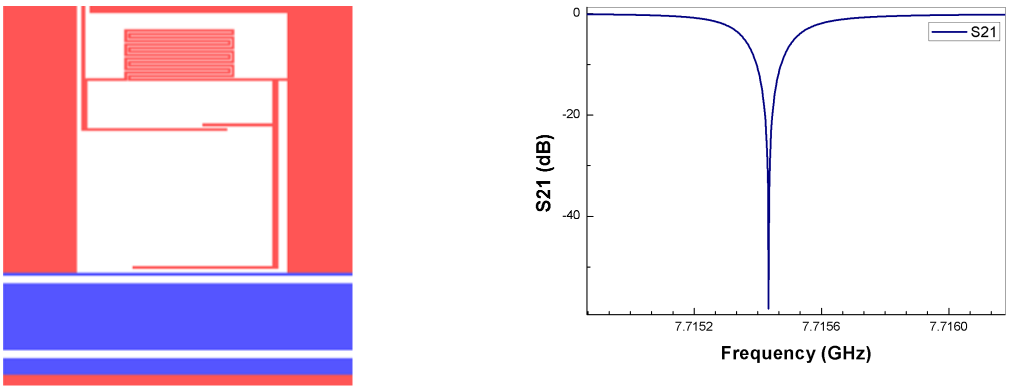

Figure 8.6: Left: Design of an MKID capable of current-biasing. The standard geometry remains unchanged, a meandered inductor and an interdigitated capacitor coupled to a co-planar wave guide transmission line. In addition, one of the nodes of the circuit is grounded and the other is connected to the current distribution line through a supply line. Right: Transmission dip of the resonator ($f_0 = 7715.4$ MHz and $Q_C = 33200$)

kinetic inductance material could be of great benefit to keep the size of the current distribution line, and the pixel size, as small as possible in order thereby increasing their packing capacity.
Granular Aluminium (grAl) could be ideal for this purpose as its critical temperature ranges between 1.2 K and 2.3 K, and kinetic inductance values as high as $1\, nH/sq$ are easily obtained.

8.3.3 Current distribution line

The main function of this current distribution line is, to provide the biasing current to all the resonators in the array that need to be re-tuned. A few problems arise when implementing a current distribution line in the previously discussed geometry. *In primis*, it is crucial to ensure that the high frequency energy loss is as small as possible in order to maximise the resonator's quality factor. The second, and more crucial, concern is that there is no RF signal cross-talking between two or more pixels. In which case all the reactive elements would contribute to the creation of one single resonating circuit which would, in turn, make the whole array unusable. In order to solve these two main issues, and following the important advice of A. S. Kher in (18) where the bias is achieved through a stepped-impedance filter, a multistage low-pass hairpin LC (93) filter is to be considered as a viable option. Figure 8.7 shows the implementation of such a Low-pass filter.

Given such structure, it is of great importance to know its trans-characteristics defined by its S-parameters. The main focus is to provide a filter with the lowest attenuation possible at very low frequencies, and which has at least -40 dB attenuation in the 4-8 GHz range that is our bandwidth of operation. The S_{21} curve, represented as a function of frequency, is shown in Figure 8.8 (Top). The attenuation

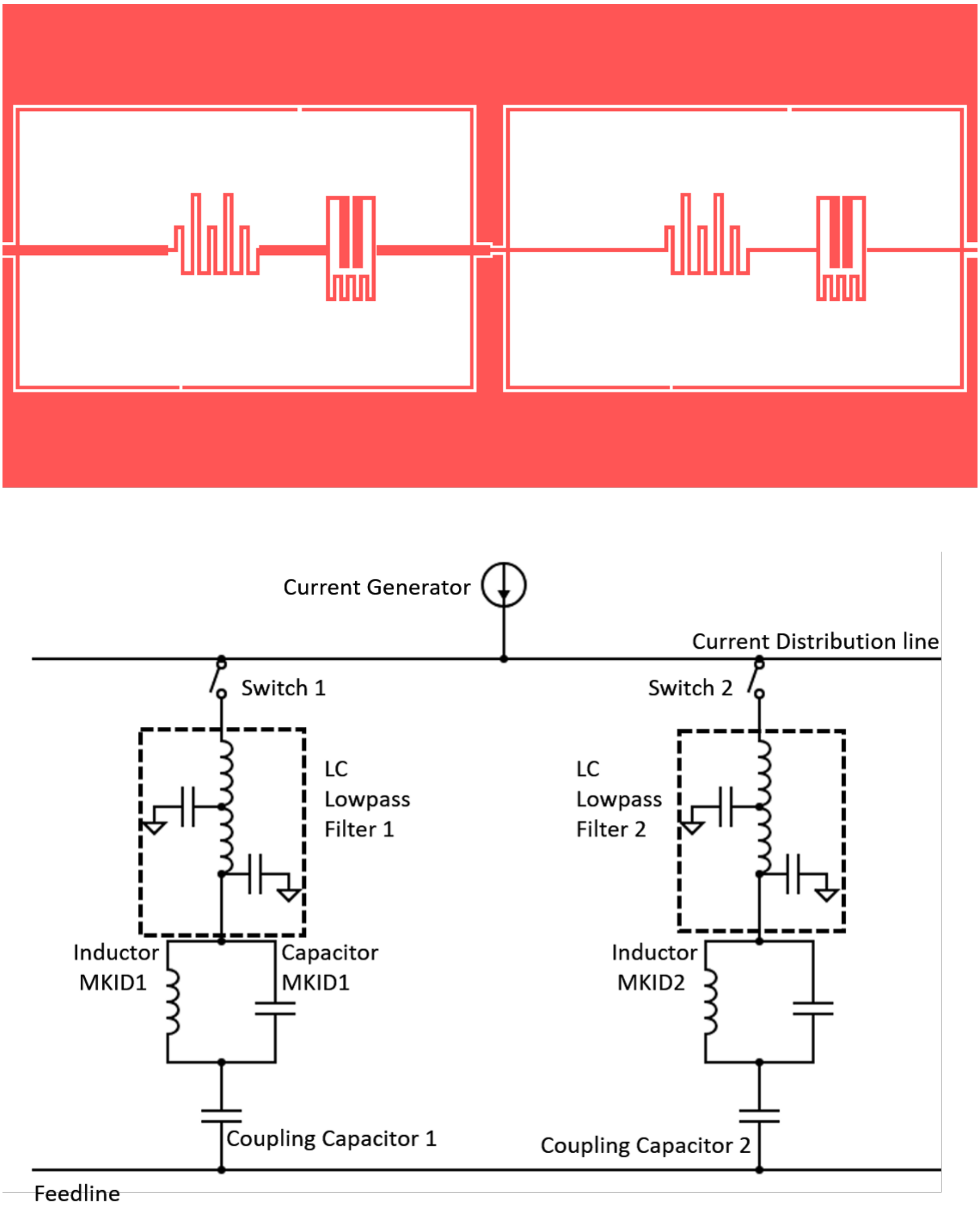

Figure 8.7: Top: Two stage Low pass hairpin LC filter, the cell is $300\,\mu m \times 250\,\mu m$. Bottom: Electrical scheme of two resonators with their current distribution line.

is negligible at very low frequencies, the transmission rolls off and is non significant across the $4-8$ GHz octave. For frequencies between 2.12 GHz and 2.6 GHz, the transmission is higher than -20 dB, but the presence of this peak is not relevant for the purpose of the filter. Such implementation allows to keep two resonators decoupled while they are electrically connected through the current distribution line. As shown in Figure 8.8 (Bottom), it is also possible to ensure a coupling quality factor which is comparable to standard MKIDs

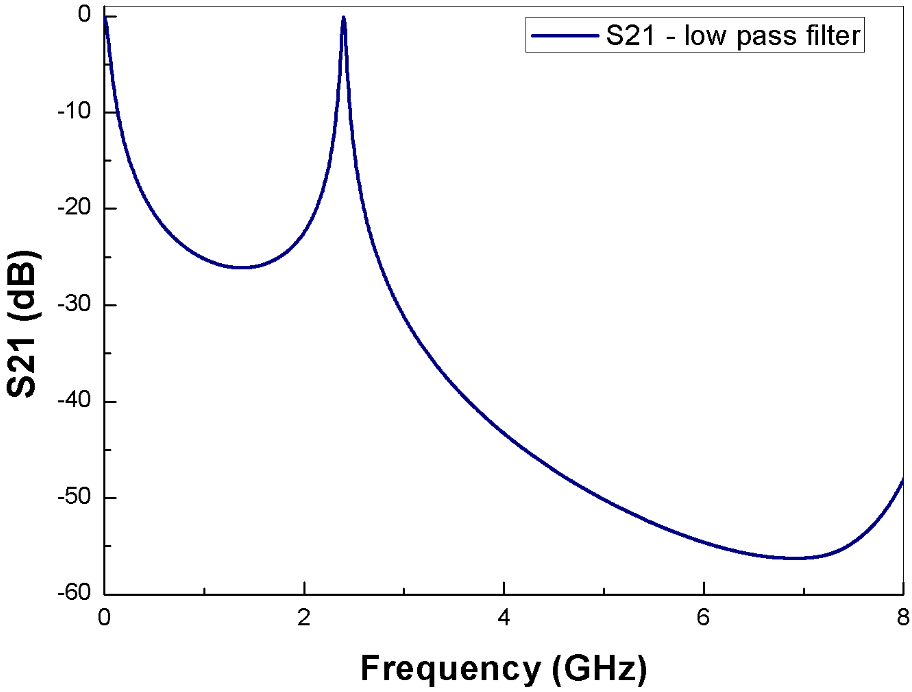

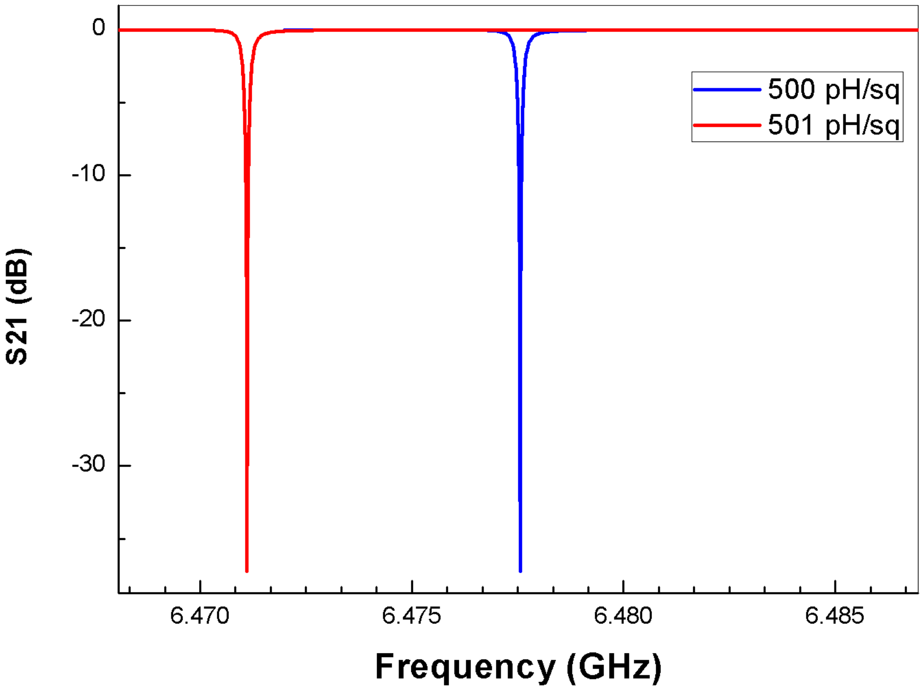

Figure 8.8: Top: Trans-characteristic of the two stage Low pass hairpin LC filter as simulated in SONNET. Bottom: SONNET simulation of a frequency shift due to a change in Kinetic inductance. The blue curve represents the unbiased resonator ($f_0 = 6.4775569$ GHz and $Q_C = 33700$); the red curve represents the same resonator when the sheet inductance of the layer is increased by 0.2% ($f_0 = 6.4711046$ GHz and $Q_C = 33700$).

Instead of showing an image of the designed MKIDs laid out on the lithographic mask as just done, when it comes to the multiplexing of different resonators on the same feedline, it is agreeable that an electrical schematic of the circuit is more efficient and a better explanatory tool. The schematic can be found in Figure 8.7 (Bottom).
A hairpin LC two-stage filter is not the only possible way to achieve a wide-band low pass filter. For applications in which high packing ratios are crucial or, in case a cryostat with high cooling power is available, a R-L low pass filter is also a viable option. The transmission of such filter is shown in Figure 8.9 (Bottom). It is obvious that the presence of a dissipative element, here imagined as 20 gold strips $1\mu m$ wide and $5\mu m$ long, with a sheet resistance of $20\Omega/sq$, induces a loss at low frequencies. The transmission curve shows an attenuation of ≈ 12 dB which corresponds to a four-fold attenuation of the power applied. Biasing a resonator with a current of $1\,\mu$A, which is reasonable for such applications, implies a dissipated power of $100\mu W$. Retuning a whole array of 2000 pixels could be as energetically demanding as $25\,mW$; a cooling power only available in high performing dilution refrigerators (94).

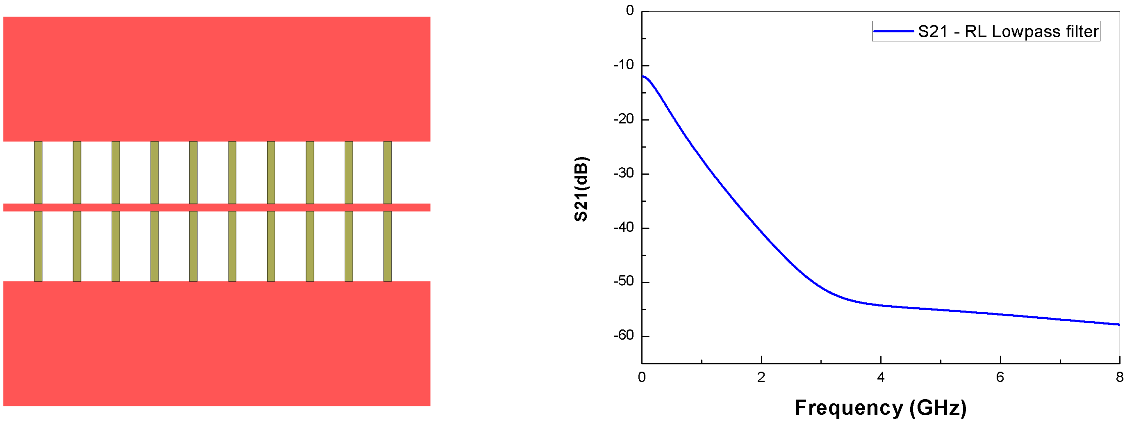

Figure 8.9: Top: R-L low pass filter, the superconductor is depicted in red, while the yellow elements are made of gold. The cell is $50\,\mu m \times 50\,\mu m$. Bottom: S_{21} transmission of the same R-L low pass filter.

8.3.4 DC Bias switch

The selection of which resonators have to be re-tuned is made by electrically connecting the resonators to the Current Distribution Line. Basically, one can physically decide whether each individual resonator has to be connected to the distribution line or not. Two approaches are here possible, one is "additive" and the other "subtractive". In the first case, the photo-lithographic mask would include bond pads to connect the filter to the distribution line. This way, it is possible to electrically connect the resonators to the distribution line through well placed aluminium bond wires. Instead, the "subtractive" approach, has all the resonators already connected to the distribution line when fabricated and one can decide which resonators to disconnect. Each method has its own benefits; only having to bond the resonator one wants to re-tune is very obvious and relies on less connections, which could get damaged during the fabrication. On the contrary, the second scheme, already has all the resonators connected to the distribution line and it is possible to etch away the connections to the distribution line for those resonators that need no connection. The "subtractive" approach could be beneficial in case one wants to probe and test the array when biased with different currents. This way when optimising the yield of the array one does not rely on the expected behaviour of the biased resonators. Each resonator can be characterised first and the selection of the resonators to keep connected and their ideal bias current is made in light of their real behaviour. It is important to state that, due to the inherent characteristics of the filters, when connecting or disconnecting the resonator to the current distribution line, a shift in frequency of ≈ 2 MHz, in either direction, has to be taken into account, breaking the connection between the resonator and the distribution line will increase its resonant frequency without affecting the quality factor and vice-versa. This frequency shift seems to be independent on the resonance frequency of the resonator and, in first approximation, constant across the $4-8$ GHz band. Sonnet simulations proved that the quantity of this shift is independent on the geometry of the MKID. On the other hand, it is not independent on the properties of the superconducting layer. A change in sheet inductance results in a change in the the fixed shift. Increasing the sheet inductance to 550 pH/square in the simulation, the resulting shift in resonance frequency, when connecting/disconnecting the resonator from the current distribution line went down to ≈ 40 kHz. A further increase to 600 ph/square reduces the shift to within 10 kHZ, which two orders of magnitude smaller than the accuracy that is desired.

8.3.5 Routing scheme

Routing two different lines through an array of resonators in a way that the current distribution line doesn't cross the feed-line could sound difficult. Provided that a routing based on trial and error could be attempted, a Python code, based on Kruskal's algorithm (95), was implemented in order to find the minimum spanning tree, the shortest combination of segments that connects to all the points in a graph, that would allow the biasing of all the resonators. Then the feed-line was routed in order to be coupled to the MKIDs. At the cost of almost doubling the length of the feed-line, it is possible to route two non intersecting lines that connect to the pixels. For the sake of clarity, Figure 8.10 shows a 8×8 matrix with the two different routing paths. It is obvious that this wiring pattern can be extended to any rectangular array. In principle, having the current distribution line to cross-over the feedline would not result in a problem, but will make the fabrication process significantly more difficult, therefore the approach here described is based on the desire to have the current distribution line co-planar with the feed-line.

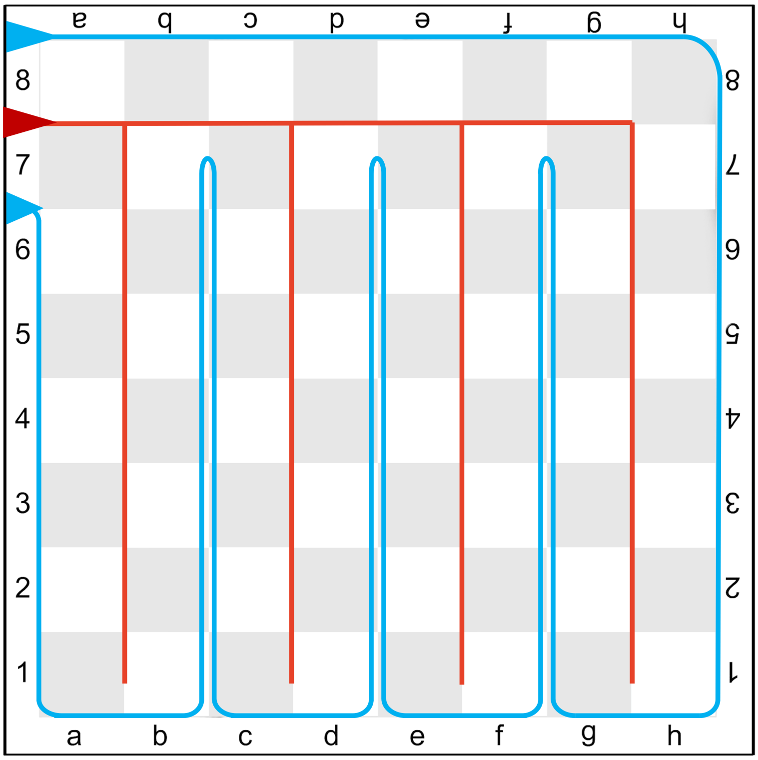

Figure 8.10: Routing scheme of the feed-line, in blue, and the current distribution line, in red, snaking around a generic 8×8 square array. An MKID and a filter is imagined placed at the centre of each square of the chess board.

8.4 Conclusion

Building on the state of the art of Microwave Kinetic Inductance Detectors, we proposed a possible implementation of a geometry that allows the DC bias re-tuning of an MKIDs array. Python simulations show that, with just one current value to bias the resonators with, it is possible to increase the percentage of pixels with individual frequencies from 75% to above 85% with minimal degradation of coupling and quality factors. The material identified as optimal for this application is granular aluminium with sheet inductance as high as $500\,pH/sq$ which is ideal in order to keep the dimensions of the filter as small as possible and, in turn, grAl is expected to withstand a higher current density when compared to superconductors with lower critical temperature. Two possible geometries have been imagined for the current distribution line, one based on a LC multi stage hairpin low pass filter, a medium-performance low dissipation filter, and the other, a single pole R-L low pass filter, which has a much better performance in terms of filtering that comes with a high energetic dissipation. This makes it only suitable for high cooling power dilution refrigerators. A routing scheme, based off Kruskal minimum spanning tree, that allows the wiring of two non intersecting lines around a rectangular array of any size has been identified. Work is ongoing for first experimental tests of the devices here proposed.

9 Kinetic Inductance Detectors

This chapter contains the full characterisation of a number Microwave Kinetic Inductance Detectors. Due to some insurmountable difficulties that arose over 2020 and 2021 in CRANN, the fabrication of these resonators was outsourced and produced in the Tyndall National Laboratories.
The superconductor from which the resonators here described are obtained is a multilayered stacking of Titanium Nitride and Titanium, encapsulating a thicker Ti layer between two thinner TiN layers which act as a capping layer to protect the Ti from oxidising and, most importantly, contribute to the regulation of the critical temperature through proximity effect. The thickness of the middle layer of the stack has been varied empircally in order to obtain the desired critical temperature.

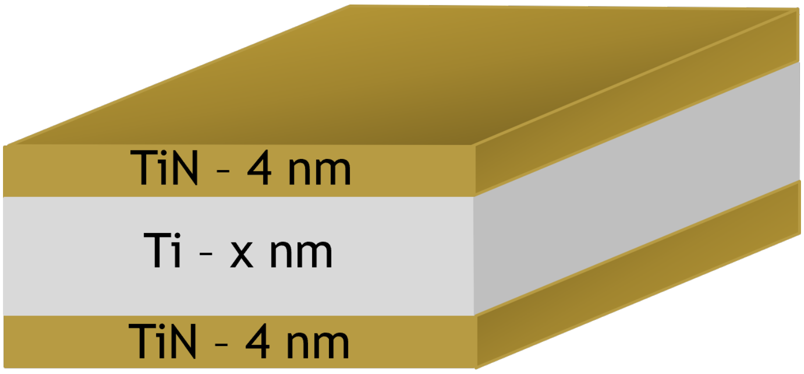

Figure 9.1: Schematic picture of a TiN/Ti/TiN multilayer. The top and bottom layers, of stoichiometric Titanium Nitride sandwich a pure Titanium layer of variable thickness to control the critical temperature of the stack.

While many different depositions runs have been performed to optimise for the desired critical temperature and improve the internal quality factor as desired, this section only reports data gathered on some selected fabrication runs.

9.1 TiN|Ti|TiN – 4|39|4

The first deposition we attempted was so to have designed critical temperature of about 800 mK.This was attempted with a trilayer of respective thicknesses 4 *nm*, 39 *nm* and 4 *nm*. Such a low temperature of Tc would be ideal. Being about one order of magnitude higher than the lowest temperature the cryostat can hold would ensure a full depletion of the superconductor from unpaired electrons. According to the two-fluid model (4, 43) of a superconductor, the fraction of paired electrons is given by:

$$\frac{n_{qp}}{n} = 1 - (\frac{T}{T_c})^4 \tag{1}$$

This results in a fraction of unpaired equations at a temperature of 100 mK that is smaller than 0.1%. A low critical temperature also is reflected in a higher number of quasi particles produced per every impinging photon and also results in a higher energy resolution. This deposition resulted in a superconducting film with a critical temperature of $885\,mK\ \pm 20\,mK$ across the whole wafer. Unfortunately, a frequency sweep of the resonators performed with the VNA showed that the resonator dips (in frequency) were extremely shallow. Only the best resonators were as deep as $2dB$. Although a fitting of the resonators' I-Q loop is not greatly informative when the resonance is so shallow, it returned extremely low values for the internal quality factors of the resonators ($Q_i \leq 25000$). While the reasons for such low values of Q_i could be further investigated, it was decided to proceed to the fabrication of a new wafer with a different elemental composition and different value of critical temperature.

9.2 TiN|Ti|TiN – 4|10|4

For the second successful fabrication run, the target critical temperature was set to be around $1.5\,K$ and, through linear interpolation the ideal thickness of the central layer was determined to be $10\,nm$. A metallic film with such characteristics was seen to exhibit a critical temperature of $1.52\,K$ in good accordance with the desired value. Approximately 20 chiplets were fabricated on this wafer and one was measured. By sweeping the full bandwidth of the VNA ($1-9$ GHz), 26 resonators were identified, and further sweeps, with higher accuracy, centred around the resonance frequency of each resonator were used for an estimate of parameters such as resonance frequency, coupling quality factor Q_c and internal quality factor Q_i. The values thus obtained are reported in 9.1 where the optimal power for each individual resonator is reported. It is worth noting that the value is the power outsourced by the VNA, and a number of power attenuators are present on the line that delivers it to the resonator array. The resonators seem to exhibit an excess phase noise which produces a "banana" shaped scatter when the resonator is not illuminated. This scatter, which for an ideal system would be gaussian in both the Q and I direction, results in a phase fluctuation, in dark, of about $\pm 15°$. While the nature of the phase noise is still unknown, one culprit could be a non negligible amount of thermal infrared photons that impinge on the detector array. In order to test it, the chiplet was cooled down to a temperature of $100\,mK$ while keeping the lid closed on top of the sample box. This

res. no.	Res. Frequency (MHz)	Q_c	Q_i	Power (dBm)
#1	3307.6352	203000	151000	-70
#2	3347.9744	299000	96000	-65
#3	3373.0215	11000	151000	-65
#4	3856.4771	51000	96000	-65
#5	3875.9534	47000	5000	-65
#6	3899.0937	62000	160000	-60
#7	3919.5487	53000	166000	-65
#8	3939.8756	63000	137000	-60
#9	3968.5402	42000	194000	-65
#10	4485.0944	5000	94000	-60
#11	4521.7163	45000	175000	-65
#12	4577.2740	26000	103000	-60
#13	4589.6831	33000	150000	-65
#14	4628.7958	17000	126000	-65
#15	4629.8683	16000	141000	-65
#16	5192.6870	17000	152000	-60
#17	5213.3005	85000	118000	-65
#18	5216.2165	74000	36000	-70
#19	5218.9122	47000	94000	-65
#20	5219.8032	24000	101000	-65
#21	5222.1575	33000	294000	-65
#22	5230.3588	14000	147000	-65
#23	5230.4682	14000	147000	-65
#24	5238.8583	20000	111000	-65
#25	5351.0186	20000	105000	-60
#26	5356.3177	254000	120000	-60

Table 9.1: Resonators map with resonance frequency, Q_i, Q_c and best driving power

way only self radiation at $100\,mK$ will illuminate the sensors. In doing this, the "banana" shaped scatter reduced marginally to $\pm 12°$. While closing the lid on the sample box had a visible effect on the noise baseline of the resonator, it is rather clear that infrared thermal radiation is not the main cause of it.

9.2.1 Noise figure of the MKID

As previously discussed, the resonators have been read out by driving the MKID at their resonant frequency while reading out the in phase (I) and quadrature (Q) components of the transmission figure. In doing so, the readout electronics samples the data with a frequency of $1\,\mathrm{MHz}$. Microscopic and macroscopic elements induce a random scatter around the I-Q position of the resonance frequency. In well behaving resonators, this scatter is known to appear isotropic in both the in phase and quadrature components and only covers a small fraction of the arc. Such a scatter results in a typical baseline noise, for well-behaved resonators, of $\pm 5°$.

The resonators here described, unfortunately, exhibited an excess noise. The scatter

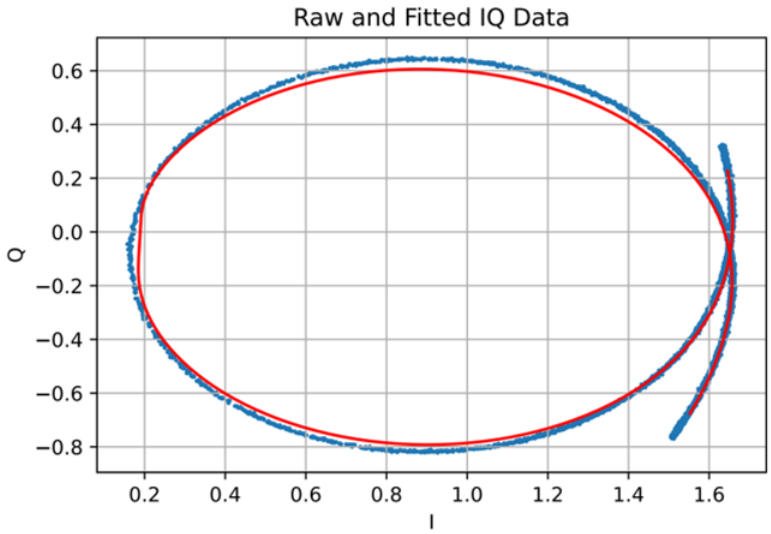

Figure 9.2: 4|10|4 – A resonator in the IQ plane is represented by a loop. In blue the data and the red line represents the fit to it. Its resonance frequency is $4579,46$ MHz and its total quality factor is 22000. The S_{21} figures for this resonator are shown in Figure 9.3

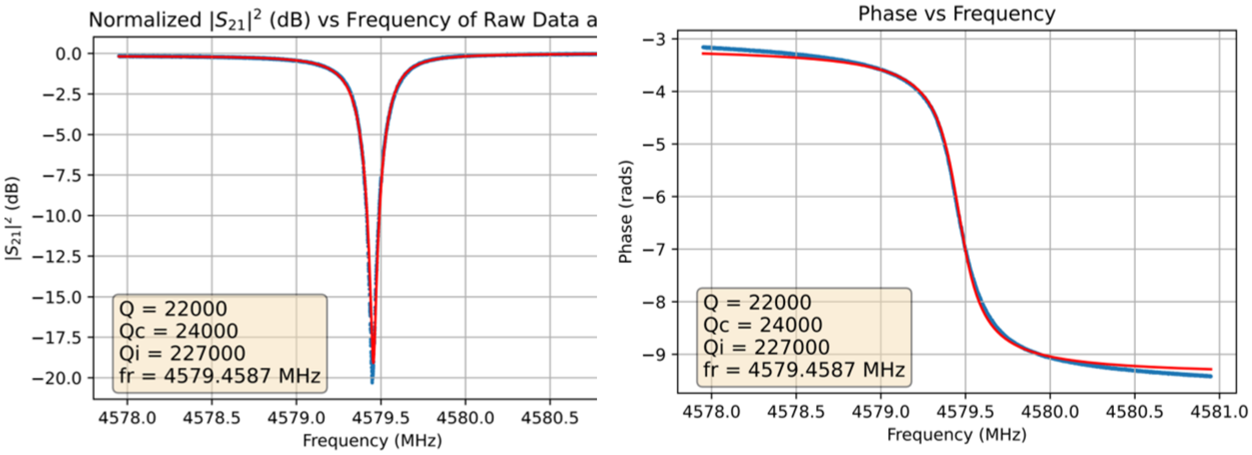

Figure 9.3: Left: The S_{21} transmission curve of the resonator in fig 9.2 . Right: The phase change across the resonance frequency of the same resonator. The legends includes the best estimates for important parameters such as the quality factors ($Q_{tot} = 22000$ and the resonance frequency $4579,46$ MHz.

around the position of the resonance frequency in the I-Q plane, is not isotropic. Looking at the scatter in the IQ plane, its tangential component is dominant over the noise in the amplitude direction and the respective baseline noise is $\pm 10°$. This is clearly visible when looking at the resonator in the IQ plane; Figure 9.4 represents data from the resonator described in Fig. 9.2 and 9.3. It shows a 500 point scatter, sampled at 1 MSPS, around the position of the resonance frequency in the IQ plane and how it follows the resonator's loop. Looking at it in terms of angle spanned by the noise, this is reflected in the baseline noise of $\pm 10°$ that was discussed earlier. Looking at the noise in terms of Analogue-to-Digital Units (digital units in the ADC converter), the 'banana' scatter is approximately 1500×500 units wide as can be seen from Figure 9.4. Further details on the noise characterisation of the resonator can be found in Appendix A3

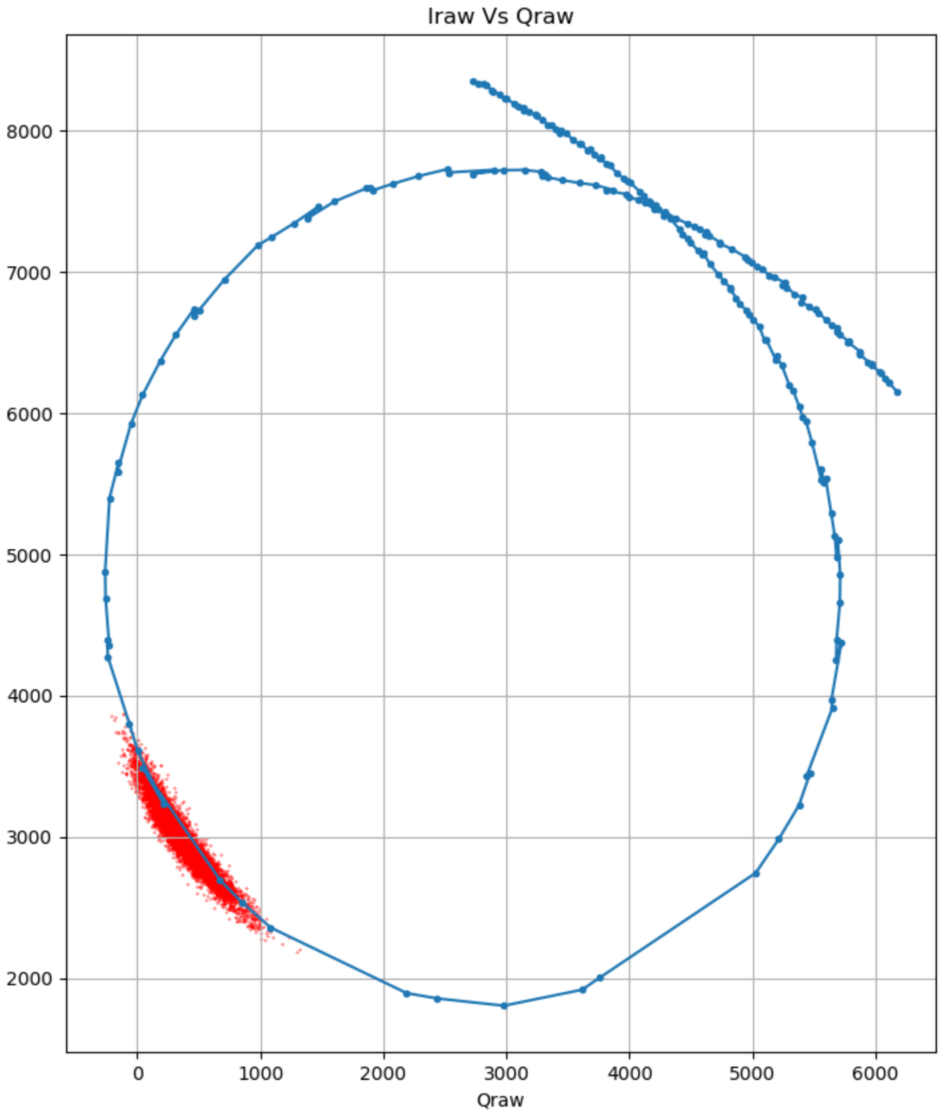

Figure 9.4: Snapshot of the resonator driven at resonance frequency (4579.46 MHz): 500 points sampled at 1 MSPS. The 'banana-shaped' scatter around the resonance frequency describes an arc of ~ 30°. The blue curve represents the resonators loop as per data pre-acquired.

9.2.2 Light-induced electron trapping

An interesting phenomenon that was observed when characterising the resonators from this production, is a systematic shift in resonance frequency when the resonators are illuminated with the light of the visible lasers contained in the laser box. For both lasers, the power coming out of the fibre is $\leq 2x10^{-8} W$. The peculiarity of what was observed is that upon turning off the light sources, it would take the resonator approximately 10 minutes to relax and creep back to its original resonance frequency, *i.e.* the one measured in dark before turning the lasers on. It might be speculated that this phenomenon is caused by a heating effect induced by the light and that the chip is either swamped with visible photons. This has been tested fully by heating up the sample space through the cryostat's P-I-D controller to the temperature that produces the same shift in resonance frequency as the impinging light and sweeping the resonator in frequency to fit it. By comparing the fits, it is clear that the two phenomena are not related as there is a significant reduction in Q_i when the sample is heated that is not as present when the resonator is illuminated.

In order to conduct further testing the resonators were illuminated with light of the same wavelengths, $450\,nm$ and $635\,nm$ but produced from a lamp and filtered by a monochromator. The optical power thus sourced to the resonators is at least two orders of magnitude higher than that produced by the laser box. When doing this one further effect was observed: upon turning the light source off, a first, quick relaxation with a time-scale of a few seconds is observed as well as the previously discussed slow drift. This seems to point towards the presence of trapped electrons in inter-band states of different energy and the different relaxation times are characteristic of electron traps of different energies.

Since we avail of a monochromator that can span from $400\,nm$ to $2500\,nm$ we could sweep the light source from the lowest energy upwards in steps of $50\,nm$ and this sweep exhibited that for wavelengths above $1350\,nm$ no initial shift of resonance frequency could be observed. This might be indicative of some inter-band states due to impurities in the silicon, perhaps due to the oxidation of the silicon wafer during the fabrication process. SiO_2 is known to be the main cause for TLS noise. It is worth stating that the effect couldn't be seen for long wavelengths because such photons are not capable of lifting an electron into the traps.

9.2.3 Pulse detection

When a photon strikes the superconductor, it is absorbed and its energy deposited in the superconductor breaks down a number of cooper pair in a phonon-mediated cascade process (85). The broken cooper pairs result in an increased kinetic inductance in the proximity of the area where the photon struck and ultimately is reflected in a resonance frequency shift of the MKID. After the strike and a very rapid change in resonance frequency, the broken cooper pairs tend to recombine with their typical quasi-particle recombination time, and after a period of time that is dependent on such parameter the MKID relaxes back to its original resonance frequency. As previously discussed, this can be monitored in terms of a change in amplitude of the S_{21} dip at resonance frequency and in terms of a change of the phase value at resonance frequency. While this sounds very intuitive, the best way to observe this phenomenon is in the IQ plane where it is possible to track any change in resonance frequency of the MKID and will appear totally like a "pulse" when monitoring phase angle from the 'zero' defined by the position of the resonance frequency on the IQ loop when the detector is not illuminated.

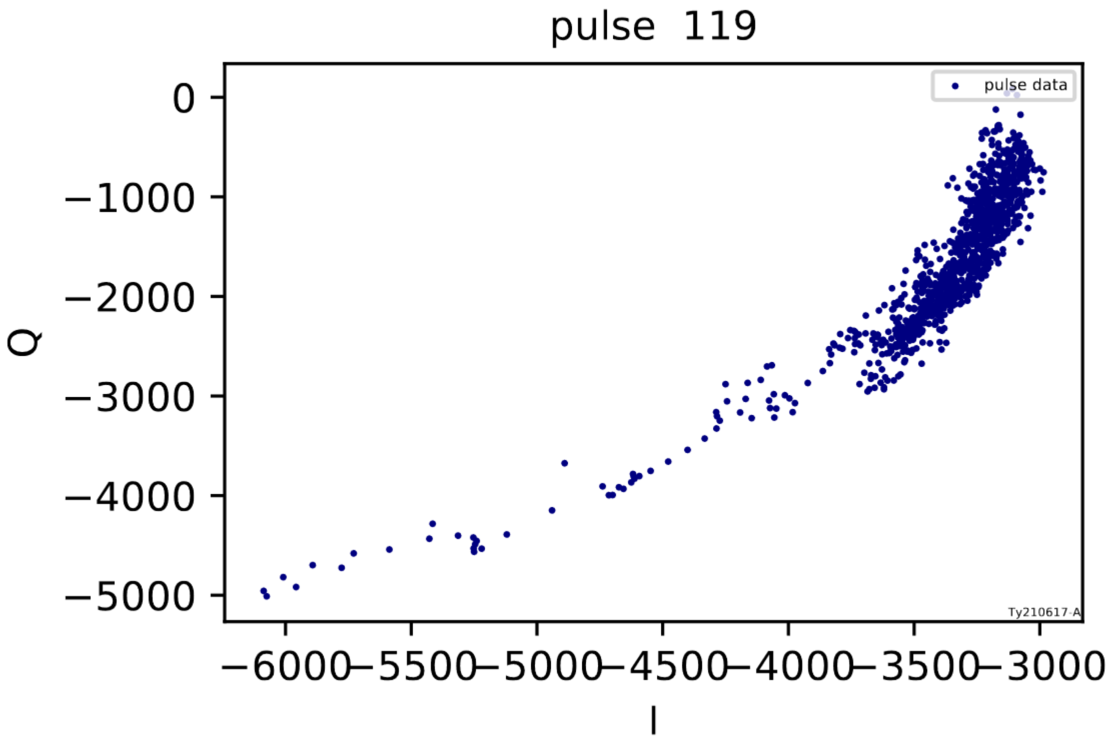

Figure 9.5: Cosmic ray event monitored in IQ-plane. The same pulse is described in time-domain in Figure 9.6.

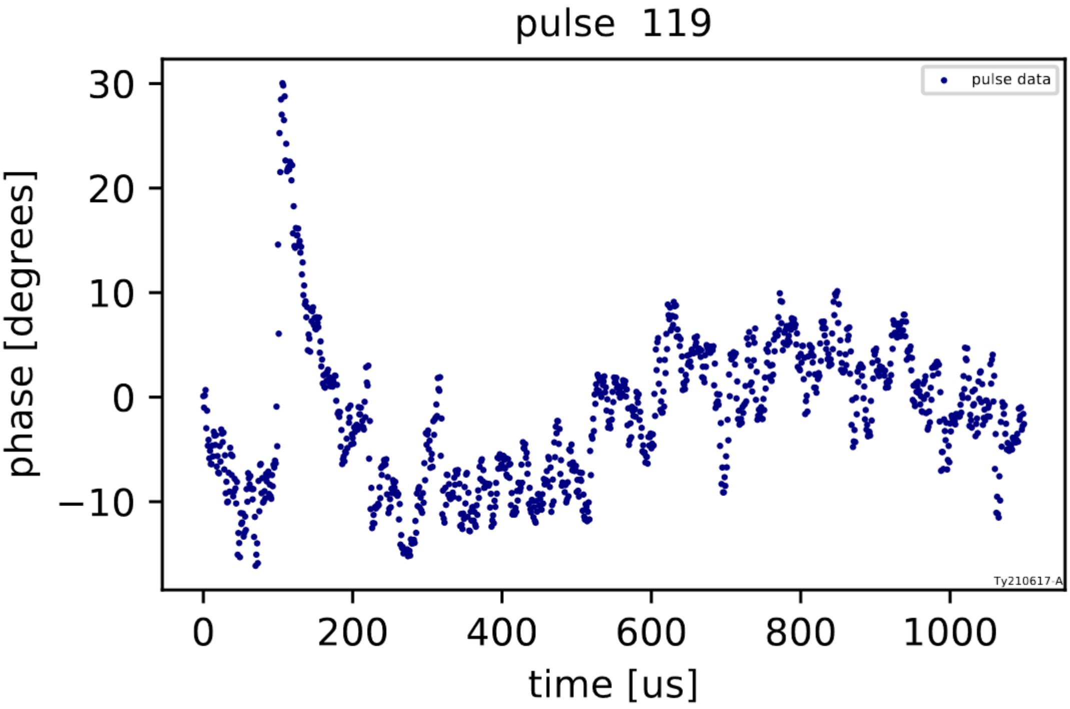

Figure 9.6: Same pulse represented in 9.5 but represented in time-domain. Each data point is acquired with an individual time-stamp and is 1 μs away from the previous. The figure represents a sudden change in phase angle and the relaxation. After the pulse, the fluctuation in baseline (described in Figure 9.4) is clearly visible.

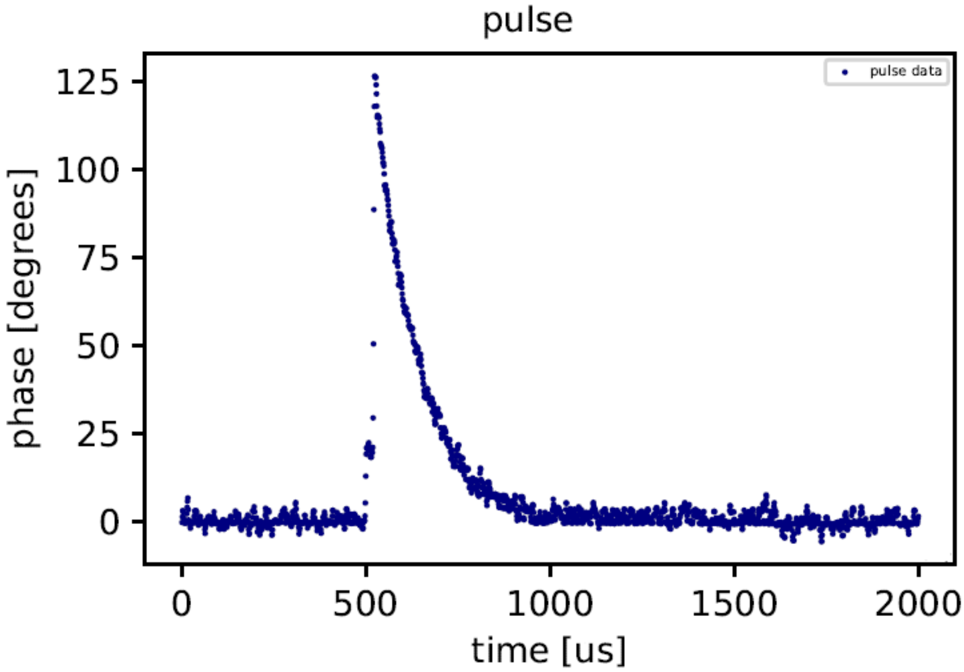

Figure 9.7: Cosmic ray event observed by the MKID

Figure 9.5 shows an example of what was just discussed. Before the cosmic ray hits the photodetector, the resonator lies in its resting position around its original resonance frequency and its position in the IQ is determined within the 'banana' scatter as previously discussed. When the particle hits the superconductor and its energy is then converted into the excitation of quasi-particles, the resonance frequency of the MKID abruptly changes and the resonator suddenly jumps into an out of equilibrium position only to slowly drift back into its resting position with a time constant that is identified as the quasi-particle recombination time. The angle spanned by this "pulse" is defined as the height of the pulse in terms of phase angles and is proportional to the energy of the photon that struck the photodetector. This is probably clearer when looked at in time domain. Figure 9.6 represents the same pulse shown in Figure 9.5 but in terms of phase angles described by the MKID plotted as a function of time, identified as a timestamp produced by the readout electronics and unique for each μs of data. The triggering mechanism of the readout electronics identified the pulse and acquired 1200 data points in correspondence of the pulse. In this pulse two of the components of the baseline noise are also clearly visible: a jitter around its zero-value with an amplitude of $\pm 5°$ and a slower noise source, perhaps induced by Two-Level Systems which contributes to a baseline fluctuation of $\pm 10°$ on a different time scale than the aforementioned jitter.

9.2.4 Cosmic ray event

Figure 9.7 shows the response of the MKID when the array has been struck by a cosmic ray. The definition of cosmic rays is scientifically vague, but for the sake of this work we intend secondary particles produced in showers by the interaction of highly energetic particles, of solar and galactic origins, in the atmosphere (96). It is easy to identify an event like a cosmic ray strike as the highly energetic particle striking anywhere on the array will be absorbed exciting phonons in the silicon substrate, therefore resulting in the heating up of the substrate. The propagation of the hot phonons in the silicon induces the breakdown of a number of cooper pairs in the superconductor, thus a pulse is produced through the same mechanism that is produced by a photon event.

The rejection of a cosmic ray event is a rather simple task. Three main features distinguish a cosmic ray event from a photon event: being a phonon mediated process, the rise and fall times of the pulses are not anymore directly linked to the ring-down time and the quasi-particle recombination time, but the characteristic times of these processes are mediated through the propagation speed of the phonons in the silicon and the thermal contact with the cold finger of the refrigerator. The time features of the pulses are a great way to identify a cosmic ray event and reject it; one other interesting feature is that such energetic particles tend to produce pulses at very high phase-angles. An unexpectedly high pulse will also hint in the direction of it being caused by a cosmic ray and towards rejection.

In the event of an array readout, *i.e.* reading out multiple resonators at the same time, the identification of a cosmic ray event is extremely trivial. The hot phonons produced by the absorption of the cosmic ray will diffuse isotropically in the substrate triggering pulses in multiple pixels with, approximately the same time stamps.

9.3 Post-fabrication annealing

In order to try and mitigate the issue of the 'banana' shaped phase noise and the excessive baseline noise that was observed in the sample, a post-fabrication annealing has been attempted. This is meaningful under the assumption that the excess noise is caused by the oxidation of silicon, or perhaps the titanium layer, which is an undesired byproduct of the fabrication recipe Tyndall has developed. The origin of this undesired oxidation might be identified in the process of stripping the hardened resist after the ICP etch. While the recipe developed in CRANN involves the wet stripping of the photoresist in a heated bath of 1165 photoresist remover, Tyndall burns off the resist in an O_2 atmosphere which, can result in undesired chemical reactions between the oxygen in the atmosphere and either the exposed Silicon to form SiO_2 or the Titanium to form one of the following titanium oxides: TiO, TiO_2, Ti_2O_3, Ti_3O, or Ti_2O. And perhaps the oxidation of the Titanium layer

could possibly account for the inconsistency with what is commonly known. It is expected that MKIDs that exhibit excess noise due to Two-Level Systems also exhibit rather low internal quality factors. This is due to the fact that the excitation of TLS produces lossy particles that disperse their energies while travelling through the substrate. Instead in the previous section it was shown that the MKID taken into analysis exhibited a high internal quality factor $Q_i = 227000$ that wouldn't be commonly associated with resonators that exhibit high levels of TLS noise. It could be speculated, and this is still under investigation, that it is the exposed Titanium exposed in the side-profile of the stack that has oxidised and account for the excess noise that has been measured. The personnel in Tyndall suggested, based on their experience working with Titanium for other commercial customers, that an annealing could be attempted to get rid of the oxygen content in the sample.
The post fabrication annealing process they suggested involved heating up the MKID array to a temperature of $500°C$ in Forming Gas $(95:5 - N_2:H_2)$ for 30 minutes. This process is meant to induce a reaction between the gaseous hydrogen and the bound oxygen in the oxide to form water which is then evaporated in the atmosphere and pumped out of the chamber thus removing the oxidation from the film. The characterisation of an annealed array is presented in Section 9.4

9.4 TiN|Ti|TiN – 4|10|4 post annealing

In order to investigate the claim that annealing the multilayers could get rid of the excess noise, a chip from the previous fabrication run has been sent back to Tyndall for annealing. The newly annealed chip was mounted in a sample box, bonded and cooled down in the Adiabatic Demagnetisation Refrigerator. Knowing that a good estimate for the kinetic inductance before the annealing process was $5.5 \pm 0.5 pH/square$, it was decided to investigate the feedline to which the resonators designed for a film with a sheet inductance of $5 pH/square$.
The same analysis previously discussed has been carried out with this sample. Firstly, spanning the full bandwidth of the VNA $(1 - 9\, GHz)$ permitted the identification of 20 uniquely distinct resonators. This time their resonance frequencies were not laid in the $2 - 4\, GHz$ octave. The depth of the transmission dips was significantly reduced and only the best resonators exhibited an amplitude greater than 8dB. This coincided also with a decreased internal quality factor to $Q_i \sim 60000$ and a shift in critical temperature ($\sim 600 - 750\, mK$ as can be deducted from in Figure 9.10). These unexpected changes quite clearly reflect a change in the intrinsic properties of the superconducting layer. A quick calculation suggests an increase in the sheet inductance of the film from $5.5\, pH/square$ to $\sim 20 pH\, /square$. The mismatch between the designed resonance frequency and coupling quality factor Q_c can partly account for a reduced performance of the detector. Fortunately, the design

of the chiplet includes, along with the $5pH/square$ feedline, two feedlines designed for a sheet inductance of $0.3pH/square$ and $20pH/square$. The latter will soon be tested. Unfortunately the unexpected reduction in internal quality factor cannot be mitigated, and might be explained by the possible mixing of the pure Titanium and Titanium Nitrdide layers producing somewhat of a generally sub-stoichiometric layer of Titanium Nitride which would also be reflected in the change in critical temperature of the film.
A list of resonators, with their resonance frequency, the fitted values of Q_i and Q_c and the best readout power can be found in Table 9.2.

res. no.	Res. Frequency (MHz)	Q_c	Q_i	Power (dBm)
#1	2072.4188	180000	78000	-70
#2	2072.4768	7000	3000	-74.5
#3	2097.2917	204000	93000	-74.5
#4	2107.2371	409000	77000	-74.5
#5	2368.0773	303000	77000	-70
#6	2372.7621	124000	67000	–65
#7	2392.2318	142000	50000	-65
#8	2393.3849	57000	67000	-65
#9	2415.0648	74000	74000	-65
#10	2438.9977	6000	4000	-65
#11	2772.0753	98000	54000	-65
#12	2802.7133	62000	60000	-65
#13	2816.7073	30000	59000	-65
#14	2818.1691	41000	51000	-65
#15	2855.4876	159000	205000	-65
#16	2856.1628	99000	128000	-65
#17	2873.3233	95000	50000	-65
#18	2892.8496	37000	60000	-65
#19	3225.2354	193000	49000	-74.5
#20	3229.822	181000	52000	-74.5

Table 9.2: List of resonators identified on the annealed sampled with resonance frequency, Q_i, Q_c and best driving power.

As a starting point for the characterisation of the array, the deepest resonator has been characterised in full. With an amplitude of 9dB, the resonator that seemed to be the most promising is the one with a resonance frequency of $2892.852\,MHz$.
A fine frequency scan and its fit provide a good estimate for parameters such as Q_c and Q_i, while these parameters for all the resonators on the array can be found in Table 9.2, the best values for these parameters can also be found in Figure 9.8 and Figure 9.9. For this particular resonators, the best estimate for $Q_c = 22000$ and $Q_i = 60000$ have resulted from the fit.

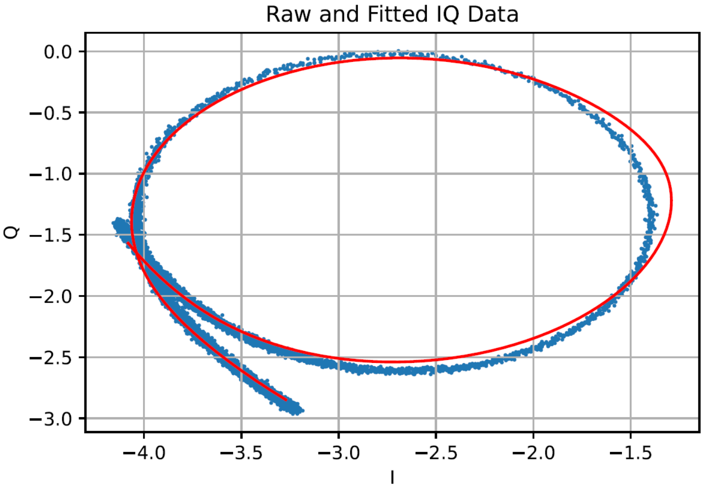

Figure 9.8: Caption

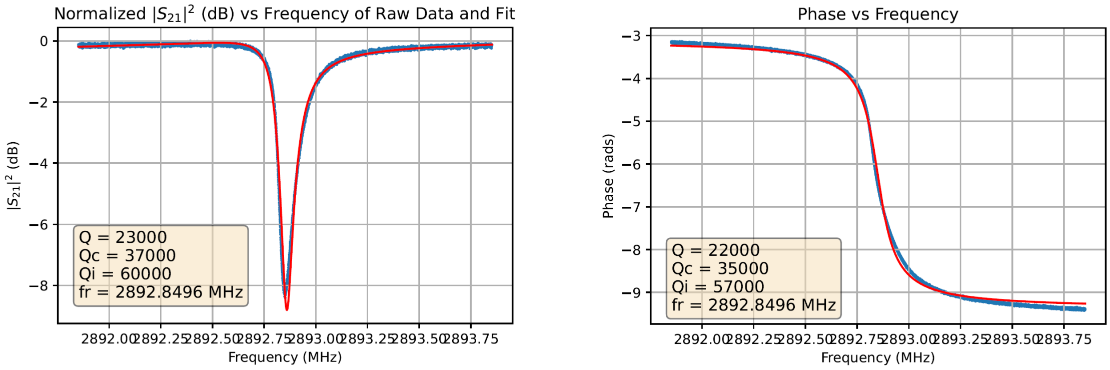

Figure 9.9: Left: The S_{21} transmission curve of the resonator in fig 9.2 . Right: The phase change across the resonance frequency of the same resonator. The legends includes the best estimates for important parameters such as the quality factors ($Q_{tot} = 22000$ and the resonance frequency $4579, 46$ MHz.

Figure 9.10 represents the transmission dip of the resonator as measured by the VNA at different temperatures of the cryostat spanning from $150\,mK$ down to $75\,mK$ which is the lowest temperature that can be reached by the ADR of which DIAS avails.
This was necessary to understand the behaviour in temperature of the Microwave Kinetic Inductance Detector. As the operating temperature decreases, the number of unpaired electrons in the superconductor decreases further until the film is fully depleted of non-superconducting electrons. A reduction in the total number of electrons results in a decrease in the kinetic inductance of the film, thus an increased resonance frequency, and a reduction of the energetic losses in the superconductor, therefore an increase in Q_i and consequently an increased Q_{tot}.
Knowing that high-frequency losses become negligible at temperatures $T_c/8 - T_c/10$ (97, 98) and that when the superconductor is fully depleted of unpaired electrons, both the resonance frequency and the amplitude of the resonator saturate to their maximum value, it is possible to give a rough estimate of the critical temperature of

the film to be withing $600 - 750\,mK$. Unfortunately, before further repairs are done to the cryostat, the lowest temperature that can be held for a meaningful amount of time ($\approx 3h$) is $100mK$ and all the measurements described in the rest of this Chapter are to be intended at $100mK$ unless otherwise specified.

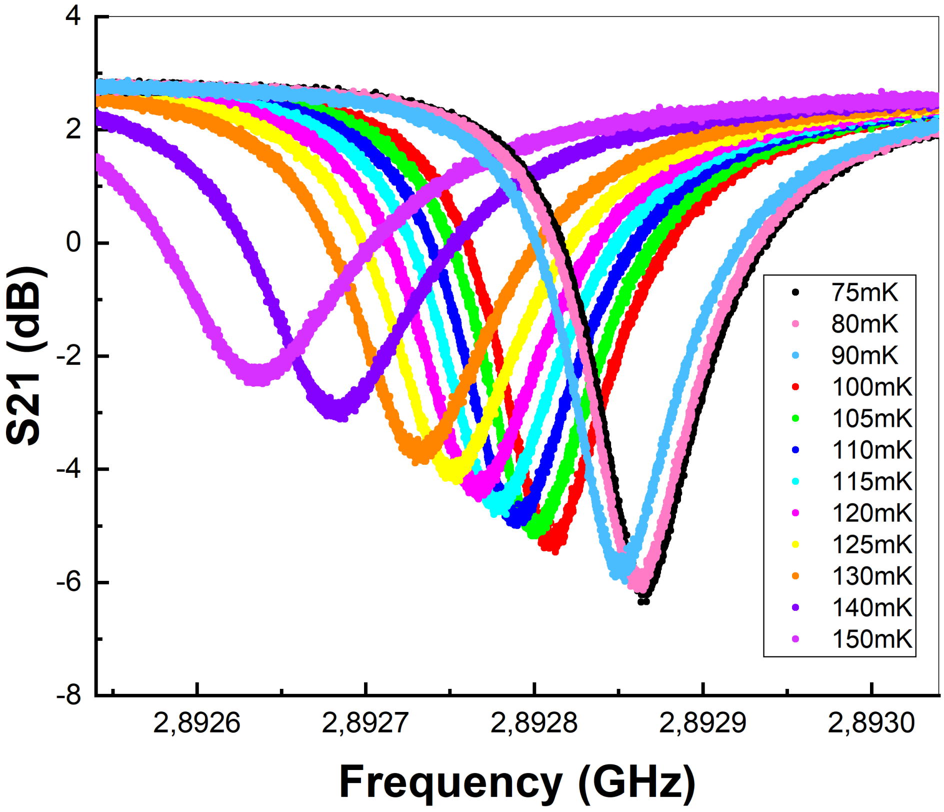

Figure 9.10: Resonator's transmission S_{21} at different temperatures ranging from $150\,mK$ (in lilac on the left) down to $75\,mK$ (in black on the right).

To everyone's surprise, when driving-illuminated resonator with its resonance frequency and observing it in I-Q plane, the 'banana' shaped noise figure was gone and replaced by a much smaller and rather circular scatter, that is isotropic in both I and Q, around the position of resonance frequency. As Figure 9.11 shows, in terms of phase angle, the scatter results in a fluctuation of $\pm 5°$ of 500 points sampled at $1MSPS$, the noise exhibited by this resonator is comparable to what is observed for most well-behaved detectors. In terms of Analogue-to-Digital Units, the scatter cloud is approximately 500×500 units wide, about three times smaller than the scatter observed for a non annealed sample.

9.4.1 Photon detection

Since the 'banana' shaped noise cloud is not present in this sample, it is valuable to illuminate the detectors with optical and near infrared photons so to analyse the

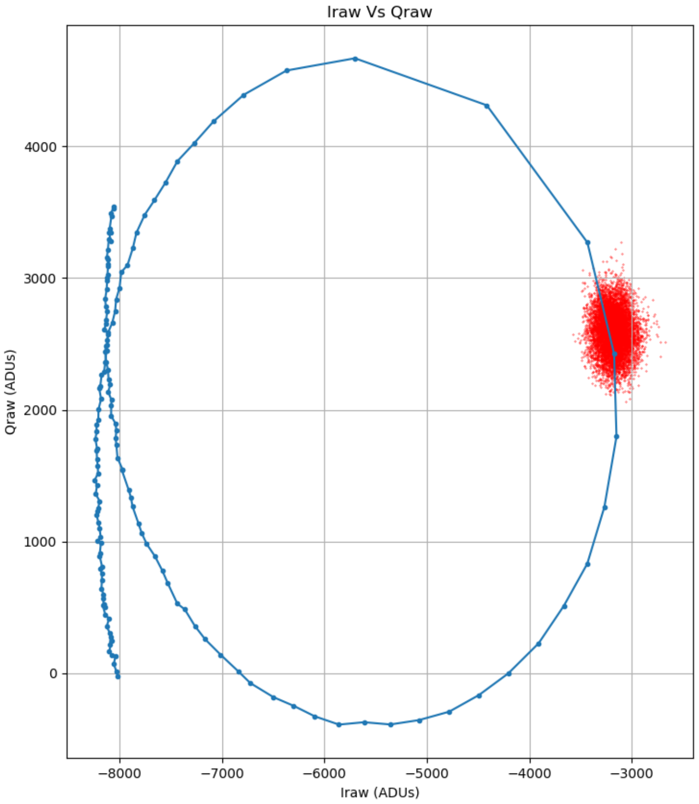

Figure 9.11: Snapshot of the resonator driven at resonance frequency (2892.852 MHz): 500 points sampled at 1 MSPS. The 'banana-shaped' scatter has vanished and the scatter cloud is isotropic in I and Q around the resonance frequency. The noise cloud describes an arc of ±5°. The blue curve represents the resonators loop as per data pre-acquired.

performance of the detector and as a proof of concept demonstrate the energy resolution of the prototype MKID.

In order to illuminate the detector with monochromatic light, the monochromator (described in Chapter 3 and Chapter 4) was deployed. The monochromator is attached to a halogen lamp and the overall spectrum of the setup can be found in Appendix A1. Also, the typical spectral line-width of the light produced by the monochromator, with the slits set at $1\,mm$ is $10\,nm$. Five wavelengths have been identified for a first characterisation of the detectors: $400nm$, which is the shortest wavelength the monochromator can produce, $525nm$, $650nm$, $775nm$ and $900nm$ which is the longest wavelength the resonator can respond to and still produce a signal that is consistently above the baseline noise while retaining a signal-to-noise ratio of ≈ 2.

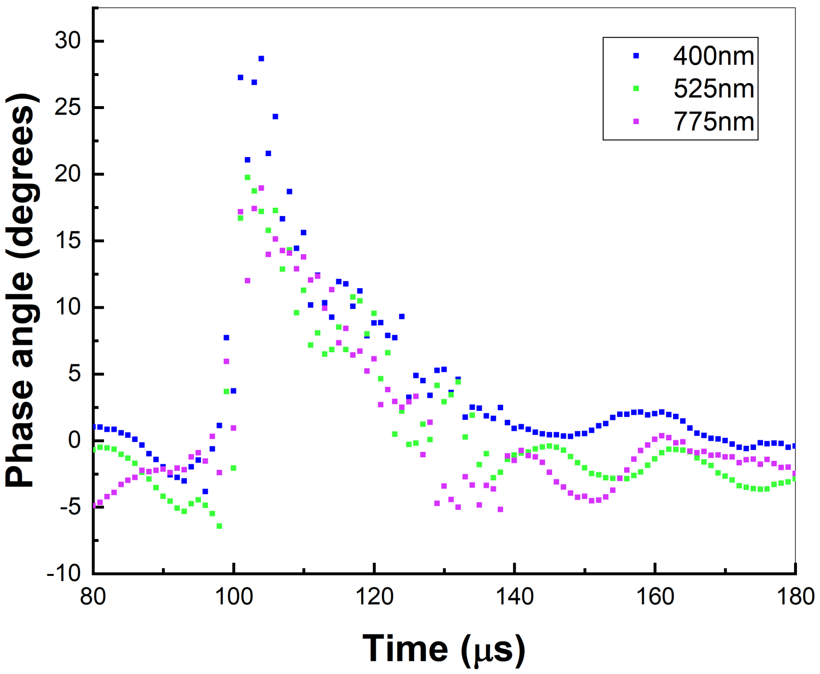

Figure 9.12: Pulse height as a function of time of three selected pulses produced by photons of different wavelengths: 400nm (blue), 525nm (green) and 775nm (lilac). A 10 point rolling average has been applied, only for the purpose of this plot, to the baseline before and after the pulse to make the pulse more visible in the baseline noise.

Figure 9.12 shows the response of the detector under analysis at a temperature of $100mK$ to photons of different energies (and wavelengths).

It can be seen that, as expected, the height of the phase pulse, intended as a temporary phase shift induced by the change in kinetic inductance due to the photon breaking a number of Cooper pairs that is proportional to its energy, is indeed proportional to the energy of the photon. The pulse produced by a blue photon ($400nm$) is $\approx 23°$ while an infrared photon ($900nm$) only produces a phase pulse that is $\approx 12°$ high.

In order to investigate the energy resolution of the detector under study, about 50000 pulses have been collected per each wavelength and at each wavelength a histogram was populated with the maximum of each pulse.

The histograms are in the shape of a bell curve around the best estimate of the real value of the phase shift produced by the photon with each specific energy. From the mean value and the width of each curve it is possible to evaluate the resolving power of the detector as $R = E/\Delta E$ where E represents the mean value of the distribution and ΔE the FWHM. Figure 9.13 shows the distributions just described per each wavelength (a,b,c,d,e) and next to each other (f).

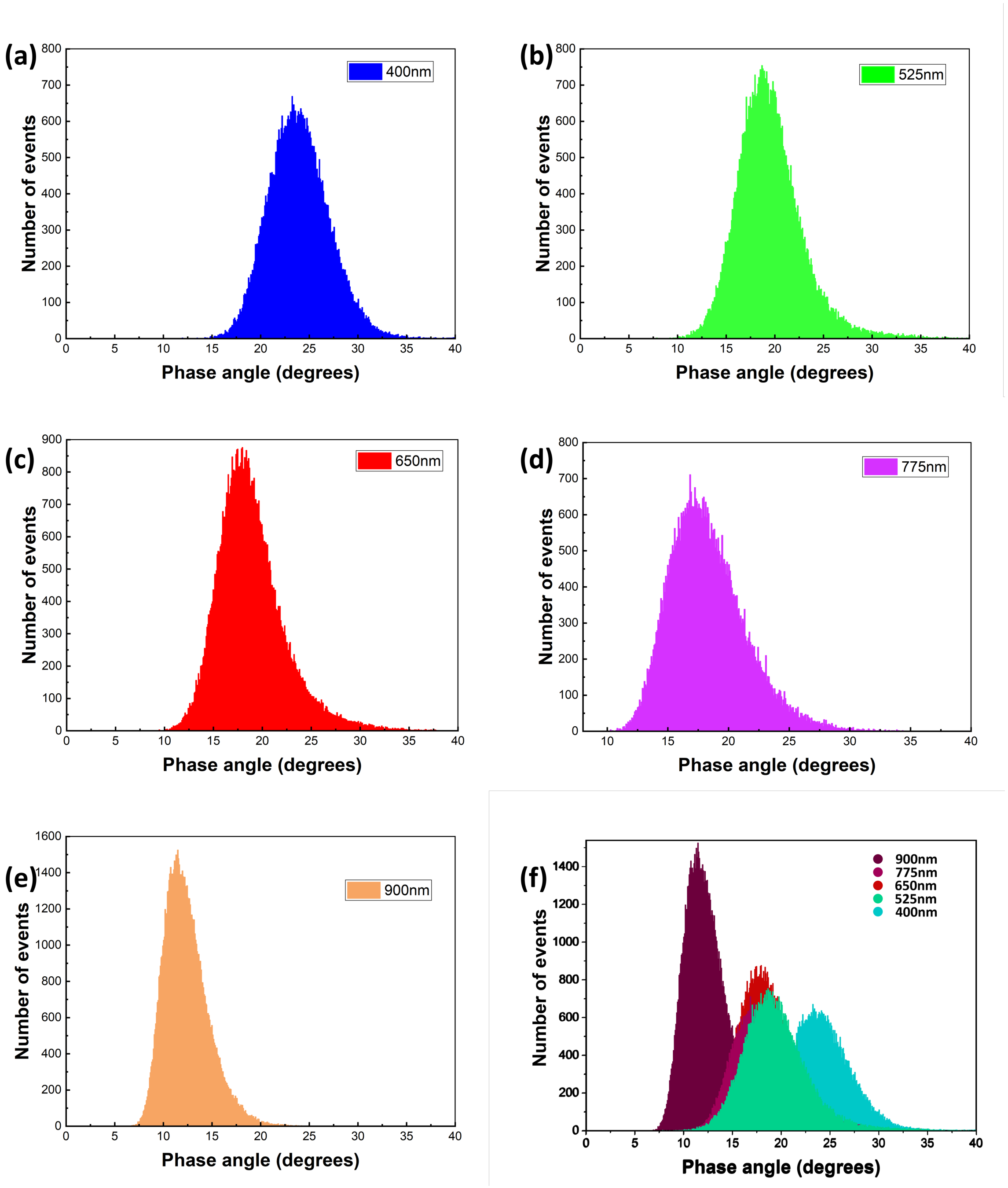

Figure 9.13: Histogram of the maxima for about 5000 pulses at different wavelengths: (a) $400nm$, (b) $525nm$, (c) $650nm$, (d) $775nm$ and (e) $900nm$. (f) The previous five histogram next to each other on the same axis.

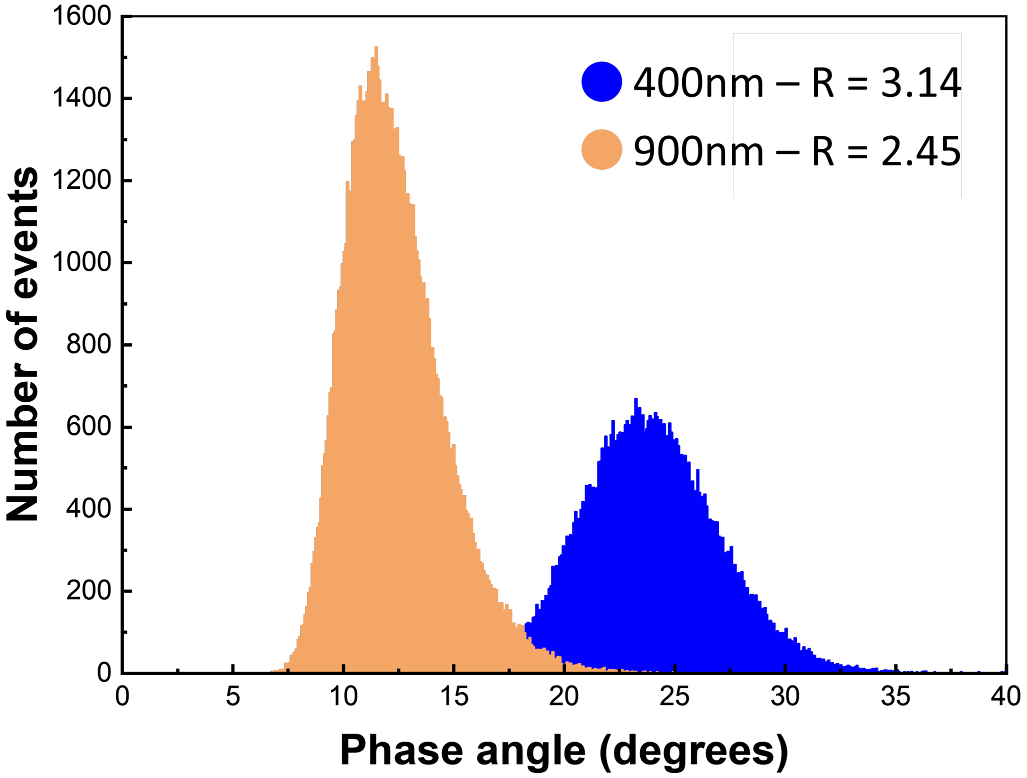

Figure 9.14: Histogram of the maxima for about 50000 pulses at two different wavelengths: 400nm (blue) and 900nm (orange).

While the previous figure is very informative, one clear way of visualising the data is to only plot the left most and the right most histograms on the same plot as shown in Figure 9.14. Here, given the moderate energy resolution of the detector, it is possible to appreciate the mean value and the width of the distribution induced by blue photons ($400nm$) and infrared photons ($900nm$). The best estimate for the detector's resolving power at each wavelength can be found in Table 9.3.

wavelength (nm)	Resolving Power
400nm	3.14
525nm	3.01
650nm	2.60
775nm	2.57
900nm	2.45

Table 9.3: Table with Resolving Power values per each wavelength measured.

This is extremely preliminary result as this is the first working prototype fully fabricated and analysed for the sake of this the development of Microwave Kinetic Inductance Detectors DIAS has embarked on. Further testing as well as a better data analysis procedure are necessary. Event rejection and optimal filtering could result in a significant improvement to the energy resolution of this specific detector and further optimisation of the fabrication process can push the resolving power of the MKIDs developed in DIAS much closer to the best results other groups report and the theoretical limit described earlier in this thesis.

9.5 Comparison with state of the art MKIDs

This last section is intended to show how the DIAS MKID compares in terms of Resolving power to optical and near-infrared Microwave Kinetic Inductance Detectors developed by other groups.

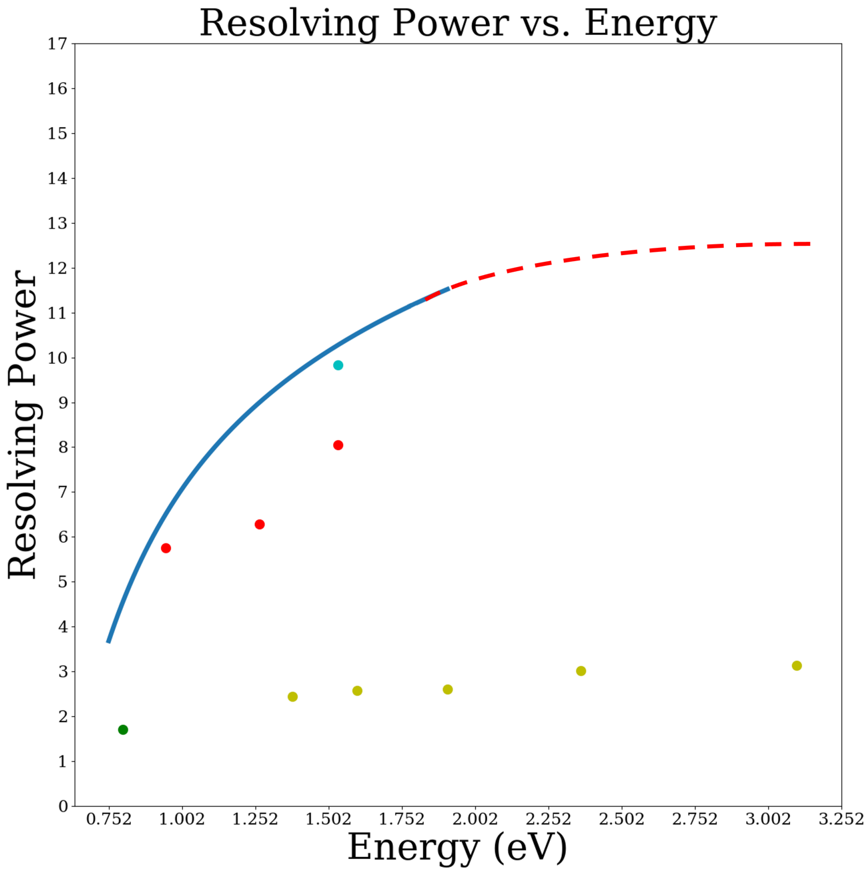

Figure 9.15: Comparison in resolving power between the DIAS MKID (yellow) with MKIDs produced by other groups. Green - (16), Cyan - (17), Red - (11). The solid blue line represents the model described earlier in this thesis (7 and the red dashed line described an expected extension of the same model.

Figure 9.15 shows the resolving power of the DIAS MKID (yellow) in context with the same quantities as published by other groups: Red ((11)), Cyan ((17)) and Green ((16)). The solid blue curve represents the model described in this thesis 7 and the dashed red one represents an expected extension of the model to lower wavelengths. It is clear that the performance of the DIAS MKID is not yet comparable to the resolution other groups can achieve and it is still far from its expected limit. Being this the first detector that was characterised for the scope of the project, and knowing the issues that have arisen, one can expect large room for improvement and further optimisation of the detector. The annealing has changed the properties of the film resulting in a decreased internal quality factor and a lower critical temperature as well as a much higher sheet inductance of the film. In addition to this, the model described earlier is based on the assumption that the MKID produces a $180°$ phase signal when struck by a red photon ($650nm$) while the DIAS MKID is far from saturation, producing a pulse that is $18 \pm 3°$ high.

10 Conclusions

This thesis details the research I have carried out over the last four years aimed at improving our understanding of Microwave Kinetic Inductance Detectors and developing a prototype MKID for applications in optical and near-infrared astronomy. This Chapter provides a break-down of the main results and achievements that originated from the last four years of my work.

10.1 Setting up a cryogenic laboratory

The first task I had was to commission a cryogenic laboratory in the Astronomy and Astrophysics section of the Dublin Institute for Advanced Studies. The first task was to purchase a cryostat capable of reaching and holding temperatures as low as $100\,mK$ for at least 12 hours. The Adiabatic Demagnetisation Refrigerator (ADR) from Entropy GmbH met these requirements. The cryostat had to be equipped with coaxial cables (superconducting and non superconducting), two High Electron Mobility Transistor (HEMT) amplifiers and a critical temperature setup which consists of two transition boards mounted on a copper finger that is connected to the coldest stage of the cryostat (FAA). In order to allow the illumination of the MKIDs with visible and near-infrared photons, it was necessary to set up a series of view ports through the different shields of the cryostat. The infrared radiation produced by the $300\,K$ and $70\,K$ shields has to be filtered out in order to prevent the heating up of the MKIDs mounted on the FAA stage. As of today, the cryostat in the DIAS MKID laboratory hosts the coldest place in Ireland.

The room temperature electronics also had to be purchased and developed; a Vector Network Analyser was purchased in order to achieve a first characterisation of the resonators. A resistance bridge was purchased, and a LabVIEW code was developed, to allow critical temperature measurements of the thin films produced.

In order to illuminate the resonators, we employed two sources of light. A laser box was built to provide six discrete wavelengths. Additionally, in order to extend the wavelength range, a monochromator was purchased and a LabVIEW code was developed to automate it.

10.2 Developing a fabrication recipe

The second challenge was to develop a comprehensive recipe for the fabrication of an array of Microwave Kinetic Inductance Detectors.
This involved several steps, including the design and simulation of the lithographic mask and each individual resonator. Another crucial step was the optimisation of the sputtering process which controls the thickness, the composition and the critical temperature of the thin films. By varying these properties, the performances of an MKID can be optimised. The lithographic process including the etching procedure was optimised to produce resonator arrays with the highest yield possible.

10.3 What influences the performances of an array of Microwave Kinetic Inductance Detectors?

Given the current knowledge available on Microwave Kinetic Inductance Detectors, the first scientific question I chose to address was "what are the main limiting factors to the performance of an MKIDs array ?". In particular, my focus was to try and understand how critical temperature inhomogeneities affect the fabrication yield of an MKIDs array. I produced a 2D map which correlated the fabrication yield with the total quality factor of the resonators and a parameter, σ, which represents the scatter of the resonance frequencies, around their designed value. This is due to inhomogeneities in critical temperature of the thin films. Whilst carrying out this work, I also investigated what influences the energy resolution of a Microwave Kinetic Inductance Detector. Multiple factors are known to limit the performance of these detectors. I developed a model for the performance of an MKID which could fit experimental data from the scientific community. This gave further credence to the new hypothesis that the noise induced by the losses of hot phonons is currently the limiting factor to the energy resolution of an MKID. The noise induced by the HEMT or Two Level Systems (TLS) is also significant whereas he contribution of current inhomogeneities and the Fast Fourier Transform is not.

10.4 Retuning an MKIDs array

Building on the understanding of what limits the fabrication yield, I proposed the retuning of a number of selected resonators by biasing them with DC current. Since the kinetic inductance is a non linear function of the current flowing through the superconductor, it is possible to decouple a pair of colliding resonators by biasing one of them. This subsequently changes it's kinetic inductance, and therefore it's resonance frequency. A Python-based simulation showed that the fabrication yield of an array can be increased by an overall 12.5%, from $\sim$ 75% to 87.5%, while using one single current value. I propose a possible new geometry, which includes a filtering stage and a current distribution and does not intersect the feedline, that allows the selection of the resonators to retune. This is achieved by connecting the current distribution line to the each resonator via bond wires.

10.5 Industrial collaboration with Tyndall

In order to overcome technical difficulties,accentuated by the COVID-19 pandemic, which at times rendered the CRANN cleanroom inoperable. I had the privilege of establishing an industrial collaboration with the Tyndall National Institute.
The Tyndall National Institute is a flagship facility of the University College Cork and provides a national focal point for excellence in deep-tech research, in particular micro and nano-electronics, photonics, materials and software. The Institute has cleanroom facilities and their equipment and personnel could produce Microwave Kinetic Detectors arrays for the sake of this project at a affordable commercial rate. This is one of the first examples of MKIDs produced through a commercial collaboration between a semi-private facility and a research institute, such as DIAS. This collaboration paves the way to the development of Microwave Kinetic Inductance Detectors as commercial devices.

10.6 Photo detection as a proof of concept

In ultimis, the full characterisation of a Microwave Kinetic Inductance Detectors array, and that of one resonator in the array with an internal quality factor $Q_i \sim 150000$, served as a proof of concept that the detection of photons is achievable with this detector. It also shows that the rejection of cosmic ray events is possible. Chapter 9 also addresses the issue of unexpected excess baseline noise that results in a banana-shaped scatter around the resting position of the resonator. Further investigation is necessary to determine whether this noise originates due to the presence of silicon dioxide on the sample.
A post-fabrication annealing process appears to have mitigated the issue of the 'banana' shaped phase noise. The annealed resonators have been fully characterised and the pulse detection of optical photons has been demonstrated. A moderate energy resolution (3.14 - 2.45), between 400nm and 900nm, has been achieved. Unfortunately, the annealing process has also altered the properties of the superconducting film, including the critical temperature and the sheet inductance. Whilst the first results are promising, further optimisation is necessary.
Further research that I have suggested as a continuation of this project can be found in Chapter 12

11 Other MKIDs applications

For the entirety of this thesis, it has been assumed that the main application of Microwave Kinetic Inductance Detectors is for observational astronomy in the optical and near-infrared region of the spectrum. While MKIDs were developed with this specific purpose, over the last two decades multiple other applications have been found for detectors with such interesting characteristics. This chapter is only reporting on the most interesting and successful applications of MKIDs outside of optical astronomy. Further information on the instruments listed here and further applications, can be found in the 2021 paper from Ulbricht et al. (40).

Infrared Astronomy

As pair-breaking detector MKIDs are at great advantage on the competition by having a band gap that is three to four orders of magnitude smaller than that of silicon based detectors (33). The meV band gap allows MKIDs to be sensitive down to very small photon energies. MKIDs although sensitive are not capable of producing a detectable signal when struck by a photon of such low energy, but can be operated as bolometers (99). In this regime a steady flux results in a constant quasi-particle generation rate which will reach an equilibrium with quasi-particle recombination resulting in a constant density of quasi-particles which depends on the number of photons per second and their energies. When operated as bolometers MKIDs cannot distinguish between photon flux and wavelength and filters are often used in front of the detector to break this degeneracy. MKIDs in this wavelength range are used as both imaging detectors as well as spectrometers.

11.0.1 Infrared Imagers

Early MKIDs instruments in the infrared and sub-millimetre include MUSIC (MUltiwavelength Sub-millimeter Inductance Camera) (100, 101) and its precursor DemoCam (102), which have 16 pixels and two sensitivity bands at $0,9\,mm$ and $1,2\,mm$ (103).
Arguably, the most successful MKID instrument is the New IRAM KIDs Array (NIKA) (104) and its 2015 successor, NIKA-2 (105). NIKA-2 is a 3440-pixel

cryogenic camera for astronomical observations with the 30 m IRAM telescope on Pico Veleta, Spain and covers two bands centred around $2,0\,mm$ ($150\,GHz$) and $1,15\,mm$ ($260\,GHz$) and offers a 1040 pixels array for 150 GHz and two arrays with 1200 pixels each for both polarisation directions of the 260 GHz band.
The world's largest single aperture telescope for mm astronomy is the Large Millimeter Telescope (LMT) (106) in Sierra Negra, Mexico. Two MKID camera instruments are being worked on for LMT: MUSCAT, the Mexico UK Sub-mm Camera forAsTronomy (107) is a collaborative effort to install a 1600 pixels MKID camera at the LMT with a sensitivity band centred around $1,1\,mm$ ($270\,GHz$).
TolTEC (108) is the second MKID camera project for the LMT. It is intended as millimetre-wave imaging polarimeter with three bands around $1,1$, $1,4$, and $2,0\,mm$ (280, 220, and $150\,GHz$).
Ground-based observations of the Cosmic Microwave Background (CMB) have been a significant driving force behind the development of low temperature detectors for many years. In this field of study multiple instruments already deploy MKIDs as their sensing elements or are considering MKIDs as detectors for their instruments. Among these, GroundBIRD (109), ACTPol (110) and BICEP-Array (111) are the most prominent.

Infrared On-Chip Spectrometers

DESHIMA (DEep Spectroscopic HIgh-redshift MApper) (112, 113) is a single pixel microwave spectrometer sensitive between 332 and $377\,GHz$ (903–$795\,\mu m$). It uses an on-chip microwave antenna on which incoming light is focused on in order to couple incoming photons into a superconducting feedline which is coupled to 49 MKIDs each with its own individual resonance frequency. DESHIMA achieves an energy resolution $R = \frac{E}{\Delta E} = 380$ (112). The design of an on-chip filter-bank spectrometer using MKIDs is also pursued by SuperSpec which is targeting the 195–310 GHz (1.54–0.97 mm) frequency range and is aiming for up to 500 channels to achieve a spectral resolution R of 700.
CAMELS (114) aims at achieving an energy resolution of 3000 using 512 filter channels in the region between 103 and $114,7\,GHz$ (2.9 –$2.6\,mm$).
Micro-Spec (115) is an MKIDs based project designed to measure spectra in the $0,5$ – $1.0\,mm$ with an expected energy resolution between 512 and 1200. Micro-Spec is designed to be a miniaturised diffraction grating and is proposed as a detector for the EXCLAIM (116) instrument which would operate as a low resolution mapper for the night sky.

11.1 Particle Physics

Although it could sound like astronomy is the only application for Microwave Kinetic Inductance Detectors, many applications for such impressive detectors have been proposed for particle physics experiments.
CALDER (the Cryogenic wide-Area Light Detectors with Excellent Resolution) (117, 118) is an instrument proposed for rare event searches and deploys phonon-mediated MKIDs to detect Cherenkov radiation in TeO_2 crystals. Its main scientific purpose is to investigate whether neutrinos are Majorana particles and to investigate the deep nature of Dark Matter. Currently the CALDER collaborations is investigating the feasibility of using MKIDs as sensing elements (118).
HOLMES (119) is an experiment which aim is to measure the mass of neutrino in ^{163}Ho crystals (120). While it currently deploys Transition Edge Sensors, MKIDs are being developed as possible sensors for such an experiment (121) as they are easier to fabricate, would require a simpler readout electronics and eventually would achieve sub-eV energy resolution in the desired energy range.

MKIDs have been proposed as possible detectors for multiple applications in the search of Dark Matter Particles: WIMPS, Axions and Dark Photons.
Golwala et al. (122) pioneered the idea of MKIDs as dark matter detectors. The interaction in a massive absorber with dark matter particles would produce phonons that can then be detected with kinetic inductance detectors. The first proposed detectors would use Tantalum (Ta) absorbers and Aluminium MKIDs. This idea has been further expanded in 2020 by Colantoni et al (123). BullKID exploits 105 Si-voxels of the weight of $0.29\,g$ each as absorbers and MKIDs would be then fabricate on the backside of the wafer where the voxels are produced. The resonators would allow the identification of photons produced by the dark matter particles interacting in the silicon voxels.
Derenzo et al. (124) propose the coupling of MKIDs with scintillating elements such as CsI, NaI and GaAs. The detection of scintillation photons can result in lower backgrounds. MKIDs are especially suitable for this application as they are inherently energy resolving detectors (afterglow and phosphorescence events rejection) and are, for most practical purposes, effectively dark count free.
An MKID based experiment has been proposed to detect axions with masses in the range of $0,25 - 2,5$ eV (125, 126).

11.2 Material Science

Microwave Kinetic Inductance Detectors are excellent X-Ray detectors and have been proposed as detectors for synchrotron radiation. Ulbricht et al. (127) developed

Thermal Kinetic Inductance Detectors (TKIDs) for X-Ray imaging spectroscopy which have applications in both synchrotron spectroscopy and X-Ray astronomy with an energy resolution of ≈ 75 eV at energies of 5.9 keV. Using MKIDs as detector element in synchrotron beam lines allows to exploit their major advantages of energy resolution and their ability to be multiplexed to large arrays, and only having to deal with the disadvantage of requiring advanced cryogenics to cool them down to milli-Kelvin temperatures (128, 129, 130).

11.3 Security

MKIDs have been developed also for security applications. Passive GHZ and THz imaging cameras are being developed in Cardiff (131) , Glasgow (132), Rome (133), Groeningen (134) and Helsinki (135). MKIDs are extremely promising detectors, as they allow for the multiplexing of large arrays of fast detectors that are sensitive between 100 and 300 GHz. At such frequencies some materials that are be optically opaque become transparent. Passive security allows for airport passengers to be scanned while simply walking in front of a camera (131, 132, 133, 135).
Doyle et al. (131) in Cardiff developed a 350 GHz camera that operates at a frame rate of 2 Hz and a test run successfully detected objects inside a subject's coat including a wallet, an air pistol and some coins.
Hassel et al. (135) in Helsinki developed an imaging system that operates at a frequency band centred at 250 GHz and demonstrated the detection of an aluminium bar as well as plastic and paper hidden underneath a person's jacket.

11.4 Further Applications

Microwave Kinetic Inductance Detectors are a relatively new technology that has not been exploited to its fullest. Two applications that have been proposed but have not been discussed in the previous sections are the possibility of using polarisation sensitive MKIDs for plasma diagnostics as proposed by F. Mazzocchi (136). Also, MKIDs could be used as detectors in Quantum-Limited Atomic Force Microscopy where MKIDs would be used as strain detectors to monitor the resonant frequency of the cantilever as discussed by Baglioni et al. (137).

12 Future Work

Microwave Kinetic Inductance Detectors are very promising detectors for many applications in many fields of science, from astronomy to particle physics, dark matter detectors and even as X-Ray detectors for synchrotrons (40).
While some established instruments already deploy MKIDs, as single detectors or in arrays, as their sensing elements, the development and optimisation of superconducting resonators is still under progress.
As already discussed in this thesis, Section 2.3, the parameters that define the performance of a single photon resolving MKID array are the following:

- Fabrication Yield
- Energy resolution
- Quantum efficiency
- Responsivity

While the responsivity of a detector is easy to control by changing the thickness of the superconducting film, other parameters are not as easy to optimise and future work in the field has to tackle them in order to provide MKID arrays that can really be competitive with more established technologies.
I will address a few possible ways to improve the performance of Microwave Kinetic Inductance Detectors on each of those aspects.

12.1 Fabrication Yield

The fabrication yield of an MKIDs array is defined by the number of uniquely identifiable resonators as a fraction of the total number of resonators that were intended to be present on the array. In reality, a thorough analysis of the performance of each individual pixel can further reduce the yield if one defines it as the ratio between the number of pixels which meet specific energy resolution and noise requirements to the desired number of resonators in the array. Many factors account into the fabrication yield of an array, including fabrication defects and microscopic and macroscopic inhomogeneities in the superconducting films. These inhomogeneities are expected to be most significant when the superconducting film is not made of an elemental metal but is produced through reactive processes, and it is even more present in the case of sub-stoichiometric Titanium Nitride (TiN_x). Possible improvements in this direction include switching from a research-grade cleanroom to a professional cleanroom, and our work with the facilities at the Tyndall National Institute are a first step in this direction. Other improvements include further testing of multi-stacks of different superconducting films in order to achieve the desired critical temperature through proximity effect but relying on the high uniformity of elemental titanium and stoichiometric titanium nitride. The multilayers described in this thesis exhibited little to no macroscopic inhomogeneities with a difference in critical temperature between centre and edge of the wafer fully within our measurement accuracy of $20\,mK$.

Other attempts at improving the fabrication yield after the full fabrication of an array include a post-production trimming of the capacitor legs to tune the resonant frequency of the colliding resonators (82) and, as discussed in this thesis, the possibility of achieving the same retuning through a DC bias of the resonator (91). Further experiments would be required to deem the latter option as possible.

12.2 Energy Resolution

The energy resolution of a detector is a parameter that describes how sharp the response of said detector is when illuminated with perfectly monochromatic radiation. The higher the energy resolution, or what is somewhat its inverse, the resolving power, the better. Currently, the most MKIDs seem to exhibit moderate resolving powers of 10 to 15 and increasing this value is one of the biggest concerns in the community.

This thesis investigates what are the biggest limitations to the energy resolution of a kinetic inductance detector. The two main hindrances come from the noise introduced by the High Electron Mobility Transistor Amplifier and, of course, Fano noise with special consideration to hot phonon losses. Unfortunately not much can be done when it comes to push the Fano limit, but it seems that a phononic crystal or a suspended membrane can reduce the hot phonon losses resulting in a resolving power of about 50 (85). In this direction, the fabrication of the inductor on a Kaptiza resistance could produce the same benefits without the need to fabricate a suspended membrane. Two or more acoustically mismatched materials can be put together in order to confine phonons in one of the layers. The difference in vibrational properties in different materials effectively create a barrier so that when a phonon attempts to traverse the interface, it will scatter at the interface. The probability of transmission after scattering will depend on the available energy states on side 1 and side 2 of the interface.

Today HEMT Amplifiers are the best option in terms of gain and noise performance, and companies such as Low Noise Factory are actively working to push down the noise figure of these amplifiers. One other promising option, that might be still a few years down the line, involves using a parametric amplifier as described in (70) which exhibit a way lower noise temperature and a comparable gain.

12.3 Quantum Efficiency

The quantum efficiency of a detector represents the amount of photons detected as a fraction of the total number of photons that impinge on the detector. It is an inherent property of the material. Being most superconductors metallic, a rather high reflectivity is an issue, and while it is been thought to deposit anti-reflective coating on the sensitive surface of the detectors, it is also a common concern that this might reduce the quality factor of the resonators. In general, testing new materials and exploring their optical properties, with Granular Aluminium being one eminent example, might produce results in the desired direction.

12.4 Further Improvements

Further improvements on MKIDs would include the development of new readout systems which feature the new Xilinx Board RFSoC 2x2 and custom-made intermediate frequency boards that would reduce readout cost to about 1 euro per pixel.

Sapphire substrate could be used to deposit TiN/Ti/TiN multilayers, and might result in resonators with lower TLS noise as two level systems are less dominant in sapphire than in silicon.

12.5 Granular Aluminium

One very interesting material for MKIDs is Granular Aluminium (grAl). Granular Aluminium is made of nanometric sized granules of aluminium coupled together through aluminium oxide. The critical temperature of the film depends on the size of the grains and this parameter can be controlled during the deposition process. GrAl is well known for its outstanding kinetic inductance and very long particle recombination times, as of today its optical properties have not been measured yet and could result in a material with better quantum efficiency than other superconductors, especially Al and Ti which are very reflective.

12.6 Mixing up the technologies

One further route that is worth pursuing relies on the TiN_X deposited in CRANN. The Trifolium Dubium is capable of depositing a highly uniform layer of TiN_x with a critical temperature of ≈ 2.9K. The high uniformity of this layer combined with a lower critical temperature than that of stoichiometric TiN, could be employed in multilayer stackings. The advantage of a TiN_x/Ti/TiN_x multilayer over a TiN/Ti/TiN multilayer resides in a critical temperature that is easier to control around $800\,mK$, a reduced carrier density and therefore higher kinetic inductance, and the uniformity of trilayers.

12.7 Reflecitivity below Tc

One final thing that might be worth trying out, is to measure the optical properties, such as reflectivity, of the same films at thermal equilibrium at room temperature and below its critical temperature. When discussing the reflectivity of thin films in the community, it is often referred to the room temperature reflectivity of the bulk material. The opening of the superconducting band gap when the thin film is cooled down below its critical temperature might influence the adsorption properties of the film and this would be an interesting information to provide to the MKIDs community.

12.8 Elemental composition analysis

When working with sub-stoichiometric titanium nitride films, the best way to uniquely identify a film is through the critical temperature of the film and the ratio of gases in the atmosphere of the deposition chamber. Unfortunately, the latter parameters are instrument dependent; two different sputter systems will produce films with completely different critical temperatures when running a deposition with the same gas ratio. One option that is still to be explored is the possibility of using Energy Disperive X-Ray Spectroscopy to characterise the elemental composition of the thin film. If this technique were to be deemed fruitful, it would provide a way to compare film layers deposited in different tools and by different research groups. Furthermore, a broad scan on the whole chip would highlight both microscopic and macroscopic inhomogeneities giving way to the pre-visualisation of possible issues such as a reduced fabrication yield.

12.9 Resonator design automation

As previously discussed, Microwave Kinetic Inductance Detector arrays are known to only exhibit a moderate yield and only the best arrays reach a yield of ≈ 80%. In the process of designing the array, often only approximately a tenth of the resonators are designed and simulated. Then, by changing the length of the capacitor's fingers as predicted through linear interpolation, all the other resonators are designed and fabricated. Since the task of simulating each individual resonator in the array would require an incredible amount of man-hours, the practice of producing resonators through linear interpolation is widely accepted for test arrays and purely demonstration-purpose arrays. More recently, through the use of SONNET's parametric sweep, a non-linear fit to the design of the resonator can be performed to predict the resonator's placement in frequency space. Thankfully newer versions of SONNET allow the interfacing of its EM engine and design suite to MatLab through a library called SonnetLab. SonnetLab can run a Montecarlo-like simulation in order to produce a design that meets the required parameters such as resonance frequency and coupling quality factor. Unfortunately, programming MatLab for this task is not straightforward and the project of optimising the Montecarlo-like simulation by changing the geometries at play in the design to produce the design files for the resonators with the desired properties. Such a project would be rather intensive and would constitute for a masters project on its own.

Bibliography

[1] Julianne Dalcanton, Sara Seager, Suzanne Aigrain, Steve Battel, Niel Brandt, Charlie Conroy, Lee Feinberg, Suvi Gezari, Olivier Guyon, Walt Harris, Chris Hirata, John Mather, Marc Postman, Dave Redding, David Schiminovich, H. Philip Stahl, and Jason Tumlinson. From cosmic birth to living earths: The future of uvoir space astronomy, 2015.

[2] B. A. Mazin, S. R. Meeker, M. J. Strader, P. Szypryt, D. Marsden, J. C. van Eyken, G. E. Duggan, A. B. Walter, G. Ulbricht, M. Johnson, and et al. Arcons: A 2024 pixel optical through near-ir cryogenic imaging spectrophotometer. *Publications of the Astronomical Society of the Pacific*, 125 (933):1348–1361, Nov 2013. ISSN 1538-3873. doi: 10.1086/674013. URL `http://dx.doi.org/10.1086/674013`.

[3] Seth R. Meeker, Benjamin A. Mazin, Alex B. Walter, Paschal Strader, Neelay Fruitwala, Clint Bockstiegel, Paul Szypryt, Gerhard Ulbricht, Grégoire Coiffard, Bruce Bumble, Gustavo Cancelo, Ted Zmuda, Ken Treptow, Neal Wilcer, Giulia Collura, Rupert Dodkins, Isabel Lipartito, Nicholas Zobrist, Michael Bottom, J. Chris Shelton, Dimitri Mawet, Julian C. van Eyken, Gautam Vasisht, and Eugene Serabyn. DARKNESS: A microwave kinetic inductance detector integral field spectrograph for high-contrast astronomy. *Publications of the Astronomical Society of the Pacific*, 130(988):065001, apr 2018. doi: 10.1088/1538-3873/aab5e7. URL `https://doi.org/10.1088%2F1538-3873%2Faab5e7`.

[4] G. Grosso and G.P. Parravicini. *Solid State Physics*. Elsevier Science, 2000. ISBN 9780080481029. URL `https://books.google.ie/books?id=L5RrQbbvWn8C`.

[5] Daijiro Yoshioka. Meissner effect cannot be explained classically. 03 2012.

[6] S Doerner, A Kuzmin, K Graf, I Charaev, S Wuensch, and M Siegel. Compact microwave kinetic inductance nanowire galvanometer for cryogenic detectors at 4.2 k. *Journal of Physics Communications*, 2(2):025016, feb 2018. doi:

10.1088/2399-6528/aaaa8e. URL
`https://doi.org/10.1088%2F2399-6528%2Faaaa8e`.

[7] Seth R. Meeker. *DARKNESS: The First Microwave Kinetic Inductance Detector Integral Field Spectrograph for Exoplanet Imaging*. PhD thesis, University of California, Santa Barbara, 2017.

[8] Eoin Baldwin. *MKIDS readout ?* PhD thesis, Trinity college Dublin, School of Physics, 2022.

[9] M Fabian, Elfed Lewis, Thomas Newe, and Steffen Lochmann. Optical fibre cavity for ring-down experiments with low coupling losses. *Measurement Science and Technology*, 21:094034, 07 2010. doi: 10.1088/0957-0233/21/9/094034.

[10] M. A. Bilokur, Angus Gentle, Markus Tobias Arnold, Michael B. Cortie, and George Baxter Smith. Optical properties of refractory tin , aln and (ti , al) n coatings. 2015.

[11] P. Szypryt, S. R. Meeker, G. Coiffard, N. Fruitwala, B. Bumble, G. Ulbricht, A. B. Walter, M. Daal, C. Bockstiegel, G. Collura, and et al. Large-format platinum silicide microwave kinetic inductance detectors for optical to near-ir astronomy. *Optics Express*, 25(21):25894, Oct 2017. ISSN 1094-4087. doi: 10.1364/oe.25.025894. URL `http://dx.doi.org/10.1364/OE.25.025894`.

[12] Benjamin A. Mazin. *Microwave Kinetic Inductance Detectors*. California Institute of Technology, 2004.

[13] Michael R. Vissers, Jiansong Gao, Jeffrey S. Kline, Martin Sandberg, Martin P. Weides, David S. Wisbey, and David P. Pappas. Characterization and in-situ monitoring of sub-stoichiometric adjustable superconducting critical temperature titanium nitride growth. *Thin Solid Films*, 548:485–488, Dec 2013. ISSN 0040-6090. doi: 10.1016/j.tsf.2013.07.046. URL
`http://dx.doi.org/10.1016/j.tsf.2013.07.046`.

[14] M Faverzani, E Ferri, A Giachero, C Giordano, B Margesin, R Mezzena, A Nucciotti, and A Puiu. Characterization of the low temperature behavior of thin titanium/titanium nitride multilayer films. *Superconductor Science and Technology*, 33(4):045009, feb 2020. doi: 10.1088/1361-6668/ab7435. URL
`https://doi.org/10.1088%2F1361-6668%2Fab7435`.

[15] Michael R. Vissers, Jiansong Gao, Martin Sandberg, Shannon M. Duff, David S. Wisbey, Kent D. Irwin, and David P. Pappas. Proximity-coupled ti/tin multilayers for use in kinetic inductance detectors. *Applied Physics Letters*, 102(23):232603, 2013. doi: 10.1063/1.4804286. URL
`https://doi.org/10.1063/1.4804286`.

[16] W. Guo, X. Liu, Y. Wang, Q. Wei, L. F. Wei, J. Hubmayr, J. Fowler, J. Ullom, L. Vale, M. R. Vissers, and et al. Counting near infrared photons with microwave kinetic inductance detectors. *Applied Physics Letters*, 110(21): 212601, May 2017. ISSN 1077-3118. doi: 10.1063/1.4984134. URL `http://dx.doi.org/10.1063/1.4984134`.

[17] Benjamin A. Mazin, Jeb Bailey, Jo Bartlett, Clint Bockstiegel, Bruce Bumble, Gregoire Coiffard, Thayne Currie, Miguel Daal, Kristina Davis, Rupert Dodkins, Neelay Fruitwala, Nemanja Jovanovic, Isabel Lipartito, Julien Lozi, Jared Males, Dimitri Mawet, Seth Meeker, Kieran O'Brien, Michael Rich, Jenny Smith, Sarah Steiger, Noah Swimmer, Alex Walter, Nick Zobrist, and Jonas Zmuidzinas. Optical and near-ir microwave kinetic inductance detectors (mkids) in the 2020s, 2019.

[18] Aditya S. Kher. *Superconducting Nonlinear Kinetic Inductance Devices*. PhD thesis, California Institute of Technology, 2016.

[19] Asahi spectra ysc1100 transmission data, Feb 2022. URL `https://www.asahi-spectra.com/opticalfilters/detail.asp?key=YSC1100`.

[20] Thorlabs bk7 transmission data, Feb 2022. URL `https://www.thorlabs.com/newgrouppage9.cfm?objectgroup_id=1117`.

[21] A. Einstein. Über einen die erzeugung und verwandlung des lichtes betreffenden heuristischen gesichtspunkt. *Annalen der Physik*, 322(6):132–148, 1905. doi: 10.1002/andp.19053220607. URL `https://onlinelibrary.wiley.com/doi/abs/10.1002/andp.19053220607`.

[22] Ove Christensen. Quantum efficiency of the internal photoelectric effect in silicon and germanium. *Journal of Applied Physics*, 47(2):689–695, 1976. doi: 10.1063/1.322635. URL `https://doi.org/10.1063/1.322635`.

[23] Christopher W. Walter. The super-kamiokande experiment. *Neutrino Oscillations*, page 19–43, Mar 2008. doi: 10.1142/9789812771971_0002. URL `http://dx.doi.org/10.1142/9789812771971_0002`.

[24] The Pierre Auger Collaboration, A. Aab, P. Abreu, M. Aglietta, E. J. Ahn, I. Al Samarai, I. F. M. Albuquerque, I. Allekotte, P. Allison, A. Almela, J. Alvarez Castillo, J. Alvarez-Muñiz, R. Alves Batista, M. Ambrosio, A. Aminaei, L. Anchordoqui, S. Andringa, C. Aramo, F. Arqueros, N. Arsene, H. Asorey, P. Assis, J. Aublin, M. Ave, M. Avenier, G. Avila, N. Awal, A. M. Badescu, K. B. Barber, J. Bäuml, C. Baus, J. J. Beatty, K. H. Becker, J. A. Bellido, C. Berat, M. E. Bertaina, X. Bertou, P. L. Biermann, P. Billoir, S. G. Blaess, A. Blanco, M. Blanco, J. Blazek, C. Bleve, H. Blümer, M. Boháčová,

D. Boncioli, C. Bonifazi, N. Borodai, J. Brack, I. Brancus, A. Bridgeman, P. Brogueira, W. C. Brown, P. Buchholz, A. Bueno, S. Buitink, M. Buscemi, K. S. Caballero-Mora, B. Caccianiga, L. Caccianiga, M. Candusso, L. Caramete, R. Caruso, A. Castellina, G. Cataldi, L. Cazon, R. Cester, A. G. Chavez, A. Chiavassa, J. A. Chinellato, J. Chudoba, M. Cilmo, R. W. Clay, G. Cocciolo, R. Colalillo, A. Coleman, L. Collica, M. R. Coluccia, R. Conceição, F. Contreras, M. J. Cooper, A. Cordier, S. Coutu, C. E. Covault, J. Cronin, R. Dallier, B. Daniel, S. Dasso, K. Daumiller, B. R. Dawson, R. M. de Almeida, S. J. de Jong, G. De Mauro, J. R. T. de Mello Neto, I. De Mitri, J. de Oliveira, V. de Souza, L. del Peral, O. Deligny, H. Dembinski, N. Dhital, C. Di Giulio, A. Di Matteo, J. C. Diaz, M. L. Díaz Castro, F. Diogo, C. Dobrigkeit, W. Docters, J. C. D'Olivo, A. Dorofeev, Q. Dorosti Hasankiadeh, M. T. Dova, J. Ebr, R. Engel, M. Erdmann, M. Erfani, C. O. Escobar, J. Espadanal, A. Etchegoyen, H. Falcke, K. Fang, G. Farrar, A. C. Fauth, N. Fazzini, A. P. Ferguson, M. Fernandes, B. Fick, J. M. Figueira, A. Filevich, A. Filipčič, B. D. Fox, O. Fratu, M. M. Freire, B. Fuchs, T. Fujii, B. García, D. Garcia-Pinto, F. Gate, H. Gemmeke, A. Gherghel-Lascu, P. L. Ghia, U. Giaccari, M. Giammarchi, M. Giller, D. Głas, C. Glaser, H. Glass, G. Golup, M. Gómez Berisso, P. F. Gómez Vitale, N. González, B. Gookin, J. Gordon, A. Gorgi, P. Gorham, P. Gouffon, N. Griffith, A. F. Grillo, T. D. Grubb, F. Guarino, G. P. Guedes, M. R. Hampel, P. Hansen, D. Harari, T. A. Harrison, S. Hartmann, J. L. Harton, A. Haungs, T. Hebbeker, D. Heck, P. Heimann, N. Hemery, A. E. Herve, G. C. Hill, C. Hojvat, N. Hollon, E. Holt, P. Homola, J. R. Hörandel, P. Horvath, M. Hrabovský, D. Huber, T. Huege, A. Insolia, P. G. Isar, I. Jandt, S. Jansen, C. Jarne, J. A. Johnsen, M. Josebachuili, A. Kääpä, O. Kambeitz, K. H. Kampert, P. Kasper, I. Katkov, B. Kégl, B. Keilhauer, A. Keivani, E. Kemp, R. M. Kieckhafer, H. O. Klages, M. Kleifges, J. Kleinfeller, R. Krause, N. Krohm, O. Krömer, D. Kuempel, G. Kukec Mezek, N. Kunka, D. LaHurd, L. Latronico, R. Lauer, M. Lauscher, P. Lautridou, S. Le Coz, D. Lebrun, P. Lebrun, M. A. Leigui de Oliveira, A. Letessier-Selvon, I. Lhenry-Yvon, K. Link, L. Lopes, R. López, A. López Casado, K. Louedec, L. Lu, A. Lucero, M. Malacari, S. Maldera, M. Mallamaci, J. Maller, D. Mandat, P. Mantsch, A. G. Mariazzi, V. Marin, I. C. Mariş, G. Marsella, D. Martello, L. Martin, H. Martinez, O. Martínez Bravo, D. Martraire, J. J. Masías Meza, H. J. Mathes, S. Mathys, J. Matthews, J. A. J. Matthews, G. Matthiae, D. Maurizio, E. Mayotte, P. O. Mazur, C. Medina, G. Medina-Tanco, R. Meissner, V. B. B. Mello, D. Melo, A. Menshikov, S. Messina, R. Meyhandan, M. I. Micheletti, L. Middendorf, I. A. Minaya, L. Miramonti, B. Mitrica, L. Molina-Bueno, S. Mollerach, F. Montanet, C. Morello, M. Mostafá, C. A. Moura, M. A. Muller, G. Müller,

S. Müller, R. Mussa, G. Navarra, S. Navas, P. Necesal, L. Nellen, A. Nelles, J. Neuser, P. H. Nguyen, M. Niculescu-Oglinzanu, M. Niechciol, L. Niemietz, T. Niggemann, D. Nitz, D. Nosek, V. Novotny, L. Nožka, L. Ochilo, F. Oikonomou, A. Olinto, N. Pacheco, D. Pakk Selmi-Dei, M. Palatka, J. Pallotta, P. Papenbreer, G. Parente, A. Parra, T. Paul, M. Pech, J. Pekala, R. Pelayo, I. M. Pepe, L. Perrone, E. Petermann, C. Peters, S. Petrera, Y. Petrov, J. Phuntsok, R. Piegaia, T. Pierog, P. Pieroni, M. Pimenta, V. Pirronello, M. Platino, M. Plum, A. Porcelli, C. Porowski, R. R. Prado, P. Privitera, M. Prouza, V. Purrello, E. J. Quel, S. Querchfeld, S. Quinn, J. Rautenberg, O. Ravel, D. Ravignani, D. Reinert, B. Revenu, J. Ridky, S. Riggi, M. Risse, P. Ristori, V. Rizi, W. Rodrigues de Carvalho, G. Rodriguez Fernandez, J. Rodriguez Rojo, M. D. Rodríguez-Frías, D. Rogozin, J. Rosado, M. Roth, E. Roulet, A. C. Rovero, S. J. Saffi, A. Saftoiu, F. Salamida, H. Salazar, A. Saleh, F. Salesa Greus, G. Salina, F. Sánchez, P. Sanchez-Lucas, E. Santos, E. M. Santos, F. Sarazin, B. Sarkar, R. Sarmento, R. Sato, C. Scarso, M. Schauer, V. Scherini, H. Schieler, D. Schmidt, O. Scholten, H. Schoorlemmer, P. Schovánek, F. G. Schröder, A. Schulz, J. Schulz, J. Schumacher, S. J. Sciutto, A. Segreto, M. Settimo, A. Shadkam, R. C. Shellard, I. Sidelnik, G. Sigl, O. Sima, A. Śmiałkowski, R. Šmída, G. R. Snow, P. Sommers, J. Sorokin, R. Squartini, Y. N. Srivastava, D. Stanca, S. Stanič, J. Stapleton, J. Stasielak, M. Stephan, A. Stutz, F. Suarez, T. Suomijärvi, A. D. Supanitsky, M. S. Sutherland, J. Swain, Z. Szadkowski, O. A. Taborda, A. Tapia, A. Tepe, V. M. Theodoro, C. Timmermans, C. J. Todero Peixoto, G. Toma, L. Tomankova, B. Tomé, A. Tonachini, G. Torralba Elipe, D. Torres Machado, P. Travnicek, M. Trini, R. Ulrich, M. Unger, M. Urban, J. F. Valdés Galicia, I. Valiño, L. Valore, G. van Aar, P. van Bodegom, A. M. van den Berg, S. van Velzen, A. van Vliet, E. Varela, B. Vargas Cárdenas, G. Varner, R. Vasquez, J. R. Vázquez, R. A. Vázquez, D. Veberič, V. Verzi, J. Vicha, M. Videla, L. Villaseñor, B. Vlcek, S. Vorobiov, H. Wahlberg, O. Wainberg, D. Walz, A. A. Watson, M. Weber, K. Weidenhaupt, A. Weindl, F. Werner, A. Widom, L. Wiencke, H. Wilczyński, T. Winchen, D. Wittkowski, B. Wundheiler, S. Wykes, L. Yang, T. Yapici, A. Yushkov, E. Zas, D. Zavrtanik, M. Zavrtanik, A. Zepeda, Y. Zhu, B. Zimmermann, M. Ziolkowski, Z. Zong, and F. Zuccarello. The pierre auger observatory upgrade - preliminary design report, 2016.

[25] D. S. Leckrone, E. S. Cheng, L. D. Feinberg, J. T. Trauger, F. D. Macchetto, and J. W. MacKenty. Wide Field Camera 3 (WFC3) - A Facility Instrument For The Hubble Space Telescope. In *American Astronomical Society Meeting Abstracts #192*, volume 192 of *American Astronomical Society Meeting Abstracts*, page 35.08, May 1998.

[26] M. Actis, G. Agnetta, F. Aharonian, A. Akhperjanian, J. Aleksić, E. Aliu, D. Allan, I. Allekotte, F. Antico, and et al. Design concepts for the cherenkov telescope array cta: an advanced facility for ground-based high-energy gamma-ray astronomy. *Experimental Astronomy*, 32(3):193–316, Nov 2011. ISSN 1572-9508. doi: 10.1007/s10686-011-9247-0. URL `http://dx.doi.org/10.1007/s10686-011-9247-0`.

[27] Pilbratt, G. L., Riedinger, J. R., Passvogel, T., Crone, G., Doyle, D., Gageur, U., Heras, A. M., Jewell, C., Metcalfe, L., Ott, S., and Schmidt, M. Herschel space observatory* - an esa facility for far-infrared and submillimetre astronomy. *A&A*, 518:L1, 2010. doi: 10.1051/0004-6361/201014759. URL `https://doi.org/10.1051/0004-6361/201014759`.

[28] W. S. Holland, D. Bintley, E. L. Chapin, A. Chrysostomou, G. R. Davis, J. T. Dempsey, W. D. Duncan, M. Fich, P. Friberg, M. Halpern, and et al. Scuba-2: the 10 000 pixel bolometer camera on the james clerk maxwell telescope. *Monthly Notices of the Royal Astronomical Society*, 430(4):2513–2533, Mar 2013. ISSN 0035-8711. doi: 10.1093/mnras/sts612. URL `http://dx.doi.org/10.1093/mnras/sts612`.

[29] C. Arnaboldi, F. Avignone, M. Balata, M. Barucci, J. Beeman, C. Brofferio, C. Bucci, S. Capelli, L. Carbone, S. Cebrian, O. Cremonesi, R. J. Creswick, H. A. Farach, E. Fiorini, G. Frossati, A. Giuliani, E. E. Haller, I. G. Irastorza, R. J. McDonald, A. Morales, E. B. Norman, A. Nucciotti, V. Palmieri, M. Pavan, M. Pedretti, G. Pessina, S. Pirro, C. Pobes, E. Previtali, A. R. Smith, M. Vanzini, G. Ventura, A. de Waard, and L. Zanotti. The cuore experiment. *AIP Conference Proceedings*, 605(1):469–472, 2002. doi: 10.1063/1.1457688. URL `https://aip.scitation.org/doi/abs/10.1063/1.1457688`.

[30] D. H. Andrews, W. F. Brucksch, W. T. Ziegler, and E. R. Blanchard. Attenuated superconductors i. for measuring infra-red radiation. *Review of Scientific Instruments*, 13(7):281–292, 1942. doi: 10.1063/1.1770037. URL `https://doi.org/10.1063/1.1770037`.

[31] Jason R. Stevens, Nicholas F. Cothard, Eve M. Vavagiakis, Aamir Ali, Kam Arnold, Jason E. Austermann, Steve K. Choi, Bradley J. Dober, Cody Duell, Shannon M. Duff, and et al. Characterization of transition edge sensors for the simons observatory. *Journal of Low Temperature Physics*, Feb 2020. ISSN 1573-7357. doi: 10.1007/s10909-020-02375-9. URL `http://dx.doi.org/10.1007/s10909-020-02375-9`.

[32] Chandra M Natarajan, Michael G Tanner, and Robert H Hadfield. Superconducting nanowire single-photon detectors: physics and applications.

Superconductor Science and Technology, 25(6):063001, apr 2012. doi: 10.1088/0953-2048/25/6/063001. URL `https://doi.org/10.1088%2F0953-2048%2F25%2F6%2F063001`.

[33] Peter K. Day, Henry G. LeDuc, Benjamin A. Mazin, Anastasios Vayonakis, and Jonas Zmuidzinas. A broadband superconducting detector suitable for use in large arrays. *Nature*, 425(6960):817–821, 2003. ISSN 00280836. doi: 10.1038/nature02037.

[34] G. Tinetti, P. Drossart, P. Eccleston, P. Hartogh, A. Heske, J. Leconte, G. Micela, M. Ollivier, G. Pilbratt, L. Puig, D. Turrini, B. Vandenbussche, P. Wolkenberg, E. Pascale, J.-P. Beaulieu, M. Güdel, M. Min, M. Rataj, T. Ray, I. Ribas, J. Barstow, N. Bowles, A. Coustenis, V. Coudé du Foresto, L. Decin, T. Encrenaz, F. Forget, M Friswell, M. Griffin, P. O. Lagage, P. Malaguti, A. Moneti, J. C. Morales, E. Pace, M. Rocchetto, S. Sarkar, F. Selsis, W. Taylor, J. Tennyson, O. Venot, I. P. Waldmann, G. Wright, T. Zingales, and M. R. Zapatero-Osorio. The science of ARIEL (Atmospheric Remote-sensing Infrared Exoplanet Large-survey). In Howard A. MacEwen, Giovanni G. Fazio, Makenzie Lystrup, Natalie Batalha, Nicholas Siegler, and Edward C. Tong, editors, *Space Telescopes and Instrumentation 2016: Optical, Infrared, and Millimeter Wave*, volume 9904, pages 658 – 667. International Society for Optics and Photonics, SPIE, 2016. doi: 10.1117/12.2232370. URL `https://doi.org/10.1117/12.2232370`.

[35] The LUVOIR Team. The luvoir mission concept study final report, 2019.

[36] B. Scott Gaudi, Sara Seager, Bertrand Mennesson, Alina Kiessling, Keith Warfield, Kerri Cahoy, John T. Clarke, Shawn Domagal-Goldman, Lee Feinberg, Olivier Guyon, Jeremy Kasdin, Dimitri Mawet, Peter Plavchan, Tyler Robinson, Leslie Rogers, Paul Scowen, Rachel Somerville, Karl Stapelfeldt, Christopher Stark, Daniel Stern, Margaret Turnbull, Rashied Amini, Gary Kuan, Stefan Martin, Rhonda Morgan, David Redding, H. Philip Stahl, Ryan Webb, Oscar Alvarez-Salazar, William L. Arnold, Manan Arya, Bala Balasubramanian, Mike Baysinger, Ray Bell, Chris Below, Jonathan Benson, Lindsey Blais, Jeff Booth, Robert Bourgeois, Case Bradford, Alden Brewer, Thomas Brooks, Eric Cady, Mary Caldwell, Rob Calvet, Steven Carr, Derek Chan, Velibor Cormarkovic, Keith Coste, Charlie Cox, Rolf Danner, Jacqueline Davis, Larry Dewell, Lisa Dorsett, Daniel Dunn, Matthew East, Michael Effinger, Ron Eng, Greg Freebury, Jay Garcia, Jonathan Gaskin, Suzan Greene, John Hennessy, Evan Hilgemann, Brad Hood, Wolfgang Holota, Scott Howe, Pei Huang, Tony Hull, Ron Hunt, Kevin Hurd, Sandra Johnson, Andrew Kissil, Brent Knight, Daniel Kolenz, Oliver Kraus, John Krist, Mary Li, Doug Lisman, Milan Mandic, John Mann, Luis Marchen, Colleen Marrese-Reading, Jonathan

McCready, Jim McGown, Jessica Missun, Andrew Miyaguchi, Bradley Moore, Bijan Nemati, Shouleh Nikzad, Joel Nissen, Megan Novicki, Todd Perrine, Claudia Pineda, Otto Polanco, Dustin Putnam, Atif Qureshi, Michael Richards, A. J. Eldorado Riggs, Michael Rodgers, Mike Rud, Navtej Saini, Dan Scalisi, Dan Scharf, Kevin Schulz, Gene Serabyn, Norbert Sigrist, Glory Sikkia, Andrew Singleton, Stuart Shaklan, Scott Smith, Bart Southerd, Mark Stahl, John Steeves, Brian Sturges, Chris Sullivan, Hao Tang, Neil Taras, Jonathan Tesch, Melissa Therrell, Howard Tseng, Marty Valente, David Van Buren, Juan Villalvazo, Steve Warwick, David Webb, Thomas Westerhoff, Rush Wofford, Gordon Wu, Jahning Woo, Milana Wood, John Ziemer, Giada Arney, Jay Anderson, Jesús Maíz-Apellániz, James Bartlett, Ruslan Belikov, Eduardo Bendek, Brad Cenko, Ewan Douglas, Shannon Dulz, Chris Evans, Virginie Faramaz, Y. Katherina Feng, Harry Ferguson, Kate Follette, Saavik Ford, Miriam García, Marla Geha, Dawn Gelino, Ylva Götberg, Sergi Hildebrandt, Renyu Hu, Knud Jahnke, Grant Kennedy, Laura Kreidberg, Andrea Isella, Eric Lopez, Franck Marchis, Lucas Macri, Mark Marley, William Matzko, Johan Mazoyer, Stephan McCandliss, Tiffany Meshkat, Christoph Mordasini, Patrick Morris, Eric Nielsen, Patrick Newman, Erik Petigura, Marc Postman, Amy Reines, Aki Roberge, Ian Roederer, Garreth Ruane, Edouard Schwieterman, Dan Sirbu, Christopher Spalding, Harry Teplitz, Jason Tumlinson, Neal Turner, Jessica Werk, Aida Wofford, Mark Wyatt, Amber Young, and Rob Zellem. The habitable exoplanet observatory (habex) mission concept study final report, 2020.

[37] Su-Shu Huang. The problem of life in the universe and the mode of star formation. *Publications of the Astronomical Society of the Pacific*, 71:421, oct 1959. doi: 10.1086/127417. URL `https://doi.org/10.1086%2F127417`.

[38] S. Udry, C. Lovis, F. Bouchy, A. Collier Cameron, T. Henning, M. Mayor, F. Pepe, N. Piskunov, D. Pollacco, D. Queloz, A. Quirrenbach, H. Rauer, R. Rebolo, N. C. Santos, I. Snellen, and F. Zerbi. Exoplanet Science with the European Extremely Large Telescope. The Case for Visible and Near-IR Spectroscopy at High Resolution. *arXiv e-prints*, art. arXiv:1412.1048, November 2014.

[39] Jonas Zmuidzinas. Superconducting microresonators: Physics and applications. *Annual Review of Condensed Matter Physics*, 3(1):169–214, 2012. doi: 10.1146/annurev-conmatphys-020911-125022. URL `https://doi.org/10.1146/annurev-conmatphys-020911-125022`.

[40] Gerhard Ulbricht, Mario De Lucia, and Eoin Baldwin. Applications for microwave kinetic induction detectors in advanced instrumentation. *Applied*

Sciences, 11(6):2671, Mar 2021. ISSN 2076-3417. doi: 10.3390/app11062671. URL `http://dx.doi.org/10.3390/app11062671`.

[41] J. Bardeen, L. N. Cooper, and J. R. Schrieffer. Theory of superconductivity. *Phys. Rev.*, 108:1175–1204, Dec 1957. doi: 10.1103/PhysRev.108.1175. URL `https://link.aps.org/doi/10.1103/PhysRev.108.1175`.

[42] Neil W. Ashcroft and N. David Mermin. *Solid State Physics*. Cengage Learning, 1976.

[43] Michael Tinkham. *Introduction to Superconductivity*. Dover Publications, 2 edition, June 2004. ISBN 0486435032. URL `http://www.worldcat.org/isbn/0486435032`.

[44] R. Meservey and P. M. Tedrow. Measurements of the kinetic inductance of superconducting linear structures. *Journal of Applied Physics*, 40(5):2028–2034, 1969. doi: 10.1063/1.1657905. URL `https://doi.org/10.1063/1.1657905`.

[45] A. B. Pippard and William Lawrence Bragg. Field variation of the superconducting penetration depth. *Proceedings of the Royal Society of London. Series A. Mathematical and Physical Sciences*, 203(1073):210–223, 1950. doi: 10.1098/rspa.1950.0135. URL `https://royalsocietypublishing.org/doi/abs/10.1098/rspa.1950.0135`.

[46] Alfred Brian Pippard and William Lawrence Bragg. An experimental and theoretical study of the relation between magnetic field and current in a superconductor. *Proceedings of the Royal Society of London. Series A. Mathematical and Physical Sciences*, 216(1127):547–568, 1953. doi: 10.1098/rspa.1953.0040. URL `https://royalsocietypublishing.org/doi/abs/10.1098/rspa.1953.0040`.

[47] M. R. Vissers, J. Hubmayr, M. Sandberg, S. Chaudhuri, C. Bockstiegel, and J. Gao. Frequency-tunable superconducting resonators via nonlinear kinetic inductance. *Applied Physics Letters*, 107(6):062601, 2015. doi: 10.1063/1.4927444. URL `https://doi.org/10.1063/1.4927444`.

[48] A. G. Kozorezov, A. F. Volkov, J. K. Wigmore, A. Peacock, A. Poelaert, and R. den Hartog. Quasiparticle-phonon downconversion in nonequilibrium superconductors. *Phys. Rev. B*, 61:11807–11819, May 2000. doi: 10.1103/PhysRevB.61.11807. URL `https://link.aps.org/doi/10.1103/PhysRevB.61.11807`.

[49] D. C. Mattis and J. Bardeen. Theory of the anomalous skin effect in normal and superconducting metals. *Phys. Rev.*, 111:412–417, Jul 1958. doi:

10.1103/PhysRev.111.412. URL
`https://link.aps.org/doi/10.1103/PhysRev.111.412`.

[50] Lukas Grünhaupt, Nataliya Maleeva, Sebastian T. Skacel, Martino Calvo, Florence Levy-Bertrand, Alexey V. Ustinov, Hannes Rotzinger, Alessandro Monfardini, Gianluigi Catelani, and Ioan M. Pop. Loss mechanisms and quasiparticle dynamics in superconducting microwave resonators made of thin-film granular aluminum. *Physical Review Letters*, 121(11), Sep 2018. ISSN 1079-7114. doi: 10.1103/physrevlett.121.117001. URL
`http://dx.doi.org/10.1103/PhysRevLett.121.117001`.

[51] F. Levy-Bertrand, T. Klein, T. Grenet, O. Dupré, A. Benoît, A. Bideaud, O. Bourrion, M. Calvo, A. Catalano, A. Gomez, and et al. Electrodynamics of granular aluminum from superconductor to insulator: Observation of collective superconducting modes. *Physical Review B*, 99(9), Mar 2019. ISSN 2469-9969. doi: 10.1103/physrevb.99.094506. URL
`http://dx.doi.org/10.1103/PhysRevB.99.094506`.

[52] F. Caspers. Rf engineering basic concepts: S-parameters, 2012.

[53] Jiansong Gao. *The Physics of Superconducting Microwave Resonators*. California Institute of Technology, 2008. doi: 10.7907/RAT0-VM75.

[54] Low Noise Technology. *LNF-LNC4_8C s/n 395Z date = November 2016, language = English,*.

[55] Alex Walter, Benjamin B. Mazin, Clint Bockstiegel, Neelay Fruitwala, Paul Szypryt, Isabel Lipartito, Seth Meeker, Nicholas Zobrist, Giulia Collura, Grégoire Coiffard, Paschal Strader, Olivier Guyon, Julien Lozi, and Nemanja Jovanovic. MEC: the MKID exoplanet camera for high contrast astronomy at Subaru (Conference Presentation). In Christopher J. Evans, Luc Simard, and Hideki Takami, editors, *Ground-based and Airborne Instrumentation for Astronomy VII*, volume 10702. International Society for Optics and Photonics, SPIE, 2018. doi: 10.1117/12.2311586. URL
`https://doi.org/10.1117/12.2311586`.

[56] C. E. Shannon. Communication in the presence of noise. *Proceedings of the IRE*, 37(1):10–21, 1949.

[57] H. Nyquist. Certain topics in telegraph transmission theory. *Transactions of the American Institute of Electrical Engineers*, 47(2):617–644, 1928.

[58] Benjamin A. Mazin. Microwave kinetic inductance detectors: The first decade. *AIP Conference Proceedings*, 1185(1):135–142, 2009. doi: 10.1063/1.3292300. URL `https://aip.scitation.org/doi/abs/10.1063/1.3292300`.

[59] Joris van Rantwijk, Martin Grim, Dennis van Loon, Stephen Yates, Andrey Baryshev, and Jochem Baselmans. Multiplexed readout for 1000-pixel arrays of microwave kinetic inductance detectors. *IEEE Transactions on Microwave Theory and Techniques*, 64(6):1876–1883, Jun 2016. ISSN 1557-9670. doi: 10.1109/tmtt.2016.2544303. URL `http://dx.doi.org/10.1109/TMTT.2016.2544303`.

[60] J. C. van Eyken, M. J. Strader, A. B. Walter, S. R. Meeker, P. Szypryt, C. Stoughton, K. O'Brien, D. Marsden, N. K. Rice, Y. Lin, and et al. The arcons pipeline: Data reduction for mkid arrays. *The Astrophysical Journal Supplement Series*, 219(1):14, Jul 2015. ISSN 1538-4365. doi: 10.1088/0067-0049/219/1/14. URL `http://dx.doi.org/10.1088/0067-0049/219/1/14`.

[61] G. Coiffard, K.-F. Schuster, E. F. C. Driessen, S. Pignard, M. Calvo, A. Catalano, J. Goupy, and A. Monfardini. Uniform non-stoichiometric titanium nitride thin films for improved kinetic inductance detector arrays. *Journal of Low Temperature Physics*, 184(3-4):654–660, Jan 2016. ISSN 1573-7357. doi: 10.1007/s10909-016-1489-9. URL `http://dx.doi.org/10.1007/s10909-016-1489-9`.

[62] R. L. Falge. Superconductivity of titanium. *Phys. Rev. Lett.*, 11:248–250, Sep 1963. doi: 10.1103/PhysRevLett.11.248. URL `https://link.aps.org/doi/10.1103/PhysRevLett.11.248`.

[63] N.A. Saveskul, N.A. Titova, E.M. Baeva, A.V. Semenov, A.V. Lubenchenko, S. Saha, H. Reddy, S.I. Bogdanov, E.E. Marinero, V.M. Shalaev, A. Boltasseva, V.S. Khrapai, A.I. Kardakova, and G.N. Goltsman. Superconductivity behavior in epitaxial tin films points to surface magnetic disorder. *Physical Review Applied*, 12(5), Nov 2019. ISSN 2331-7019. doi: 10.1103/physrevapplied.12.054001. URL `http://dx.doi.org/10.1103/PhysRevApplied.12.054001`.

[64] W. Spengler, R. Kaiser, A. N. Christensen, and G. Müller-Vogt. Raman scattering, superconductivity, and phonon density of states of stoichiometric and nonstoichiometric tin. *Phys. Rev. B*, 17:1095–1101, Feb 1978. doi: 10.1103/PhysRevB.17.1095. URL `https://link.aps.org/doi/10.1103/PhysRevB.17.1095`.

[65] Henry G. Leduc, Bruce Bumble, Peter K. Day, Byeong Ho Eom, Jiansong Gao, Sunil Golwala, Benjamin A. Mazin, Sean McHugh, Andrew Merrill, David C. Moore, Omid Noroozian, Anthony D. Turner, and Jonas Zmuidzinas. Titanium nitride films for ultrasensitive microresonator detectors. *Applied Physics*

Letters, 97(10):102509, 2010. doi: 10.1063/1.3480420. URL `https://doi.org/10.1063/1.3480420`.

[66] Plamen Kamenov, Wen-Sen Lu, Konstantin Kalashnikov, Thomas DiNapoli, Matthew T. Bell, and Michael E. Gershenson. Granular aluminum meandered superinductors for quantum circuits, 2019.

[67] Lukas Grünhaupt, Nataliya Maleeva, Sebastian T. Skacel, Martino Calvo, Florence Levy-Bertrand, Alexey V. Ustinov, Hannes Rotzinger, Alessandro Monfardini, Gianluigi Catelani, and Ioan M. Pop. Loss mechanisms and quasiparticle dynamics in superconducting microwave resonators made of thin-film granular aluminum. *Phys. Rev. Lett.*, 121:117001, Sep 2018. doi: 10.1103/PhysRevLett.121.117001. URL `https://link.aps.org/doi/10.1103/PhysRevLett.121.117001`.

[68] Fabio Henriques, Francesco Valenti, Thibault Charpentier, Marc Lagoin, Clement Gouriou, Maria Martínez, Laura Cardani, Marco Vignati, Lukas Grünhaupt, Daria Gusenkova, and et al. Phonon traps reduce the quasiparticle density in superconducting circuits. *Applied Physics Letters*, 115(21):212601, Nov 2019. ISSN 1077-3118. doi: 10.1063/1.5124967. URL `http://dx.doi.org/10.1063/1.5124967`.

[69] I. A. Tanaeva, A. T. A. M. de Waele, U. Lindemann, N. Jiang, and G. Thummes. The superfluid vortex cooler. *Journal of Applied Physics*, 98(3): 034911, 2005. doi: 10.1063/1.2001730. URL `https://doi.org/10.1063/1.2001730`.

[70] Nicholas Zobrist, Byeong Ho Eom, Peter Day, Benjamin A. Mazin, Seth R. Meeker, Bruce Bumble, Henry G. LeDuc, Grégoire Coiffard, Paul Szypryt, Neelay Fruitwala, and et al. Wide-band parametric amplifier readout and resolution of optical microwave kinetic inductance detectors. *Applied Physics Letters*, 115(4):042601, Jul 2019. ISSN 1077-3118. doi: 10.1063/1.5098469. URL `http://dx.doi.org/10.1063/1.5098469`.

[71] Collaboration for Astronomy Signal Processing and Electronics Research. Reconfigurable open architecture computing hardware, 2013. URL `https://casper.ssl.berkeley.edu/wiki/ROACH`.

[72] Digicom electronics roach and roach2 systems, Mar 2022. URL `https://www.digicom.org/roach-board.html`.

[73] Matthew James Strader. *Digital Readout for Microwave Kinetic Inductance Detectors and Applications in High Time Resolution Astronomy*. PhD thesis, University of California, Santa Barbara, 2016.

[74] Enzo Pascale, Paul Eccleston, and Giovanna Tinetti. The ariel space mission. In *2018 5th IEEE International Workshop on Metrology for AeroSpace (MetroAeroSpace)*, pages 31–34, 2018. doi: 10.1109/MetroAeroSpace.2018.8453588.

[75] Giovanna Tinetti, Paul Eccleston, Carole Haswell, Pierre-Olivier Lagage, Jérémy Leconte, Theresa Lüftinger, Giusi Micela, Michel Min, Göran Pilbratt, Ludovic Puig, Mark Swain, Leonardo Testi, Diego Turrini, Bart Vandenbussche, Maria Rosa Zapatero Osorio, Anna Aret, Jean-Philippe Beaulieu, Lars Buchhave, Martin Ferus, Matt Griffin, Manuel Guedel, Paul Hartogh, Pedro Machado, Giuseppe Malaguti, Enric Pallé, Mirek Rataj, Tom Ray, Ignasi Ribas, Robert Szabó, Jonathan Tan, Stephanie Werner, Francesco Ratti, Carsten Scharmberg, Jean-Christophe Salvignol, Nathalie Boudin, Jean-Philippe Halain, Martin Haag, Pierre-Elie Crouzet, Ralf Kohley, Kate Symonds, Florian Renk, Andrew Caldwell, Manuel Abreu, Gustavo Alonso, Jerome Amiaux, Michel Berthé, Georgia Bishop, Neil Bowles, Manuel Carmona, Deirdre Coffey, Josep Colomé, Martin Crook, Lucile Désjonqueres, José J. Díaz, Rachel Drummond, Mauro Focardi, Jose M. Gómez, Warren Holmes, Matthijs Krijger, Zsolt Kovacs, Tom Hunt, Richardo Machado, Gianluca Morgante, Marc Ollivier, Roland Ottensamer, Emanuele Pace, Teresa Pagano, Enzo Pascale, Chris Pearson, Søren Møller Pedersen, Moshe Pniel, Stéphane Roose, Giorgio Savini, Richard Stamper, Peter Szirovicza, Janos Szoke, Ian Tosh, Francesc Vilardell, Joanna Barstow, Luca Borsato, Sarah Casewell, Quentin Changeat, Benjamin Charnay, Svatopluk Civiš, Vincent Coudé du Foresto, Athena Coustenis, Nicolas Cowan, Camilla Danielski, Olivier Demangeon, Pierre Drossart, Billy N. Edwards, Gabriella Gilli, Therese Encrenaz, Csaba Kiss, Anastasia Kokori, Masahiro Ikoma, Juan Carlos Morales, João Mendonça, Andrea Moneti, Lorenzo Mugnai, Antonio García Muñoz, Ravit Helled, Mihkel Kama, Yamila Miguel, Nikos Nikolaou, Isabella Pagano, Olja Panic, Miriam Rengel, Hans Rickman, Marco Rocchetto, Subhajit Sarkar, Franck Selsis, Jonathan Tennyson, Angelos Tsiaras, Olivia Venot, Krisztián Vida, Ingo P. Waldmann, Sergey Yurchenko, Gyula Szabó, Rob Zellem, Ahmed Al-Refaie, Javier Perez Alvarez, Lara Anisman, Axel Arhancet, Jaume Ateca, Robin Baeyens, John R. Barnes, Taylor Bell, Serena Benatti, Katia Biazzo, Maria Błęcka, Aldo Stefano Bonomo, José Bosch, Diego Bossini, Jeremy Bourgalais, Daniele Brienza, Anna Brucalassi, Giovanni Bruno, Hamish Caines, Simon Calcutt, Tiago Campante, Rodolfo Canestrari, Nick Cann, Giada Casali, Albert Casas, Giuseppe Cassone, Christophe Cara, Manuel Carmona, Ludmila Carone, Nathalie Carrasco, Quentin Changeat, Paolo Chioetto, Fausto Cortecchia, Markus Czupalla, Katy L. Chubb, Angela Ciaravella, Antonio Claret, Riccardo Claudi, Claudio Codella, Maya Garcia Comas, Gianluca Cracchiolo, Patricio Cubillos, Vania Da Peppo, Leen Decin,

Clemence Dejabrun, Elisa Delgado-Mena, Anna Di Giorgio, Emiliano Diolaiti, Caroline Dorn, Vanessa Doublier, Eric Doumayrou, Georgina Dransfield, Luc Dumaye, Emma Dunford, Antonio Jimenez Escobar, Vincent Van Eylen, Maria Farina, Davide Fedele, Alejandro Fernández, Benjamin Fleury, Sergio Fonte, Jean Fontignie, Luca Fossati, Bernd Funke, Camille Galy, Zoltán Garai, Andrés García, Alberto García-Rigo, Antonio Garufi, Giuseppe Germano Sacco, Paolo Giacobbe, Alejandro Gómez, Arturo Gonzalez, Francisco Gonzalez-Galindo, Davide Grassi, Caitlin Griffith, Mario Giuseppe Guarcello, Audrey Goujon, Amélie Gressier, Aleksandra Grzegorczyk, Tristan Guillot, Gloria Guilluy, Peter Hargrave, Marie-Laure Hellin, Enrique Herrero, Matt Hills, Benoit Horeau, Yuichi Ito, Niels Christian Jessen, Petr Kabath, Szilárd Kálmán, Yui Kawashima, Tadahiro Kimura, Antonín Knížek, Laura Kreidberg, Ronald Kruid, Diederik J. M. Kruijssen, Petr Kubelík, Luisa Lara, Sebastien Lebonnois, David Lee, Maxence Lefevre, Tim Lichtenberg, Daniele Locci, Matteo Lombini, Alejandro Sanchez Lopez, Andrea Lorenzani, Ryan MacDonald, Laura Magrini, Jesus Maldonado, Emmanuel Marcq, Alessandra Migliorini, Darius Modirrousta-Galian, Karan Molaverdikhani, Sergio Molinari, Paul Mollière, Vincent Moreau, Giuseppe Morello, Gilles Morinaud, Mario Morvan, Julianne I. Moses, Salima Mouzali, Nariman Nakhjiri, Luca Naponiello, Norio Narita, Valerio Nascimbeni, Athanasia Nikolaou, Vladimiro Noce, Fabrizio Oliva, Pietro Palladino, Andreas Papageorgiou, Vivien Parmentier, Giovanni Peres, Javier Pérez, Santiago Perez-Hoyos, Manuel Perger, Cesare Cecchi Pestellini, Antonino Petralia, Anne Philippon, Arianna Piccialli, Marco Pignatari, Giampaolo Piotto, Linda Podio, Gianluca Polenta, Giampaolo Preti, Theodor Pribulla, Manuel Lopez Puertas, Monica Rainer, Jean-Michel Reess, Paul Rimmer, Séverine Robert, Albert Rosich, Loic Rossi, Duncan Rust, Ayman Saleh, Nicoletta Sanna, Eugenio Schisano, Laura Schreiber, Victor Schwartz, Antonio Scippa, Bálint Seli, Sho Shibata, Caroline Simpson, Oliver Shorttle, N. Skaf, Konrad Skup, Mateusz Sobiecki, Sergio Sousa, Alessandro Sozzetti, Judit Šponer, Lukas Steiger, Paolo Tanga, Paul Tackley, Jake Taylor, Matthias Tecza, Luca Terenzi, Pascal Tremblin, Andrea Tozzi, Amaury Triaud, Loïc Trompet, Shang-Min Tsai, Maria Tsantaki, Diana Valencia, Ann Carine Vandaele, Mathieu Van der Swaelmen, Adibekyan Vardan, Gautam Vasisht, Allona Vazan, Ciro Del Vecchio, Dave Waltham, Piotr Wawer, Thomas Widemann, Paulina Wolkenberg, Gordon Hou Yip, Yuk Yung, Mantas Zilinskas, Tiziano Zingales, and Paola Zuppella. Ariel: Enabling planetary science across light-years, 2021. URL `https://arxiv.org/abs/2104.04824`.

[76] Sonnet. `www.sonnetsoftware.com`.

[77] Eda solutions, l-edit ic, Mar 2022. URL `https://www.eda-solutions.com/products/tanner-l-edit-ic-layout/`.

[78] Boe / hf – silicon dioxide etching standard operating procedure, 2018. URL `https://d1rkab7tlqy5f1.cloudfront.net/TNW/Afdelingen/Quantum%20Nanoscience/Kavli%20Nanolab%20Delft/Equipment/BOE-HF%20SOP%20Silicon%20Etching.pdf`.

[79] J.I. Goldstein, D.E. Newbury, J.R. Michael, N.W.M. Ritchie, J.H.J. Scott, and D.C. Joy. *Scanning Electron Microscopy and X-Ray Microanalysis.* Springer New York, 2017. ISBN 9781493966769. URL `https://books.google.ie/books?id=D0I_DwAAQBAJ`.

[80] A. Ul-Hamid. *A Beginners' Guide to Scanning Electron Microscopy.* Springer International Publishing, 2018. ISBN 9783319984827. URL `https://books.google.ie/books?id=Wyt1DwAAQBAJ`.

[81] L. Reimer, P.W. Hawkes, A.L. Schawlow, K. Shimoda, A.E. Siegman, and T. Tamir. *Scanning Electron Microscopy: Physics of Image Formation and Microanalysis.* Springer Series in Optical Sciences. Springer, 1998. ISBN 9783540639763. URL `https://books.google.ie/books?id=0Fm3T6F6_LEC`.

[82] X. Liu, W. Guo, Y. Wang, M. Dai, L. F. Wei, B. Dober, C. M. McKenney, G. C. Hilton, J. Hubmayr, J. E. Austermann, J. N. Ullom, J. Gao, and M. R. Vissers. Superconducting micro-resonator arrays with ideal frequency spacing. *Applied Physics Letters*, 111(25):252601, 2017. doi: 10.1063/1.5016190. URL `https://doi.org/10.1063/1.5016190`.

[83] Anthony J Annunziata, Daniel F Santavicca, Luigi Frunzio, Gianluigi Catelani, Michael J Rooks, Aviad Frydman, and Daniel E Prober. Tunable superconducting nanoinductors. *Nanotechnology*, 21(44):445202, Oct 2010. ISSN 1361-6528. doi: 10.1088/0957-4484/21/44/445202. URL `http://dx.doi.org/10.1088/0957-4484/21/44/445202`.

[84] W.R. Leo. *Techniques for Nuclear and Particle Physics Experiments: A How to Approach.* 1987. ISBN 978-3-540-57280-0.

[85] Pieter J. de Visser, Steven A. H. de Rooij, Vignesh Murugesan, David J. Thoen, and Jochem J. A. Baselmans. Phonon-trapping enhanced energy resolution in superconducting single photon detectors, 2021.

[86] B.G. Lowe. Measurements of fano factors in silicon and germanium in the low-energy x-ray region. *Nuclear Instruments and Methods in Physics Research Section A: Accelerators, Spectrometers, Detectors and Associated Equipment*, 399(2):354 – 364, 1997. ISSN 0168-9002. doi: https://doi.org/10.1016/S0168-9002(97)00965-0. URL `http://www.sciencedirect.com/science/article/pii/S0168900297009650`.

[87] S. J. C. do Carmo, F. I. G. M. Borges, F. L. R. Vinagre, and C. A. N. Conde. Experimental study of the w-values and fano factors of gaseous xenon and ar-xe mixtures for x-rays. *IEEE Transactions on Nuclear Science*, 55(5):2637–2642, 2008.

[88] P. J. de Visser, S. J. C. Yates, T. Guruswamy, D. J. Goldie, S. Withington, A. Neto, N. Llombart, A. M. Baryshev, T. M. Klapwijk, and J. J. A. Baselmans. The non-equilibrium response of a superconductor to pair-breaking radiation measured over a broad frequency band. *Applied Physics Letters*, 106 (25), 6 2015. ISSN 0003-6951. doi: 10.1063/1.4923097.

[89] F. B. Hagedorn and P. M. Hall. Right-angle bends in thin strip conductors. *Journal of Applied Physics*, 34(1):128–133, 1963. doi: 10.1063/1.1729052. URL `https://doi.org/10.1063/1.1729052`.

[90] Jiansong Gao, Miguel Daal, John M. Martinis, Anastasios Vayonakis, Jonas Zmuidzinas, Bernard Sadoulet, Benjamin A. Mazin, Peter K. Day, and Henry G. Leduc. A semiempirical model for two-level system noise in superconducting microresonators. *Applied Physics Letters*, 92(21):212504, 2008. doi: 10.1063/1.2937855. URL `https://doi.org/10.1063/1.2937855`.

[91] M. De Lucia, E. Baldwin, G. Ulbricht, C. Bracken, P. Stamenov, and T. P. Ray. Multiplexable frequency retuning of MKID arrays using their non-linear kinetic inductance. In Andrew D. Holland and James Beletic, editors, *X-Ray, Optical, and Infrared Detectors for Astronomy IX*, volume 11454, pages 580 – 590. International Society for Optics and Photonics, SPIE, 2020. doi: 10.1117/12.2560384. URL `https://doi.org/10.1117/12.2560384`.

[92] M. Calvo, J. Goupy, S. Leclercq, A. Catalano, A. Bideaud, A. Monfardini, and E. F. C. Driessen. Increased multiplexing of superconducting microresonator arrays by post-characterization adaptation of the on-chip capacitors. *AIP*, 113 (8):082603, aug 2018. doi: 10.1063/1.5040968. URL `https://doi.org/10.1063%2F1.5040968`.

[93] Ju-Hyun Cho and Jong-Chul Lee. Compact microstrip stepped-impedance hairpin resonator low-pass filter with aperture. *Microwave and Optical Technology Letters*, 46(6):517–520, 2005. doi: 10.1002/mop.21033. URL `https://onlinelibrary.wiley.com/doi/abs/10.1002/mop.21033`.

[94] M.W. Ahmed, R. Alarcon, A. Aleksandrova, S. Baeßler, L. Barron-Palos, L.M. Bartoszek, D.H. Beck, M. Behzadipour, I. Berkutov, J. Bessuille, M. Blatnik, M. Broering, L.J. Broussard, M. Busch, R. Carr, V. Cianciolo, S.M. Clayton, M.D. Cooper, C. Crawford, S.A. Currie, C. Daurer, R. Dipert, K. Dow, D. Dutta, Y. Efremenko, C.B. Erickson, B.W. Filippone, N. Fomin, H. Gao,

R. Golub, C.R. Gould, G. Greene, D.G. Haase, D. Hasell, A.I. Hawari, M.E. Hayden, A. Holley, R.J. Holt, P.R. Huffman, E. Ihloff, S.K. Imam, T.M. Ito, M. Karcz, J. Kelsey, D.P. Kendellen, Y.J. Kim, E. Korobkina, W. Korsch, S.K. Lamoreaux, E. Leggett, K.K.H. Leung, A. Lipman, C.Y. Liu, J. Long, S.W.T. MacDonald, M. Makela, A. Matlashov, J.D. Maxwell, M. Mendenhall, H.O. Meyer, R.G. Milner, P.E. Mueller, N. Nouri, C.M. O'Shaughnessy, C. Osthelder, J.C. Peng, S.I. Penttila, N.S. Phan, B. Plaster, J.C. Ramsey, T.M. Rao, R.P. Redwine, A. Reid, A. Saftah, G.M. Seidel, I. Silvera, S. Slutsky, E. Smith, W.M. Snow, W. Sondheim, S. Sosothikul, T.D.S. Stanislaus, X. Sun, C.M. Swank, Z. Tang, R. Tavakoli Dinani, E. Tsentalovich, C. Vidal, W. Wei, C.R. White, S.E. Williamson, L. Yang, W. Yao, and A.R. Young. A new cryogenic apparatus to search for the neutron electric dipole moment. *Journal of Instrumentation*, 14(11):P11017–P11017, nov 2019. doi: 10.1088/1748-0221/14/11/p11017. URL `https://doi.org/10.1088%2F1748-0221%2F14%2F11%2Fp11017`.

[95] Thomas H. Cormen, Charles E. Leiserson, Ronald L. Rivest, and Clifford Stein. *Introduction to Algorithms*. The MIT Press, 2nd edition, 2001. ISBN 0262032937. URL `http://www.amazon.com/Introduction-Algorithms-Thomas-H-Cormen/dp/0262032937%3FSubscriptionId%3D13CT5CVB80YFWJEPWS02%26tag%3Dws%26linkCode%3Dxm2%26camp%3D2025%26creative%3D165953%26creativeASIN%3D0262032937`.

[96] J. F. Ziegler. Terrestrial cosmic rays. *IBM Journal of Research and Development*, 40(1):19–39, 1996. doi: 10.1147/rd.401.0019.

[97] Benjamin A. Mazin. Superconducting materials for microwave kinetic inductance detectors, 2020. URL `https://arxiv.org/abs/2004.14576`.

[98] Kenichi Karatsu, Masato Naruse, Tom Nitta, Masakazu Sekine, Yutaro Sekimoto, Takashi Noguchi, Yoshinori Uzawa, Hiroshi Matsuo, and Hitoshi Kiuchi. Development of 1000 arrays MKID camera for the CMB observation. In Wayne S. Holland, editor, *Millimeter, Submillimeter, and Far-Infrared Detectors and Instrumentation for Astronomy VI*, volume 8452, pages 200 – 208. International Society for Optics and Photonics, SPIE, 2012. doi: 10.1117/12.925775. URL `https://doi.org/10.1117/12.925775`.

[99] P. D. Mauskopf. Transition edge sensors and kinetic inductance detectors in astronomical instruments. *Publications of the Astronomical Society of the Pacific*, 130(990):1–28, 2018. ISSN 00046280, 15383873. URL `https://www.jstor.org/stable/26660634`.

[100] Jack Sayers, Clint Bockstiegel, Spencer Brugger, Nicole G. Czakon, Peter K. Day, Thomas P. Downes, Ran P. Duan, Jiansong Gao, Amandeep K. Gill, Jason Glenn, Sunil R. Golwala, Matthew I. Hollister, Albert Lam, Henry G. LeDuc, Philip R. Maloney, Benjamin A. Mazin, Sean G. McHugh, David A. Miller, Anthony K. Mroczkowski, Omid Noroozian, Hien Trong Nguyen, James A. Schlaerth, Seth R. Siegel, Anastasios Vayonakis, Philip R. Wilson, and Jonas Zmuidzinas. The status of MUSIC: the multiwavelength sub-millimeter inductance camera. In Wayne S. Holland and Jonas Zmuidzinas, editors, *Millimeter, Submillimeter, and Far-Infrared Detectors and Instrumentation for Astronomy VII*, volume 9153, pages 57 – 74. International Society for Optics and Photonics, SPIE, 2014. doi: 10.1117/12.2055444. URL `https://doi.org/10.1117/12.2055444`.

[101] R. Duan, V. Khaikin, M. Lebedev, V. Shmagin, G. Yakopov, V. Vdovin, G. Bubnov, X. Zhang, C. Niu, Di Li, and I. Zinchenko. Toward eurasian submillimeter telescopes: the concept of multicolor subthz mkid-array demo camera musicam and its instrumental testing, 2020.

[102] James A. Schlaerth, Nicole G. Czakon, Peter K. Day, Thomas P. Downes, Ran Duan, Jiansong Gao, Jason Glenn, Sunil R. Golwala, Matthew I. Hollister, Henry G. LeDuc, Benjamin A. Mazin, Philip R. Maloney, Omid Noroozian, Hien T. Nguyen, Jack Sayers, Seth Siegel, John E. Vaillancourt, Anastasios Vayonakis, Philip R. Wilson, and Jonas Zmuidzinas. MKID multicolor array status and results from DemoCam. In Wayne S. Holland and Jonas Zmuidzinas, editors, *Millimeter, Submillimeter, and Far-Infrared Detectors and Instrumentation for Astronomy V*, volume 7741, pages 59 – 69. International Society for Optics and Photonics, SPIE, 2010. doi: 10.1117/12.857688. URL `https://doi.org/10.1117/12.857688`.

[103] Philip R. Maloney, Nicole G. Czakon, Peter K. Day, Thomas P. Downes, Ran Duan, Jiansong Gao, Jason Glenn, Sunil R. Golwala, Matt I. Hollister, Henry G. LeDuc, Benjamin A. Mazin, Sean G. McHugh, Omid Noroozian, Hien T. Nguyen, Jack Sayers, James A. Schlaerth, Seth Siegel, John E. Vaillancourt, Anastasios Vayonakis, Philip Wilson, and Jonas Zmuidzinas. MUSIC for sub/millimeter astrophysics. In Wayne S. Holland and Jonas Zmuidzinas, editors, *Millimeter, Submillimeter, and Far-Infrared Detectors and Instrumentation for Astronomy V*, volume 7741, pages 124 – 134. International Society for Optics and Photonics, SPIE, 2010. doi: 10.1117/12.857751. URL `https://doi.org/10.1117/12.857751`.

[104] A. Monfardini, L. J. Swenson, A. Bideaud, F. X. Désert, S. J. C. Yates, A. Benoit, A. M. Baryshev, J. J. A. Baselmans, S. Doyle, B. Klein, M. Roesch, C. Tucker, P. Ade, M. Calvo, P. Camus, C. Giordano, R. Guesten,

C. Hoffmann, S. Leclercq, P. Mauskopf, and K. F. Schuster. Nika: A millimeter-wave kinetic inductance camera. *Astronomy and Astrophysics*, 521: A29, Oct 2010. ISSN 1432-0746. doi: 10.1051/0004-6361/201014727. URL `http://dx.doi.org/10.1051/0004-6361/201014727`.

[105] M. Calvo, A. Benoît, A. Catalano, J. Goupy, A. Monfardini, N. Ponthieu, E. Barria, G. Bres, M. Grollier, G. Garde, J.-P. Leggeri, G. Pont, S. Triqueneaux, R. Adam, O. Bourrion, J.-F. Macías-Pérez, M. Rebolo, A. Ritacco, J.-P. Scordilis, D. Tourres, A. Adane, G. Coiffard, S. Leclercq, F.-X. Désert, S. Doyle, P. Mauskopf, C. Tucker, P. Ade, P. André, A. Beelen, B. Belier, A. Bideaud, N. Billot, B. Comis, A. D'Addabbo, C. Kramer, J. Martino, F. Mayet, F. Pajot, E. Pascale, L. Perotto, V. Revéret, A. Ritacco, L. Rodriguez, G. Savini, K. Schuster, A. Sievers, and R. Zylka. The nika2 instrument, a dual-band kilopixel kid array for millimetric astronomy. *Journal of Low Temperature Physics*, 184(3-4):816–823, Mar 2016. ISSN 1573-7357. doi: 10.1007/s10909-016-1582-0. URL `http://dx.doi.org/10.1007/s10909-016-1582-0`.

[106] Hans Juergen Kaercher and Jacob W. M. Baars. Design of the Large Millimeter Telescope/Gran Telescopio Millimetrico (LMT/GTM). In Harvey R. Butcher, editor, *Radio Telescopes*, volume 4015, pages 155 – 168. International Society for Optics and Photonics, SPIE, 2000. doi: 10.1117/12.390407. URL `https://doi.org/10.1117/12.390407`.

[107] Tom Brien, Simon M. Doyle, Edgar Castillo-Domínguez, Daniel Ferrusca, David H. Hughes, Enzo Pascale, Sam Rowe, Carole Tucker, Peter A. R. Ade, Amber L. Hornsby, Peter Barry, Thomas Gascard, Victor Gomez, Peter Hargrave, Josie Parrianen, Abel Perez, and Salvador Ventura González. Muscat: the mexico-uk sub-millimetre camera for astronomy. *Millimeter, Submillimeter, and Far-Infrared Detectors and Instrumentation for Astronomy IX*, Jul 2018. doi: 10.1117/12.2313697. URL `http://dx.doi.org/10.1117/12.2313697`.

[108] J. E. Austermann, J. A. Beall, S. A. Bryan, B. Dober, J. Gao, G. Hilton, J. Hubmayr, P. Mauskopf, C. M. McKenney, S. M. Simon, J. N. Ullom, M. R. Vissers, and G. W. Wilson. Millimeter-wave polarimeters using kinetic inductance detectors for toltec and beyond. *Journal of Low Temperature Physics*, 193(3-4):120–127, May 2018. ISSN 1573-7357. doi: 10.1007/s10909-018-1949-5. URL `http://dx.doi.org/10.1007/s10909-018-1949-5`.

[109] Shugo Oguri, Jihoon Choi, Thushara Damayanthi, Makoto Hattori, Masashi Hazumi, Hikaru Ishitsuka, Kenji Kiuchi, Ryo Koyano, Hiroki Kutsuma, Kyungmin Lee, Satoru Mima, Makoto Minowa, Makoto Nagai, Taketo

Nagasaki, Chiko Otani, Yutaro Sekimoto, Munehisa Semoto, Jun'ya Suzuki, Tohru Taino, Osamu Tajima, Nozomu Tomita, Eunil Won, Tomohisa Uchida, and Mitsuhiro Yoshida. GroundBIRD: observations of CMB polarization with fast scan modulation and MKIDs. In Helen J. Hall, Roberto Gilmozzi, and Heather K. Marshall, editors, *Ground-based and Airborne Telescopes VI*, volume 9906, pages 1288 – 1294. International Society for Optics and Photonics, SPIE, 2016. doi: 10.1117/12.2231672. URL `https://doi.org/10.1117/12.2231672`.

[110] Bradley R. Johnson, Daniel Flanigan, Maximilian H. Abitbol, Peter A. R. Ade, Sean Bryan, Hsiao-Mei Cho, Rahul Datta, Peter Day, Simon Doyle, Kent Irwin, Glenn Jones, Sarah Kernasovskiy, Dale Li, Philip Mauskopf, Heather McCarrick, Jeff McMahon, Amber Miller, Giampaolo Pisano, Yanru Song, Harshad Surdi, and Carole Tucker. Polarization sensitive Multi-Chroic MKIDs. In Wayne S. Holland and Jonas Zmuidzinas, editors, *Millimeter, Submillimeter, and Far-Infrared Detectors and Instrumentation for Astronomy VIII*, volume 9914, pages 216 – 227. International Society for Optics and Photonics, SPIE, 2016. doi: 10.1117/12.2233243. URL `https://doi.org/10.1117/12.2233243`.

[111] Michael Crumrine, P. A. R. Ade, Z. Ahmed, R. W. Aikin, K. D. Alexander, D. Barkats, S. J. Benton, C. A. Bischoff, J. J. Bock, R. Bowens-Rubin, J. A. Brevik, I. Buder, E. Bullock, V. Buza, J. Connors, J. Cornelison, B. P. Crill, M. Dierickx, L. Duband, C. Dvorkin, J. P. Filippini, S. Fliescher, J. A. Grayson, G. Hall, M. Halpern, S. A. Harrison, S. R. Hildebrandt, G. C. Hilton, H. Hui, K. D. Irwin, J. H. Kang, K. S. Karkare, E. Karpel, J. P. Kaufman, B. G. Keating, S. Kefeli, S. A. Kernasovskiy, J. M. Kovac, C. L. Kuo, N. A. Larsen, K. Lau, E. M. Leitch, M. V. Lueker, K. G. Megerian, L. Moncelsi, T. Namikawa, C. B. Netterfield, H. T. Nguyen, R. O'Brient, R. W. Ogburn IV, S. Palladino, C. Pryke, B. Racine, S. Richter, R. Schwarz, A. Schillaci, C. D. Sheehy, A. Soliman, T. St. Germaine, Z. K. Staniszewski, B. Steinbach, R. V. Sudiwala, G. P. Teply, K. L. Thompson, J. E. Tolan, C. E. Tucker, A. D. Turner, C. Umiltà, A. G. Vieregg, A. Wandui, A. C. Weber, D. V. Wiebe, J. Willmert, C. L. Wong, W. L. K. Wu, E. Yang, K. W. Yoon, and C. Zhang. BICEP Array cryostat and mount design. In Jonas Zmuidzinas and Jian-Rong Gao, editors, *Millimeter, Submillimeter, and Far-Infrared Detectors and Instrumentation for Astronomy IX*, volume 10708, pages 303 – 312. International Society for Optics and Photonics, SPIE, 2018. doi: 10.1117/12.2312829. URL `https://doi.org/10.1117/12.2312829`.

[112] Akira Endo, Kenichi Karatsu, Yoichi Tamura, Tai Oshima, Akio Taniguchi, Tatsuya Takekoshi, Shin'ichiro Asayama, Tom J. L. C. Bakx, Sjoerd Bosma, Juan Bueno, Kah Wuy Chin, Yasunori Fujii, Kazuyuki Fujita, Robert Huiting, Soh Ikarashi, Tsuyoshi Ishida, Shun Ishii, Ryohei Kawabe, Teun M. Klapwijk,

Kotaro Kohno, Akira Kouchi, Nuria Llombart, Jun Maekawa, Vignesh Murugesan, Shunichi Nakatsubo, Masato Naruse, Kazushige Ohtawara, Alejandro Pascual Laguna, Junya Suzuki, Koyo Suzuki, David J. Thoen, Takashi Tsukagoshi, Tetsutaro Ueda, Pieter J. de Visser, Paul P. van der Werf, Stephen J. C. Yates, Yuki Yoshimura, Ozan Yurduseven, and Jochem J. A. Baselmans. First light demonstration of the integrated superconducting spectrometer. *Nature Astronomy*, 3(11):989–996, Aug 2019. ISSN 2397-3366. doi: 10.1038/s41550-019-0850-8. URL `http://dx.doi.org/10.1038/s41550-019-0850-8`.

[113] Jochem J. A. Baselmans, Sjoerd Bosma, Soh Ikarashi, Teun M. Klapwijk, Nuria Llombart, Alejandro Pascual Laguna, David J. Thoen, Pieter J. de Visser, Ozan Yurduseven, Akira Endo, and More Authors. Deshima on aste: On-sky responsivity calibration of the integrated superconducting spectrometer. *Journal of Low Temperature Physics*, 199(1-2):231–239, 2020. ISSN 0022-2291. doi: 10.1007/s10909-020-02338-0. Green Open Access added to TU Delft Institutional Repository 'You share, we take care!' – Taverne project https://www.openaccess.nl/en/you-share-we-take-care Otherwise as indicated in the copyright section: the publisher is the copyright holder of this work and the author uses the Dutch legislation to make this work public.

[114] C. N. Thomas, S. Withington, R. Maiolino, D. J. Goldie, E. de Lera Acedo, J. Wagg, R. Blundell, S. Paine, and L. Zeng. The cambridge emission line surveyor (camels), 2014.

[115] Giuseppe Cataldo, Wen-Ting Hsieh, Wei-Chung Huang, S. Harvey Moseley, Thomas R. Stevenson, and Edward J. Wollack. Micro-spec: an ultracompact, high-sensitivity spectrometer for far-infrared and submillimeter astronomy. *Appl. Opt.*, 53(6):1094–1102, Feb 2014. doi: 10.1364/AO.53.001094. URL `http://opg.optica.org/ao/abstract.cfm?URI=ao-53-6-1094`.

[116] P. A. R. Ade, C. J. Anderson, E. M. Barrentine, N. G. Bellis, A. D. Bolatto, P. C. Breysse, B. T. Bulcha, G. Cataldo, J. A. Connors, P. W. Cursey, N. Ehsan, H. C. Grant, T. M. Essinger-Hileman, L. A. Hess, M. O. Kimball, A. J. Kogut, A. D. Lamb, L. N. Lowe, P. D. Mauskopf, J. McMahon, M. Mirzaei, S. H. Moseley, J. W. Mugge-Durum, O. Noroozian, U. Pen, A. R. Pullen, S. Rodriguez, P. J. Shirron, R. S. Somerville, T. R. Stevenson, E. R. Switzer, C. Tucker, E. Visbal, C. G. Volpert, E. J. Wollack, and S. Yang. The experiment for cryogenic large-aperture intensity mapping (exclaim). *Journal of Low Temperature Physics*, 199(3-4):1027–1037, Jan 2020. ISSN 1573-7357. doi: 10.1007/s10909-019-02320-5. URL `http://dx.doi.org/10.1007/s10909-019-02320-5`.

[117] Nicola Casali, Fabio Bellini, L. Cardani, M. Castellano, Ivan Colantoni, C. Cosmelli, A. Cruciani, Antonio D'Addabbo, S. Domizio, M. Martinez, L. Minutolo, C. Tomei, and M. Vignati. *Cryogenic Light Detectors for Background Suppression: The CALDER Project: Volume 2*, pages 267–270. 08 2018. ISBN 978-981-13-1315-8. doi: 10.1007/978-981-13-1316-5_50.

[118] L. Cardani, F. Bellini, N. Casali, M. G. Castellano, I. Colantoni, A. Coppolecchia, C. Cosmelli, A. Cruciani, S. Di Domizio, C. Tomei, and M. Vignati. Calder: Cryogenic light detectors for background-free searches. *AIP Conference Proceedings*, 1672(1):130001, 2015. doi: 10.1063/1.4928011. URL `https://aip.scitation.org/doi/abs/10.1063/1.4928011`.

[119] M. Faverzani, B. Alpert, D. Backer, D. Bennet, Michele Biasotti, C. Brofferio, Valentina Ceriale, G. Ceruti, Dario Corsini, Peter Day, Matteo De Gerone, R. Dressler, E. Ferri, Jie Fowler, Elisa Fumagalli, Johnathon Gard, Flavio Gatti, Andrea Giachero, J. Hays-Wehle, and Leila Vale. The holmes experiment. *Journal of Low Temperature Physics*, 184, 08 2016. doi: 10.1007/s10909-016-1540-x.

[120] A. De Rújula and M. Lusignoli. Calorimetric measurements of 163holmium decay as tools to determine the electron neutrino mass. *Physics Letters B*, 118 (4):429–434, 1982. ISSN 0370-2693. doi: https://doi.org/10.1016/0370-2693(82)90218-0. URL `https://www.sciencedirect.com/science/article/pii/0370269382902180`.

[121] A. Giachero, P. K. Day, P. Falferi, M. Faverzani, E. Ferri, C. Giordano, M. Maino, B. Margesin, R. Mezzena, R. Nizzolo, A. Nucciotti, A. Puiu, and L. Zanetti. Development of microwave superconducting microresonators for neutrino mass measurement in the holmes framework. *Journal of Low Temperature Physics*, 184(1–2):123–130, Jan 2016. ISSN 1573-7357. doi: 10.1007/s10909-015-1441-4. URL `http://dx.doi.org/10.1007/s10909-015-1441-4`.

[122] S. Golwala, Jiachen Gao, David Moore, B. Mazin, Megan Eckart, B. Bumble, Peter Day, Henry Leduc, and Jonas Zmuidzinas. A wimp dark matter detector using mkids. *Journal of Low Temperature Physics*, 151, 04 2008. doi: 10.1007/s10909-007-9687-0.

[123] I. Colantoni, C. Bellenghi, M. Calvo, R. Camattari, L. Cardani, N. Casali, A. Cruciani, S. Di Domizio, J. Goupy, V. Guidi, H. Le Sueur, M. Martinez, A. Mazzolari, A. Monfardini, V. Pettinacci, G. Pettinari, M. Romagnoni, and M. Vignati. BULLKID: BULky and Low-Threshold Kinetic Inductance Detectors. *Journal of Low Temperature Physics*, 199(3-4):593–597, February 2020. doi: 10.1007/s10909-020-02408-3.

[124] Stephen Derenzo, Rouven Essig, Andrea Massari, Adrían Soto, and Chiu-Tien Yu. Direct detection of sub-gev dark matter with scintillating targets. *Physical Review D*, 96, 07 2016. doi: 10.1103/PhysRevD.96.016026.

[125] H.; Mazin B.; Van Tilburg K.; Weld D. Baryakhtar M.; Craig N.; Daal M.; Huang J.; Lasenby R.; Lippincott. Sub-ev dark matter detection with mkid haloscopes. *Snowmass 2021 - Letter of Interest*, 2020. URL `www.snowmass21.org/docs/files/summaries/CF/SNOWMASS21-CF1_CF2-IF2_IF1_Ben_Mazin-004.pdf`.

[126] Dunne K.; Gudmundsson J.; Lawson M.; Millar A.; Morampudi S.; Newman N.; Peiris H.V.; Wilczek F. Tunable plasma haloscope. *Snowmass 2021 - Letter of Interest*, 2020. URL `https://www.snowmass21.org/docs/files/summaries/IF/SNOWMASS21-IF1-CF2-003.pdf`.

[127] Gerhard Ulbricht, Benjamin A. Mazin, Paul Szypryt, Alex B. Walter, Clint Bockstiegel, and Bruce Bumble. Highly multiplexible thermal kinetic inductance detectors for x-ray imaging spectroscopy, 2015.

[128] Yeukuang Hwu and Giorgio Margaritondo. Synchrotron radiation and sensors: A history of synergies. *IEEE Sensors Journal*, 21(11):12764–12773, 2021. doi: 10.1109/JSEN.2020.3023292.

[129] Thomas Cecil, Antonino Miceli, Lisa Gades, Aaron Datesman, Orlando Quaranta, V. Yefremenko, Val Novosad, and B. Mazin. Kinetic inductance detectors for x-ray spectroscopy. *Physics Procedia*, 37:697–702, 12 2012. doi: 10.1016/j.phpro.2012.03.719.

[130] Thomas Cecil, Antonino Miceli, Orlando Quaranta, Chian Liu, Daniel Rosenmann, Sean McHugh, and Benjamin Mazin. Tungsten silicide films for microwave kinetic inductance detectors. *Applied Physics Letters*, 101(3):032601, Jul 2012. ISSN 1077-3118. doi: 10.1063/1.4737408. URL `http://dx.doi.org/10.1063/1.4737408`.

[131] Sam Rowe, Enzo Pascale, Simon Doyle, Chris Dunscombe, Peter Hargrave, Andreas Papageorgio, Ken Wood, Peter A. R. Ade, Peter Barry, Aurélien Bideaud, Tom Brien, Chris Dodd, William Grainger, Julian House, Philip Mauskopf, Paul Moseley, Locke Spencer, Rashmi Sudiwala, Carole Tucker, and Ian Walker. A passive terahertz video camera based on lumped element kinetic inductance detectors. *Review of Scientific Instruments*, 87(3):033105, Mar 2016. ISSN 1089-7623. doi: 10.1063/1.4941661. URL `http://dx.doi.org/10.1063/1.4941661`.

[132] D. Morozov, Simon Doyle, Archan Banerjee, Thomas Brien, Dilini Hemakumara, Iain Thayne, Ken Wood, and Robert Hadfield. Design and

characterisation of titanium nitride subarrays of kinetic inductance detectors for passive terahertz imaging. *Journal of Low Temperature Physics*, 193, 11 2018. doi: 10.1007/s10909-018-2023-z.

[133] Gabriele C. Messina, Valentina Brosco, Angelo Cruciani, Lara Benfatto, Sara Cibella, Giorgio Pettinari, Maria Gabriella Castellano, Alfonso A. Tanga, Michele Ortolani, Leonetta Baldassarre, Marco Vignati, and José Lorenzana. High-tc superconducting kinetic inductance detectors for terahertz imaging. In *2019 44th International Conference on Infrared, Millimeter, and Terahertz Waves (IRMMW-THz)*, pages 1–2, 2019. doi: 10.1109/IRMMW-THz.2019.8874002.

[134] C. de Jonge, A.M. Baryshev, L. Ferrari, S. J. C. Yates, J.J.A. Baselmans, and A. Endo. Development of a passive stand-off imager using mkid technology for security and biomedical applications. In *2012 37th International Conference on Infrared, Millimeter, and Terahertz Waves*, pages 1–2, 2012. doi: 10.1109/IRMMW-THz.2012.6380107.

[135] Juha Hassel, Shahab Oddin Dabironezare, Erio Gandini, Leif Grönberg, Hannu Sipola, Anssi Rautiainen, Aleksi Tamminen, Mikko Leivo, Hannu Lindström, Hannu Vasama, Arttu Luukanen, and Nuria Llombart. Dual-band submillimeter-wave kinetic inductance bolometers and an imaging system for contraband object detection. In David A. Wikner and Duncan A. Robertson, editors, *Passive and Active Millimeter-Wave Imaging XXI*, volume 10634, pages 107 – 112. International Society for Optics and Photonics, SPIE, 2018. doi: 10.1117/12.2304722. URL `https://doi.org/10.1117/12.2304722`.

[136] Mazzocchi F; Driessen E.F.C.; Shu S.; Grossetti G.; Strauss D.; Scherer T. Development of nbn polarization sensitive kid for fusion applications. *In Proceedings of 43rd International Conference on Infrared, Millimeter, and Terahertz Waves (IRMMW-THz), Nagoya, JAPAN,*, 151, 09 2018.

[137] Gabriele Baglioni. *Investigation of strain-induced electromechanical coupling in kinetic inductance.* PhD thesis, KTH, School of Engineering Sciences, 2020.

A1 Ariel Filter Test

Low Temperatue Characterisation Of The Dichroic D3 for ARIEL

Mario De Lucia, Eoin Baldwin, Gerhard Ulbricht, Jack Piercy
and Deirdre Coffey and Tom Ray

Dublin Institute for Advanced Studies,
Astronomy and Astrophysics, 31 Fitzwilliam Place, D02XF86,
Dublin, Ireland

delucia@cp.dias.ie

December 14, 2021

1 Introduction

This report documents the tests the D3 dichroic filter has undergone and also contains a thorugh description of the methods and processes through which the tests were performed. We report data on the cryogenic cycles that were performed to test the filter's capability of withstanding temperatures as low as $4\,K$. We're also reporting on the optical characteristics, visible (Vis) to near-infrared (NIR) of the filter measured at both room temperature ($300\,K$) and at cryogenic temperatures (namely $4\,K$, but in realtity between $4,5\,K$ and $6,5\,K$). All measurements were taken in vacuum, with pressures $\leq 10^{-3}\,mbar$ at $300\,K$ and $\leq 10^{-6}\,mbar$ at $4\,K$. All the data refers to transmission measured with an Angle Of Incidence (AOI) of 20° between the optical axis and the dichroic filter D3 unless otherwise stated.

2 Cryogenic Cycles

The D3 filter has been mounted in an off-the-shelf filter mount from Thorlabs (part number LMR05/M) with a torque of the holding screw of 0.2 Nm. The filter mount was connected to the 4 K plate of our two-stage pulse tube cooled, dry cryogenic system and was thermally cycled 20 times. The typical shape of a full thermal cycle of the fridge is shown in Figure 1. After 20 thermal cycles, the minimum temperatures of which are shown in Table 1, no damage or changes to the D3 dichroic were observed whilst using a compound optical microscope with magnification up to x800.

#	$T(K)$	#	$T(K)$	#	$T(K)$	#	$T(K)$
1	2.92	6	4.12	11	2.92	16	2.88
2	2.97	7	3.03	12	3.03	17	4.08
3	3.13	8	2.89	13	3.01	18	3.63
4	4.15	9	3.24	14	2.97	19	4.07
5	4.14	10	2.97	15	2.89	20	4.13

Table 1: Base temperature reached with each cooldown cycle

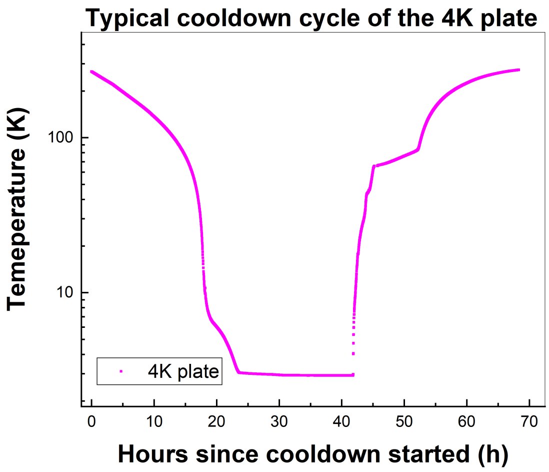

Figure 1: Standard thermal cycle of the $4\,K$ plate to which the dichoric is mounted.

3 Optical tests

The main purpose of the tests carried out in DIAS was the optical characterisation of the D3 filter in terms of transmission spectrum at, both, room temperature ($300\,K$) and $4\,K$ to ensure no unexpected changes occur in the transmission spectrum at cryogenic temperatures including changes to the transmission features or the engineeered onset of transmission. This was achieved through the use of a Quantum Design monochromator (MSH 150) coupled to a 100 W halogen lamp (LSH 102) to illuminate the filter with light which has a linewidth of $\approx 2.5\,nm$ over the whole spectrum of $400\,nm$ to $2500\,nm$. The light is detected with two off-the-shelf photodiodes from Thorlabs: S120C is sensitive and calibrated for wavelengths between $400\,nm$ and $1100\,nm$ (Vis-NIR).Whereas the "S148C" detector is calibrated between $1200\,nm$ and $2500\,nm$ (NIR), but is sensitive for wavelengths down to 1100 as shown in Figure 2. A comprehensive description of the characteristics of each instrument can be found in the Appendix B

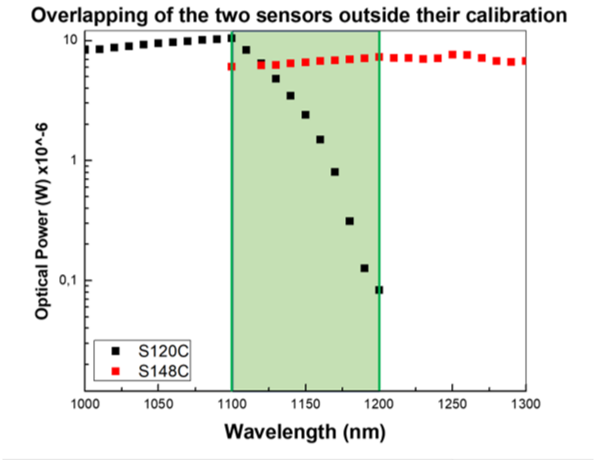

Figure 2: Response of the detectors outside their range of calibration, $1100\,nm$ to $1200\,nm$. Both detectors are responsive, however $S148C$ produced a higher and flatter signal, and is therefore the one designated for operation across this calibration gap

3.1 Experimental setup

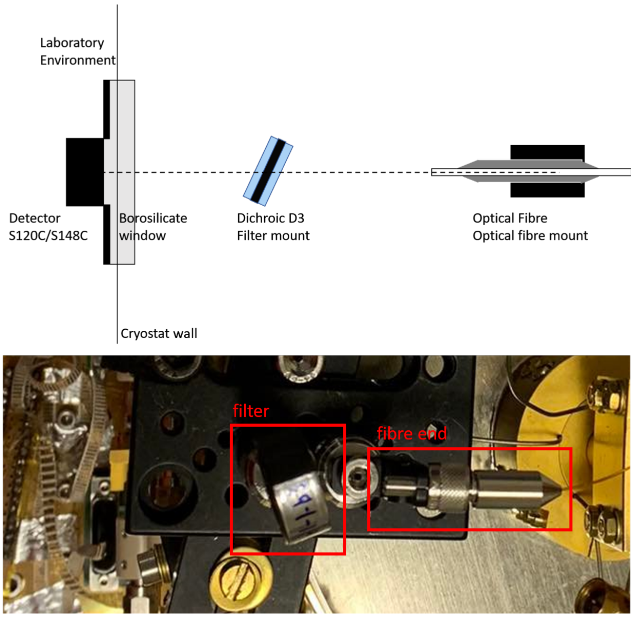

Figure 3: Top: Schematic of the optical setup for the filter test. Bottom: picture of the mounting plate anchored to the $4\,K$ stage of the cryostat with the optical fibre, its mounting, the filter and its mounting.

Figure 3 (top) shows a schematic of the experimental setup used for the measurements including the optical fibre (Ocean Optics OCF-107593) with its mounting, the dichroic and its mounting, the vacuum compatible borosilicate glass window and the detector. They are aligned on the optical axis represented as a dashed line. The fibre is connected to a halogen lamp which acts as a light source and the wavelength is selected through a monochromator. The light source and the monochromator are not shown in the schematic. The lamp is set in a configuration that maximises its coupling to the monochromator and the optical throughput of the monochromator, for which both the entrance and exit slit are fixed at a width of $0.5\ mm$. This configuration results in a nominal minimum linewidth of the spectrum (according to the manual provided by the manufacturer) of $2.5\,nm$. At the output of the monochromator, the light is coupled into an optical fibre which is then fed into the cryostat through a vacuum-tight optical feedthrough. Three more fibres are used to reach the $4\,K$ stage of the cryostat where a metal plate is mounted so that the filter is on axis with the optical window of the cryostat. Both the filter and the fibre are kept in place on the plate through apposite mounting parts which are also off the shelf from Thorlabs. The detectors are mounted at room temperature on the outside of the cryostat so not to require cryogenic detectors. Figure 3 (bottom) shows a view of the setup in the fridge. A labVIEW Virtual Instrument to interface with the monochromator and the detectors was developed. For details see appendix **??**.

3.2 $400\,nm$ - $1100\,nm$

The interesting part of the wavelength range is around the transition edge which, is designed to be at $\approx 800\,nm$. This region is where the lamp is the brightest and is fully covered by the low wavelength detector "S120C". Three different scans were performed at each temperature of interest: one broad scan to acquire data on the shape of the transmission curve and two finely stepped scans around two areas of interest which are where the filter presents light leaks at low wavelengths and the transmission edge. All the measurements were performed with an integration time of $1\,s$. The broad scan, which measures between $400\,nm$ and $1100\,nm$ was performed with wavelength intervals of $1\,nm$, whereas $0.1\,nm$ was used for finer scans. Figure 4 shows the transmission curve produced by the broad scan after having subtracted the dark current contribution to the signal from the detectors and then normalising the curves so that the transmission obtained is defined as the ratio of the spectrum obtained with the filter in divided by the spectrum with the filter out of the optical axis. All data presented in this report, represents spectra obtained after dark current subtractions. Figure 4 shows the presence of a transition edge around $800\,nm$ and some non negligible transmission in the low-wavelength region between $450\,nm$ and $500\,nm$. The two further scans, whose data is shown in Figure 5 (Top and Bottom), were performed to capture the fine structure of the transmission edge and the low-wavelength peaks. Figures in Appendix A show the individual measurements produced by the detector in two different conditions: with the filter in and with the filter out for both temperatures of interest ($300\,K$(Top) and $4\,K$(Bottom)).

3.3 $1100\,nm$ - $2500\,nm$

For wavelengths above $1100\,nm$ a different sensor and different settings were used. The decreased brightness

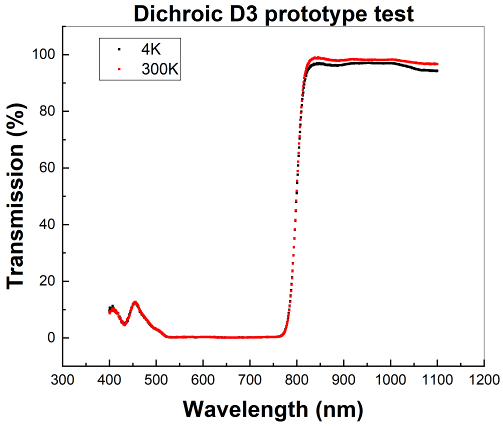

Figure 4: Broad scan of the transmission curve of the dichroic filter D3 mounted at an AOI of 20° at 300 K (red) and 4 K (black) between 400 nm and 1100 nm

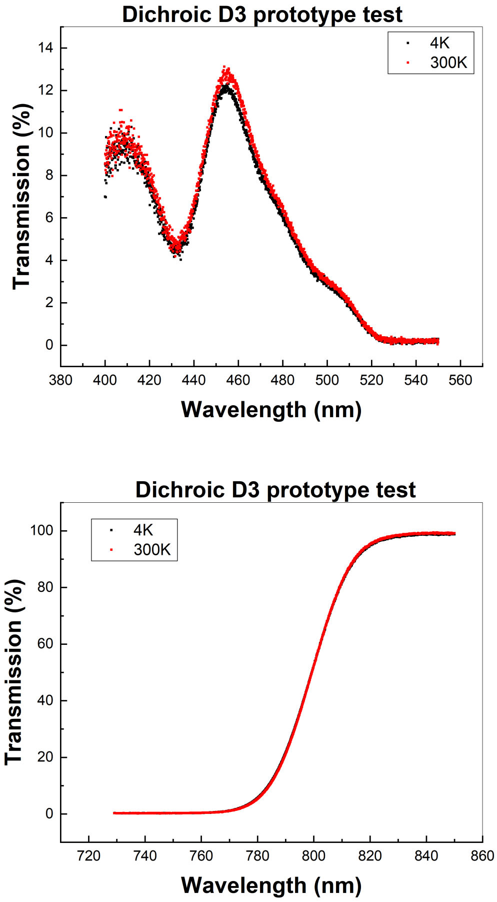

Figure 5: Fine scans of D3 filter transmission, significantly oversampled as a 0.1 nm step size but at a nominal monochromator resolution of only 2.5 nm was used. Black dots show low temperature (4 K) measurements, red dots represent room temperature, all data taken with AOI of 20°. Top: Low wavelength filter transmission leaks. Bottom: Zoom into the filter transmission edge.

of the lamp in the NIR region, and the smaller sensitivity and the smaller collection area of the "S148C" detector, results in measurements with increased noise in the 1100 nm - 2500 nm region compared to those of 400 nm - 1100 nm. In order to counterbalance this undesired side effect of the experimental setup, a longer integration time is required. Unfortunately the detector's embedded circuitry sets a maximum integration time of 10 s per measurement point. So eventually the whole spectrum has been scanned 10 times with said 10 s integration time per each point and the values thus obtained have been averaged to produce an effective 100 s average for each measurement point. The NIR measurements were conducted with a wavlength interval of 5 nm.

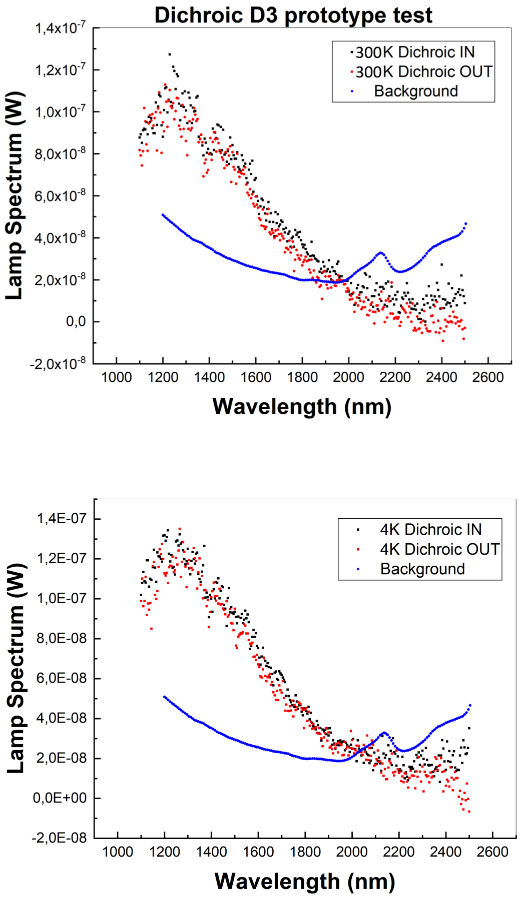

Figure 6: Top: Lamp spectrum measured at a temperature of 300 K with the filter in the beam path (black), and without the filter (red). The blue line represents the noise floor of the detector. (See below)
Bottom: Lamp spectrum measured at at temperature of 4 K with the filter in the beam path (black), and without the filter in the beam path (red). The blue line represents the noise floor of the detector.

We will present the transmission curve in section 4, instead in this section we are going to show the data points obtained after subtracting the dark current of the detectors in the two possible configurations: with the filter in the optical beam and with the filter removed from the optical beam at both 300 K and 4 K (Figure 6 (Top and Bottom)). It is worth discussing the blue curve that, in both figures, represents the minimum energy above which our detector is considered sensitive. Our dark current has two components: a constant offset and a scatter noise distribution around it. The threshold (namely, Background in the plots) of our detector is intended as 3σ of the dark current distribution, around its zero value, multiplied by the calibration curve. It is clear that the noise dominates the signal from 2000 nm onwards, meaning that the measurements have little interpretative value in this region. However, in order to try and mitigate the effects of the small signal to noise ratio, when plotting the transmission curves (see Section 4), a 10-point moving average has been applied to the the data shown in Figure 6.

4 Results

Figure 7 (Top) shows the two transmission spectra of the D3 dichroic filter over the whole wavelength range, one measured at 300 K (in red) and one measured at 4 K (in black).The separation between the two curves: 300 K and 4 K can be accounted to possible drifts in the lamp performance. Since a full thermal cycle takes about three days and a measurement run takes one full day, the time difference between the measurements with the filter in is 5 days, while the measurements taken with the filter out are taken 10 days apart. The jump at 1100 nm is also due to the diminished performance of the halogen lamp. In order to mitigate this effect, further 10-point moving average smoothing was applied between 1080 nm and 1200 nm in order to compensate a gap that shows up at 1100 nm. The smoothed out curve is shown in Figure 7 (Bottom).

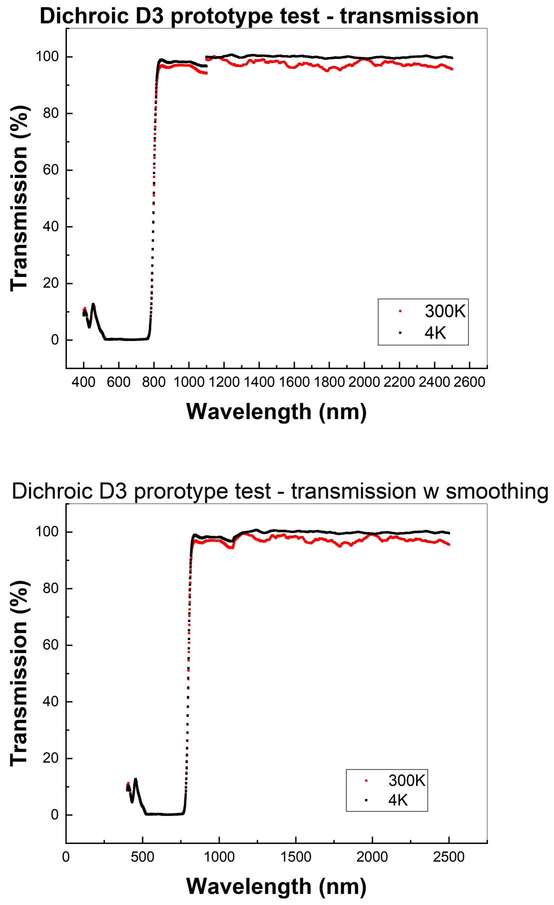

Figure 7: (Top): Transmission curve measured for the dichroic D3 with an AOI 20° at 300 K (red) and 4 K (black). (Bottom): smoothed out curve as per (Top) in order to remove the artifact in the spectrum through a second stage of 10-point moving average between 1080 nm and 1200 nm.

5 Discussion

No measurable difference has been observed in the transmission profile of the filter when measured at 300 K and 4 K. In particular, the transmission edge was observed not to show any change at 4 K from its 300 K characteristic, nor did the lower wavelength features exhibit an increase in transmission. In the following two sections we will discuss concerns reading the designing the experiments.

5.1 Best slit width

One of the main challenges was the optimisation of the width of both slits of the monochromator. In principle, the wider the slits, the more light couples into the optical fibre and consequently the signal to noise ratio increases. The drawback here is that the wider the slit, the less monochromatic the light that illuminates the filter is. In addition to that, by manufacturer's design the monochromator switches between the two gratings at exactly 800 nm, precisely where the transition edge lies. This switch of gratings produced an asymmetric spectral profile of the light produced at around the switching wavelength and, paired with the transition edge, this produced a gap in the transmission curve. This artefact only vanishes for slit widths smaller than 0.5 mm. Unfortunately the signal to noise ratio plummets when closing further the slits.

5.2 Lamp emission stability

As we have to directly compare filter-in to filter-out measurements that had to be taken up to 10 days apart (caused by fridge warm-up and cool-down times) lamp emission stability is important for the reliability of our results. As per usual with halogen light sources, the lamp needs time to warm up. We observed that it takes approximately one hour for the lamp to warm up to a point where its emissivity is maximum. In particular, in order not to damage the bulb, the lamp is only biased with 50 % of its bias voltage for the first 15 minutes from the switching on of the lamp. In order to test its stability over one measurement day, the lamp spectrum was measured connecting directly the detectors through an optical fibre to the monochromator without going through the cryostat at the beginning and at the end of every day of measurements. This measurement is, of course, affected by the inherent noise of the detectors, but it is possible to state that the lamp spectrum is stable over 12 hours and the curves overlap fully. The convolution of the lamp noise and the detectors noise produce an upper limit of uncertainty of about $\pm 3\,\%$ for the $S148C$ infrared detector and about $\pm 0.5\,\%$ for the $S120C$ detector. The lamp is expected to have experienced a reduction in emissivity over the experimental run, which took approximately a month, and might account for the differences visible in the transmission curves.

5.3 $4\,K$ plate temperature

There is one point that requires further explanation and it concernes the definition of the $4\,K$ plate tempeature. It might appear that there is a contraddiction between the temepratures reported in Table 1 and the temperature of the $4\,K$ plate as intended in the rest of the report (ranging $4,5\,K$ to $6,5\,K$). The confusion might arise from lack of explanation. When the filter was tested to prove it could withstand a thermal cycle, no optical fibres were installed in the cryostat and, in this configuration, the base temperatures of the cryostat would range according to Table 1. In order to perform the optical characterisation of the filter, it was necessary to feed optical fibres into the cryostat. Unfortunately their thermal conductivity is not negligible and their presence increased the thermal load on the $4\,K$ plate of the cryostat resulting in a higher base temperature, which now ranges, as reported in the text, between $4,5\,K$ and $6,5\,K$.

6 Conclusion

In conclusion, the purpose of the first part of this experimental run was to test that the dichroic filter D3 designed and produced for the ARIEL collaboration could withstand multiple cryogenic cycles without shattering, cracking or exhibiting any signs of wear. This was demonstrated by cooling the dichroic down multiple times in a cryostat down to a temperature between $2.8\,K$ and $4.15\,K$ as described in Table 1. The filter was checked after every cryogenic cycle and showed and continues to show no no visible sign of strain, cracking or any other damage. Secondly, the optical characteristics of the dichroic D3 was measured at room temperature, namely $300\,K$ and compared to those measured at cryogenic temperatures, namely $4\,K$. The data shown in Section 3.2 demonstrates that there is no visible shift of the transition edge and that there are no new transmission peaks that open up, while the peaks' amplitude remained unchanged.

A Supplementary images

A.1 filter pictures

Figure 8: Top: Filter before first thermal cycle. Middle: The filter after the last cryogenic cycle showing no visible sign of wear. The Thorlabs LMR05/M shown in both pictures is the filter mount in which the dichroic D3 was mounted for cryogenic tests and optical characterisation. Bottom: Filter not mounted in the LMR05/M.

A.2 Individual spectra

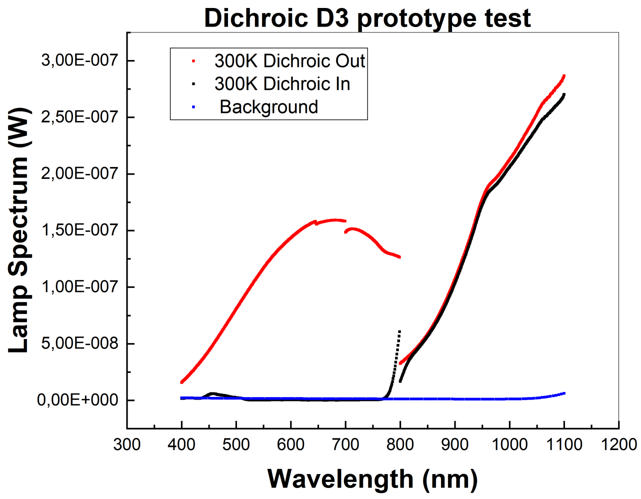

Figure 9: 300 K Spectrum 400 nm to 1100 nm as described in Figure 6. As per the previous picture, in black: spectrum with the filter in the optical axis, in red: spectrum without the filter in the optical axis. Blue: background noise.

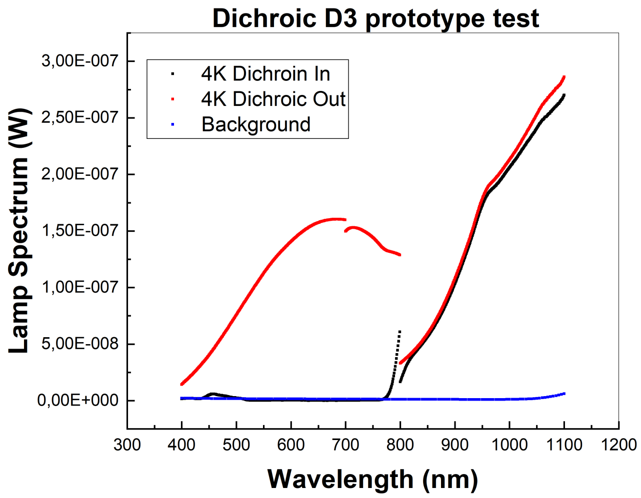

Figure 10: Spectrum 400 nm to 1100 nm as described in Figure 6. As per the previous picture, in black: spectrum with the filter in the optical axis, in red: spectrum without the filter in the optical axis. Blue: background noise. Top: curves at 300 K Bottom: curves at 4 K

B Experimental Setup specs

B.1 Monochromator

The factory calibrated $MSH-150$ has a focal length of 150 mm and uses a Czerny-Turner layout to minimise scattered light and maximise throughput. Effective internal baffling reduces general scatter whilst the mirror arrangement avoids rediffracted light.

Slits	10 μm to 10 mm
Aperture Ratio	$f/4.6$
Wavelength Reproducibility	$\pm 0.05\,nm$
Grating 1	MSG-S-600-500
Grating 2	MSG-S-600-1600
Theoretical Resolution for 1 mm slit	10 nm

Table 2: Monochromator specifications

B.2 Detectors

Two photodiode detectors are used, giving an effective detectable wavelength range of 400 nm to 2500 nm. Monochromatic light is delivered from the monochromatic exit slit to them via an optical fibre.

Thorlabs - Silicon Detector (S120C)

Detector Type	Silicon Photodiode
Wavelength Range	400 - 1100 nm
Optical Power Range	50 nW - 50 mW
Resolution	1 nW
Measurement uncertainity	±3% 440-980 nm ±5% 400-439 nm ±7% 981-1100 nm
Response time	$\leq 1\mu s$
Active Area	9.7 mm × 9.7 mm

Table 3: S120C specifications

Thorlabs - Integrating Sphere Power Sensor with Extended InGaAs Detector (S148C)

Detector Type	Extended InGaAS Photodiode
Wavelength Range	1200 - 2500 nm
Optical Power Range	1μW - 1000 mW
Resolution	1 nW
Measurement uncertainity	±5%
Response time	$\leq 1\mu s$
Active Area	$\phi\,1mm$

Table 4: S148C specifications

Acknowledgements

Thanks to CILAS for producing the Dichroic D3 prototype and for providing us with a preliminary testing which was of great help while carrying out experimental work.

A2 Equation derivation

A2.1 HEMT Noise

Here we want to calculate the equation that describes the HEMT noise contribution to the energy resolution. We will go through the maths that lead to equation 2 and **??** in Chapter 7. The basic assumption for this model is that the HEMT contributes equally to the in phase (I) and in quadrature (Q) noise in the I-Q plane. There is no strong argument for this to be considered an unreasonable starting point as already discussed by Zmuidzinas in (39). This assumption corresponds to saying that the HEMT is responsible for a perfectly circular scatter in the I-Q plane about the "resting" position of the resonator with diameters being $< I >$ and $< Q >$.
Zmuidzinas in (39) describes the fluctuation in the forward measured transmission as:

$$< \delta I(\nu)\delta I^*(\nu') >=< \delta Q(\nu)\delta Q^*(\nu') >= \frac{K_B T_A}{2P_g}\delta(\nu - \nu')$$

This means that cross-correlation between different frequencies (between ν and ν') vanish and that P_g is the power spectral density observed by the MKID, while T_A is the temperature noise of the amplifier. Henceforth, for brevity we will drop the delta notation and we will identify $< \delta I \delta I* >$ with $< I^2 >$ and likewise for $< Q^2 >$ which is reflected in the values of $< I >$ and $< Q >$ that represent the radius of the circular scatter just described.
This equation looks at the power spectral density of the noise, hence, only accounts for the noise in an infinitely sharp frequency bin. In reality, and given the readout electronics described in Chapter 2.4, the Fast Fourier Transform and its bandwidth have to come into play. The Fast Fourier Transform acquires 1μs of data and produces and therefore its frequency bin has a finite width. Since it can be assumed that the HEMT produces white noise across all frequencies, the width of the FFT bin, or the Bandwidth (BW) which is its reverse, defines the total power noise in the I and Q components. An hypothetical Fast Fourier Transform that uses an infinite amount of data would result in an infinitely sharp FFT bin and produce less noisy values of I and Q.
The second assumption made for the sake of this derivation is that the following identity is true: $< I >= \sqrt{< I^2 >}$ and likewise for $< Q >$. Under these circumstances, the diameter of the circular scatter is given by:

$$HEMT_{noise} =< I >=< Q >= \sqrt{\frac{K_B T_A G}{2P_g} BW}$$

Where G is the gain of the HEMT and P_g is the power spectral density as seen by the MKID, therefore . And here we're assuming no power loss in the MKID itself.
A small discussion on the gain of the amplifier is needed in this very specific instance. The amplifier is imagined as a four-terminal device that accepts a voltage input and

outputs a voltage. This model of the amplifier is imagined as an input resistance and an ideal amplifying stage and the noise temperature is defined as the temperature the input resistor would be at to produce the same amount of Johnson-Nyquist noise as the noise spectral power produced by the real amplifier. In this situation, the output spectral power noise produced by a change in temperature of the resistor can be described by the following equation:

$$P_{output} = K_B T_A G$$

A2.2 Energy resolution

We need to understand how to calculate how to translate this fluctuation in transmission into an uncertainty in energy resolution. This is achieved through some geometrical considerations. First of all, it is interesting to evaluate what angle, i.e. phase, is covered by $HEMT\_noise$.

$$\Delta\alpha = \frac{HEMT\_noise}{radius}$$

Here, considering a perfect transmission and therefore a unitary circle given by the transmission line, and since the minimum of the transmission is the closest point to the origin, it is possible to conclude that the diameter of the loop $d = 1 - min|S21|$. Simple geometrical considerations, such as shown in Figure A2.1 prove the previous statement.
By definition, the coupling quality factor Q_c is defined as $Q_c = \frac{Q_{tot}}{1-min|S21|}$. Hereby it is possible to substitute this into the previous equation; and solving for radius, rather than diameter one obtains the following relation:

$$\Delta\alpha = 2\frac{HEMT\_noise}{} Q_c Q_{tot} \tag{1}$$

This equation describes the width of the distribution of phase uncertainty given by the HEMT noise, in order to get a maximum value, it is common practice to take into account 3 sigmas, therefore multiply by 3 obtaining the equation used in Chapter 7. On a further note, for the sake of clarity it is important to understand that the naming of Q_{tot} has been changed to Q which is not to be mixed up with the quantity <Q> previously discussed.

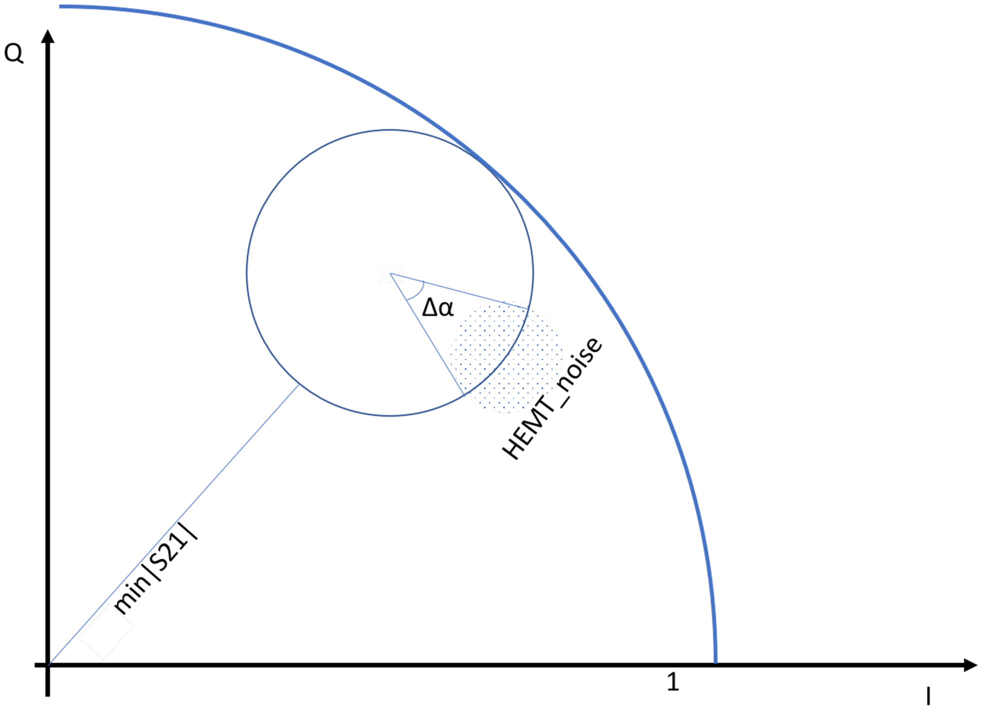

Figure A2.1: resonator loop in IQ plane. The outer circle describes the feed line delay while the inner circle represents the resonators' loop. The quantities in the figure reflect those described in the paragraph.

A3 Phase noise characterisation

A3.1 Understanding the phase noise

This section is intended as a place where to add a few extra words on the phase noise analysis performed and discussed in Section 9.2.1.
It was expected that a non illuminated resonator driven with its own resonant frequency, would have been seen in the IQ plane as an isotropic scatter around the position of the resonance frequency, and that the noise produced by the electronics, including the HEMT, would have been of the same magnitude in the radial direction as in the tangential direction (often referred to as phase). In order to investigate the nature of the phase noise described in Section 9.2.1, it was decided to drive the resonator with a frequency that is off resonance, and look at the feed-line delay loop. As soon as the driving frequency is off the resonance loop, the resonator noise returns to the expected circular scatter. Figure A3.1 shows that the scatter around the driving frequency is circular, isotropic and in terms of Analogue-to-Digital Units (units in the 12-bits sampler) the I and Q components, it is a circle of about 40 ADU and it represents the ADC noise in the sampling. It is noteworthy that the noise measured at resonance frequency (shown in Figure 9.4) is 1500 units long in the tangential direction (Phase) and about 500 units wide in amplitude direction.

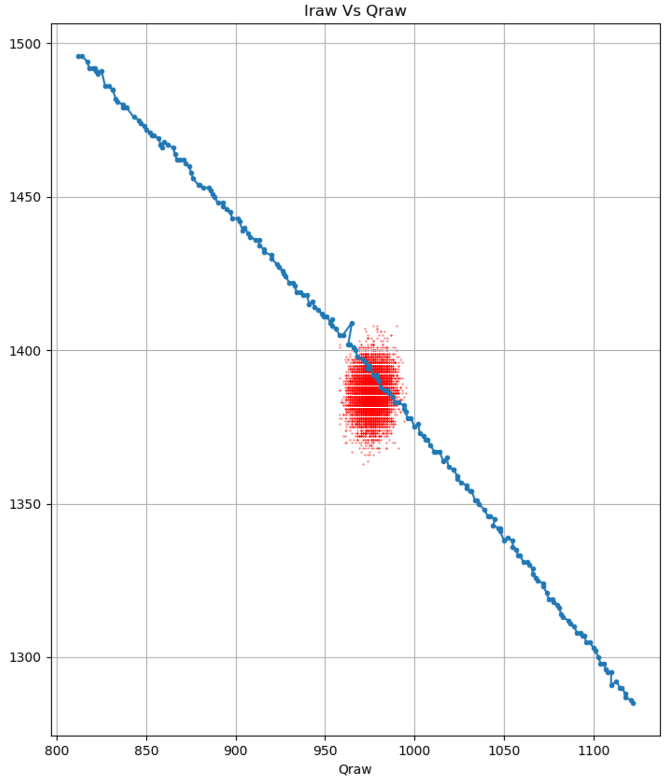

Figure A3.1: DAC noise on the cable delay loop. Out of resonance the noise has a diameter of approximately 40 Analogue-to-Digital Units. This confirms that the noise observed in the resonator at resonance frequency is not induced by the readout electronics.

A4 Transmission curves of different glasses

A4.1 Asahi YSC1100 Super Cold filter

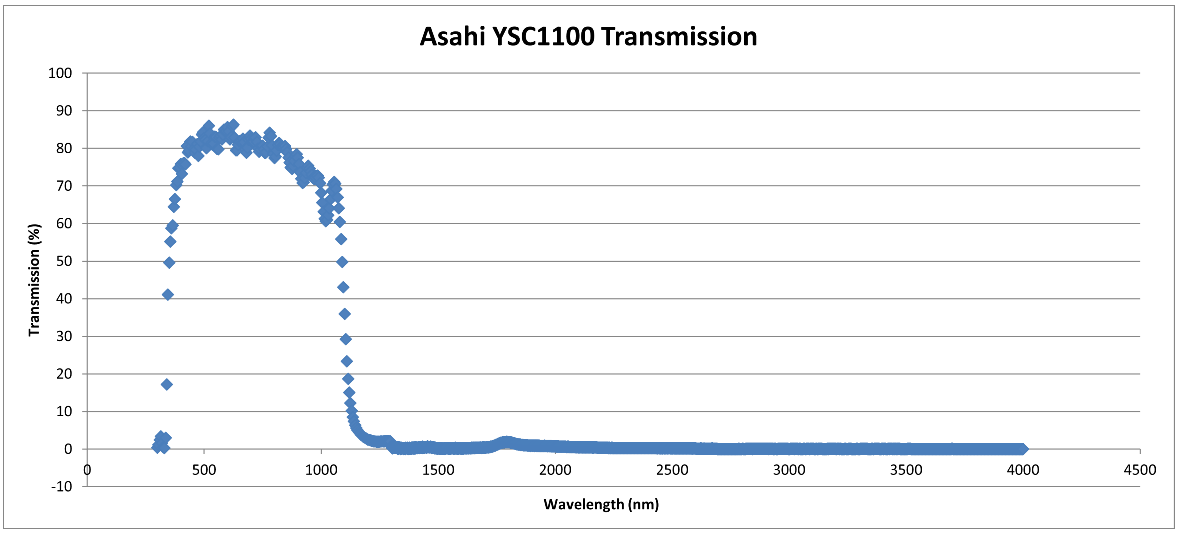

Figure A4.1: Transmission curve of the Asahi YSC1100 Super Cold Filter as provided by the manufacturer in (19)

A4.2 BK7 Glass filters

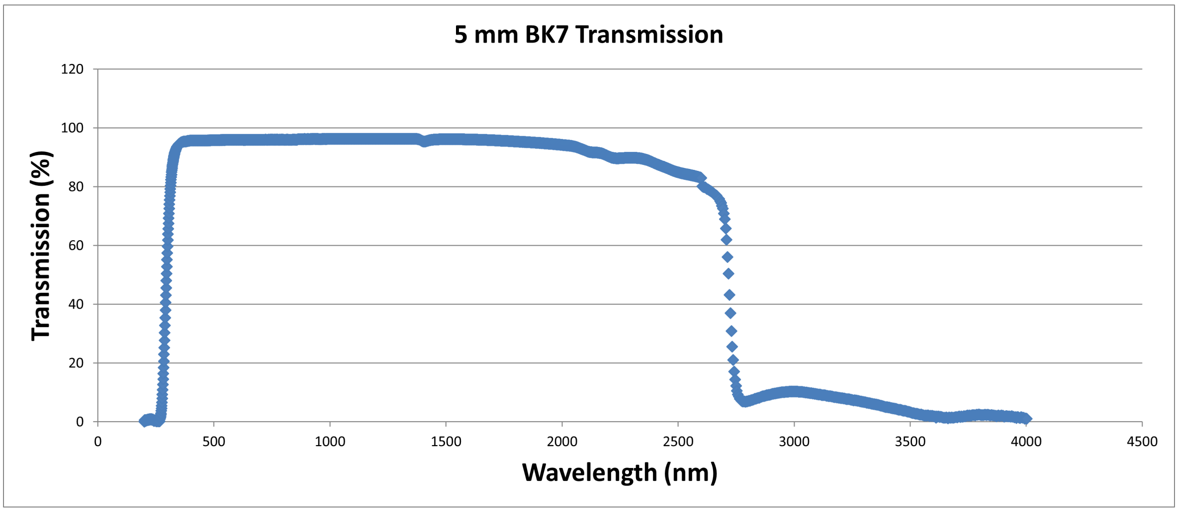

Figure A4.2: Transmission curve of 5mm thick BK7 glass as provided by the manufacturer in (20)

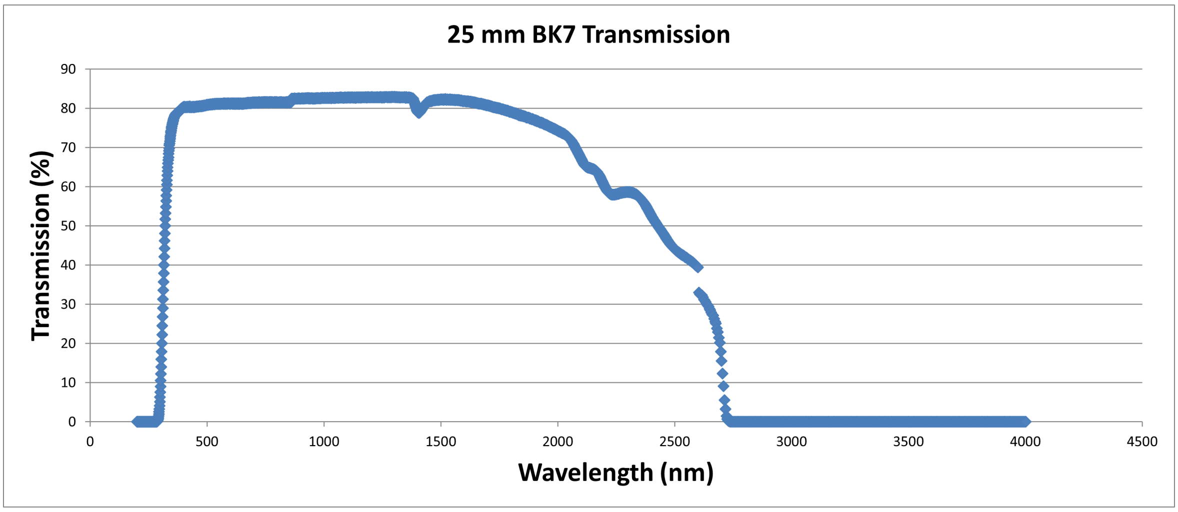

Figure A4.3: Transmission curve of 5mm thick BK7 glass as provided by the manufacturer in (20)

A4.3 Filters stacking

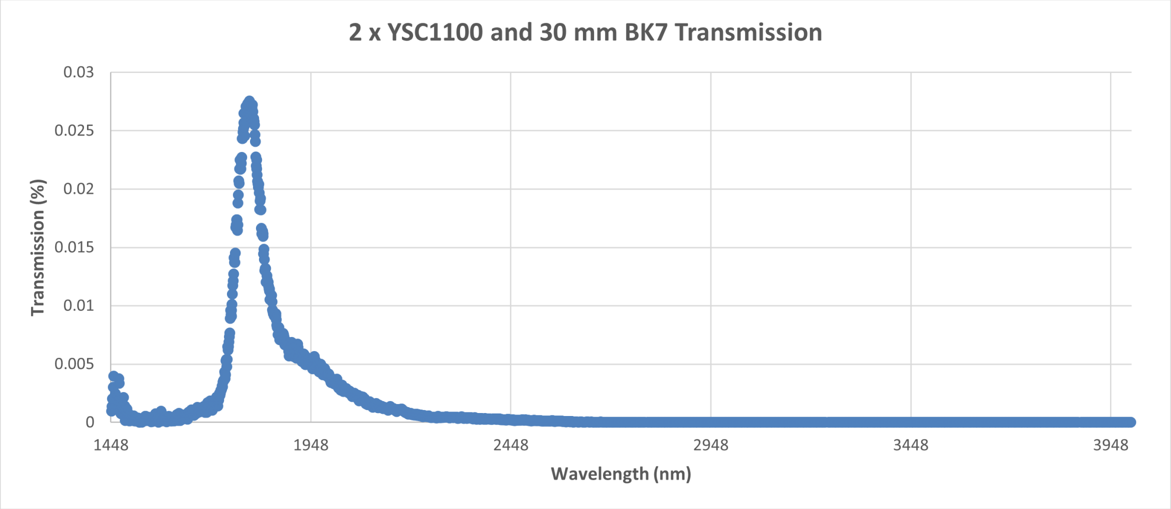

Figure A4.4: Transmission curve of 2 stacks of Asahi YSC1100 supercold filters and a total of 30mm (25mm + 5mm) of BK7 glass

A5 Residual Gas Analysis

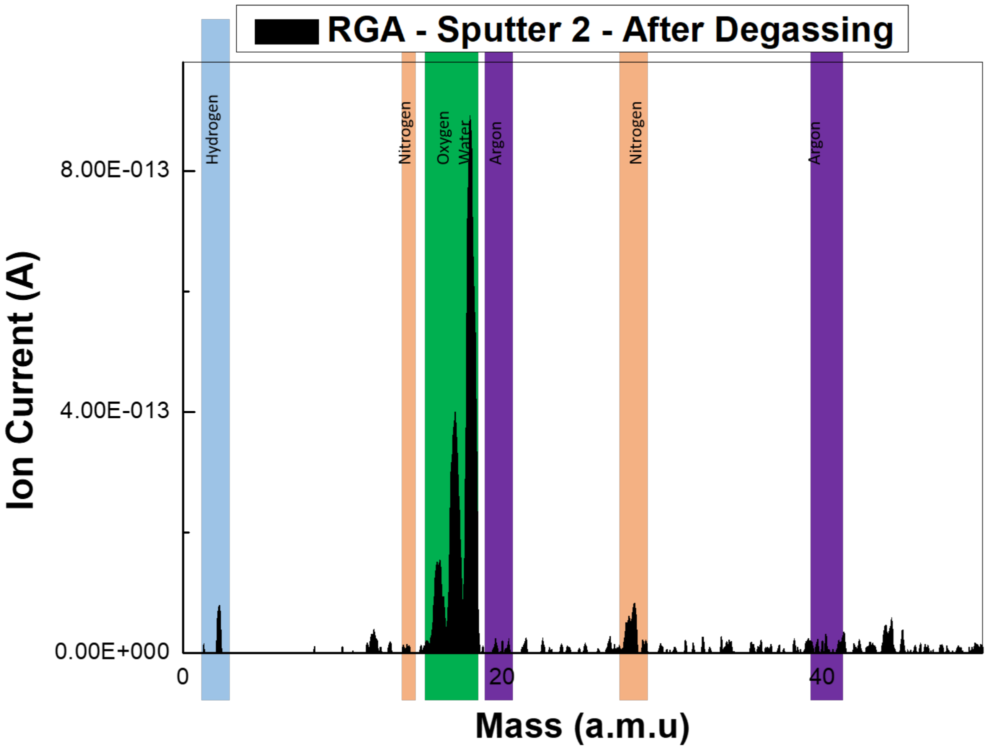

Figure A5.1: Residual Gas Analysis of the sputter chamber after the degassing process. Each different gaseous molecule is identifiable with a different colour: Cyan - Hydrogen ; Orange - Nitrogen ; Green - Water ; Purple - Argon

A5.1 Trifolium Dubium

The Trifolium Dubium sputter system was installed in the clean room in CRANN in the second half of 2018 and the Sputter chamber #2 suffered some issues including a sever malfunctioning of the wafer manipulator, after the robotic arm crashed into it during its commissioning phase. Once the manipulator got repaired and the deposition of Ti-based films was restarted, we couldn't deposit any Ti-based films that would exhibit superconducting properties, and some of them exhibited an unusual blue colour. It turned out that the Ti target had oxidised and was producing titanium oxynitride (TiO_xN_y) and required a rather long, high-power pre-sputter cleaning. During this investigation a residual gas analysis (mass spectrometry of the chamber atmosphere) has been performed so to characterise the sputtering chamber and its conditions before the deposition phase. Here is reported that at pressures $\approx 5 \times 10^{-9} mbar$ only small amounts of light gases can be found (Hydrogen, Nitrogen) and some amount of water that in these conditions does not constitute a hindrance to our deposition recipes.

A5.2 Mathematical derivation of equation 1 in Chapter 7

Let us assume that the n-th resonator is distributed according to a Gaussiand distribution around the frequency $n\Delta$, where n is an integer and Δ is the ideal spacing between adjacent resonators. And let us define a collision window around the 0th resonator of width w where is an integer and w is the line-width of the resonator. Under these assumptions, it is possible to define P_{n0}, the probability that the n-th resonator does not collide with the 0-th resonator, as:

$$P_{n0} = 1 - \frac{1}{\sqrt{2\pi\sigma}} \int\limits_{-\chi w}^{+\chi w} e^{\frac{1}{2}(\frac{(f_n - n\Delta}{\sigma})^2} df_n \tag{1}$$

It is possible to perform a change in the integration variable from f$_n$ to $t = \frac{f_n - n\Delta}{\sigma}$, therefore the integral changes from df$_n$ to dt $= \frac{1}{\sqrt{2}\sigma} df_n$. When changing the variables, it is important to remember to change the integration limits. Under the new variables, we have χw becoming $\frac{\chi w + \Delta n}{\sqrt{2}\sigma}$ and $-\chi w$ becoming $\frac{+\Delta n - \chi w}{\sqrt{2}\sigma}$.
The integral becomes:

$$\frac{1}{\sqrt{\pi}} \int\limits_{\frac{\Delta n - \chi w}{\sqrt{2}\sigma}}^{+\frac{\chi w + \Delta n}{\sqrt{2}\sigma}} e^{-t^2} dt \tag{2}$$

The error function $Erf(x)$ is defined as $Erf(x) = \frac{1}{\sqrt{\pi}} \int\limits_{-x}^{x} e^{-t^2} dt$, and it is immediate, given the size of the two intervals in question and the negative parity of the error function, that P_{n0} can be rewritten as:

$$P_{n0} = 1 - \frac{Erf(\frac{\chi w + n\Delta}{\sqrt{2}\sigma}) - Erf(\frac{n\Delta - \chi w}{\sqrt{2}\sigma})}{2} \tag{3}$$

q.e.d.